



**Università degli Studi ROMA TRE**

---

DEPARTMENT of ENGINEERING  
MECHANICAL and INDUSTRIAL SECTION  
Ph.D. Course in Mechanical and Industrial Engineering

PH.D. THESIS

**Experimental investigation of compressible and  
incompressible jet aeroacoustics in free and installed  
configurations through advanced time-frequency analysis**

Ph.D. candidate:  
**Eng. Matteo Mancinelli**

Advisor:  
**Prof. Roberto Camussi**

Ph.D. Course Coordinator:  
**Prof. Edoardo Bemporad**



*We are all born mad. Some remain so.*

Samuel Beckett (1906-1989)





## Abstract

In the present work advanced time-frequency analysis techniques have been applied to experimental jet aeroacoustic data. The study in the time and frequency domains has been carried out by standard Fourier analysis and innovative wavelet-based procedures. The objective of the thesis project was to exploit the potentialities of time-frequency analysis approach to get a better understanding of the jet physics and lay foundations for jet noise modelling. Two experimental applications were taken into account.

The first one concerns the decomposition of the near pressure field of a free jet into its hydrodynamic and acoustic components. Simultaneous near- and far-field pressure measurements on a single-stream compressible jet installed in a fully anechoic chamber were exploited to derive three innovative wavelet-based techniques for the separation of the hydrodynamic and acoustic pressures. The statistical and spectral features of the two components were characterized addressing the effect of the jet Mach number and the spatial location of the near-field microphone. For the first time, a direct link between the separated acoustic pressure in the near field and the actual noise measured in the far field was established, highlighting the different physical nature of the sound and pseudo-sound components.

The second application concerns the interaction between an incompressible jet and a surface. Experimental tests were carried out on a simplified laboratory-scale model where a rigid flat-plate was installed tangentially to the nozzle axis for different radial distances of the plate from the jet. Simultaneous velocity and wall pressure measurements were performed in order to assess the effect of the plate on the aerodynamic field and to characterize the wall pressure statistics and spectral content. Velocity/pressure cross-statistics was provided in the time and frequency domains as well. Furthermore, the jet flow acceleration was computed starting from the measured velocity field. The acceleration field was characterized in both free and installed jet conditions. Cross-correlations and cross-spectra between acceleration and wall pressure signals were investigated as well. Finally, a conditional sampling procedure based on wavelet transform was applied to the database in order to characterize the coherent flow signatures related to the velocity/acceleration and wall pressure fluctuations underlying the jet-plate interaction phenomena.



# Acknowledgements

I am sincerely thankful to my advisor Prof. Roberto Camussi for his cordiality, guidance and support during my Ph.D. research project.

I am also grateful to Dr. Tiziano Pagliaroli for his comments and the useful discussions on the topics. I cannot forget to mention Eng. Marco Terzitta for his help and suggestions. I appreciated very much the nice working environment we created. Dr. Alessandro Di Marco is acknowledged as well.

I would like to thank Dr. Emiliano Carnielo and my colleagues Eng. Riccardo Pellegrini, Eng. Gabriele Battista, Eng. Gianluca Coltrinari and Eng. Luca Mauri for these three years spent enjoying together. I also want to mention some of the Bachelor's Degree, Master's Degree students and interns I had the pleasure to supervise. Stefano Muzi, Matteo Tarantino, Dario Celli, Edoardo Grande, Giulia Gigante, Eleonora Venditti, Matteo Zanchi, Andrea Fagotto, Ilaria Cioffi, Daniele Sacchetti, Veronica Della Rovere and Flavio Napoli, Federico Caruso, Tommaso Tondi, Stefano Meloni are acknowledged for their hard work and for the help they provided to achieve my Ph.D. project targets.

I would like to thank my parents and my family (especially my little sweet niece Ambrosia) for the support they provided me. Hope to give back all I have taken one day...

I want to spend a few but sweet words for my girlfriend Eleonora. I always felt her beside me having the feeling that the time spent and shared together was our best time.

Finally I want to thank all of my friends for the fun we had in the free time. Special mention for Flavio Panetta and Alessandro Resse for the hours spent playing Xbox together throwing out "frustration".

At last but not least, I would like to acknowledge the group of the Centre Acoustique of Laboratoire de Mécanique des Fluides et d'Acoustique at the École Centrale de Lyon in the person of Dr. Thomas Castelain for the support provided.

Finally, the author acknowledges the partial support of the EU Collaborative projects ORINOCO (ACP0-GA-2010-266103) and JERONIMO (ACP2-GA-2012-314692) funded under the 7th Framework Program.



# Contents

<b>I</b>	<b>Preface</b>	<b>1</b>
<b>1</b>	<b>Introduction</b>	<b>3</b>
1.1	Motivations . . . . .	3
1.2	Objectives . . . . .	4
<b>2</b>	<b>Short discussion on time-frequency analysis</b>	<b>5</b>
2.1	Generalities . . . . .	5
2.2	Wavelet approach . . . . .	7
2.2.1	Wavelet vs. Fourier . . . . .	9
2.2.2	Why use wavelets in turbulent flows . . . . .	12
<b>II</b>	<b>Hydrodynamic/acoustic pressure decomposition</b>	<b>15</b>
<b>3</b>	<b>Introduction</b>	<b>17</b>
<b>4</b>	<b>Wavelet-based separation techniques</b>	<b>19</b>
4.1	Wavelet technique 'WT1' . . . . .	20
4.1.1	Validation of the choice of the optimal threshold value . . . . .	20
4.2	Wavelet technique 'WT2' . . . . .	21
4.3	Wavelet technique 'WT3' . . . . .	22
<b>5</b>	<b>Experimental set-up</b>	<b>25</b>
5.1	Facility description . . . . .	25
5.2	Instrumentation . . . . .	25
<b>6</b>	<b>Results</b>	<b>27</b>
6.1	Jet assessment . . . . .	27
6.1.1	Jet aerodynamics . . . . .	27
6.1.2	Jet aeroacoustics . . . . .	29
6.1.2.1	Near field . . . . .	29
6.1.2.2	Far field . . . . .	33
6.2	Fourier-based separation procedure . . . . .	36
6.3	Validation of the novel separation techniques . . . . .	39
6.4	Characterization of hydrodynamic/acoustic pressures . . . . .	42
6.4.1	Spectral characterization . . . . .	44
6.4.2	Analysis of pseudo-sound and sound components in the time domain	44
6.4.2.1	Cross-correlations . . . . .	47
6.4.2.2	Statistical analysis of hydrodynamic and acoustic pressures	49

<b>III Jet-surface interaction</b>	<b>55</b>
<b>7 Introduction</b>	<b>57</b>
<b>8 Experimental apparatus</b>	<b>59</b>
8.1 Jet facility description . . . . .	59
8.2 Experimental set-up . . . . .	60
8.3 Instrumentation . . . . .	60
<b>9 Wavelet-based conditional sampling procedure</b>	<b>65</b>
9.1 Auto-conditioning procedure . . . . .	66
9.2 Cross-conditioning procedure . . . . .	67
<b>10 Results</b>	<b>69</b>
10.1 Free-jet characterization . . . . .	69
10.1.1 Velocity field . . . . .	69
10.1.1.1 Auto-conditioned velocity signatures . . . . .	74
10.1.2 Acceleration field . . . . .	74
10.1.2.1 Acceleration computation . . . . .	75
10.1.2.2 Statistics of the acceleration field . . . . .	76
10.1.2.3 Spectral characterization . . . . .	76
10.1.2.4 Auto-conditioned acceleration signatures . . . . .	80
10.2 Plate effect on the velocity field . . . . .	80
10.3 Plate effect on the acceleration field . . . . .	85
10.4 Wall pressure field characterization . . . . .	87
10.4.1 Statistical analysis . . . . .	87
10.4.1.1 Probability Density Functions . . . . .	91
10.4.1.2 Cross-correlation between wall pressure signals . . . . .	93
10.4.2 Spectral characterization . . . . .	93
10.4.3 Wall pressure fluctuations modelling . . . . .	95
10.4.3.1 Scaling criterion for auto-spectra . . . . .	95
10.4.3.2 Coherence function . . . . .	97
10.5 Cross-statistics: velocity vs wall pressure . . . . .	98
10.5.1 Cross-correlations . . . . .	101
10.5.2 Cross-spectra . . . . .	103
10.6 Cross-statistics: acceleration vs wall pressure . . . . .	106
10.6.1 Cross-correlations . . . . .	106
10.6.2 Cross-spectra . . . . .	109
10.7 Wavelet analysis . . . . .	110
10.7.1 Velocity auto-conditioning . . . . .	110
10.7.1.1 Scaling criterion for velocity signatures . . . . .	114
10.7.2 Wall pressure auto-conditioning . . . . .	115
10.7.3 Pressure/pressure cross-conditioning . . . . .	117
10.7.4 Velocity/pressure cross-conditioning . . . . .	117
10.7.4.1 Implications for velocity signatures modelling . . . . .	120
10.7.5 Acceleration/pressure cross-conditioning . . . . .	123

<b>IV</b>	<b>Conclusions</b>	<b>127</b>
<b>11</b>	<b>Final remarks</b>	<b>129</b>
11.1	Hydrodynamic/acoustic pressure separation . . . . .	129
11.1.1	Future developments . . . . .	131
11.2	Jet-plate interaction . . . . .	132
11.2.1	Future developments . . . . .	136
	<b>Bibliography</b>	<b>137</b>





# List of Figures

2.1	Representation in the time and frequency domains of the Dirac function used as basis for the Shannon transform: (a) $\delta(t - t_0)$ with $t_0 = 0$ s, (b) $\hat{\delta}(f)$ . . . . .	6
2.2	Representation in the time and frequency domains of the sine function used as basis for the Fourier transform: (a) $S(t) = \sin(2\pi f_0 t)$ with $f_0 = 20$ Hz, (b) $\hat{S}(f)$ . . . . .	6
2.3	Representation in the time and frequency domains of the basis adopted for the Gabor transform. (a) Time domain $S(t) = \sin(2\pi f_0 t) e^{-a\pi(t-\tau)^2}$ : (I) $f_0 = 40$ Hz, (II) $f_0 = 20$ Hz, (III) $f_0 = 10$ Hz. (b) $\hat{S}(t, f)$ : (I) $f_0 = 40$ Hz, (II) $f_0 = 20$ Hz, (III) $f_0 = 10$ Hz. . . . .	8
2.4	Representation in the time and frequency domains of the Mexican Hat wavelet at different scales. (a) Time domain $\psi(t)$ . (b) $\hat{\psi}(f)$ . . . . .	10
2.5	Example of the time-scale representation using the wavelet transform. . . . .	11
2.6	Comparison between the spectrum obtained by the standard Fourier transform and the wavelet approach. As an example, a wall pressure time series obtained by experimental measurements on the interaction between the incompressible jet and the flat-plate has been taken into account. . . . .	12
2.7	Example of the time-scale representation of the modulus of the wavelet coefficients of the academic signal $x_1(t) + x_2(t)$ . . . . .	13
4.1	Separation technique WT1: cross-correlation coefficient peak along the number of iterations of the acoustic and hydrodynamic components with the measured far-field pressure. Jet Mach number $M_j = 0.6$ , near-field microphone axial location $x/D = 8.7$ , far-field microphone polar position $\psi = 140^\circ$ . The separation point for which the convergence criterion is satisfied is highlighted with an arrow. . . . .	21
4.2	Wavelet technique WT1: comparison between the pressure spectra obtained by the gradient-based optimization method and the Particle Swarm Optimization. . . . .	22
4.3	Separation technique WT2: Probability Density Functions of original, hydrodynamic and acoustic pressures and comparison with the standard Gaussian distribution. Jet Mach number $M_j = 0.6$ , microphone axial position $x/D = 5.6$ . . . . .	23
4.4	Separation technique WT3: trend along the iterations of the number of wavelet coefficients of the acoustic pressure normalized by the total number of the wavelet coefficients of the original signal. Jet Mach number $M_j = 0.6$ , microphone axial position $x/D = 7.4$ . . . . .	24

5.1	Sketch of the experimental set-up and scheme of the microphones disposition	26
6.1	Dimensionless mean and fluctuating velocity profiles along the non-dimensional radial coordinate $\eta$ at different axial positions $x$ for jet Mach number $M_j = 0.6$ : (a) mean velocity, (b) relative turbulence level. . . .	28
6.2	Axial evolution of the pressure spectra: (a) jet Mach number $M_j = 0.6$ , (b) jet Mach number $M_j = 0.9$ . . . . .	30
6.3	Contour plot of the Sound Pressure Spectrum Level along the stream-wise direction for both jet Mach numbers. . . . .	31
6.4	Dimensionless pressure spectra for jet Mach number $M_j = 0.6$ at different axial distances. . . . .	31
6.5	Axial evolution of the cross-correlation coefficient between two consecutive microphone signals in the near field: (a) jet Mach number $M_j = 0.6$ , (b) jet Mach number $M_j = 0.9$ . . . . .	32
6.6	Polar trend of the far-field pressure spectra for jet condition $M_j = 0.9$ . .	33
6.7	Comparison between experimental pressure spectra and results obtained by the application of the Tam's model. . . . .	34
6.8	Polar evolution of the OverAll Sound Pressure Level for both jet Mach numbers. . . . .	34
6.9	Polar evolution of the <i>PDFs</i> of the far-field pressure for both jet conditions. Dashed line refers to the standard Gaussian distribution. . . . .	35
6.10	Polar evolution of the skewness and flatness factors of the far-field pressure for both jet conditions. . . . .	35
6.11	Normalized wavenumber-frequency spectrum of the near pressure field for both jet flow conditions. (a) jet Mach number $M_j = 0.6$ , (b) jet Mach number $M_j = 0.9$ . Dashed lines refer to the speed of sound, dash-dotted lines refer to the convection velocity. . . . .	37
6.12	$k - \omega$ technique: space-time map of original, hydrodynamic and acoustic near pressure fields separated by the Fourier filtering technique for both jet velocities. . . . .	38
6.13	$k - \omega$ technique: cross-correlation coefficient peak map of hydrodynamic and acoustic components with measured far-field pressure at all the axial and polar positions for both jet Mach numbers. . . . .	38
6.14	<i>SPSLs</i> of hydrodynamic and acoustic pressures separated with all the different wavelet techniques at axial position $x/D = 7.8$ for $M_j = 0.9$ : (a) hydrodynamic component, (b) acoustic component. . . . .	40
6.15	Axial evolution of the cross-correlation coefficient peak of near-field hydrodynamic and acoustic components with far-field pressure for polar position $\psi = 140^\circ$ at $M_j = 0.6$ . . . . .	41
6.16	Polar evolution of the cross-correlation coefficient peak of far-field pressure with near-field hydrodynamic and acoustic components at axial position $x/D = 6.1$ at $M_j = 0.6$ . . . . .	41
6.17	Axial evolution of the normalized convection and acoustic propagation velocities for jet Mach number $M_j = 0.6$ . . . . .	42
6.18	Wavelet technique WT1: effect of the far-field polar angle chosen to perform the separation on the hydrodynamic and acoustic pressure spectra at near-field axial location $x/D = 6.6$ for jet Mach number $M_j = 0.9$ . (a) Hydrodynamic pressure, (b) acoustic pressure. . . . .	43

6.19	Wavelet technique WT1: <i>SPSL</i> of the original, hydrodynamic and acoustic pressure signals for a microphone axial position $x/D = 7.8$ for both jet flow conditions. (a) $M_j = 0.6$ , (b) $M_j = 0.9$ . . . . .	45
6.20	Wavelet technique WT1: axial evolution of <i>SPSLs</i> of separated hydrodynamic and acoustic pressures for both jet flow conditions. . . . .	46
6.21	Wavelet technique WT1: contour map of the stream-wise evolution of the <i>SPSL</i> of the separated hydrodynamic and acoustic pressures for both jet Mach numbers. . . . .	46
6.22	Wavelet technique WT1: axial evolution of the <i>OASPL</i> of near-field original, hydrodynamic and acoustic pressures for both jet flow conditions. . . . .	47
6.23	Wavelet technique WT1: representation of the relative energy level of the separated hydrodynamic and acoustic pressure components function of the corresponding number of wavelet coefficients normalized by the total amount of wavelet coefficients. . . . .	48
6.24	Wavelet technique WT1: space-time contour map of the original, the hydrodynamic and the acoustic near pressure fields. . . . .	48
6.25	Wavelet technique WT1: cross-correlation coefficient of the original, hydrodynamic and acoustic near-field pressures at axial location $x/D = 7.8$ with the far-field pressure at polar position $\psi = 140^\circ$ for jet Mach number $M_j = 0.6$ . . . . .	49
6.26	Wavelet technique WT1: Cross-correlation coefficient between two consecutive near-field microphone signals at axial positions $x/D = 5.6$ and $x/D = 6.1$ for both jet flow conditions: (a) $M_j = 0.6$ , (b) $M_j = 0.9$ . . . . .	50
6.27	Wavelet technique WT1: Cross-correlation coefficient map along the stream-wise direction of original, hydrodynamic, acoustic pressures for both jet Mach numbers. . . . .	51
6.28	Wavelet technique WT1: axial evolution of the skewness factor of original, hydrodynamic and acoustic pressures for both jet conditions. . . . .	51
6.29	Wavelet technique WT1: axial evolution of the flatness factor of original, hydrodynamic and acoustic pressures for both jet conditions. . . . .	52
6.30	Wavelet technique WT1: axial evolution of the probability density functions of the hydrodynamic and acoustic pressures for both jet Mach numbers. . . . .	53
8.1	Representation of the jet facility. Hon# and S# indicate the honeycomb panels and the mesh screens, respectively. . . . .	60
8.2	Sketch of the experimental set-up for the jet-plate configuration. . . . .	61
8.3	Representation of the pin-hole design for the wall pressure measurements on the flat-plate. . . . .	62
8.4	Sketch of the instrumentation set-up. $\alpha$ is the jet spreading angle. . . . .	63
9.1	Example of the selection procedure of the most energetic events in a time signal based on the <i>LIM</i> computation. (a) Time-frequency map of the <i>LIM</i> . (b) 1D plot of the <i>LIM</i> at a given scale/frequency; the local maxima are highlighted with a circle whereas the trigger threshold level is represented by a dash-dotted line. (c) Portion of the wall pressure signal; the segments corresponding to large values of the <i>LIM</i> are highlighted with a dashed-line window. . . . .	66

10.1	Mean velocity profiles along the $z$ -axis. (a) Velocity profiles in the potential core region normalized by the nozzle exhaust velocity. (b) Velocity profiles in the turbulent jet region normalized by the mean velocity along the jet axis and radial distance normalized by the jet half width. . . . .	70
10.2	Evolution along the jet axis of the velocity statistical moments. (a): mean axial velocity normalized by the jet velocity and velocity variance normalized by the square mean velocity on the jet axis. (b): skewness and flatness factors. . . . .	71
10.3	Inverse of the ratio between mean axial velocity and jet velocity along axial distance: $\diamond$ potential core region, $\circ$ transition region, $\square$ developed flux region. . . . .	72
10.4	Axial evolution of dimensionless velocity power spectral density along the jet axis. Dashed straight line refers to Kolmogorov's decay law. . .	73
10.5	Velocity $PSD$ map along the jet axis in free-jet conditions. . . . .	73
10.6	Stream-wise evolution of the auto-conditioned velocity signatures along the jet axis. . . . .	74
10.7	Dimensionless mean and fluctuating acceleration profiles along the $z$ -direction for different axial distances. (a) mean component, (b) standard deviation. . . . .	77
10.8	Evolution along the jet axis of the main statistical moments of acceleration. (a) mean and standard deviation, (b) skewness and flatness factors. . . . .	78
10.9	Stream-wise evolution of the dimensionless $PSDs$ of acceleration signal along the jet axis. . . . .	79
10.10	Contour map of the dimensionless $PSD$ of the acceleration signals along the jet axis. . . . .	79
10.11	Contour map of the dimensionless $PSD$ of the acceleration signals along the $z$ -direction for different axial positions. . . . .	80
10.12	Stream-wise evolution of the auto-conditioned acceleration signature. .	81
10.13	Velocity profiles normalized by $U_{MAX}$ as a function of $z/D$ at different axial distances. . . . .	82
10.14	Jet axis location at different axial positions from the nozzle exhaust for different plate distances. . . . .	83
10.15	Dimensionless mean velocity field in the plane $x - z$ for all the jet-plate configurations. Dash-dotted lines represent the nozzle axis. . . . .	83
10.16	Turbulence intensity profiles as a function of $z/D$ at different axial distances. . . . .	84
10.17	Turbulence intensity field in the plane $x - z$ for all the jet-plate distances. Dash-dotted lines represent the nozzle axis. . . . .	84
10.18	Skewness factor of the velocity field in the plane $x - z$ for all the jet-plate configurations. Dash-dotted lines represent the nozzle axis. . . . .	85
10.19	Flatness factor of the velocity field in the plane $x - z$ for all the jet-plate configurations. Dash-dotted lines represent the nozzle axis. . . . .	86
10.20	Contour map of the dimensionless mean acceleration in the plane $x-z$ for all the jet-plate configurations. . . . .	86
10.21	Contour map of the dimensionless acceleration standard deviation in the plane $x-z$ for all the jet-plate configurations. . . . .	87

10.22	Contour map of the acceleration skewness factor in the plane $x$ - $z$ for all the jet-plate configurations. . . . .	88
10.23	Contour map of the acceleration flatness factor in the plane $x$ - $z$ for all the jet-plate configurations. . . . .	88
10.24	Pressure coefficients on the flat-plate along the jet axis: (a) mean pressure, (b) root mean square pressure. . . . .	90
10.25	<i>OASPL</i> map on the flat-plate for all the surface radial distances from the nozzle axis. . . . .	91
10.26	Pressure <i>PDF</i> s at different axial positions for all the jet-plate configurations. . . . .	92
10.27	Axial evolution of the pressure <i>PDF</i> s for all the plate positions. . . . .	92
10.28	Wall pressure cross-correlation coefficient between consecutive stream-wise microphone signals on the jet axis at different axial positions for all the jet-plate configurations. . . . .	94
10.29	Convection velocity along the stream-wise direction on the jet axis for all the flat-plate radial distances. . . . .	94
10.30	<i>SPSL</i> vs Strouhal number at different axial distances for all the jet-plate configurations. . . . .	95
10.31	<i>SPSL</i> vs Strouhal number along the span-wise direction at $x/D = 15$ for all the flat-plate radial distances. . . . .	96
10.32	<i>SPSL</i> vs Strouhal number along the span-wise direction at $x/D = 25$ for all the flat-plate radial distances. . . . .	96
10.33	Dimensionless <i>PSDs</i> of wall pressure signals at axial distance $x/D = 25$ for all the jet-plate configurations. Energy decay laws function of the frequency range considered are also reported. . . . .	97
10.34	Scaled wall pressure spectra at different axial positions and flat-plate distances depending on the region reported in table 10.2. . . . .	98
10.35	Coherence function parametrized by the flat-plate distance for different axial positions. Markers are for experimental data and lines for Corcos' model fits. . . . .	99
10.36	Stream-wise evolution of the coherence function for all the flat-plate distances from the jet. Markers are for experimental data and lines for Corcos' model fits. . . . .	99
10.37	Axial evolution of the Corcos' coefficient from $x/D = 14$ to $x/D = 25$ for all the jet-plate distances. Solid and dashed lines refer to the lower and upper limit values of the Corcos' coefficient, respectively. . . . .	100
10.38	Sketch of the hot-wire and microphone disposition for the computation of the cross-correlations and cross-spectra. Red color refers to HW transverse position on the nozzle axis, black color to the jet axis position, blue color to the $\zeta$ position (for more details on the definition of the cross-wise positions see §8.2 and §10.2). . . . .	100
10.39	Cross-correlation coefficient between velocity and wall pressure signals for $H/D = 1$ at different axial positions. . . . .	102
10.40	Cross-correlation coefficient maps along the $z$ -axis between velocity and wall pressure signals for the plate radial distance $H/D = 1$ . . . . .	102
10.41	Cross-correlation coefficient maps along the axial distance for hot-wire transverse positions corresponding to the jet axis. . . . .	103

10.42	Cross-correlation coefficient maps along the axial distance for hot-wire transverse position $\zeta$ . . . . .	104
10.43	Effect of the plate radial distance on the cross-correlation coefficient between velocity and wall pressure signals for the hot-wire transverse positions on the jet axis. . . . .	104
10.44	Effect of the plate radial distance on the cross-correlation coefficient between velocity and wall pressure signals for the hot-wire transverse positions corresponding to $\zeta$ . . . . .	105
10.45	Dimensionless Cross-Power Spectral Density maps along the $z$ -direction for $H/D = 1$ at different axial positions. . . . .	106
10.46	Effect of the plate radial distance from the jet on the Cross-Power Spectral Density between consecutive velocity and wall pressure signals at axial positions. . . . .	107
10.47	Dimensionless Cross-Power Spectral Density maps along the $x$ -axis for hot-wire transverse positions corresponding to the jet axis. . . . .	107
10.48	Stream-wise evolution of the cross-correlation coefficient between acceleration and wall pressure signals at the HW transverse position on the nozzle axis for all the jet-plate configurations. . . . .	108
10.49	Stream-wise evolution of the cross-correlation coefficient between acceleration and wall pressure signals at the HW transverse position closest to the flat-plate for all the jet-surface configurations. . . . .	109
10.50	Cross-wise evolution of the cross-correlation coefficient between acceleration and wall pressure signals at different HW axial positions function of the jet-surface radial distance. . . . .	110
10.51	Cross-wise evolution of the dimensionless cross-power spectral density between acceleration and wall pressure signals at different axial distances for the jet-plate distance $H/D = 1$ . . . . .	111
10.52	Stream-wise evolution of the dimensionless cross-power spectral density between acceleration and wall pressure signals along the nozzle axis for all the jet-plate distances. . . . .	111
10.53	Axial evolution of the auto-conditioned velocity signatures along the nozzle axis for all the jet-plate configurations. . . . .	112
10.54	Contour maps of the auto-conditioned velocity signatures along the nozzle axis for all the jet-plate configurations. . . . .	113
10.55	Contour maps of the auto-conditioned velocity signatures along the stream-wise direction at the hot-wire transverse position $\zeta$ for all the jet-plate configurations. . . . .	113
10.56	Auto-conditioned velocity signatures at the hot-wire transverse position $\zeta$ for all the flat-plate radial distances. . . . .	114
10.57	Scaled auto-conditioned velocity signatures at the hot-wire transverse position $\zeta$ for all the jet-plate distances. . . . .	115
10.58	Contour maps along the stream-wise direction of the wall pressure signatures derived from the auto-conditioning technique for all the jet-plate distances. . . . .	116
10.59	Effect of the jet-plate distance on the auto-conditioned wall pressure signatures at different axial positions. . . . .	116
10.60	Stream-wise evolution of the cross-conditioned wall pressure signatures for all the jet-plate configurations at different axial distances. . . . .	117

10.61	Effect of the HW transverse position on the cross-conditioned velocity signatures at the axial location $x/D = 24$ for all the jet-plate configurations.	118
10.62	Contour maps of the cross-conditioned velocity signatures along the stream-wise direction at the hot-wire transverse location $\zeta$ for all the jet-plate configurations. . . . .	119
10.63	Contour maps of the cross-conditioned velocity signatures as a function of the dimensionless frequency/scale for all the jet-plate configurations. HW axial position $x/D = 24$ , mic axial position $x/D = 25$ . . . . .	119
10.64	Effect of the jet-plate distance on the velocity signatures conditioned on wall pressure signals for different HW axial positions. . . . .	120
10.65	Axial evolution of the normalized convection velocity computed from the time-delay of the velocity signature peaks conditioned on the wall pressure events for all the jet-plate distances: $\diamond$ $H/D = 1$ , $\circ$ to $H/D = 1.5$ , $\square$ to $H/D = 2$ , $\triangle$ to $H/D = 2.5$ . . . . .	121
10.66	Scheme of the disposition of the HW and microphone array to assess the effect of the separation distance between the probes on the cross-conditioned velocity signatures. . . . .	121
10.67	Effect of the stream-wise separation between the probes on the flow structures educed by the cross-conditioning technique for the HW probe in $\zeta$ and $x/D = 21$ and for all the jet-plate configurations. . . . .	122
10.68	Time evolution of the cross-conditioned velocity signature peaks represented in figure 10.67 for all the jet-plate distances. . . . .	123
10.69	Acceleration signature conditioned on wall pressure events at the HW axial distance $x/D = 1$ and the transverse position $z/D \approx -0.6$ for the jet-plate distance $H/D = 1$ . . . . .	124
10.70	Contour map of the dimensionless acceleration signature conditioned on wall pressure events as a function of the wavelet scale/pseudo-frequency expressed as Strouhal number. HW axial distance $x/D = 1$ , HW transverse position $z/D \approx -0.6$ , jet-plate distance $H/D = 1$ . . . . .	125
10.71	Cross-wise evolution of the dimensionless acceleration signature conditioned on wall pressure events at different HW axial distances for jet-plate distances $H/D = 1$ and $1.5$ . . . . .	126





# List of Tables

5.1	Summary of the jet flow conditions analysed and of the location of the near- and far-field microphones . . . . .	26
8.1	Summary of the experiment configurations in the first test campaign. .	63
8.2	Summary of the experiment configurations in the second test campaign.	64
10.1	Summary of the jet impact axial positions on the flat-plate. . . . .	89
10.2	Axial locations of the jet-plate interaction regions. . . . .	90



# Nomenclature

$\nu$	Kinematic viscosity [ $m^2 s^{-1}$ ]
$\beta$	Coefficient of the Corcos' model for the coherence function of the wall pressure fluctuations in a TBL
$\Delta f_{ref}$	Reference frequency equal to 1 $Hz$ used for computation of dimensionless $PSD$
$\delta_\theta$	Momentum thickness of the shear layer of the jet
$\epsilon$	Turbulent kinetic energy dissipation rate [ $m^2 s^{-3}$ ]
$\eta$	Dimensionless radial coordinate
$\gamma(\xi, \omega)$	Coherence function
$\hat{x}(f)$	Fourier transform of the generic signal $x(t)$
$\lambda_T$	Taylor micro-scale [ $m$ ]
$\langle \cdot \rangle$	Ensemble average
$\langle \cdot \rangle_t$	Time average
$\langle u_i   u_i \rangle^*$	Scaled auto-conditioned velocity signature
$\langle x'^2 \rangle$	Variance of the generic time signal $x(t)$
$\langle x'^2 \rangle^{1/2}$	Standard deviation of the generic signal $x(t)$
$\langle x'^3 \rangle / \langle x'^2 \rangle^{3/2}$	Skewness factor of the generic signal $x(t)$
$\langle x'^4 \rangle / \langle x'^2 \rangle^2$	Flatness factor or kurtosis of the generic signal $x(t)$
$\langle x(t)   x(t) \rangle$	Auto-conditioned ensemble average of signal $x(t)$
$\langle y(t)   x(t) \rangle$	Ensemble average of signal $y(t)$ conditioned on signal $x(t)$
$\Omega$	Vorticity tensor [ $s^{-1}$ ]
$\nu_t$	Turbulent kinematic viscosity [ $m^2 s^{-1}$ ]
$\omega$	Angular frequency [ $rad s^{-1}$ ]
$\Phi_x$	Auto-spectrum of signal $x(t)$
$\Phi_{xy}$	Cross-spectrum between signals $x(t)$ and $y(t)$

$\psi$	Polar angle in the far field of the jet defined positive in the upstream direction
$\Psi(t)$	Mother wavelet function
$\psi_{s,\tau}(t)$	Wavelet basis obtained by dilation and translation of the mother wavelet $\Psi(t)$
$\rho_\infty$	ambient air density $= 1.225 \text{ kg m}^{-3}$
$\rho_{xy}$	Cross-correlation coefficient between the generic time signals $x(t)$ and $y(t)$
$\tau_L$	Integral time-scale of the axial velocity [s]
$\tau^*$	Scaled time-scale for the auto-conditioned velocity signatures
$\tau_c$	Convective time-scale adopted for the scaling of the wall pressure auto-spectra $= H/U_c$
$\mathbf{E}$	Strain rate tensor [ $s^{-1}$ ]
$\mathbf{u}$	Velocity vector [ $ms^{-1}$ ]
$\varepsilon$	Tolerance value adopted for the convergence criterion in WT2
$ w_x(s, t) ^2$	Wavelet scalogram
$\xi$	Stream-wise distance between two contiguous probes
$\zeta$	Minimum transversal distance along the $z$ -axis between the hot-wire probe and the flat-plate
$a(x, t)$	Acceleration [ $m s^{-2}$ ]
$b_u$	Jet half width $\equiv R_{1/2}$ [m]
$C_\psi$	Constant to take into account the mean value of the mother wavelet $\Psi(t)$
$c_j$	Speed of sound based on the jet temperature $T_j$ at the nozzle exhaust
$c_p$	Mean pressure coefficient
$c_{PRMS}$	Root mean square pressure coefficient
$CPSD$	Dimensionless Cross-Power Spectral Density between velocity and wall pressure signals $u(t)$ and $p(t)$
$CPSD_a$	Dimensionless Cross-Power Spectral Density between acceleration and wall pressure signals.
$D$	Nozzle diameter [m]
$E(f, t)$	Local wavelet power spectrum
$E(t)$	Global wavelet power spectrum
$f$	Frequency variable [Hz]

$F(T)$	Objective function to be maximized/minimized to select the threshold level in the wavelet-based separation techniques
$f_s$	Sampling frequency for data acquisition $[Hz]$
$f_\psi$	Centroid frequency of the analysing wavelet $[Hz]$
$H$	Radial distance of the flat-plate from the nozzle axis $[m]$
$K$	Turbulent kinetic energy $[m^2s^{-2}]$
$k$	Wavenumber
$k_n$	Wavenumber of the $n^{th}$ Fourier mode $[m^{-1}]$
$k_x$	Axial wavenumber
$L$	Integral length-scale of the axial velocity $[m]$
$LIM(s, t)$	Local Intermittency Measure
$M_j$	Jet Mach number
$N_e$	Number of events satisfying the triggering condition in the conditional sampling procedure
$N_p$	Number of particles adopted in the Particle Swarm Optimization method for the choice of the threshold level in the wavelet technique WT1
$N_s$	Number of samples
$N_w$	Number of the wavelet coefficients
$N_{bin}$	Number of bins used to compute the Probability Density Function
$N_{w_x}$	Number of the wavelet coefficients associated with the wavelet transform of the time signal $x(t)$
$OASPL$	OverAll Sound Pressure Level $[dB]$
$p$	Pressure $[Pa]$
$P(k_x, \omega)$	Wavenumber-frequency spectrum of the pressure field $p(x, t)$
$p(x, t)$	Space-time pressure field
$p_A$	Acoustic pressure in the near field $[Pa]$
$p_H$	Hydrodynamic pressure $[Pa]$
$p_{amb}$	Ambient pressure $[Pa]$
$p_{FF}$	Far-field pressure $[Pa]$
$p_{NF}$	Near-field pressure $[Pa]$

$p_{ref}$	Reference pressure equal to $20 \mu Pa$ used for computation of dimensionless $PSD$
$p_{RMS}$	Root mean square of the pressure signal $p(t)$ [ $Pa$ ]
$PDF$	Probability Density Function
$PSD$	Power Spectral Density
$q_c$	Convective dynamic pressure adopted for the scaling of the wall pressure auto-spectra $1/2\rho U_c^2$
$r$	Radial distance from the nozzle axis [ $m$ ]
$R_{1/2}$	Radial position for which the mean axial velocity is 50% of the jet velocity [ $m$ ]
$R_{xy}$	Cross-correlation between signals $x(t)$ and $y(t)$
$Re$	Reynolds number
$Re_D$	Reynolds number based on the nozzle diameter $D$
$Re_T$	Taylor Reynolds number based on the Taylor micro-scale and the standard deviation of the velocity signal
$RTL$	Relative Turbulence Level
$s$	Wavelet scale [ $s$ ]
$SPSL$	Sound Pressure Spectrum Level [ $dB$ ]
$St$	Strouhal number
$St_D$	Strouhal number based on nozzle diameter
$St_H$	Strouhal number adopted to scale the wall pressure spectra $= (f H) / U_j$
$t$	Time variable [ $s$ ]
$T^*$	Optimal threshold value at the separation point for the wavelet decomposition methods
$T_0$	Initial guess for the threshold value in the wavelet-based separation procedures
$T_A$	Acquisition time for experimental tests [ $s$ ]
$T_k$	Iterative threshold value adopted in the wavelet-based separation techniques
$T_l$	Threshold for the identification of the $LIM$ peaks in the wavelet-based conditioning procedure
$T_s$	Sampling time [ $s$ ]
$T_{up}$	Maximum value of the threshold level for the Particle Swarm Optimization method in the wavelet technique WT1
$u$	Axial velocity [ $m s^{-1}$ ]

$u'(t)$	Fluctuating component of the axial velocity [ $m s^{-1}$ ]
$U(x)$	Mean component of the axial velocity [ $m s^{-1}$ ]
$U_a$	Acoustic propagation velocity [ $m s^{-1}$ ]
$U_c$	Convection velocity [ $m s^{-1}$ ]
$U_j$	Jet velocity at the nozzle exhaust [ $m s^{-1}$ ]
$U_m$	Mean velocity value along the jet axis [ $m s^{-1}$ ]
$u_n$	$n^{th}$ coefficient associated with the Fourier expansion of the axial velocity [ $m s^{-1}$ ]
$U_{MAX}$	Maximum mean velocity value along the transverse direction at each axial distance in the jet-plate experiment [ $m s^{-1}$ ]
$W(t)$	Hamming windowing function in the time domain used for the computation of the wavenumber-frequency spectrum
$W(x)$	Hamming windowing function in the space domain used for the computation of the wavenumber-frequency spectrum
$w_x(s, t)$	Wavelet coefficients associated with the generic signal $x(t)$
$x$	Stream-wise or axial distance from the nozzle exhaust [ $m$ ]
$y$	Span-wise or transverse distance from the nozzle axis [ $m$ ]
$z$	Cross-wise or transverse distance from the nozzle axis [ $m$ ]
BPR	By-Pass Ratio
CWT	Continuous Wavelet Transform
DWT	Discrete Wavelet Transform
HBPR	High By-Pass Ratio
HW	Hot-wire
IWT	Inverse Wavelet Transform
OWT	Orthogonal Wavelet Transform
RANS	Reynolds Averaged Navier-Stokes
TBL	Turbulent Boundary Layer
UHBPR	Ultra High By-Pass Ratio
WT1	Wavelet technique 1 for hydrodynamic/acoustic separation
WT2	Wavelet technique 2 for hydrodynamic/acoustic separation
WT3	Wavelet technique 3 for hydrodynamic/acoustic separation





# Part I

## Preface



# Chapter 1

## Introduction

### 1.1 Motivations

In the last 50 years the development of the aircraft transportation has brought an increasing amount of issues related to environmental aspects such as carbon and NO<sub>x</sub> emissions and noise pollution. Appropriate aircraft and engine technologies have been developed by manufacturers with the aim of reducing fuel consumption and pollutant emissions. The jet exhausting from the aircraft engines involves pollutant discharge and stands for one of the main sources of community and interior noise. Specifically, noise reduction has significant economic implications. Indeed, airline companies pay fees proportional to the sound emitted by the aircraft during take-off and landing operations. Since the legislative constraints related to the noise level conveyed to the ground during take-off and landing operations are becoming increasingly stricter, the Advisory Council for Aviation Research and innovation in Europe (ACARE) has established a 10 *dB* noise reduction goal for year 2020. In order to achieve such objective a technology breakthrough is necessary. A deeper insight on the complex physical phenomena underlying the jet noise generation and propagation mechanism is thus needed.

Current High By-Pass Ratio (HBPR) turbofan engines have just partially reached a good efficiency in terms of fuel consumption, pollution and noise emissions. Fuel consumption decrease can be achieved by reducing the jet velocity exhausting from the engines. Such device is also a benefit for the noise emissions, the sound intensity being essentially proportional to the eight power of the velocity according to Lighthill (1952). In order to keep the same thrust level, an increase of the mass flow has to be adopted to compensate the jet velocity reduction. Ultra High By-Pass Ratio (UHBPR) engine concepts provide a valid solution featuring a decrease of the jet velocity and an increase of the fan/nacelle diameter. The increase of the engine size has to be mitigated by a reduction of the nacelle length in order to minimize additional weight and drag drawbacks. The constraints in terms of ground clearance will lead to close-coupled architecture for engine installation under the wing. As reported in many papers in the literature (see e.g. Huber et al. (2009) and Huber et al. (2014)), the stronger jet-wing interaction gives rise to an increase of the radiated noise. Hence, in order to not jeopardize noise break down due to jet velocity reduction, the jet installation noise or installation effects have to be mitigated in future aircraft architectures.

Stronger flow-structure interactions can be also expected between the jet and the

fuselage. Pressure fluctuations generated by the jet impinge on the fuselage causing panels stress and vibrations. Some of these vibrations are scattered by the surface and propagate in the aeroacoustic field as vibration noise. Some of them are transmitted through the external panels to the aircraft cockpit as interior noise generating passengers' annoyance. This issue should be considerably taken into account in the future aircraft configurations in which composite materials will be largely used. The composites are in fact more transparent to sound propagation than the metal alloys classically used for aircraft structures. This characteristic could give rise to a wider use of sound absorbing materials in the fuselage.

In summary, jet noise represents a challenging topic for the scientific community and engine manufacturers due to its complexity. The integration of the engine in the aircraft architecture and the consequent interaction between the jet and the airframe surfaces makes the issue even trickier. Hence, jet noise and installation effects represent a major problem to be tackled in the design process of new aircraft configurations.

## 1.2 Objectives

In the present research activity the noise generated by a free jet and the jet-surface interaction phenomena have been studied experimentally. The aim was to exploit advanced time-frequency data analysis techniques in order to get a deeper understanding of the jet physics, the jet noise phenomena and the installation effects. Specifically, wavelet-based post-processing techniques have been developed and applied to two different databases.

In order to better understand the noise generation and propagation mechanism, pressure fluctuation measurements induced by a single-stream compressible jet installed in an anechoic wind tunnel have been performed. Particular attention was focused on the near region of the jet. Innovative wavelet-based techniques have been developed to provide the decomposition of the near-field pressure into its hydrodynamic and acoustic components. Such issue is essential for a more comprehensive understanding of the jet noise physics with the aim of developing noise control devices (e.g. chevron, micro-jets...). The separated hydrodynamic and acoustic pressures have been characterized in terms of statistical quantities and spectral content. Quantitative correlations between the separated acoustic pressure and the measured far-field noise (that is actually the sound by definition) have been established.

The installation effects have been studied by investigating the jet-surface interaction phenomena on a simplified laboratory-scale model, where a flat-plate was installed tangentially to an incompressible jet. For the present work, the compressibility effects on the jet-plate interaction phenomena have been neglected in order to further simplify the investigation. The jet-surface interaction phenomena have been studied in terms of the effect of the plate on the aerodynamic field and in terms of wall pressure field induced by the jet on the plate. Velocity/acceleration and wall pressure fields have been analysed in the time and frequency domain. Implications for wall pressure fluctuations modelling are discussed. A conditional sampling procedure based on wavelet transform was applied as well in order to educe the coherent flow structures responsible for the most energetic velocity/acceleration and wall pressure events.

# Chapter 2

## Short discussion on time-frequency analysis

### 2.1 Generalities

Signal analysis involves the application of the transform theory, whose essence implies that a problem can have a simplified representation on a suitable basis. The transform of a generic time signal  $x(t)$  is the projection of the signal over a suitable analysing function. Hence, phenomena can be represented in both physical and transformed spaces. The representation has to satisfy the well-known Heisenberg uncertainty principle (Heisenberg, 1927, 1983), for which it is not possible to have the same accuracy in the physical and transformed spaces simultaneously. Discussion about the resolution in the physical and transformed spaces is provided in the following taking into account some academic examples of different transform functions.

In the so-called Shannon transform the analysing function is the Dirac function  $\delta(t)$ . The Shannon transform of the time signal  $x(t)$  can be written as follows:

$$\hat{x} = \int_{-\infty}^{+\infty} x(t) \delta(t - t_0) dt = x(t_0) \quad (2.1)$$

Since the representation in the frequency domain of the Dirac function is a constant over all the frequencies, the Shannon transform provides the maximum resolution in the physical space ( $\Delta t \rightarrow 0$ ), but the minimum accuracy in the transformed one ( $\Delta f \rightarrow \infty$ ). Such a behaviour is exemplified in figure 2.1.

In the Fourier transform the generic signal is projected over a basis of cosine and sine functions. Taking into account the Euler's formulas for complex numbers, the Fourier transform of the signal  $x(t)$  is defined as follows:

$$\hat{x}(f) = \int_{-\infty}^{+\infty} x(t) \cos 2\pi ft dt + i \int_{-\infty}^{+\infty} x(t) \sin 2\pi ft dt = \int_{-\infty}^{+\infty} x(t) e^{-i2\pi ft} dt \quad (2.2)$$

where  $f$  is the frequency variable. The Fourier representation satisfies a lot of properties among which the most important ones are resumed in the following.

- Orthogonality, which implies that the Fourier transform can be inverted from the frequency domain back to the time domain according to the following formula:

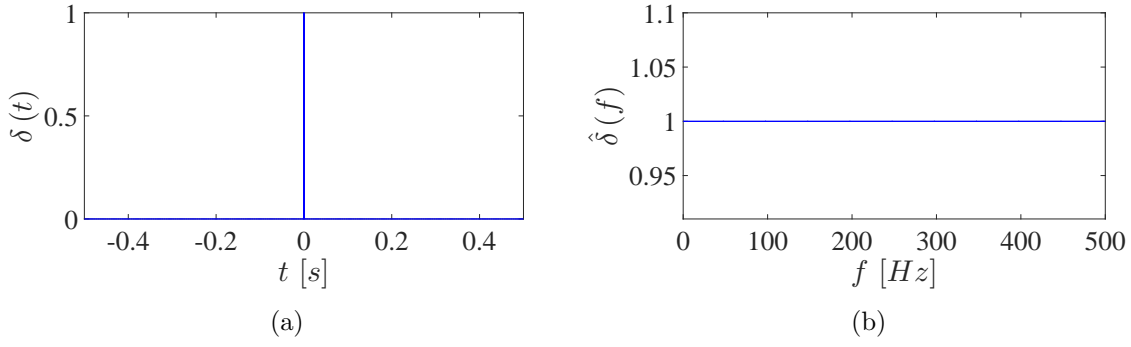


Figure 2.1: Representation in the time and frequency domains of the Dirac function used as basis for the Shannon transform: (a)  $\delta(t - t_0)$  with  $t_0 = 0$  s, (b)  $\hat{\delta}(f)$ .

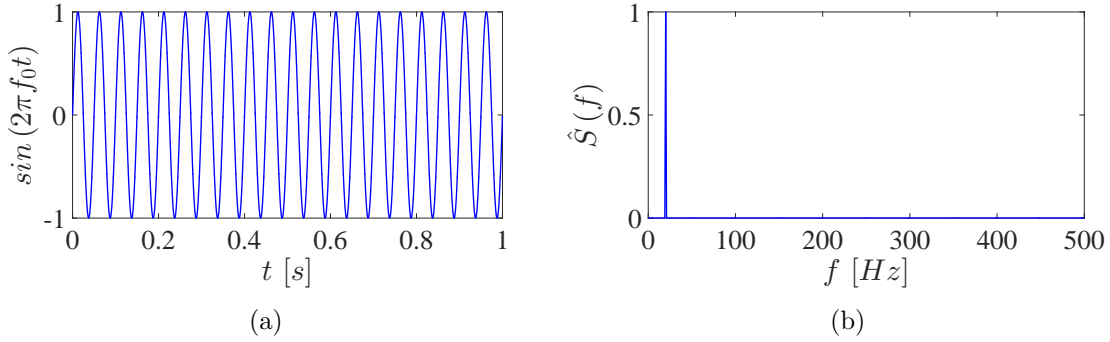


Figure 2.2: Representation in the time and frequency domains of the sine function used as basis for the Fourier transform: (a)  $S(t) = \sin(2\pi f_0 t)$  with  $f_0 = 20$  Hz, (b)  $\hat{S}(f)$ .

$$x(t) = \int_{-\infty}^{+\infty} \hat{x}(f) e^{i2\pi ft} df \quad (2.3)$$

- Parseval's theorem, which implies energy conservation in the time and frequency domain:

$$\int_{-\infty}^{+\infty} |x(t)|^2 dt = \int_{-\infty}^{+\infty} |\hat{x}(f)|^2 df \quad (2.4)$$

The Fourier transform provides the maximum accuracy in the transformed space ( $\Delta f \rightarrow 0$ ), but the minimum accuracy in the physical one ( $\Delta t \rightarrow \infty$ ). Such assertion is supported considering the sine function and its representation in the frequency domain, as reported in figure 2.2.

A compromise between the two representations illustrated above is the windowed Fourier transform or short-time Fourier transform, in which the generic time signal is divided into short segments of equal length and the Fourier transform of each segment is then computed. In this way it is possible to extract the frequency content of the signal  $x(t)$  as it changes over the time. The short-time Fourier transform of the signal  $x(t)$  is none other than the Fourier transform of the signal itself multiplied by a window function  $g(t - \tau)$  of short length. The windowed Fourier transform is defined as follows:

$$\hat{x}(t, f) = \int_{-\infty}^{+\infty} x(\tau) g(t - \tau) e^{-i2\pi f\tau} d\tau \quad (2.5)$$

A special case of the short-time Fourier transform is the Gabor transform in which the window function  $g(t - \tau)$  is a Gaussian function (Gabor, 1946). The window size in the Gabor transform has a constant length, whereas the number of oscillations can be varied modifying the frequency  $f_0$  of the sinusoidal function. This behaviour implies that the resolution in the physical and transformed spaces is a constant ( $\Delta t = \text{const}$ ,  $\Delta f = 1/\text{const}$ ), as exemplified in figure 2.3.

## 2.2 Wavelet approach

As highlighted above, the ideal transform would be characterized by the maximum accuracy in  $t$  and the maximum accuracy in  $f$  at the same time. Such feature is against the Heisenberg uncertainty principle. Gabor transform represents a compromise between the resolution in the physical and transformed spaces. The limitation of the short-time Fourier approach is mainly the fixed time support of the analysing basis. In order to analyse signal structures of different size the time support has to change. This is the main motivation underlying the development and usage of wavelets. Wavelets act as a mathematical microscope from large signal structures to smaller ones, the basis being characterized by a variable support in time. The wavelet basis is obtained by dilation and translation of a so-called mother function  $\Psi(t)$ . The mother function  $\Psi$  has to satisfy the properties listed in the following.

- Similarity  $\longrightarrow$  unlike the Gabor basis, the wavelet basis is obtained dilating and translating the mother wavelet that maintains its shape, i.e. the number of oscillations in the support time remains constant, as represented in figure 2.4.
- Regularity  $\longrightarrow \Psi(t)$  is localized in both the physical and transformed spaces
- Admissibility  $\longrightarrow$  this condition can be formally defined as follows:

$$C_\psi = \int_0^\infty |\hat{\Psi}(f)|^2 \frac{df}{|f|} < \infty \quad (2.6)$$

where  $\hat{\Psi}(f)$  is the Fourier transform of the mother function. If  $\Psi$  is integrable, this implies that the wavelet function has zero mean value:

$$\int_{-\infty}^{+\infty} \Psi(t) dt = 0 \quad (2.7)$$

- Smoothness  $\longrightarrow$  the mother wavelet function has a given number of vanishing moments of order  $m$ :

$$\int_{-\infty}^{+\infty} t^m \Psi(t) dt = 0 \quad (2.8)$$

In the Fourier domain the previous condition can be written as follows:

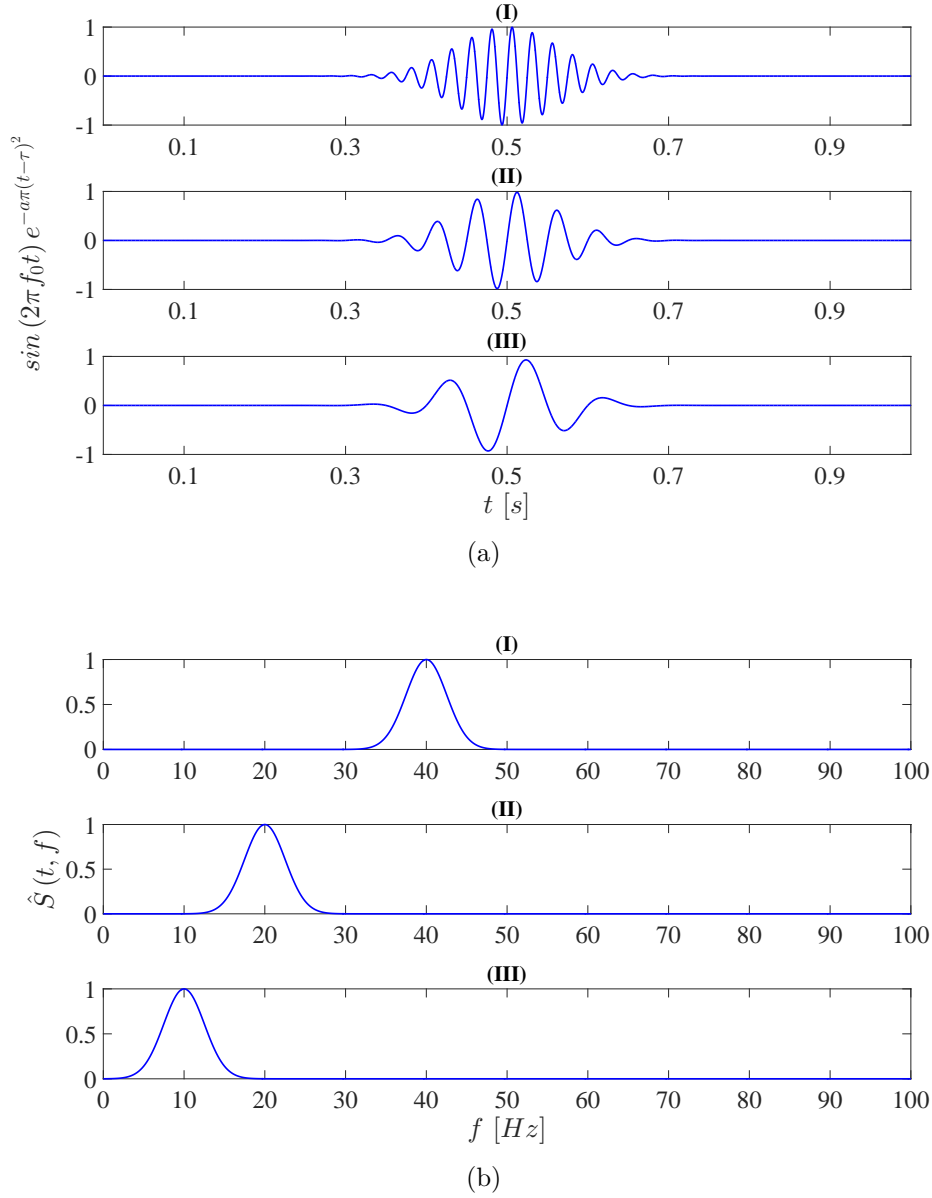


Figure 2.3: Representation in the time and frequency domains of the basis adopted for the Gabor transform. (a) Time domain  $S(t) = \sin(2\pi f_0 t) e^{-a\pi(t-\tau)^2}$ : (I)  $f_0 = 40$  Hz, (II)  $f_0 = 20$  Hz, (III)  $f_0 = 10$  Hz. (b)  $\hat{S}(t, f)$ : (I)  $f_0 = 40$  Hz, (II)  $f_0 = 20$  Hz, (III)  $f_0 = 10$  Hz.



$$\frac{d^m \hat{\Psi}(0)}{df^m} = 0 \quad (2.9)$$

The reader may refer to Mallat (1989), Daubechies (1992), Torrence and Compo (1998) and Farge (1992) for comprehensive reviews on mathematical aspects of wavelet transforms and their applications.

The Continuous Wavelet Transform (CWT) of a generic time signal  $x(t)$  consists of a projection over a basis of compact support functions obtained by dilations and translations of the mother wavelet  $\Psi(t)$ . As said above, the mother wavelet is localized in both physical and transformed spaces, the resulting wavelet coefficients being function of the time  $t$  and of the scale  $s$ , which is inversely proportional to the frequency (Meyers et al., 1993). According to Camussi et al. (2006), the CWT of a time signal can be defined as follows:

$$w_x(s, t) = C_\psi^{-1/2} s^{-1/2} \int_{-\infty}^{+\infty} x(\tau) \Psi^* \left( \frac{t - \tau}{s} \right) d\tau \quad (2.10)$$

where  $\Psi^* \left( \frac{t - \tau}{s} \right)$  is the complex conjugate of the dilated and translated  $\Psi(t)$ . An exemplifying representation in the time and scale domain of the modulus of the wavelet coefficients is shown in figure 2.5.

Instead of a continuous wavelet transform, a Discrete Wavelet Transform (DWT) can be adopted to decompose the signal  $x(t)$ . According to Meneveau (1991), if the scales  $s_j$  are arranged on a dyadic distribution, i.e.  $s_j = 2^j$ , and the considered translations are a multiple of the scale  $s_j$ , the orthonormal basis  $\psi(t)$  obtained by dilations and translations of the mother wavelet  $\Psi(t)$  can be represented by the following formula:

$$\psi_{[k]}^{(j)}(t) = 2^{-\frac{j}{2}} \Psi \left( \frac{t - 2^j k}{2^j} \right) \quad (2.11)$$

The discrete wavelet coefficients are obtained as follows:

$$w_x^{(s)}(n) = \sum_{k=-\infty}^{+\infty} \Psi^{(s)}(n - 2^s k) x(k) \quad (2.12)$$

Where  $s$  represents the discretized scale, whereas the wavelet function  $\Psi^{(s)}(n - 2^s k)$  is the discretized version of  $\Psi^{(s)}(t) = 2^{-\frac{s}{2}} \Psi \left( \frac{t}{2^s} \right)$  (Camussi and Guj, 1997).

The usage of a DWT implicate the wavelet basis to be orthogonal (also called OWT: Orthogonal Wavelet Transform), so that an Inverse Wavelet Transform (IWT) can be defined to go from the transformed space back to the physical one.

### 2.2.1 Wavelet vs. Fourier

Likewise the Fourier transform, the wavelet transform is characterized by energy conservation, i.e. the Parseval's theorem also applies in the wavelet domain:

$$\int_{-\infty}^{+\infty} |x(t)|^2 dt = \int_{-\infty}^{+\infty} \int_{-\infty}^{+\infty} |w_x(s, t)|^2 ds dt \quad (2.13)$$

The quantity  $|w_x(s, t)|^2$  is called scalogram and represents the energy content of the signal at the scale  $s$  at the time instant  $t$ . Thus, as pointed out by Farge and Schneider

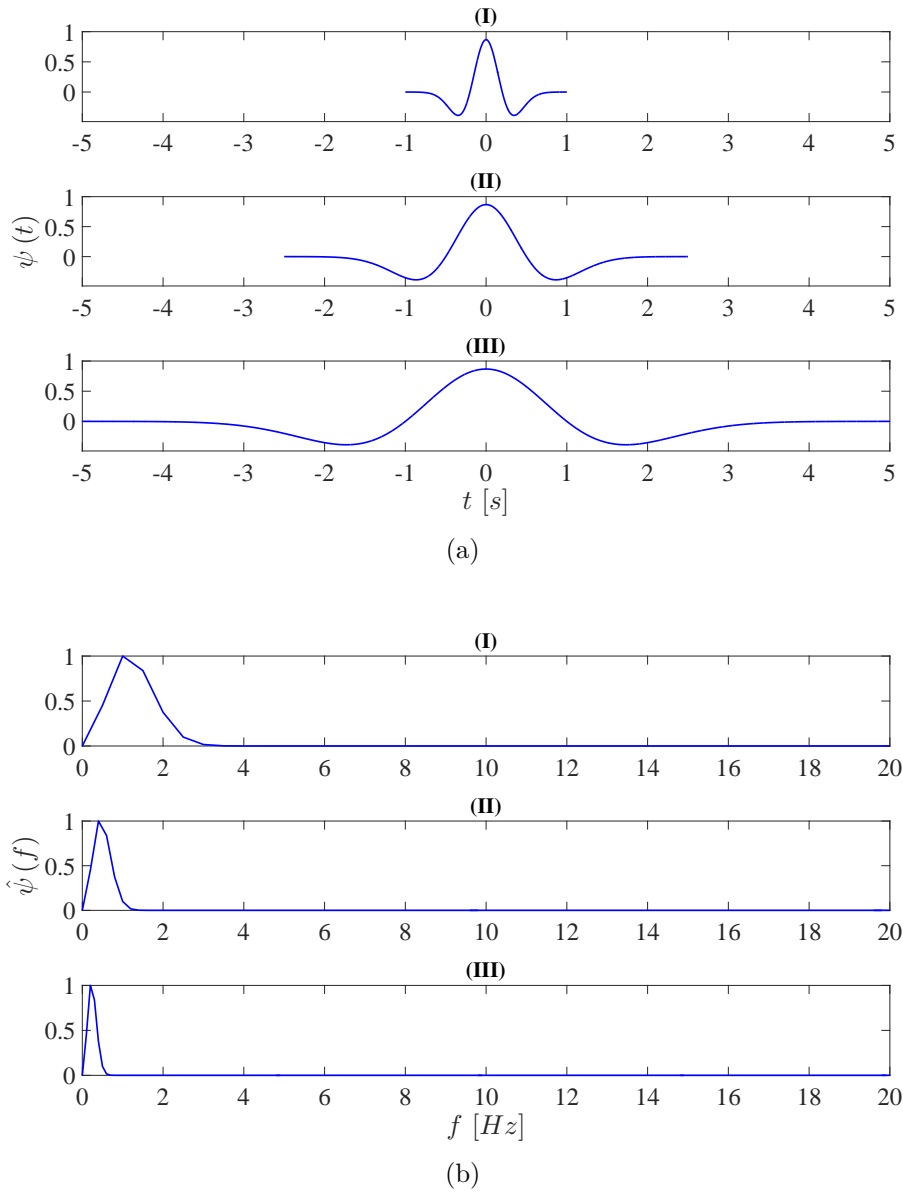


Figure 2.4: Representation in the time and frequency domains of the Mexican Hat wavelet at different scales. (a) Time domain  $\psi(t)$ . (b)  $\hat{\psi}(f)$ .

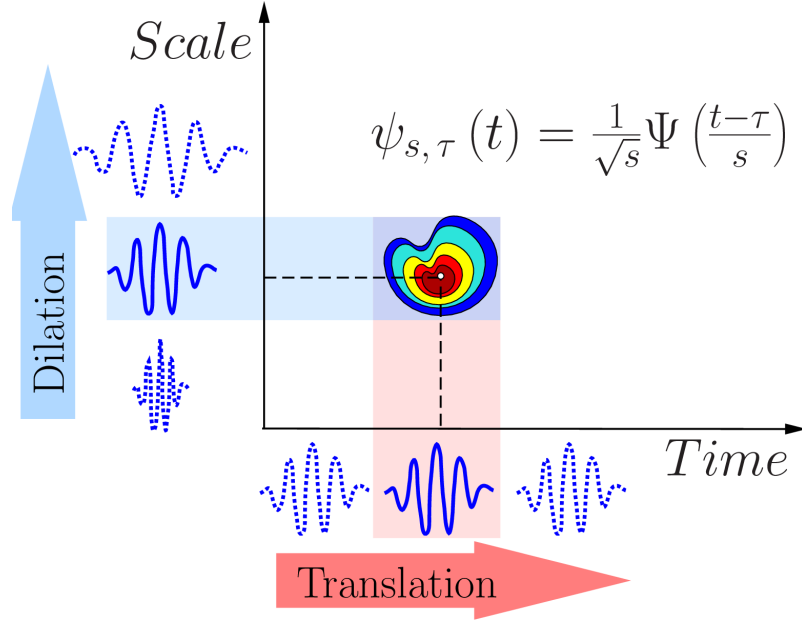


Figure 2.5: Example of the time-scale representation using the wavelet transform.

(2006), the square of the wavelet coefficients gives an estimation of the local energy, denoted as  $E(f, t)$ , according to the following equation:

$$E(f, t) = \frac{1}{2\pi C_\psi f_\psi} \left| w\left(\frac{f_\psi}{f}, t\right) \right|^2 \quad (2.14)$$

where  $f_\psi$  is the centroid frequency of the analysing wavelet. The global spectrum  $E(f)$  can be obtained by integrating along the time domain the local spectrum defined above:

$$E(f) = \int_0^T E(f, t) dt \quad (2.15)$$

where  $T$  is the acquisition time or the recorded time for experimental or numerical data, respectively.

A comparison between the *PSD* computed by the standard Fourier transform and the spectrum obtained by the wavelet approach is shown in figure 2.6. As an example, a wall pressure time series obtained by experimental tests on jet-plate interaction has been considered. The flat-plate was installed at a radial distance from the nozzle axis equal to 2.5 nozzle diameters, whereas the microphone was placed at the stream-wise and span-wise positions equal to  $x/D = 1$  and  $y/D = 0$ , respectively (for more details see §III). A good agreement between the spectrum obtained by both the Fourier and wavelet approaches is observed. More specifically, the wavelet spectrum appears to be less noisy and more accurate than the Fourier one. Indeed, the wavelet approach is particularly efficient either when the data are affected by a low signal-to-noise ratio or when the number of samples of the signal are not enough to ensure a good statistical convergence.

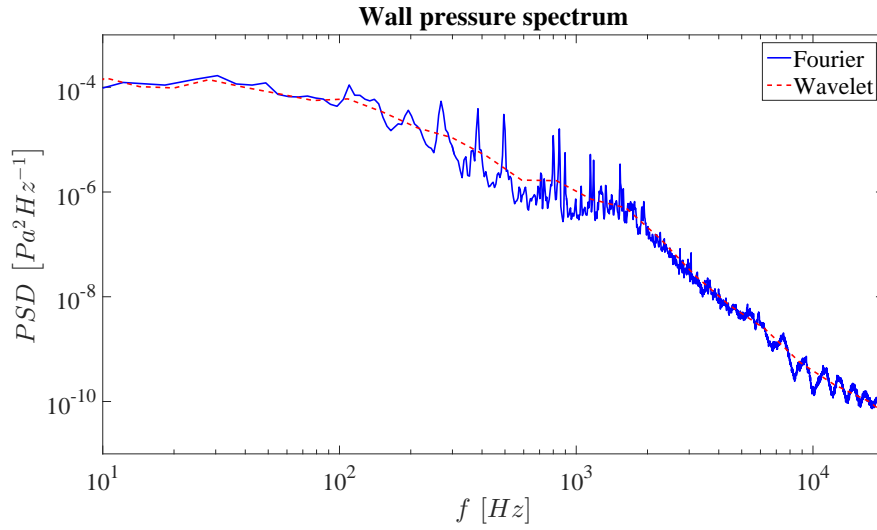


Figure 2.6: Comparison between the spectrum obtained by the standard Fourier transform and the wavelet approach. As an example, a wall pressure time series obtained by experimental measurements on the interaction between the incompressible jet and the flat-plate has been taken into account.

### 2.2.2 Why use wavelets in turbulent flows

Wavelets have been widely used to analyse turbulent flows in different research areas (see e.g. Farge (1992); Farge and Schneider (2015); Camussi and Guj (1997); Guj and Camussi (1999); Ukeiley and Ponton (2004)), including boundary layers (Camussi and Di Felice, 2006; Camussi et al., 2006) and aeroacoustics of cold jets (Grizzi and Camussi, 2012; Camussi and Grizzi, 2014)).

In the present work, the wavelet transform has been exploited together with the standard Fourier approach to analyse the aerodynamics and aeroacoustics of compressible and incompressible jets in free and installed configurations, respectively. Indeed, jet noise is mainly due to the turbulent mixing in the flow. Turbulence is a multi-scale problem whose typical feature is intermittency. Furthermore, the coherent flow structures embedded in the turbulent flow are temporally and spatially localized. Fourier modes are not so suited to analyse intermittent phenomena since they are localized only in the transformed space, as underlined in §2.1. Indeed, the usage of a wavelet basis would be more advisable for turbulent flows phenomena due to the good localization of wavelets in both physical and transformed spaces. As a further, the wavelet approach provides a multi-level or multi-resolution analysis that is very suited for the investigation of turbulence phenomena in which structures of different size or scale are found.

In order to highlight the potentialities of the wavelet approach an academic example is reported in figure 2.7. Two generic time signals  $x_1(t)$  and  $x_2(t)$  are taken into account. The signals are characterized by a signature with a different time-scale appearing at a different time instant. The two signals are summed and the wavelet transform of the total signal is computed. It is observed that the features embedded in the original signals are retrieved and isolated in the representation of the modulus of the wavelet coefficients in the scale-time domain. Such a behaviour implies that the wavelet approach can be efficiently adopted as decomposition filter of the data and to isolate structures with a given signature embedded in a chaotic time signal.

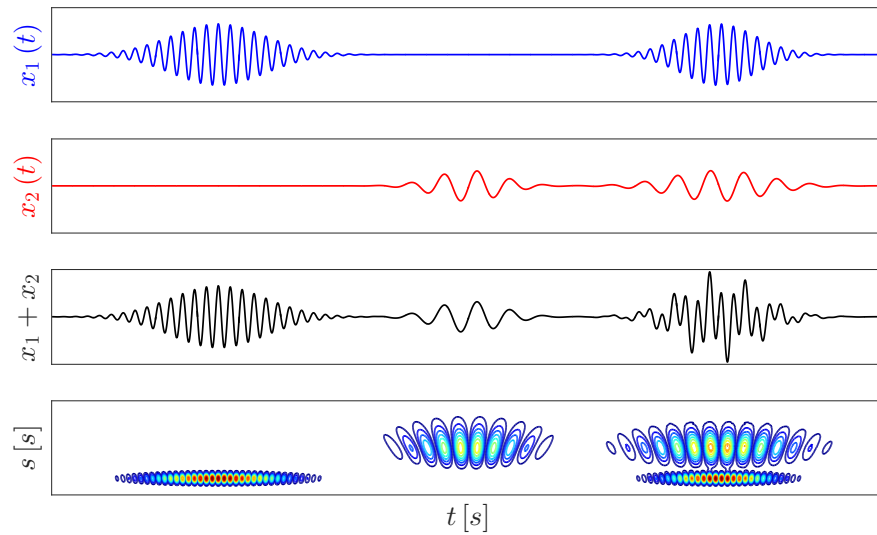


Figure 2.7: Example of the time-scale representation of the modulus of the wavelet coefficients of the academic signal  $x_1(t) + x_2(t)$ .



## Part II

# Hydrodynamic/acoustic pressure decomposition





# Chapter 3

## Introduction

Since the seminal work of Lighthill (1952), many numerical and experimental studies have been devoted to the identification and description of the noise sources in compressible subsonic free jets with the aim of modelling the noise production mechanisms and predict the sound propagation to the far field (see among many the papers of Lilley (1991), Goldstein (1984), Viswanathan (2006)). Recent papers (see Cavalieri et al. (2011) and Cavalieri et al. (2013)) have shown that the noise propagated to the far field is related to unsteady turbulent structures in the shear layer and to their mutual interactions along the jet flow. However, a clear picture of the nature of the flow structures generating noise is not yet available and further efforts in this field are needed.

To this extent, it is known that the investigation of the pressure field in a region close to the jet flow may help to identify the noise sources and better characterise the sound production mechanisms with respect to the analysis of the far-field pressure fluctuations. For these reasons, the near field of free jets has been the subject of several experimental and numerical studies in the literature (e.g. Fuchs (1972), Ukeiley and Ponton (2004), Suzuki and Colonius (2006), Bogey et al. (2012b)). Nevertheless, the physical interpretation of a pressure signal taken in the proximity of a jet is definitely tricky. As pointed out by Howes (1960), a microphone in the near field is subjected to the pressure fluctuations associated with the hydrodynamic structures convected inside the jet and the perturbations induced by the propagating acoustic waves. As firstly suggested by Ribner (1962), a distinction between '*sound*' and '*pseudo-sound*' can be made in the near field of a jet. The pseudo-sound, also called hydrodynamic component, is weakly influenced by compressibility (Ffowcs Williams, 1969), and does not radiate. On the other hand, the sound or acoustic component is associated with sound waves propagating at the speed of sound and governed by the linear wave equation (Ristorcelli, 1997).

The necessity to separate the acoustic pressure from the hydrodynamic perturbations (which does not mean isolating the acoustic sources in the jet) was explicitly addressed by Tinney et al. (2007) for the case of compressible jets. Such a separation could be achieved by a proper filtering procedure since, as pointed out by Arndt et al. (1997), the hydrodynamic component is dominant in the low-frequency region of the spectrum, whereas the acoustic component is predominant at high frequencies. A Fourier filtering procedure for the separation of hydrodynamic and acoustic pressures in the near field was presented by Kerhervé et al. (2008) and Tinney and Jordan (2008). Pseudo-sound and sound pressures were isolated on the basis of their phase velocity in the wavenumber-frequency spectrum. The only drawback of such method is represented by the large

number of near-field microphones required to provide a satisfactory resolution in the wavenumber domain. Further details on this technique are given in §6.2.

It is well known that hydrodynamic pressure, being induced by the turbulent structures inside the jet, is intrinsically intermittent (see Juvé et al. (1980), Camussi and Guj (1997), Camussi and Guj (1999) and Kearney-Fischer et al. (2013)). This physical evidence motivated the use of the wavelet decomposition rather than the Fourier transform for the analysis of vorticity and hydrodynamic pressure in turbulent flows. Indeed, as pointed out by Ruppert-Felsot et al. (2009), the Fourier modes are not well-suited to represent and describe intermittent events since they are localized in the spectral space but not in the physical one. Therefore, the use of a wavelet basis is more advisable due to its localization in both physical and transformed spaces. To the purpose of analysing the near-field pressure, such an idea was exploited by Grizzi and Camussi (2012), who developed a wavelet-based procedure to separate hydrodynamic and acoustic pressures. They assumed that the hydrodynamic contribution related to localized eddy structures compresses well onto a wavelet basis so that it can be described by large amplitude wavelet coefficients. Thus, the pseudo-sound can be extracted by selecting the wavelet coefficients exceeding a proper threshold. The acoustic counterpart associated with more homogeneous and low-energy fluctuations is represented by those coefficients having an amplitude lower than the threshold. The advantage of this wavelet-based method with respect to previous approaches was mainly in the simplicity of the required set-up. Indeed, only two microphone signals in the near field, acquired (or computed) in two positions sufficiently close to each other, are needed to compute the cross-correlation between the presumed hydrodynamic and acoustic components. The computation of the cross-correlation was necessary to determine through an iterative process the amplitude of the threshold level mentioned above (see Grizzi and Camussi (2012) for the details).

The above discussion motivated the present work where novel wavelet-based methods were derived with the aim of improving the efficiency of the method proposed by Grizzi and Camussi (2012) and further simplify the set-up required for the practical application of the procedure (e.g. by using only one microphone). Three new wavelet-based methods were developed and the main concepts underlying these approaches are illustrated in §4.

The methods are applied to simultaneous near- and far-field pressure data measured around a subsonic jet installed within the anechoic chamber available at the Centre Acoustique of Laboratoire de Mécanique des Fluides et d'Acoustique at the École Centrale de Lyon. A statistical and spectral characterization of the separated hydrodynamic and acoustic components is provided highlighting the effect of the axial location of the near-field microphone in the stream-wise direction and the effect of the jet Mach number. In order to validate the techniques, the Fourier filtering technique derived by Tinney and Jordan (2008) as well as the wavelet-based separation procedure proposed by Grizzi and Camussi (2012) are also applied to the present database.

For more details on this work the reader can refer to Mancinelli et al. (2016b) and Mancinelli et al. (2017b).

## Chapter 4

# Wavelet-based separation techniques

The separation between hydrodynamic and acoustic components of the near-field pressure is based on the application of the wavelet transform to pressure signals. For mathematical aspects on the wavelet approach the reader may refer to §2.2.

In the present work, the wavelet transform is performed using an orthogonal wavelet basis to ensure the reversibility condition and the wavelet kernel used is the Daubechies-12 type. In order to ensure the generality of the present approaches, it has been checked that the results presented in the following do not depend on the choice of the wavelet type. In all cases, the analysis is carried out using the *Matlab*<sup>®</sup> wavelet toolbox.

According to the approach proposed by Grizzi and Camussi (2012), it is assumed that the hydrodynamic component of the near-field pressure, being related to localized vortices, compresses well onto the wavelet basis. Therefore, the component of the signal associated with the hydrodynamic pressure can be extracted by selecting the wavelet coefficients exceeding, in absolute value, a proper threshold, the remaining part of the signal being assumed as acoustic pressure.

It is clear that the selection of the threshold represents a crucial step in the separation procedure and its selection has to be related to physical properties of the hydrodynamic or acoustic pressure components. Indeed, the distinction among the three procedures introduced therein is mainly based on the way the threshold is selected.

An initial guess for the threshold value  $T_0$  is adopted for all the techniques and it is based on statistical reasoning introduced in the de-noising procedure developed by Donoho and Johnstone (1994):

$$T_0 = \sqrt{2\langle p'^2 \rangle \log_2 N_s} \quad (4.1)$$

where  $\langle p'^2 \rangle$  is the variance of the pressure signal and  $N_s$  is the number of samples. The threshold is changed until a proper convergence criterion capturing the hydrodynamic or acoustic nature of the separated signals is satisfied. The iterative process differs for each technique being different the physical aspect to which the separation procedure is related. It will be shown that whatever is the initial hypothesis and the objective function to be satisfied, all the separation techniques lead to similar results.

Hereinafter, in order to simplify the description, the original near-field pressure signal will be denoted as  $p_{NF}$ , the near-field hydrodynamic and acoustic pressure signals as  $p_H$  and  $p_A$ , respectively, and the far-field pressure signal as  $p_{FF}$ .

## 4.1 Wavelet technique 'WT1'

The separation technique denoted as WT1 requires one microphone in the near field and one microphone in the far field. The iterative process for the selection of the threshold is based on the computation of the cross-correlation between the guessed acoustic component of the near-field pressure and the measured far-field pressure. The cross-correlation function, establishing a causality relation between the convoluted time series (Bogey and Bailly, 2007), is considered as an indicator of the degree of similarity between the two pressure signals. Indeed, the hypothesis at the basis of the procedure is that the amplitude of the hydrodynamic fluctuations decreases very rapidly by increasing the radial distance from the jet (Suzuki and Colonius, 2006) so that the near-field acoustic component is the only one to reach the far field and thus is the only one to provide a high-value correlation with the far-field noise.

Starting from the initial guess  $T_0$ , the threshold level is varied according to a gradient-based method until the cross-correlation peak between the acoustic pressure in the near field and the noise emitted in the far field exhibits a maximum:

$$T^* = \arg \max_{T \in \mathbb{R}^+} F(T) \quad \text{where} \quad F(T) = \max(\rho_{p_A p_{FF}}) \quad (4.2)$$

As an example, figure 4.1 shows the variation of the peak of the cross-correlation coefficient between either the separated hydrodynamic or acoustic component and the far-field pressure, as a function of the number of iterations. It is observed that the correlation between the acoustic and the far-field pressures is always much larger than the one between the hydrodynamic and the far-field pressures. Starting from the initial guess defined above, as the threshold value varies the acoustic cross-correlation peak increases rapidly until it reaches a quasi-constant trend, after which the maximum of the cross-correlation peak is reached. For such a threshold level the convergence criterion is satisfied and the pseudo-sound and sound pressures are separated successfully.<sup>1</sup>

### 4.1.1 Validation of the choice of the optimal threshold value

The accuracy of the optimal threshold value provided by the gradient-based method, that is a local optimization method, has been checked by comparison with the outcome obtained by a Particle Swarm Optimization, i.e. a global optimization method (Ebbesen et al., 2012).

The swarm consists of  $N_p$  particles, i.e a finite number of threshold values included between 0 and  $T_{up}$ , where  $T_{up}$  is a threshold value one order of magnitude greater than the initial guess  $T_0$ . The particles number was chosen as large as possible in order to be representative of all the possible threshold levels keeping acceptable computational costs.

---

<sup>1</sup>The non-zero correlation value between  $p_H$  and  $p_{FF}$  is definitely related to the fact that the acoustic component has not been completely filtered out. Such an issue surely represents a limitation of the separation technique. Therefore, a small contribution associated with the acoustic pressure is still buried in the hydrodynamic signal. Nevertheless, it has to be underlined that such leftovers are very limited, the correlation level between hydrodynamic and far-field pressures being almost one order magnitude lower than the one between the acoustic and far-field pressures. Indeed, this drawback is also found when reference separation methods are applied, as shown in §6.3.

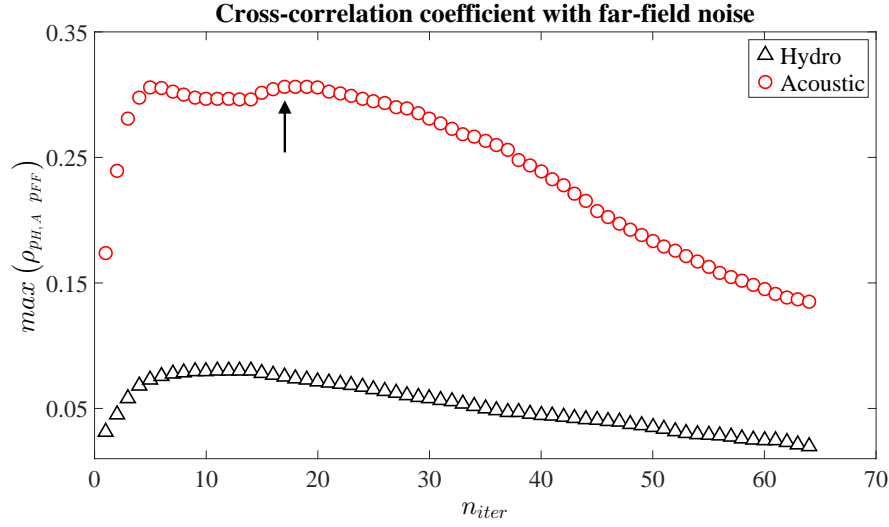


Figure 4.1: Separation technique WT1: cross-correlation coefficient peak along the number of iterations of the acoustic and hydrodynamic components with the measured far-field pressure. Jet Mach number  $M_j = 0.6$ , near-field microphone axial location  $x/D = 8.7$ , far-field microphone polar position  $\psi = 140^\circ$ . The separation point for which the convergence criterion is satisfied is highlighted with an arrow.

The formulation adopted in the present approach for the threshold value evaluation is given in the following:

$$\begin{cases} v_i^{k+1} = \phi^k v_i^k + \alpha_1 (\gamma_1 (P_i - T_i^k)) + \alpha_2 (\gamma_2 (G - T_i^k)) \\ T_i^{k+1} = T_i^k + v_i^{k+1} \end{cases} \quad (4.3)$$

Where  $v_i^k$  is the particle velocity at the  $k^{th}$  generation,  $P_i$  is the personal best position of each particle,  $G$  is the global best position observed up to the  $k^{th}$  generation and  $\phi^k$  is a weighting function.  $\gamma_1$  and  $\gamma_2$  are random variables, whereas  $\alpha_1$  and  $\alpha_2$  are acceleration parameters satisfying the necessary and sufficient conditions for the stability of the swarm reported in the following (Perez and Behdinan, 2007):

$$\begin{cases} \alpha_1 + \alpha_2 < 4 \\ \frac{\alpha_1 + \alpha_2}{2} - 1 < \phi < 1 \end{cases} \quad (4.4)$$

It has been verified that the optimization algorithm adopted did not affect the resulting decomposition, the difference between the spectra obtained with the local and global optimization methods being as low as 0.5 dB in amplitude with no changes in the spectral shape, as shown in figure 4.2.

## 4.2 Wavelet technique 'WT2'

In the method denoted as WT2 the iterative process for the threshold level selection is based on the computation of the Probability Density Function (*PDF*) of the guessed near-field acoustic pressure and its comparison with a Gaussian distribution that is assumed to be the *PDF* of the actual acoustic pressure. As it will be shown in §6.1, the analysis of the far-field pressure confirms this assumption.

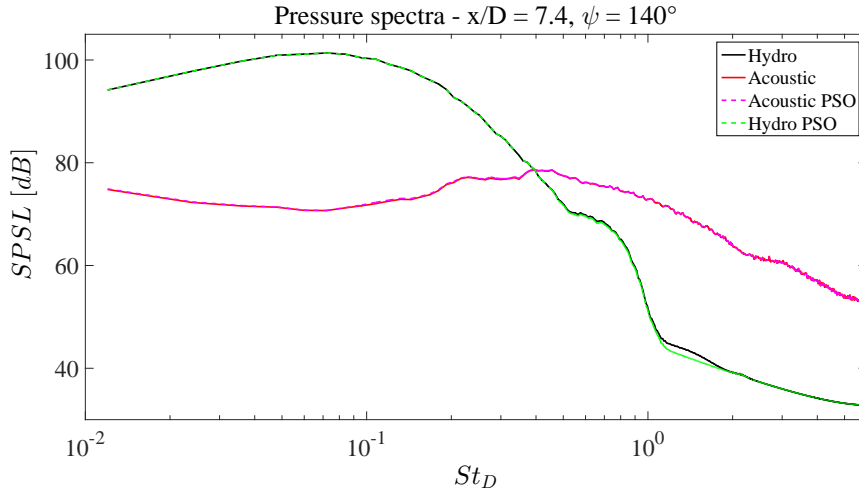


Figure 4.2: Wavelet technique WT1: comparison between the pressure spectra obtained by the gradient-based optimization method and the Particle Swarm Optimization.

The separation procedure adopted is summarized in the following steps. Starting from the initial guess  $T_0$ , the threshold value is iteratively decreased. At each iteration the normalized probability density function of the guessed near-field acoustic pressure, denoted as  $PDF_A$ , is computed and compared with a reference standard Gaussian distribution  $PDF_g$ . The estimation of the similarity between the two  $PDF$ s is accomplished through a ' $\chi$  squared test' (Chernoff and Lehmann, 1954). The iterative process ends when the departure of  $PDF_A$  from the normal distribution is less than a tolerance  $\varepsilon$ :

$$T^* = \arg \min_{T \in \mathbb{R}^+} F(T) \quad F(T) = \chi^2(T) = \sum_{k=1}^{N_{bin}} \frac{(PDF_{A_k} - PDF_{g_k})^2}{PDF_{g_k}} < \varepsilon \quad (4.5)$$

where  $\varepsilon$  has been set equal to  $10^{-4}$ , whereas  $N_{bin}$  is the number of bins used to compute the  $PDF$  for a discrete series of values. Figure 4.3 shows examples of  $PDF$ s of the original and the separated signals compared with the standard Gaussian distribution. The agreement between the acoustic and Gaussian  $PDF$ s is well verified, thus implying that the sound component can be handled as a stochastic and statistically steady phenomenon. On the contrary, the original and the hydrodynamic  $PDF$ s exhibit a significant discrepancy in the tails due to intermittent pressure events associated with the turbulence development (see §6.4.2).

### 4.3 Wavelet technique 'WT3'

The third separation procedure, denoted as WT3, is an application to the pressure field of the decomposition technique developed by Ruppert-Felsot et al. (2009) to extract coherent structures from a vorticity field. The assumption at the basis of the present approach is that the hydrodynamic pressure is related to temporally and spatially localized coherent turbulent structures convected by the jet flow. On the basis of the relation between hydrodynamic pressure and vorticity (see e.g. Landau and Lifshitz

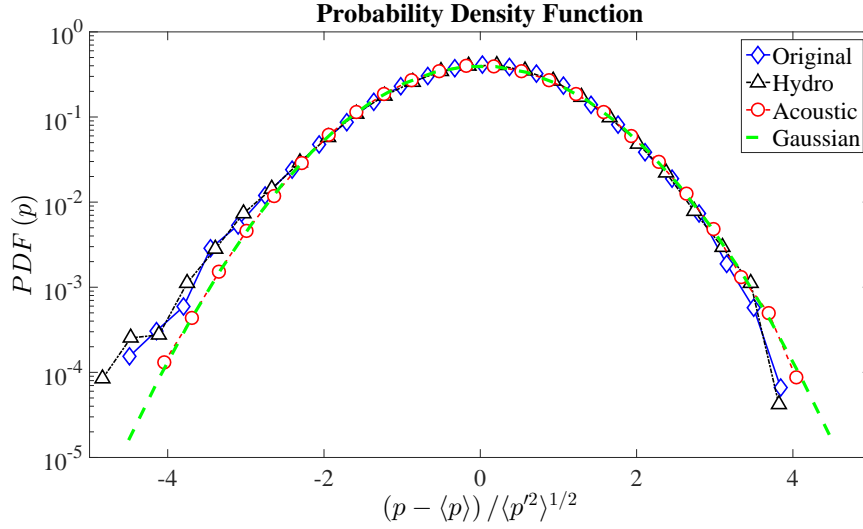


Figure 4.3: Separation technique *WT2*: Probability Density Functions of original, hydrodynamic and acoustic pressures and comparison with the standard Gaussian distribution. Jet Mach number  $M_j = 0.6$ , microphone axial position  $x/D = 5.6$ .

(1985) and more recently Hanjalić and Mullyadzhyanov (2015)), it is straightforward to assume that the method adopted in Ruppert-Felsot et al. (2009) to extract the coherent structures of the vorticity field can be efficiently used to isolate the hydrodynamic pressure (associated with the coherent vorticity) from the acoustic counterpart.<sup>2</sup>

The separation algorithm is based on the application of a recursive de-noising procedure in which the acoustic pressure field is iteratively evaluated until a convergence criterion is satisfied. Starting from the initial guess  $T_0$  defined above, the threshold

<sup>2</sup>The hydrodynamic pressure field is not affected by compressibility effects. The dimensionless form of the Navier-Stokes and mass conservation equations for an incompressible Eulerian fluid are:

$$\begin{cases} \frac{\partial \mathbf{u}}{\partial t} + \mathbf{u} \cdot \nabla \mathbf{u} = -\nabla p_H \\ \nabla \cdot \mathbf{u} = 0 \end{cases} \quad (4.6)$$

Taking the divergence of the first equation in (4.6), applying the Schwarz's rule to interchange the order of the partial derivatives and exploiting the solenoidal condition of the velocity field, the Poisson's equation is obtained:

$$-\nabla^2 p_H = (\nabla \otimes \nabla) : (\mathbf{u} \otimes \mathbf{u}) \quad (4.7)$$

The symmetric part of the velocity gradient tensor can be expressed as the strain rate tensor  $\mathbf{E}$ , whereas the anti-symmetric counterpart is related to the vorticity tensor  $\mathbf{\Omega}$ :

$$\mathbf{E} = \frac{1}{2} (\nabla \mathbf{u} + \nabla \mathbf{u}^T) \quad \mathbf{\Omega} = \frac{1}{2} (\nabla \mathbf{u} - \nabla \mathbf{u}^T) \quad (4.8)$$

As a consequence of some mathematical manipulations, the equation governing the hydrodynamic pressure field reduces to the following expression:

$$\nabla^2 p_H = \frac{1}{2} (\omega^2 - e^2) \quad (4.9)$$

where  $\omega^2 = \mathbf{\Omega} : \mathbf{\Omega}$  and  $e^2 = \mathbf{E} : \mathbf{E}$ . The previous equation means that the flux of the pressure gradient is governed by two terms: a source term related to the enstrophy, i.e. the energy associated to the vorticity, and a sink term associated to the strain rate tensor. Hence, hydrodynamic pressure can be used to track vortices and to identify coherent structures.

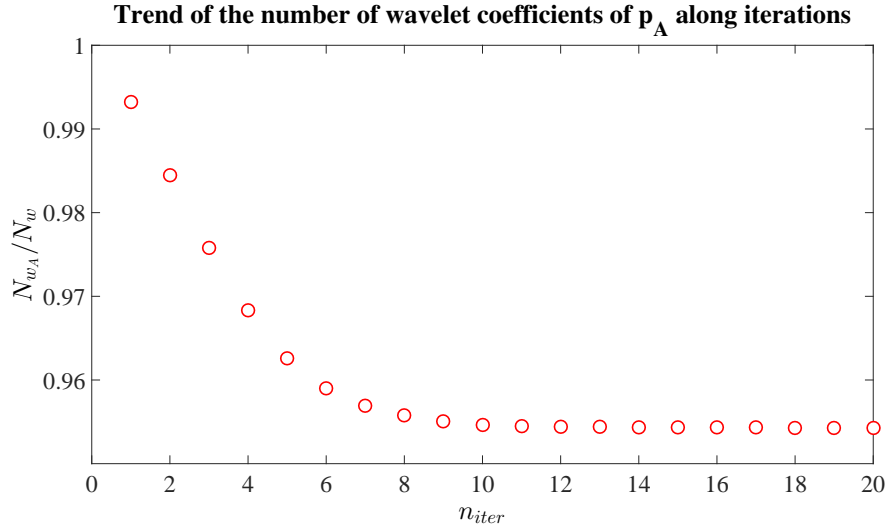


Figure 4.4: Separation technique *WT3*: trend along the iterations of the number of wavelet coefficients of the acoustic pressure normalized by the total number of the wavelet coefficients of the original signal. Jet Mach number  $M_j = 0.6$ , microphone axial position  $x/D = 7.4$ .

value is updated at each  $k^{th}$  iteration according to the following formula:

$$T_k = \sqrt{2\langle p_A'^2 \rangle_k \log_2 N_s} \quad : \quad T = T^* \Leftrightarrow N_{w_A}|_k = N_{w_A}|_{k-1} \quad (4.10)$$

where  $\langle p_A'^2 \rangle_k$  is the variance of the acoustic pressure signal at each iteration. The pseudo-sound and sound components are iteratively separated being their wavelet coefficients respectively larger or lower than the updated threshold level. A convergence analysis of the threshold value as a function of the number of samples has been preliminarily carried out in order to verify that the resulting decomposition was independent of the number of samples for  $N_s \geq N_s^*$ . The value of  $N_s^*$  was found to be equal to  $2^{18}$  for all the analysed signals. The iterative process stops when the number of wavelet coefficients of the acoustic pressure becomes constant (see also Azzalini et al. (2005)).

Figure 4.4 clarifies the procedure. It shows for a reference case the number of wavelet coefficients of the acoustic pressure ( $N_{w_A}$ ) normalized with respect to the total number of wavelet coefficients of the original pressure signal ( $N_w$ ) as a function of the iterations. It is observed that, after a certain number of iterations,  $N_{w_A}$  remains constant thus indicating that the iterative process has converged. This trend has been observed in all cases examined therein and for all the analysed signals the convergence has been achieved after a number of iterations of the order of 20.



# Chapter 5

## Experimental set-up

### 5.1 Facility description

The wavelet methods described in §4 have been applied to an existing database provided by the Centre Acoustique of Laboratoire de Mécanique des Fluides et d'Acoustique at the École Centrale de Lyon. The experimental test campaign has been carried out under the framework of the EU Collaborative project ORINOCO (ACP0-GA-2010-266103) in the anechoic wind tunnel. The fully anechoic chamber size is  $10 \times 9 \times 8 m^3$ . The feed line consists of a compressed dry air duct supplied by a compressor delivering a continuous mass flow-rate of up to  $1 kg/s$ . An electrically driven valve downstream the compressor permits the regulation of the jet velocity by controlling the incoming mass flow. The flow conditions are continuously monitored by a thermocouple and a pressure tap located 15 jet diameters upstream the nozzle exit, which permit to measure the total temperature and the static pressure of the inflow, respectively. The jet exit conditions are obtained by use of isentropic flow relations between the pressure and temperature measurements and the nozzle exit conditions. Analytical predictions were verified by *ad hoc* Pitot measurements.

Experiments were performed on a single-stream round jet for two Mach numbers:  $M_j = 0.6$  and  $M_j = 0.9$ , to which correspond Reynolds numbers respectively equal to  $Re_D \approx 7.5 \cdot 10^5$  and  $Re_D \approx 1.2 \cdot 10^6$ , which classify the jet as a high Reynolds number jet (Bogey et al., 2012a; Viswanathan, 2004).  $Re_D$  denotes the Reynolds number based on the nozzle diameter  $D = 50 mm$  and on the flow velocity at the nozzle exit  $U_j = M_j c_j$ , being  $c_j$  the speed of sound.

### 5.2 Instrumentation

Velocity measurements were carried out in order to provide a preliminary characterization of the aerodynamic field in the jet plume. The measurements were performed by a single hot-wire probe DANTEC 55P11 of  $1 mm$  length and  $5 \mu m$  diameter. The hot-wire was mounted on a traversing system with the probe in the normal direction with respect to the jet flow in order to reduce the flow disturbances. The hot-wire was connected to a constant temperature anemometer system DANTEC Streamline Pro. Velocity signals were acquired by a National Instruments PXI-4472 acquisition system with a sampling frequency set to  $25.6 kHz$  for an acquisition time of  $10 s$ .

Simultaneous near- and far-field pressure measurements have been carried out in

NEAR FIELD													
$x/D$													
2	2.5	3.3	4	4.6	5.1	5.6	6.1	6.6	7	7.4	7.8	8.1	8.7
FAR FIELD													
$\psi$													
30°	40°	50°	60°	70°	80°	90°	100°	110°	120°	130°	140°	150°	
Jet flow conditions													
$M_j$							$Re_D$						
0.6							$7.5 \cdot 10^5$						
0.9							$1.2 \cdot 10^6$						

Table 5.1: Summary of the jet flow conditions analysed and of the location of the near- and far-field microphones

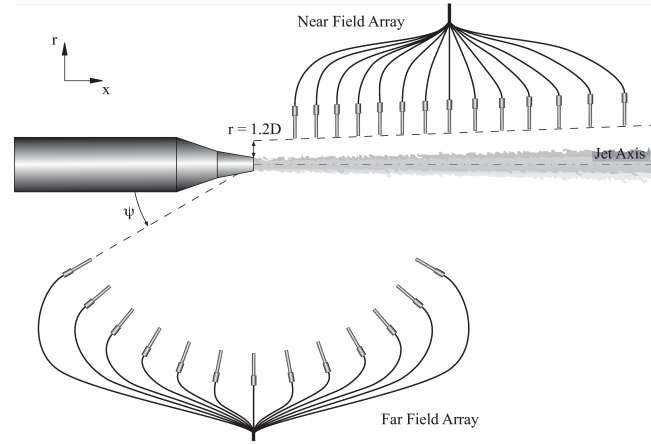


Figure 5.1: Sketch of the experimental set-up and scheme of the microphones disposition

free-jet conditions. Pressure fluctuations were measured by PCB 377B01 microphones, whose frequency response is flat in the  $4\text{ Hz} - 80\text{ kHz}$  range and whose full-scale value is  $165\text{ dB}$ . Pressure signals were acquired by National Instruments PXI-4472 system with a sampling frequency equal to  $51.2\text{ kHz}$  for an acquisition time of  $10\text{ s}$ . A near-field 14 microphones linear array was placed at a radial distance of  $r/D = 1.2$  from the jet in the so-called '*linear hydrodynamic regime*', in which a superimposition of the hydrodynamic and acoustic pressures is found (Suzuki and Colonius, 2006). The array was aligned to the jet spreading angle, which was found to be close to  $11^\circ$  from the overall aerodynamic characterization by hot-wire measurements. The microphones were not equally spaced along the stream-wise direction spanning an axial distance from the nozzle exhaust from  $x/D = 2$  to  $x/D = 8.7$ . The far-field microphones were located on a circular arc at a radial distance from the nozzle exit  $r/D = 40$  on a polar angle range spanning from  $30^\circ$  to  $150^\circ$ , the polar angle  $\psi$  being defined positive in the upstream direction. A sketch of the experimental set-up is shown in figure 5.1. A summary of the jet flow conditions analysed and of the microphones disposition is reported in table 5.1.

# Chapter 6

## Results

The results concerning the hydrodynamic/acoustic decomposition are reported in the following. First, a qualification of the jet is provided. Successively, a validation of the innovative wavelet techniques against reference separation methods found in the literature, i.e. the  $k-\omega$  procedure by Tinney and Jordan (2008) and the wavelet method by Grizzi and Camussi (2012), is presented. Finally, the hydrodynamic and acoustic pressures are characterized separately in terms of statistical and spectral content.

### 6.1 Jet assessment

#### 6.1.1 Jet aerodynamics

The aerodynamic characterization of the jet is provided in terms of mean velocity and turbulence intensity profiles along the radial distance  $r$  for different axial positions  $x$  of the hot-wire. The mean and fluctuating velocities at each position were normalized by the jet velocity at the nozzle exit  $U_j$ , whereas a non-dimensional radial coordinate  $\eta$  was computed according to the following formula:

$$\eta = \frac{r - R_{1/2}}{\delta_\theta} \quad (6.1)$$

Where  $r$  is the radial distance from the jet axis,  $R_{1/2}$  is the radial position for which the mean axial velocity is 50% of the jet velocity and  $\delta_\theta$  is the momentum thickness of the shear layer defined as follows:

$$\delta_\theta = \int_{-\infty}^{+\infty} \frac{\langle U \rangle}{\langle U(r=0) \rangle} \left( 1 - \frac{\langle U \rangle}{\langle U(r=0) \rangle} \right) dr \quad (6.2)$$

Figure 6.1 shows the dimensionless velocity and turbulence level profiles for the axial distances  $x/D = 0, 1, 3, 5, 7$ . For the sake of conciseness, the case  $M_j = 0.6$  was here considered. The shape and the evolution along the axial distance of the mean and fluctuating velocity profiles are in agreement with previous results found in the literature (Moore, 1977; Jung et al., 2004). The mean velocity profiles exhibit the typical top-hat shape with a velocity value about constant along the jet centre-line up to 5 diameters downstream of the nozzle exhaust. The Relative Turbulence Level (*RTL*) based on the jet velocity is about 1% on the jet axis close to the nozzle exhaust, it increases moving downstream in the jet and inside the shear layer reaching a maximum value of  $\approx 16\%$  for  $\eta = 0$ .

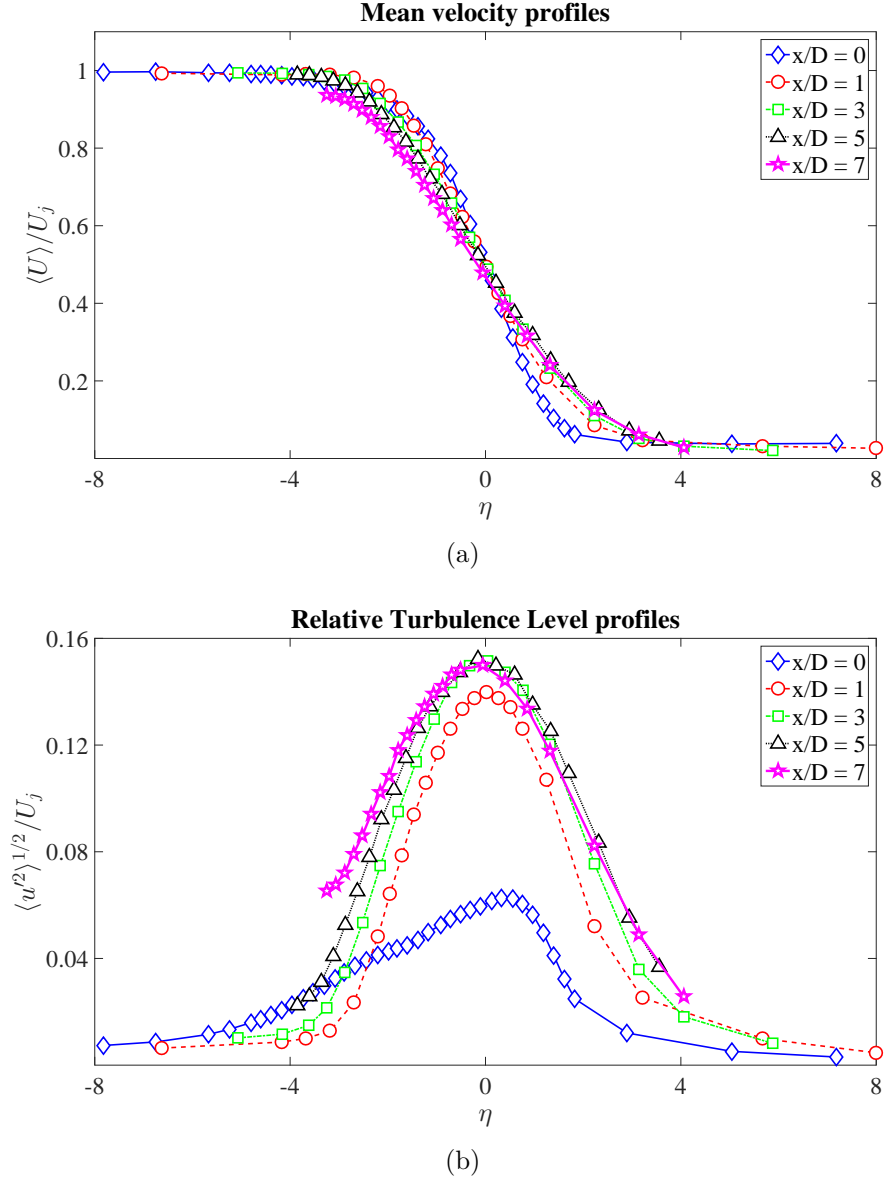


Figure 6.1: Dimensionless mean and fluctuating velocity profiles along the non-dimensional radial coordinate  $\eta$  at different axial positions  $x$  for jet Mach number  $M_j = 0.6$ : (a) mean velocity, (b) relative turbulence level.

### 6.1.2 Jet aeroacoustics

The aero-acoustic qualification of the jet is carried out by analysing both the near- and far-field pressure data. The statistical description of the far-field pressure also provides a demonstration of the Gaussian nature of the pressure fluctuations far away from the jet, a result which is fundamental for the application of the method WT2 (see §4.2).

#### 6.1.2.1 Near field

Figure 6.2 shows the stream-wise evolution of the Sound Pressure Spectrum Levels (*SPSLs*) for axial positions  $x/D = 2.5, 4.6, 6.1, 7.4$  and  $8.7$  and for the two Mach numbers considered herein. According to Pierce (1981), the *SPSL* is computed as follows:

$$SPSL = 10 \log_{10} \frac{PSD \Delta f_{ref}}{p_{ref}^2} \quad (6.3)$$

where  $\Delta f_{ref} = 1 \text{ Hz}$  and  $p_{ref} = 20 \mu\text{Pa}$  are the reference frequency and pressure, respectively. The pressure spectra are represented as a function of the Strouhal number  $St_D = f D/U_j$ . It is observed that, as the axial distance from the nozzle exit increases, the energy hump in the spectra moves from high to low frequencies, such a behaviour being related to the development of larger turbulent structures. For small axial distances an energy peak at a Strouhal number  $\approx 0.39$  associated with the Kelvin-Helmholtz instability (Danaila et al., 1997) clearly emerges for  $M_j = 0.9$ , whereas for the case  $M_j = 0.6$  higher order harmonics are detected. Moving downstream, the turbulence intensity increases and the spectral shape changes accordingly showing a broadband energy distribution. A global picture of the stream-wise evolution of the pressure spectra is depicted in figure 6.3, where a contour map of the *SPSL* is shown.

As pointed out by Arndt et al. (1997), the energy content associated with the pressure fluctuations shows far-field behaviour when the product between the axial wavenumber  $k_x$  and the radial distance  $r$  is sufficiently large ( $k_x r \gg 1$ ). According to this condition, the near-field pressure spectra are characterized by a dominant hydrodynamic component at low frequencies, whereas the acoustic component prevails at high frequencies. Such aspect is confirmed by the different energy decay laws found in the pressure spectra. Figure 6.4 shows the dimensionless spectra at  $x/D = 3.3, 4.6, 5.6, 6.1$  and for  $M_j = 0.6$ . The *PSDs* have been normalized by the dynamic pressure computed using as reference density the ambient air density  $\rho_\infty = 1.225 \text{ kg/m}^3$  and as reference velocity the jet velocity. It is observed that at low frequencies the spectra show an energy decay  $\propto St_D^{-20/3}$  typical of the hydrodynamic fluctuations, whereas at high frequencies a slope of  $-2$  related to pressure perturbations induced by sound waves is observed (Arndt et al., 1997; Tinney et al., 2007).

The interpretation of the spectra is confirmed by the analysis of the axial evolution of the cross-correlation coefficient (Ross, 2014), as shown in figure 6.5. The cross-correlation has been computed between two consecutive microphones of the near-field array. At small axial distances a pseudo-periodic behaviour is observed, such a trend being again the signature of the Kelvin-Helmholtz instability mode. Moving downstream from the jet exit, the turbulence development produces the typical negative-positive bump shape (Grizzi and Camussi, 2012), the larger correlation time-scale being related to the development of large-scale turbulent structures.

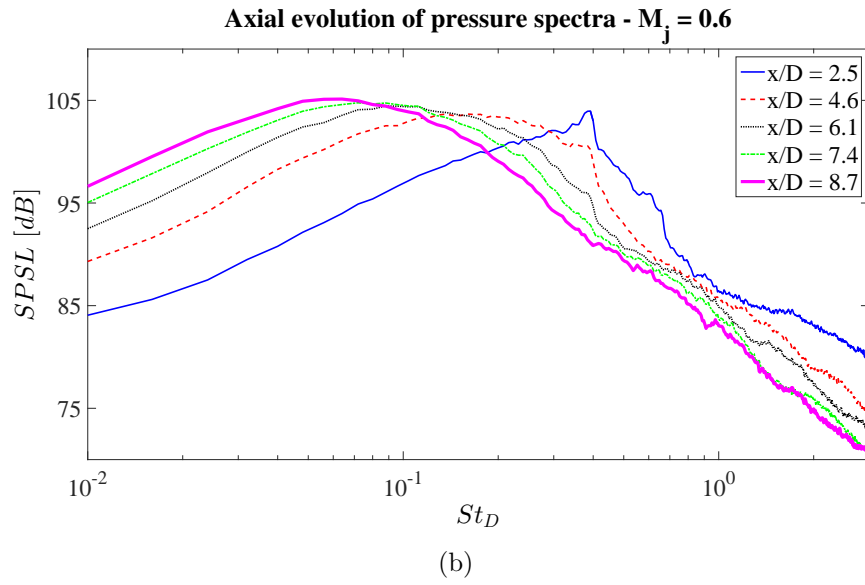
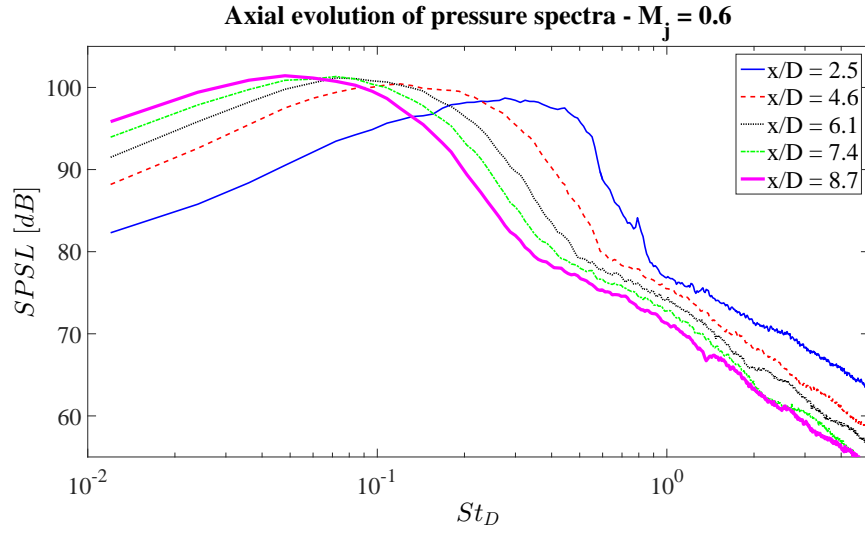


Figure 6.2: Axial evolution of the pressure spectra: (a) jet Mach number  $M_j = 0.6$ , (b) jet Mach number  $M_j = 0.9$ .

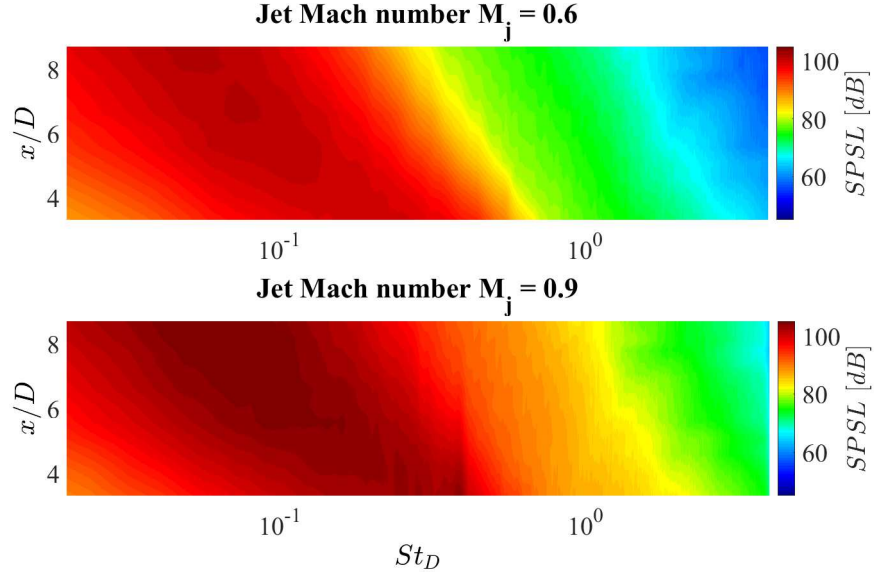


Figure 6.3: Contour plot of the Sound Pressure Spectrum Level along the stream-wise direction for both jet Mach numbers.

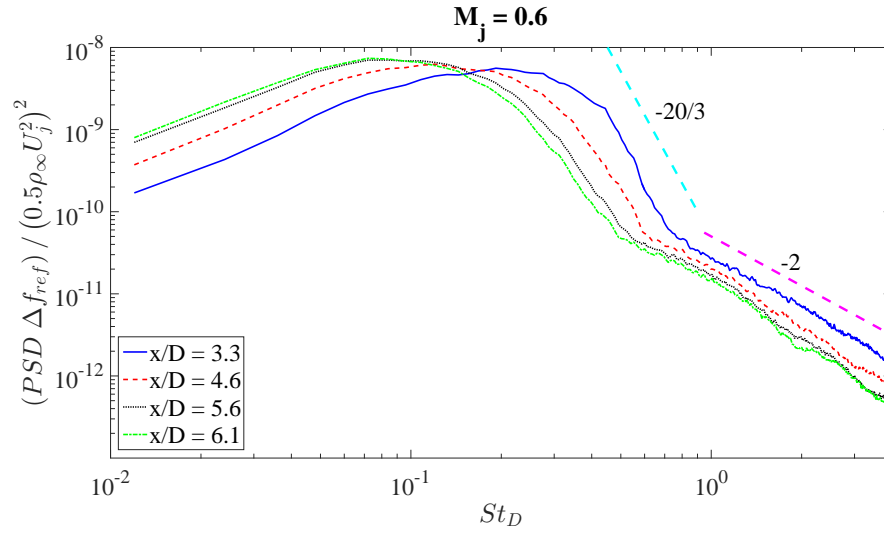


Figure 6.4: Dimensionless pressure spectra for jet Mach number  $M_j = 0.6$  at different axial distances.

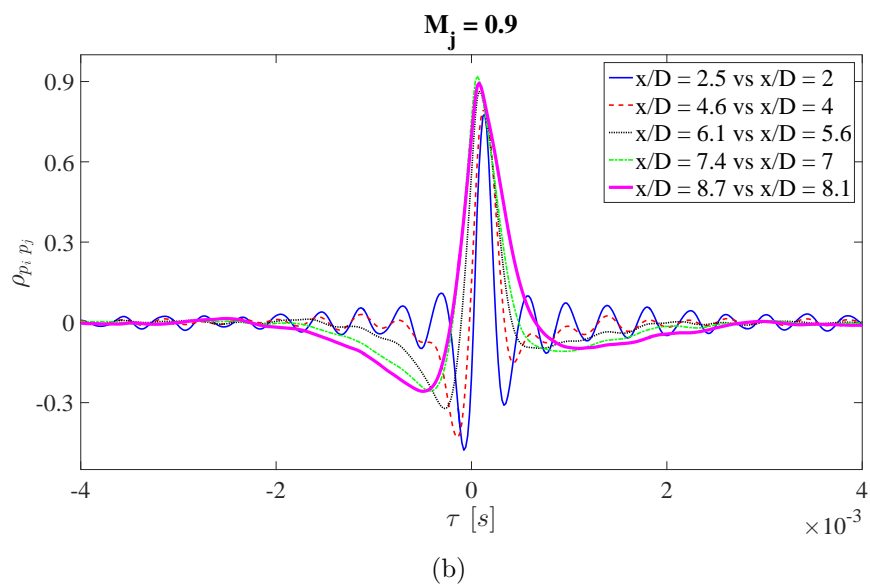
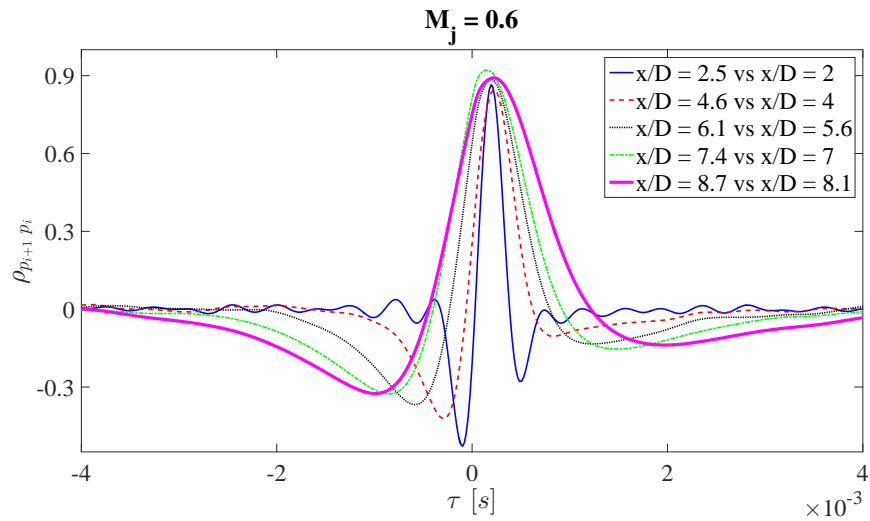


Figure 6.5: Axial evolution of the cross-correlation coefficient between two consecutive microphone signals in the near field: (a) jet Mach number  $M_j = 0.6$ , (b) jet Mach number  $M_j = 0.9$ .



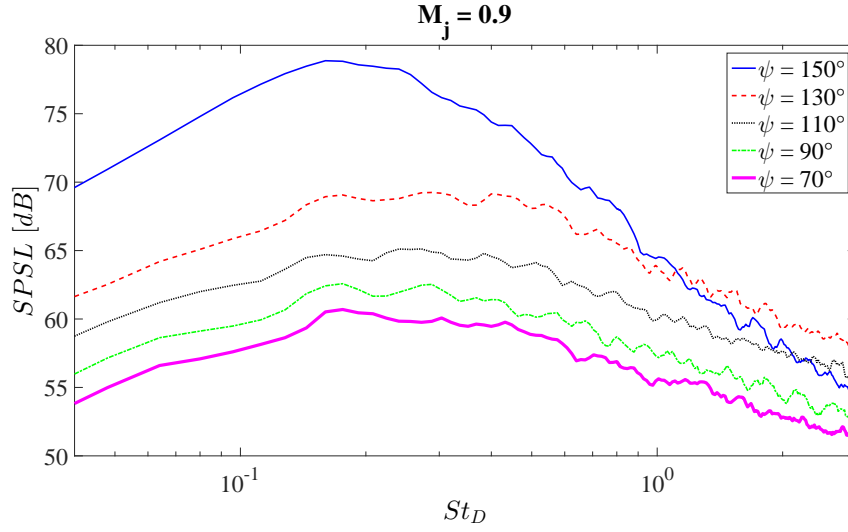


Figure 6.6: Polar trend of the far-field pressure spectra for jet condition  $M_j = 0.9$ .

#### 6.1.2.2 Far field

Figure 6.6 shows the polar evolution of the far-field pressure spectra for polar angles  $\psi = 150^\circ, 130^\circ, 110^\circ, 90^\circ, 70^\circ$  and for  $M_j = 0.9$ . As expected, the noise level as well as the spectral shape changes significantly moving from the forward to the aft arc. For large polar angles the spectra show a sharper noise peak, whereas at smaller polar angles the peak broadens and rolls off gradually. Such a trend is in agreement with the well-known prediction provided by Tam et al. (1996) and Tam et al. (2008) and it is related to the noise components associated with the large- and small-scale turbulent structures. A comparison between the experimental data and the spectra obtained by the application of the Tam's model is shown in figure 6.7. A nice agreement between experimental and modelled data is found for both  $M_j$  as in the forward arc as in the aft arc. A global evolution of the noise level along the polar angles is provided in figure 6.8, where the OverAll Sound Pressure Level ( $OASPL$ ) is represented for both jet flow conditions. The  $OASPL$  is computed according to the following formula:

$$OASPL = 20 \log_{10} \frac{\langle p'^2 \rangle^{1/2}}{p_{ref}} \quad (6.4)$$

where  $\langle p'^2 \rangle^{1/2}$  is the standard deviation of the pressure signal. As expected, the noise level raises for increasing jet Mach number and for larger polar angle positions (Tanna, 1977).

Figure 6.9 shows the polar evolution of the  $PDF$ s of the far-field pressure signals for both jet Mach numbers. Experimental data were compared with the reference standard Gaussian distribution showing a good agreement. Furthermore the polar evolution of the third and fourth order statistical moments of the far-field pressure signals is shown in figure 6.10. It is observed that the skewness and flatness factors exhibit values respectively equal to 0 and 3, as for the reference Gaussian distribution, for all the polar angles considered. Such feature further confirms that the statistics of the far-field pressure fluctuations can be assumed as Gaussian.

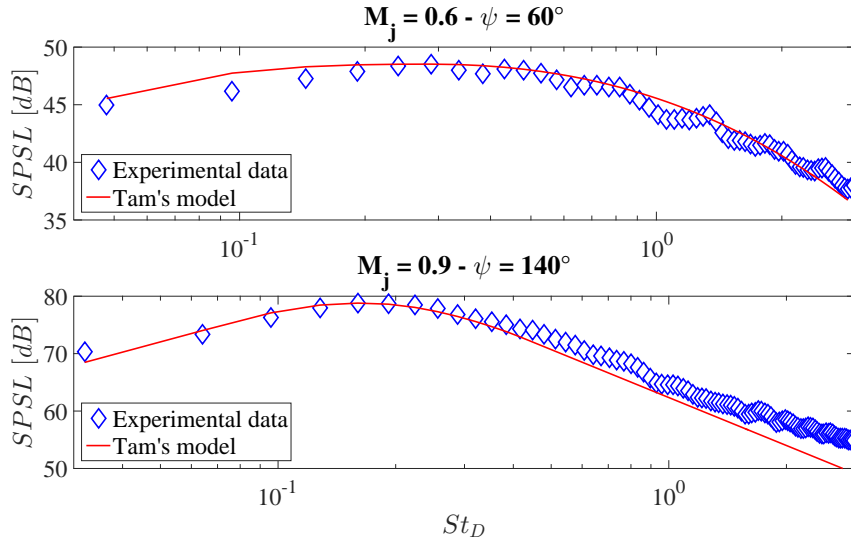


Figure 6.7: Comparison between experimental pressure spectra and results obtained by the application of the Tam's model.

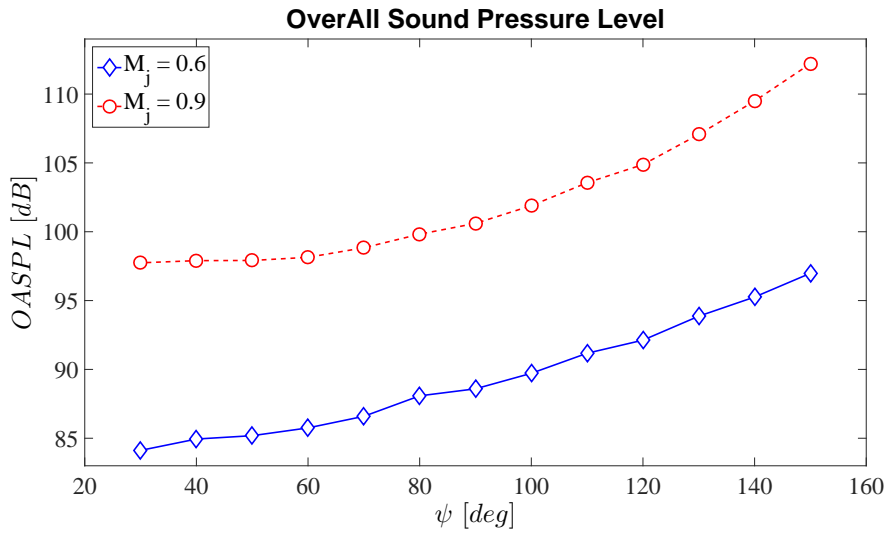


Figure 6.8: Polar evolution of the OverAll Sound Pressure Level for both jet Mach numbers.

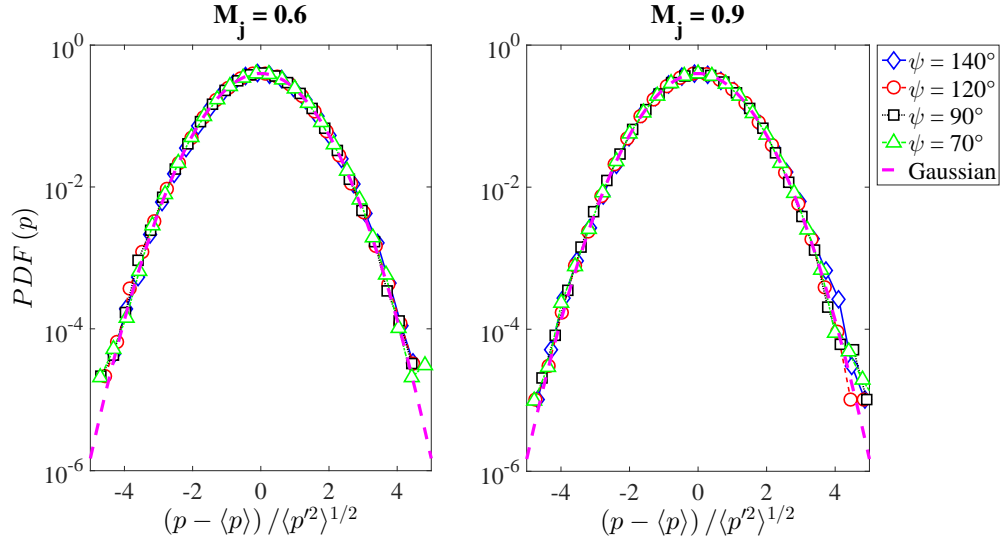


Figure 6.9: Polar evolution of the  $PDF$ s of the far-field pressure for both jet conditions. Dashed line refers to the standard Gaussian distribution.

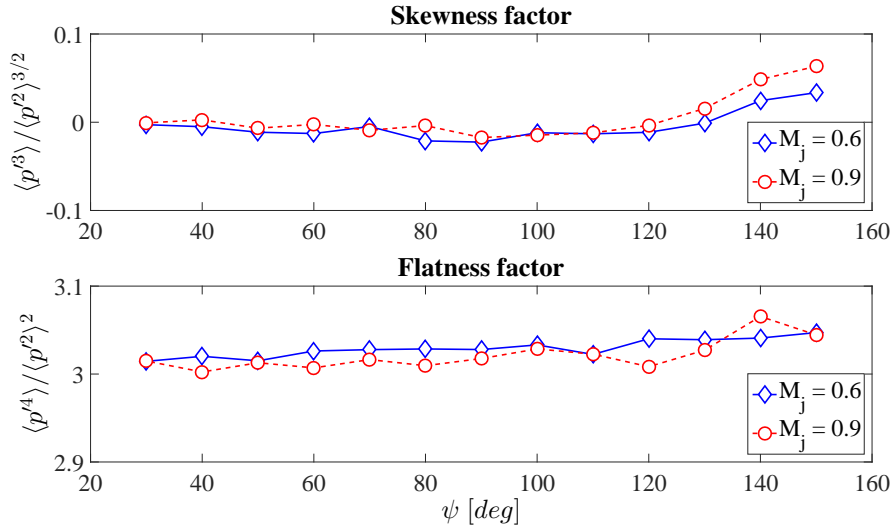


Figure 6.10: Polar evolution of the skewness and flatness factors of the far-field pressure for both jet conditions.

## 6.2 Fourier-based separation procedure

The procedure presented in Kerhervé et al. (2008) and Tinney and Jordan (2008) was briefly worked out. Such method provides interesting results shedding light on the physical nature of the hydrodynamic and acoustic pressure fluctuations. The method is based on the computation of the wavenumber-frequency spectrum obtained by the Fourier transform of the space-time pressure field  $p(x, t)$ . As mentioned in §3, this approach requires measurements with a considerable number of microphones in the near field in order to provide an acceptable resolution of the spectrum in the wavenumber domain. This constraint represents the main limitation of the method.

Formally, the 2D Fourier transform of a pressure signal can be written as:

$$\hat{p}(k_x, \omega) = \int_{-\infty}^{+\infty} p(x, t) W(x) W(t) e^{-i(k_x x + \omega t)} dx dt \quad (6.5)$$

where  $\omega$  is the angular frequency and  $W(x)$  and  $W(t)$  are Hamming windowing functions respectively in the space and time domain. The wavenumber-frequency spectrum is computed as follows:

$$P(k_x, \omega) = \hat{p}(k_x, \omega) \hat{p}^*(k_x, \omega) \quad (6.6)$$

Figure 6.11 shows the normalized  $k - \omega$  spectral map in logarithmic scale for both jet flow conditions; the map is represented against the Strouhal number and a dimensionless wavenumber based on the nozzle diameter. Two spectral lobes can be clearly observed in the Fourier domain, whose energy level and shape change depending on the jet Mach number. The two lobes are the signatures of two pressure components: the hydrodynamic pressure associated with a phase velocity comparable with the convection velocity  $U_c \approx 0.6 U_j$  (Picard and Delville, 2000) and the acoustic pressure related to a phase velocity of the order of the speed of sound. Pseudo-sound and sound components are extracted by filtering the 2D spectrum according to their phase velocities. Pressure perturbations propagating at a velocity greater than or equal to the speed of sound are related to acoustic pressure, whereas pressure fluctuations convected at a velocity lower than the speed of sound are associated with hydrodynamic pressure. Figure 6.12 shows the space-time map of the original pressure field and the separated hydrodynamic and acoustic pressure fields for both jet Mach numbers. The characteristic propagation velocities of each separated pressure component are superimposed to the maps. It can be observed that the hydrodynamic field shows a more coherent signature with pressure perturbations moving with a phase velocity equal to the convection velocity. On the other hand the acoustic field is characterized by a less organized structure with wave fronts propagating at a velocity close to the speed of sound.

The hydrodynamic and acoustic components are correlated with the pressure measured in the far field. Figure 6.13 shows a map of the peaks of these cross-correlations computed for all the axial and polar positions. It is observed that the correlation between  $p_A$  and  $p_{FF}$  is larger than that between  $p_H$  and  $p_{FF}$  for all the microphone positions considered. The value of the correlation peak between  $p_A$  and  $p_{FF}$  increases as the maximum noise emissivity region in the far field is approached ( $\psi = 130^\circ - 150^\circ$ ). Nevertheless, in this region an unexpected high correlation level between the hydrodynamic and the far-field pressures is observed especially for  $M_j = 0.9$ . Such an issue can be ascribed to a lack of resolution (Kerhervé et al., 2008) which affects the separation of the hydrodynamic and acoustic components mainly for low wavenumbers.

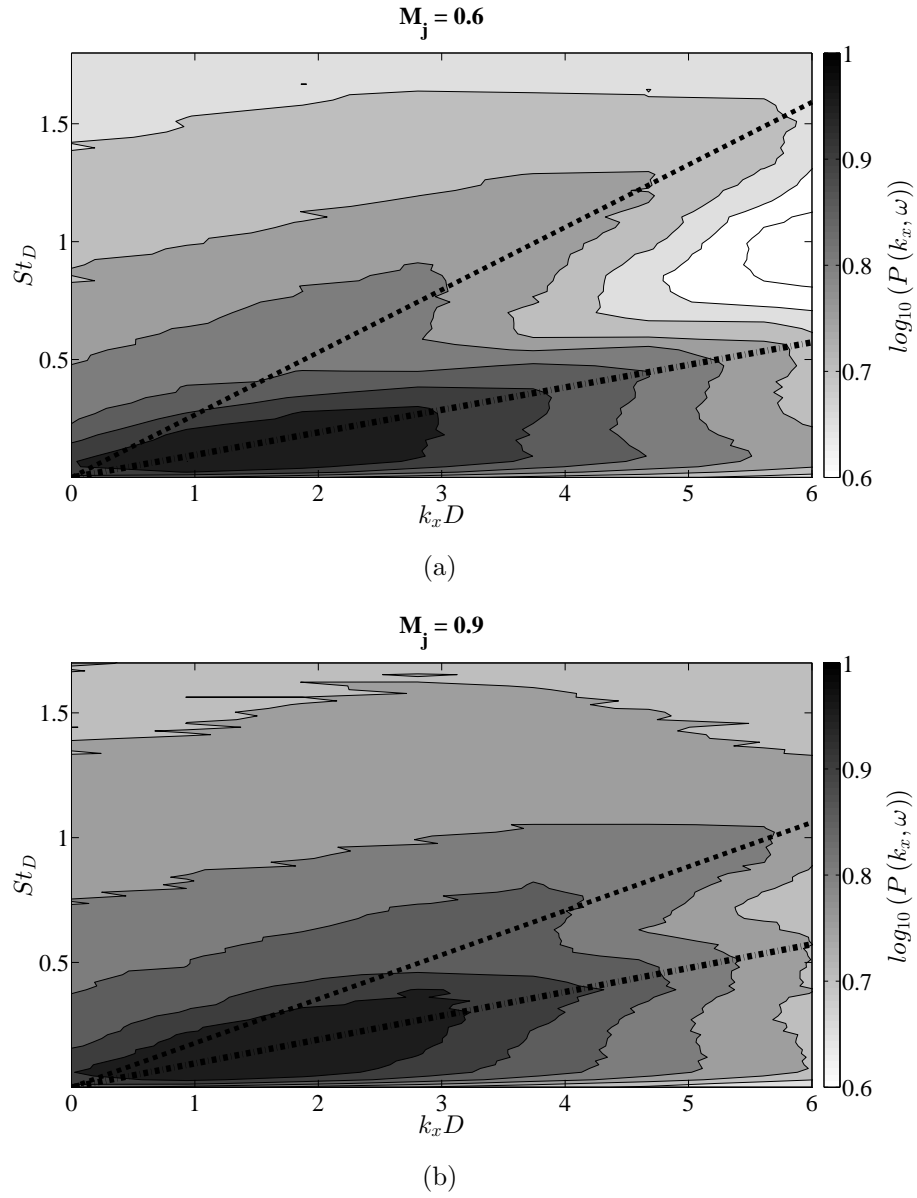


Figure 6.11: Normalized wavenumber-frequency spectrum of the near pressure field for both jet flow conditions. (a) jet Mach number  $M_j = 0.6$ , (b) jet Mach number  $M_j = 0.9$ . Dashed lines refer to the speed of sound, dash-dotted lines refer to the convection velocity.

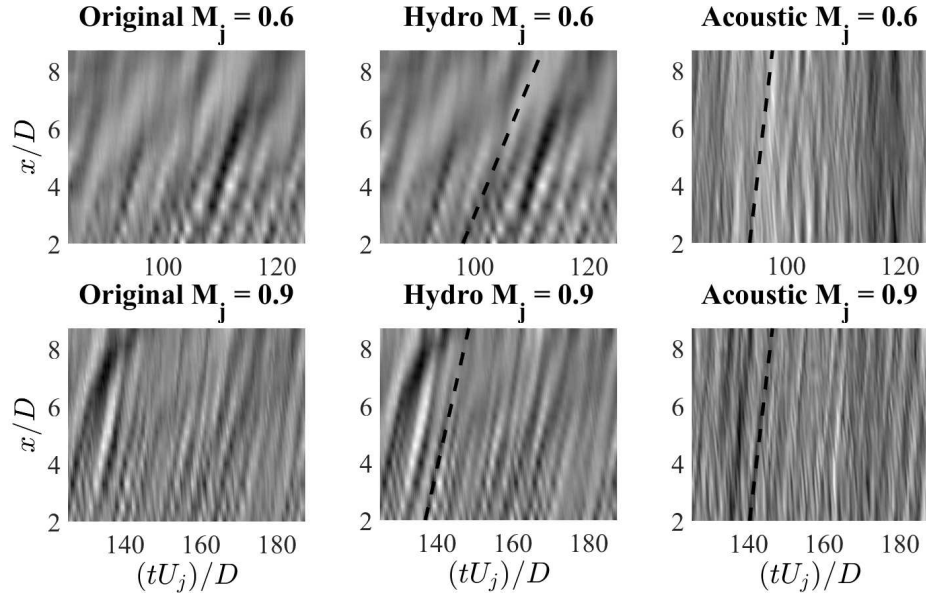


Figure 6.12:  $k-\omega$  technique: space-time map of original, hydrodynamic and acoustic near pressure fields separated by the Fourier filtering technique for both jet velocities.

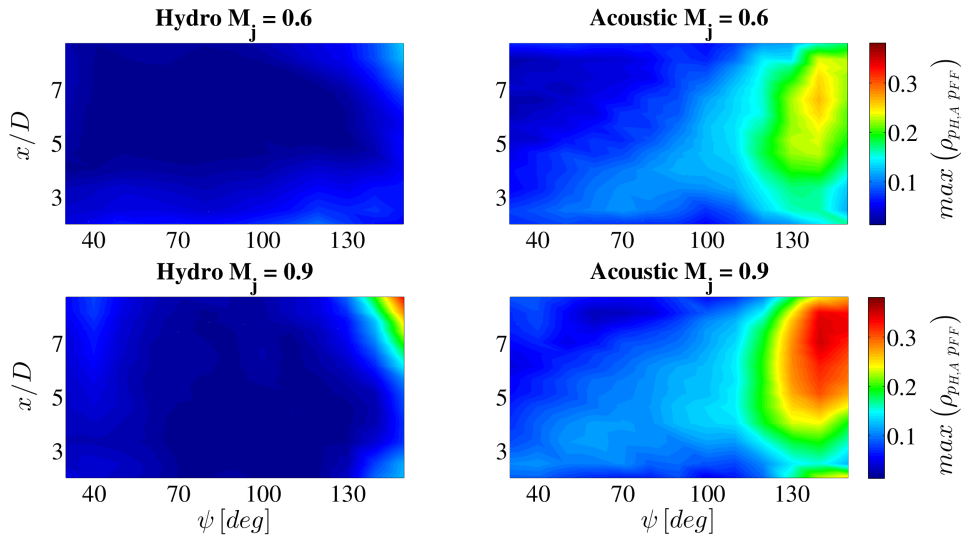


Figure 6.13:  $k-\omega$  technique: cross-correlation coefficient peak map of hydrodynamic and acoustic components with measured far-field pressure at all the axial and polar positions for both jet Mach numbers.

## 6.3 Validation of the novel separation techniques

In order to better appreciate the effectiveness and efficiency of the different methods and in order to enhance any differences, the results obtained by the application of the three wavelet-based techniques introduced therein are compared with each other. The validation of the proposed methods has been achieved by the comparison with the outcomes obtained by the application of separation procedures available in the literature, that is the  $k - \omega$  spectrum filtering and the technique introduced by Grizzi and Camussi (2012) (hereinafter indicated as  $WT_4$ ).

Figure 6.14 shows the  $SPSLs$  of the extracted hydrodynamic and acoustic components separated with the different wavelet-based techniques for the axial distance  $x/D = 7.8$  and jet Mach number  $M_j = 0.9$ . No significant differences in terms of spectral shape and amplitude can be appreciated for the hydrodynamic spectra between all the different techniques. For the acoustic pressure spectra a very small noise level discrepancy included in  $2\text{ dB}$  is detected at low frequencies.

Taking advantage of the simultaneous measurements of near- and far-field pressures, a validation of the methods has been accomplished by computing the cross-correlation of the near-field separated pressure fields with the far-field pressure, that has to be considered as the measure of the actual acoustic pressure. The performance of the separation method is satisfactory if the correlation between near-field acoustic/hydrodynamic and far-field pressure is large/small. Figure 6.15 shows the axial evolution of the cross-correlation peak values of  $p_H$  and  $p_A$  with  $p_{FF}$  at the polar position  $\psi = 140^\circ$  for Mach number  $M_j = 0.6$ . It can be seen that all the wavelet techniques perform satisfactorily since they provide large correlation between the far-field and the acoustic pressures whereas the one between the far-field and the hydrodynamic pressures is much smaller, the magnitude of the peaks being similar among all the procedures. A similar behaviour is observed also with respect to the reference  $k - \omega$  technique but with some discrepancies. Specifically, for what concerns the acoustic pressure, it is found that for small axial distances the Fourier filtering technique provides cross-correlation peaks larger than those obtained by the wavelet-based methods. The opposite result is detected moving downstream in the jet. Such a behaviour can be ascribed to the different nature of the filtering bases, the wavelet one being more suited to detect large hydrodynamic fluctuations due to its better localization in the physical and transformed spaces. Figure 6.16 shows the polar evolution of the cross-correlation coefficient peak of the far-field pressure with the hydrodynamic and acoustic pressure components at the axial position  $x/D = 6.1$ . It is observed that a very good agreement between all the wavelet and the Fourier filtering techniques is detected for all the polar angles taken into account.

Finally the propagation velocities of the hydrodynamic and acoustic pressure fluctuations have been calculated based on the time-delay associated with the cross-correlation peak between two consecutive stream-wise near-field microphones. A standard procedure used in Particle Image Velocimetry (PIV) data processing for the sub-pixel determination of the cross-correlation peak position has been used to improve the accuracy of the time-delay position, thus reducing the associated bias error (Raffel et al., 2007). Figure 6.17 shows the axial evolution of the normalized convection and sound propagation velocities at  $M_j = 0.6$  for all the separation techniques. It is observed that all the techniques provide equal velocity values. An exception for the acoustic propagation velocity obtained by the  $k - \omega$  technique is found for axial positions close

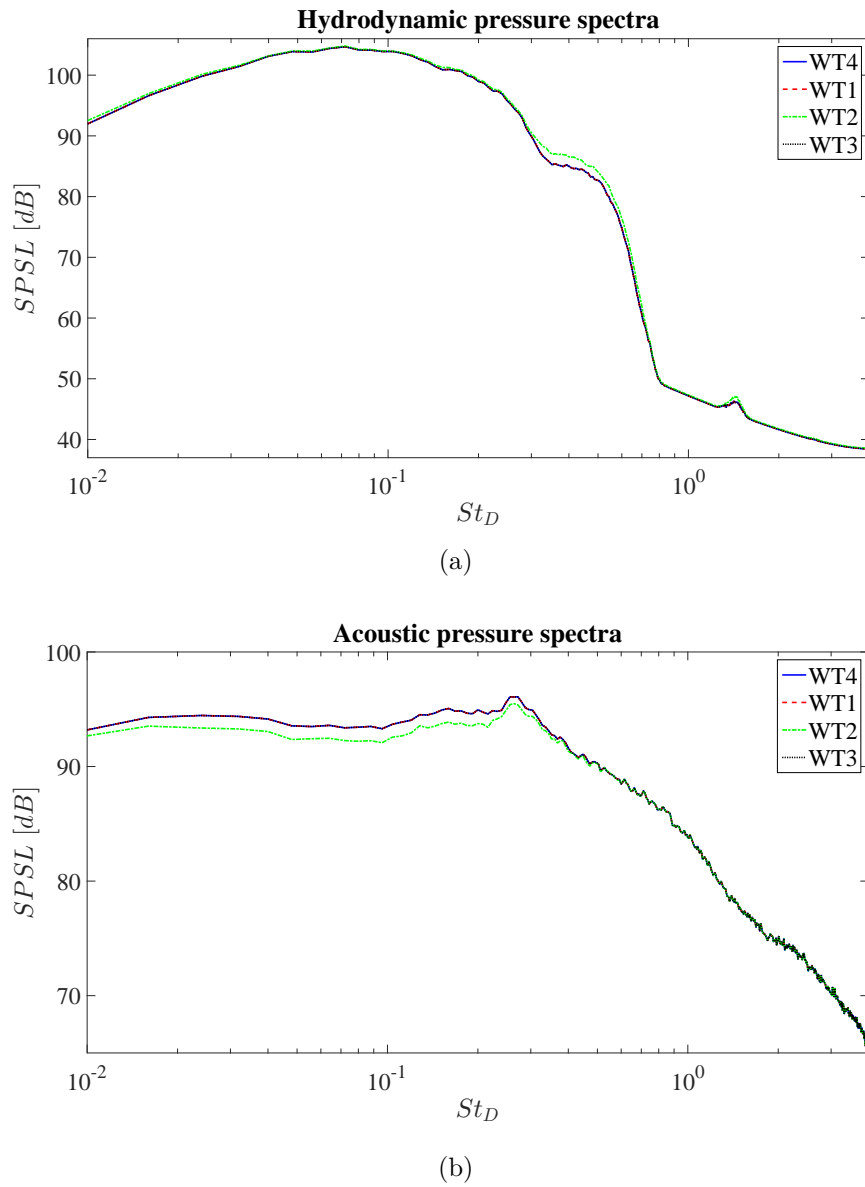


Figure 6.14: *SPSLs* of hydrodynamic and acoustic pressures separated with all the different wavelet techniques at axial position  $x/D = 7.8$  for  $M_j = 0.9$ : (a) hydrodynamic component, (b) acoustic component.



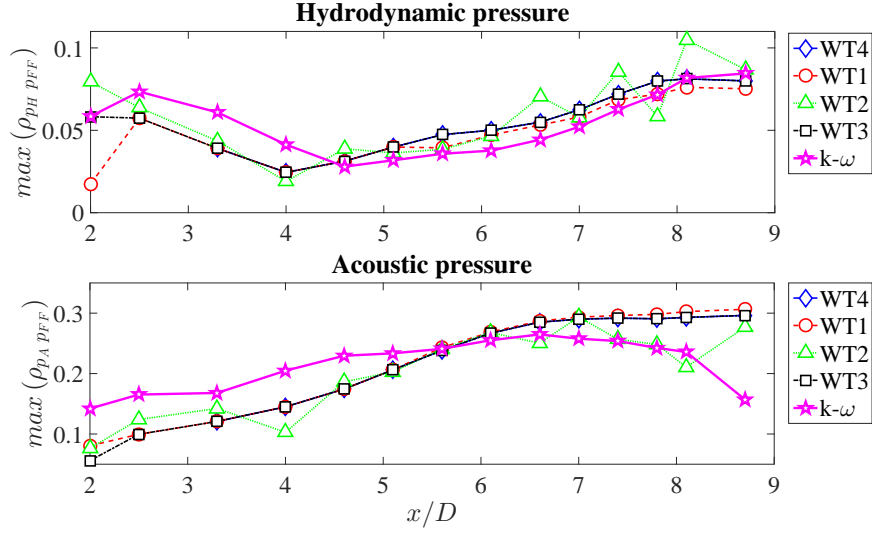


Figure 6.15: Axial evolution of the cross-correlation coefficient peak of near-field hydrodynamic and acoustic components with far-field pressure for polar position  $\psi = 140^\circ$  at  $M_j = 0.6$ .

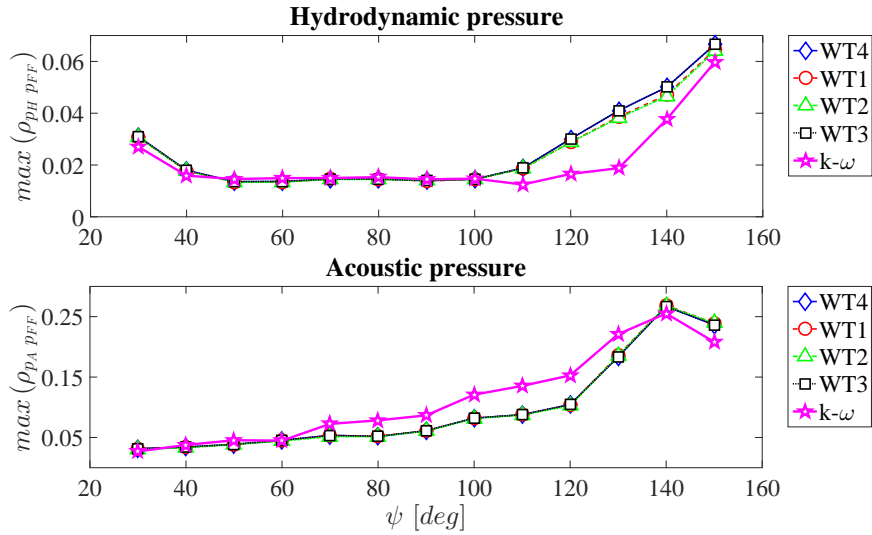


Figure 6.16: Polar evolution of the cross-correlation coefficient peak of far-field pressure with near-field hydrodynamic and acoustic components at axial position  $x/D = 6.1$  at  $M_j = 0.6$ .

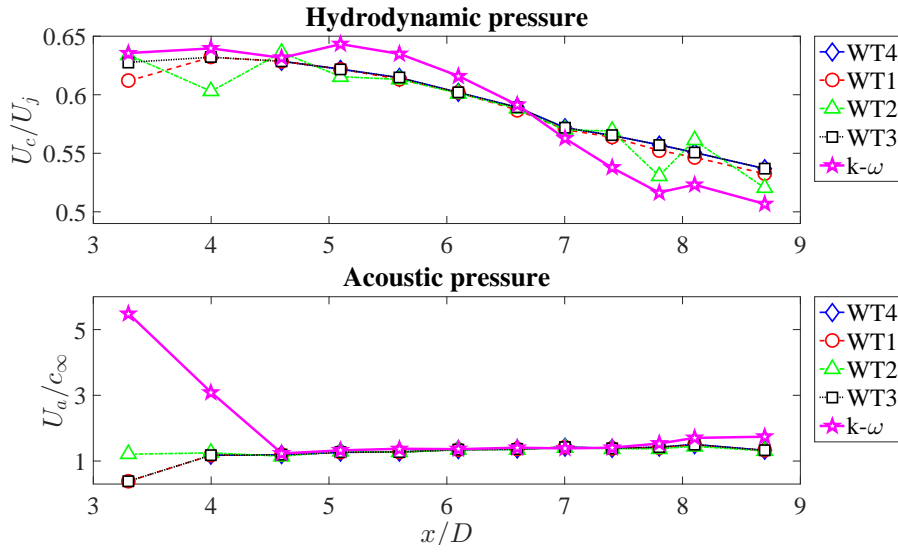


Figure 6.17: Axial evolution of the normalized convection and acoustic propagation velocities for jet Mach number  $M_j = 0.6$ .

to the nozzle exhaust, the velocity values being much larger than the ambient speed of sound. Such discrepancy can be ascribed to the propagation direction of the sound waves parallel to the microphone array axis so that a phase velocity tending to infinite can be found in this region (Tinney and Jordan, 2008). It is interesting to underline that the convection velocity values found with the wavelet approaches for axial positions close to the nozzle exhaust are in good agreement with results by Picard and Delville (2000) and Tinney and Jordan (2008).

## 6.4 Characterization of hydrodynamic and acoustic pressures

It has been shown in §6.3 that all the proposed methods provide similar results. Since the choice of the wavelet technique is not affecting the resulting decomposition of the hydrodynamic and acoustic pressures, the physical features of the pseudo-sound and sound components shown below were derived by the application of the method WT1.

It is interesting to point out that the separation achieved with the method WT1 is not dependent on the position of the far-field microphone. Such a behaviour implies that whatever is the dominant noise component radiated in the far field, i.e. sound emissions from large turbulent structures or fine-scale turbulence, the separation procedure appears to be consistent. Such a result is clearly described in figure 6.18 which reports the hydrodynamic and acoustic pressure spectra showing the weak effect of the position in the far field, the maximum amplitude discrepancy being restricted to 1.5 dB without any modification of the spectral shape.<sup>1</sup>

<sup>1</sup>This result showed that the microphone far-field position does not affect the resulting separation so that the processing technique performs well across all the polar angles. Nevertheless, it has to be pointed out that the difference between the acoustic and hydrodynamic components in terms of correlation level with the far-field pressure shrinks as the polar angle decreases. Hence, a polar position of the far-field microphone in the aft arc, i.e.  $\psi \geq 90^\circ$ , is recommended for the practical applications.

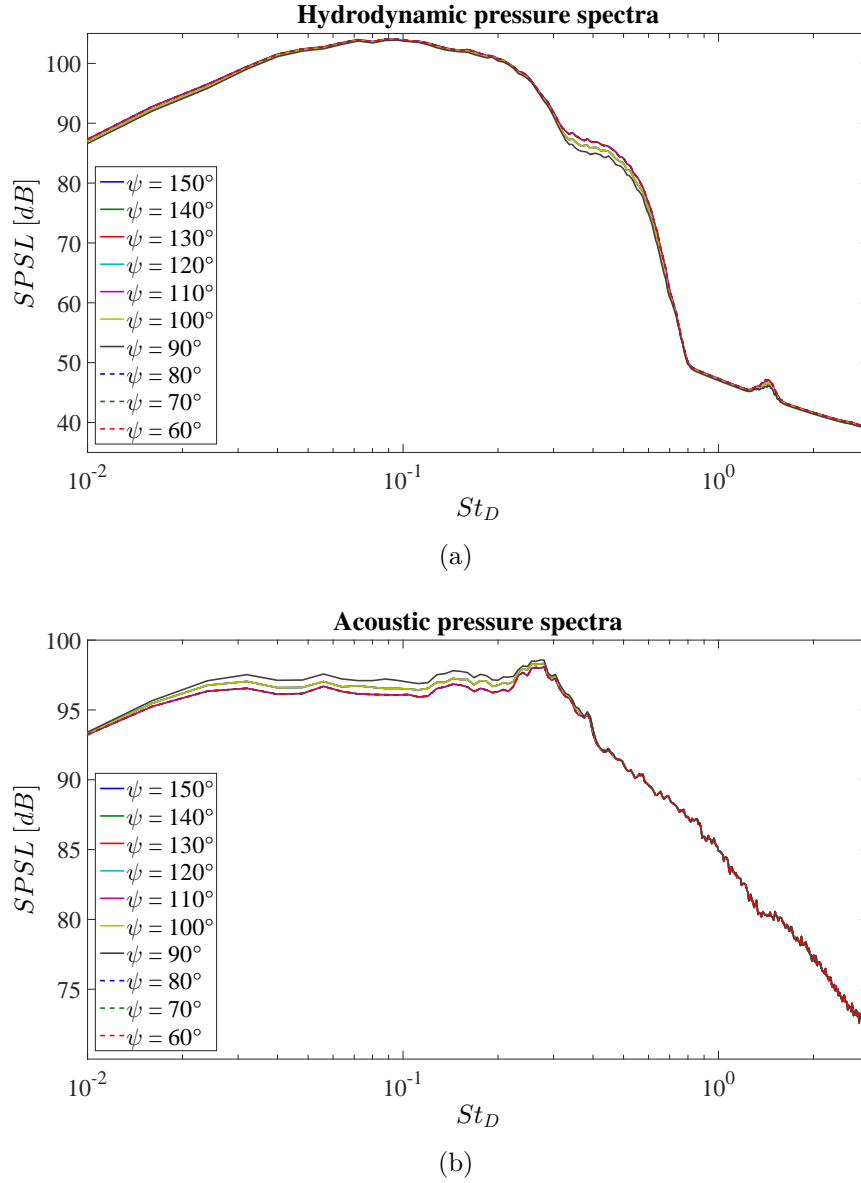


Figure 6.18: Wavelet technique WT1: effect of the far-field polar angle chosen to perform the separation on the hydrodynamic and acoustic pressure spectra at near-field axial location  $x/D = 6.6$  for jet Mach number  $M_j = 0.9$ . (a) Hydrodynamic pressure, (b) acoustic pressure.

### 6.4.1 Spectral characterization

Figure 6.19 shows the *SPSLs* of the original pressure signal and the separated hydrodynamic and acoustic components for both jet Mach numbers for the near-field position  $x/D = 7.8$ . It is observed that the acoustic spectrum has a broadband energy distribution, whereas the spectral energy of the hydrodynamic component is concentrated at low-middle frequencies. For such frequency range the hydrodynamic pressure almost comprises all the energy level, conversely the acoustic pressure is larger at higher frequencies. The switch in the contribution to the global spectrum between  $p_H$  and  $p_A$  occurs close to the frequency where a change of the spectrum energy decay law is detected (see §6.1.2.1). Finally, it is noted that the contribution of the acoustic spectrum to the global spectral energy increases with increasing jet Mach number.

Figure 6.20 shows the axial evolution of the hydrodynamic and acoustic pressure spectra for both jet flow conditions at the microphone locations  $x/D = 3.3, 4.6, 6.1, 7.4, 8.7$ . The energy hump of the hydrodynamic contribution moves to low frequencies as the axial distance from the nozzle exhaust increases, such a behaviour being ascribed to the development of larger turbulent structures in the jet plume. It is interesting to underline that the increase of the Mach number does not considerably affect the amplitude of the pseudo-sound spectra. On the contrary, the amplitude of the acoustic spectra increases significantly for all the axial positions as the Mach number increases. According to Guitton et al. (2007) and Grizzi and Camussi (2012), such a result implies that the acoustic pressure is much more sensitive to the Mach number variation than the hydrodynamic component. It is also interesting to point out that, unlike the hydrodynamic pressure, the energy level of the acoustic component decreases moving downstream in the jet. Such a trend is in agreement with the results found in the literature (Grizzi and Camussi, 2012). A global picture of the stream-wise evolution of the *SPSL* is depicted in figure 6.21, where a contour map of the pressure spectra along the axial distance is shown.

### 6.4.2 Analysis of pseudo-sound and sound components in the time domain

The physics described above is also confirmed by the axial evolution of the *OASPL* of the original, hydrodynamic and acoustic pressures for both jet flow conditions, as shown in figure 6.22. It can be observed that for  $M_j = 0.6$  the hydrodynamic component almost comprises the total noise level, whereas, as the jet Mach number increases, the contribution of the acoustic pressure to the total noise level increases significantly. It is evident that for  $M_j = 0.9$  the energy related to  $p_A$  is larger close to the nozzle exhaust. Moving downstream, the contribution of the acoustic pressure decays very rapidly whereas the hydrodynamic contribution becomes more significant.

A considerable result is shown in figure 6.23, in which the energy level of the hydrodynamic and acoustic pressures is represented against the number of the wavelet coefficients associated with each component. The wavelet coefficients number obtained from the wavelet transform of  $p_H$  and  $p_A$  is normalized by the total number of the coefficients. The variance of the two pressure components normalized by the variance of the original signal has been taken as an estimation of the overall relative energy associated with each contribution. It is observed that the hydrodynamic pressure almost comprises all the energy level with respect to the total energy amount and it is

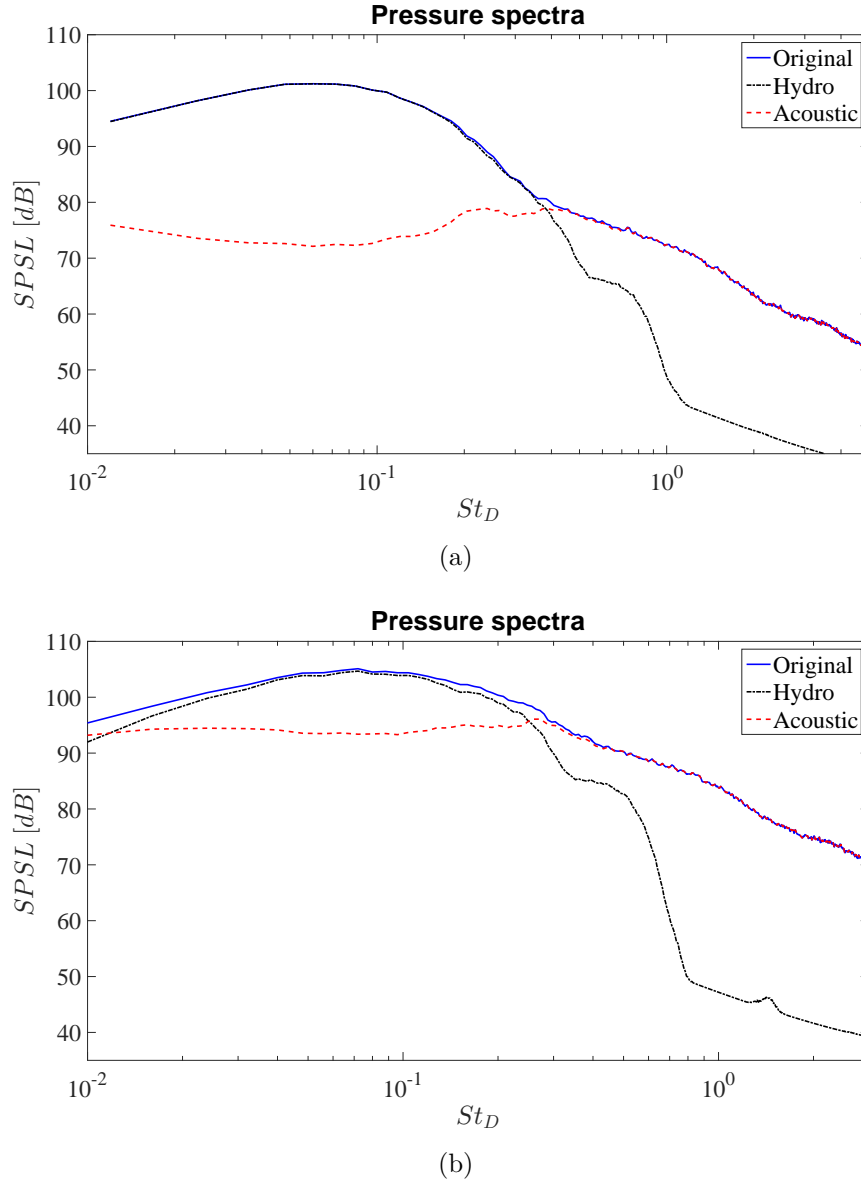


Figure 6.19: Wavelet technique WT1:  $SPSSL$  of the original, hydrodynamic and acoustic pressure signals for a microphone axial position  $x/D = 7.8$  for both jet flow conditions. (a)  $M_j = 0.6$ , (b)  $M_j = 0.9$ .

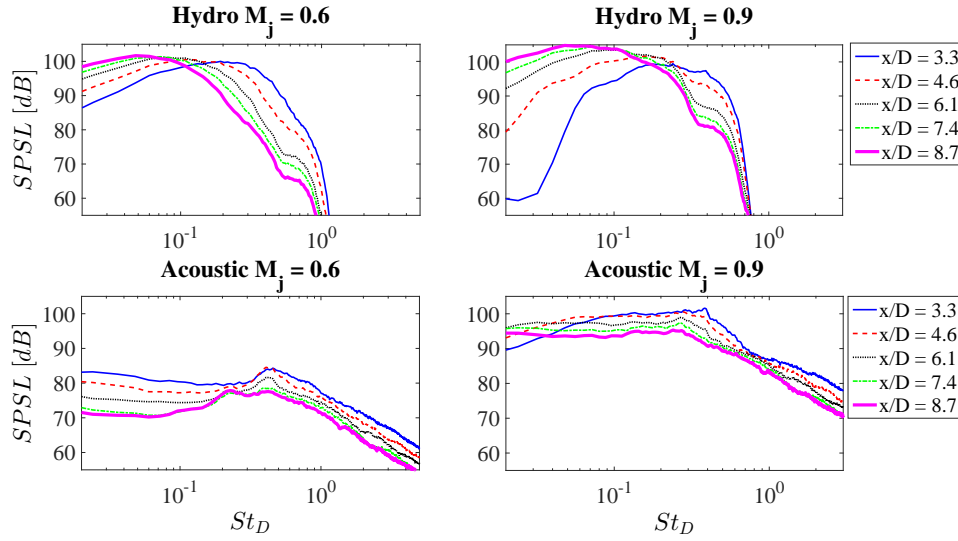


Figure 6.20: Wavelet technique WT1: axial evolution of  $SPsL$ s of separated hydrodynamic and acoustic pressures for both jet flow conditions.

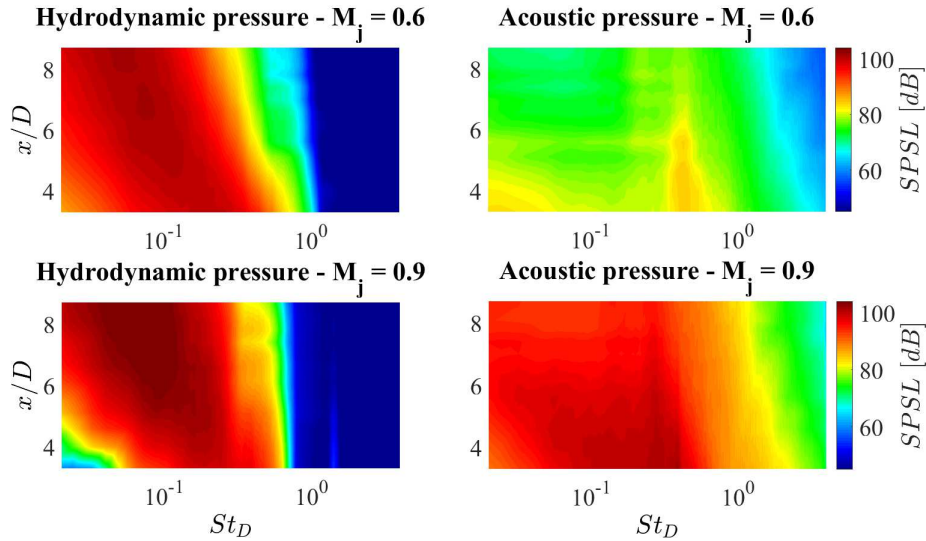


Figure 6.21: Wavelet technique WT1: contour map of the stream-wise evolution of the  $SPsL$  of the separated hydrodynamic and acoustic pressures for both jet Mach numbers.

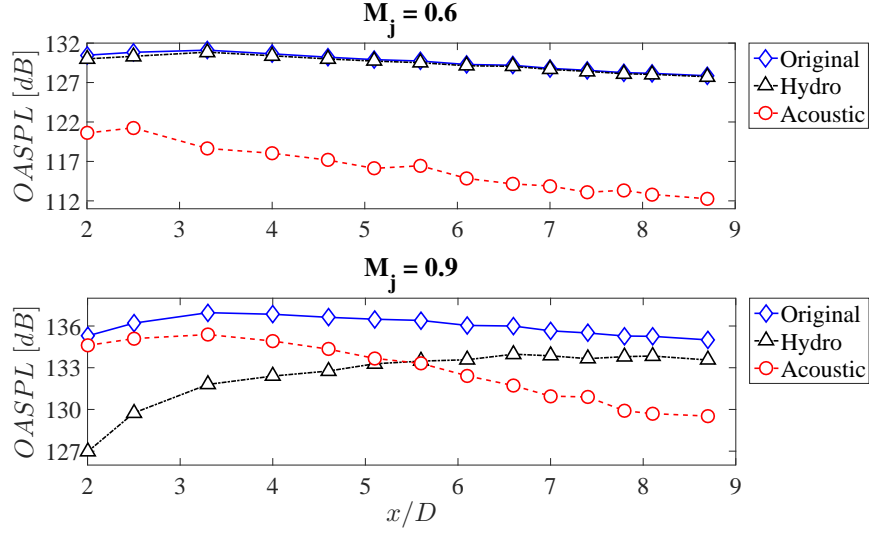


Figure 6.22: Wavelet technique WT1: axial evolution of the  $OASPL$  of near-field original, hydrodynamic and acoustic pressures for both jet flow conditions.

represented by a few but very intense wavelet coefficients. On the contrary, the acoustic pressure is characterised by a lower energy distributed on a much larger amount of wavelet coefficients. It is interesting to underline that the ratio between energy and wavelet coefficients number is a function of the jet Mach number. Specifically, it is observed that the energetic content of  $p_A$  increases with the increasing Mach number, while the energy level related to  $p_H$  falls off. Such a behaviour is in agreement with the experimental results shown so far.

A global description of the near pressure field is provided in figure 6.24, in which the space-time contour map of  $p_{NF}$ ,  $p_H$  and  $p_A$  is shown for both jet Mach numbers. It is evident that the pressure fields obtained with the wavelet separation technique are quite similar to the ones derived from the  $k - \omega$  technique shown in figure 6.12.

#### 6.4.2.1 Cross-correlations

Figure 6.25 shows the cross-correlation coefficient of the near-field pressure signal and the separated hydrodynamic and acoustic components with the measured far-field pressure for  $M_j = 0.6$ . As a reference case, the near-field axial location  $x/D = 7.8$  was selected as well as the polar position  $\psi = 140^\circ$  for the far-field pressure. As expected, a large correlation between  $p_A$  and  $p_{FF}$  is found, whereas the correlation level between  $p_H$  and  $p_{FF}$  is almost negligible. It is important to underline that the amplitude of the correlation peak associated with the extracted acoustic component is considerably larger than the one related to the original near-field pressure signal. Such a behaviour is a proof that the radiating part of the near-field pressure has been properly isolated. This statement is further supported by the location of the acoustic-far-field pressure correlation peak, whose time delay leads to a propagation velocity of  $345 \text{ m/s}$ , very close to the ambient speed of sound.

The different nature of  $p_H$  and  $p_A$  is further highlighted in figure 6.26, which shows the cross-correlation coefficient between two consecutive near-field pressure signals at axial positions  $x/D = 5.6$  and  $x/D = 6.1$  for both jet flow conditions. The hydrodynamic correlation is characterised by a larger time-scale, the typical negative-positive bump

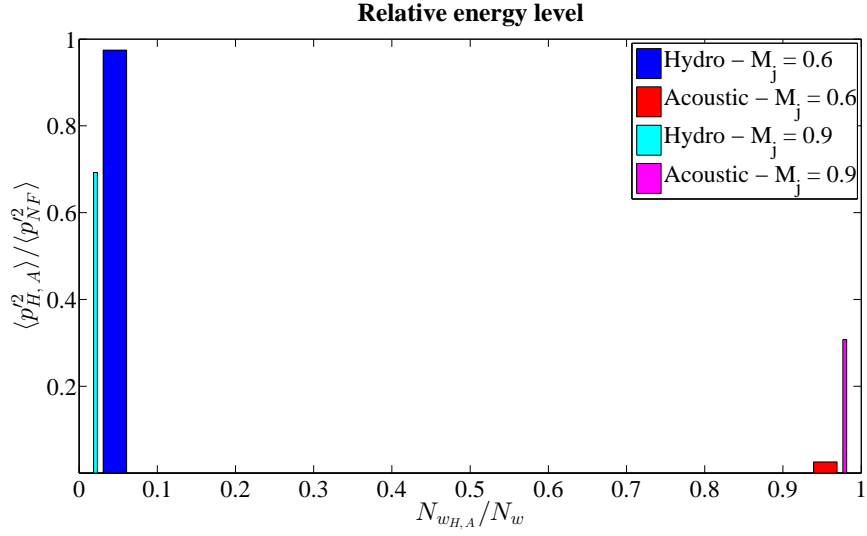


Figure 6.23: Wavelet technique WT1: representation of the relative energy level of the separated hydrodynamic and acoustic pressure components function of the corresponding number of wavelet coefficients normalized by the total amount of wavelet coefficients.

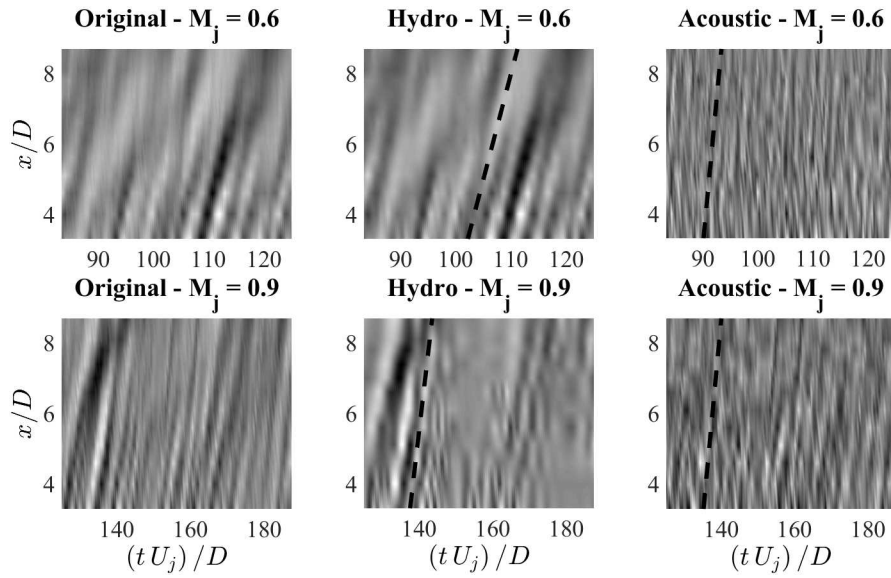


Figure 6.24: Wavelet technique WT1: space-time contour map of the original, the hydrodynamic and the acoustic near pressure fields.



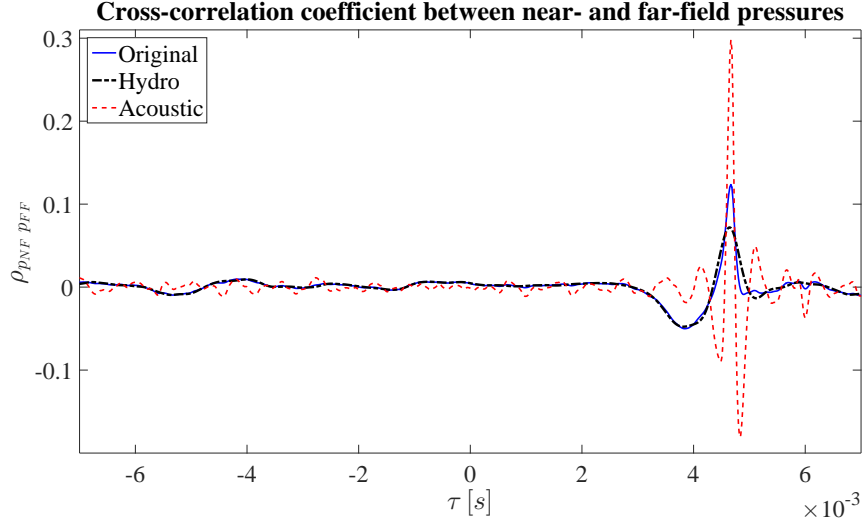


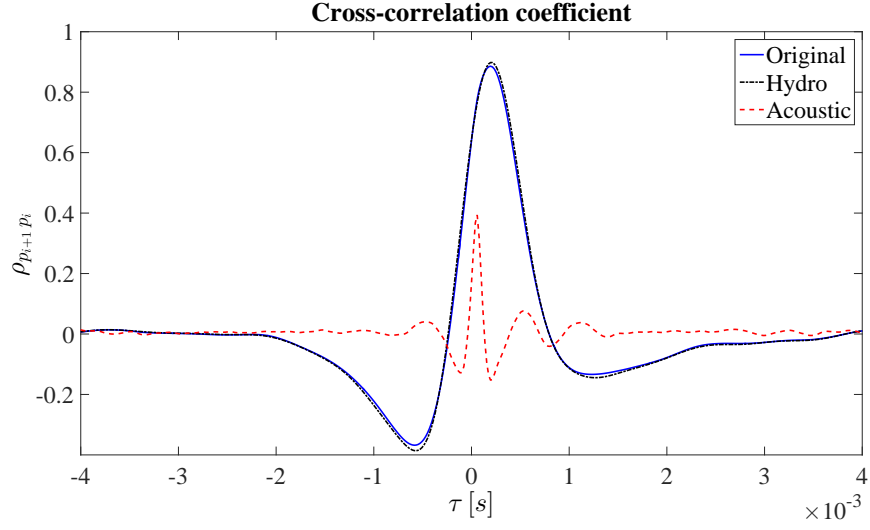
Figure 6.25: Wavelet technique WT1: cross-correlation coefficient of the original, hydrodynamic and acoustic near-field pressures at axial location  $x/D = 7.8$  with the far-field pressure at polar position  $\psi = 140^\circ$  for jet Mach number  $M_j = 0.6$ .

shape being related to the signature of vortices convected by the jet flow. The time-delay of the correlation peak is associated with a propagation velocity equal to  $125 \text{ m/s}$  for  $M_j = 0.6$  and  $186 \text{ m/s}$  for the case of  $M_j = 0.9$ , that is about 60% of the jet velocity, in agreement with Picard and Delville (2000) and Tinney and Jordan (2008). The acoustic counterpart shows a narrower and oscillatory correlation shape, very similar to the wave-packet signature reported by Jordan and Colonius (2013). The peak delay is associated with propagation velocities respectively of  $354 \text{ m/s}$  and  $343 \text{ m/s}$  for the two jet Mach numbers analysed, these values being very close to the ambient speed of sound. It is also observed that the correlation between the pseudo-sound components almost coincides with the one between the original pressure signals. This result is related to the fact that the hydrodynamic pressure dominates in the near field. The correlation level between the acoustic pressures is found to be enhanced as the jet Mach number increases, such a behaviour being in agreement with the results illustrated above. A global picture of the correlation trend along the axial distance is reported in figure 6.27, which shows the contour map of the stream-wise evolution of the cross-correlation coefficient of the original and the separated hydrodynamic and acoustic pressures. The map clearly confirms the outcome discussed above.

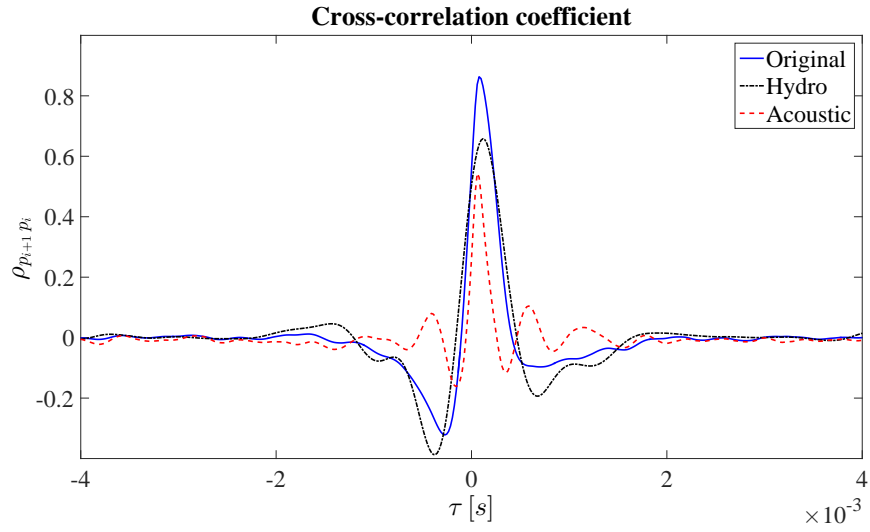
#### 6.4.2.2 Statistical analysis of hydrodynamic and acoustic pressures

A statistical description of the near pressure field is further provided by the analysis of statistical moments and *PDFs*. Figure 6.28 shows the axial evolution of the skewness factor of  $p_{NF}$ ,  $p_H$  and  $p_A$  for both jet Mach numbers. It is observed that the skewness factor of  $p_H$  decreases moving downstream in the jet for both flow velocities as an effect of the turbulence development and almost coincides with that of the original pressure signal. On the contrary, the skewness of the acoustic component remains close to 0, as for the reference Gaussian distribution, for all the axial distances considered.

Figure 6.29 reports the axial evolution of the dimensionless fourth order statistical moment of the original, hydrodynamic and acoustic pressure signals for both flow



(a)



(b)

Figure 6.26: Wavelet technique WT1: Cross-correlation coefficient between two consecutive near-field microphone signals at axial positions  $x/D = 5.6$  and  $x/D = 6.1$  for both jet flow conditions: (a)  $M_j = 0.6$ , (b)  $M_j = 0.9$ .

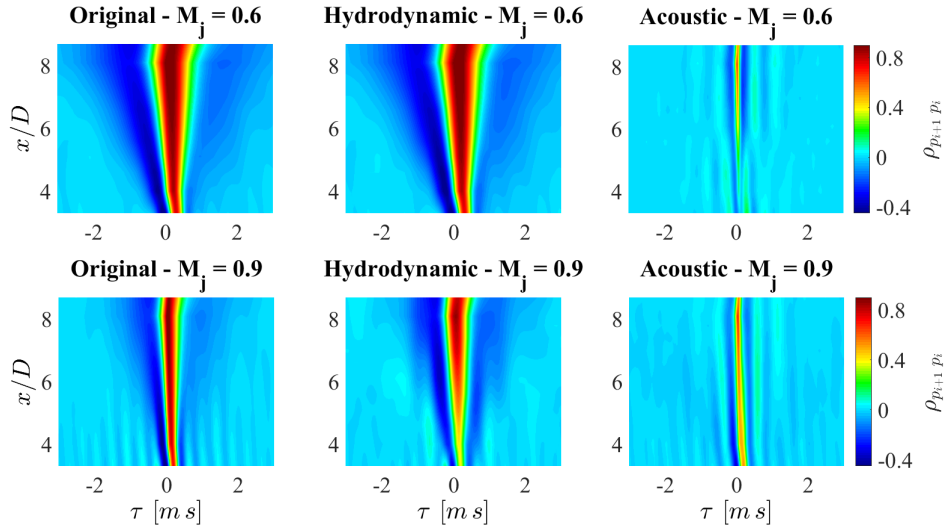


Figure 6.27: Wavelet technique WT1: Cross-correlation coefficient map along the stream-wise direction of original, hydrodynamic, acoustic pressures for both jet Mach numbers.

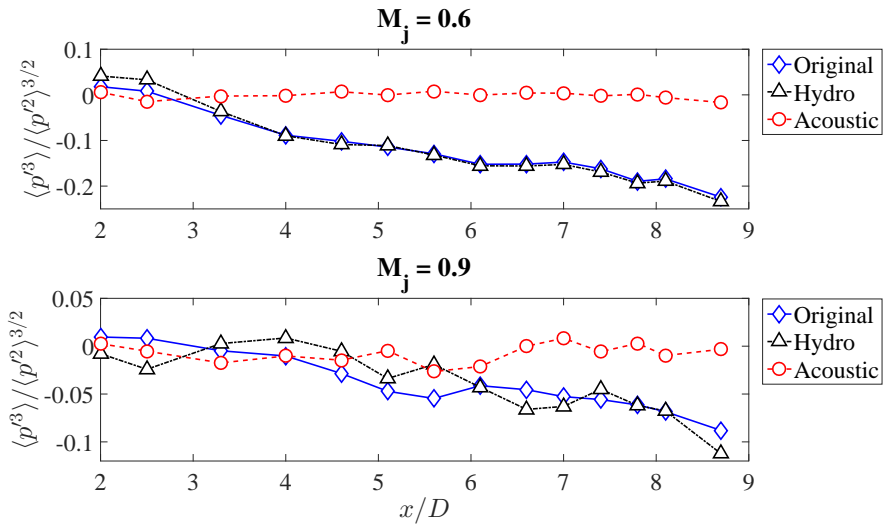


Figure 6.28: Wavelet technique WT1: axial evolution of the skewness factor of original, hydrodynamic and acoustic pressures for both jet conditions.

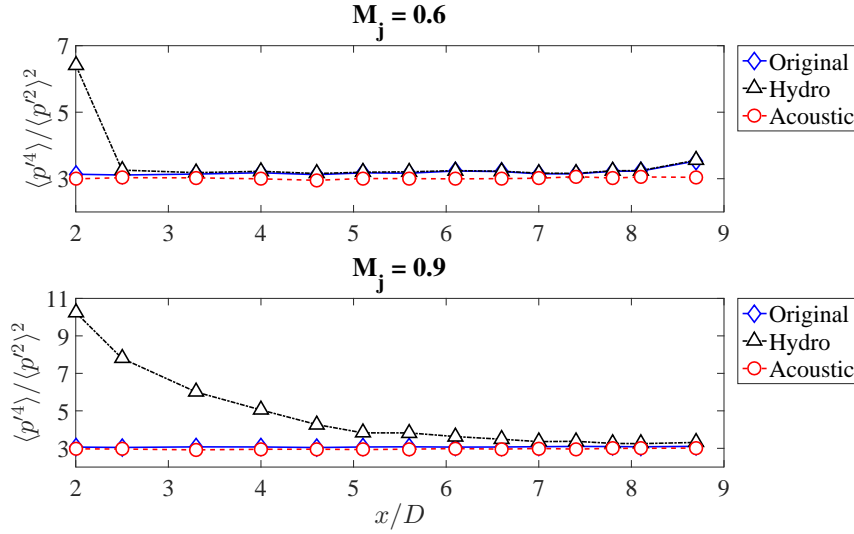


Figure 6.29: Wavelet technique WT1: axial evolution of the flatness factor of original, hydrodynamic and acoustic pressures for both jet conditions.

velocities. It is observed that  $p_H$  is characterised by very high values close to the nozzle exhaust; as the axial distance increases the flatness factor level reduces but remains larger than 3. The trend just described is more evident for the highest jet Mach number. On the contrary the  $p_A$  flatness factor is equal to 3 for all the axial distances and velocities considered. The physics described highlights the different nature of the two pressure components in the near field: the hydrodynamic pressure is characterised by intermittent high-energy events, whereas the acoustic pressure has a nearly Gaussian nature. Such inference is further supported by the trend of the probability density functions.

Figure 6.30 shows the axial evolution of the *PDFs* of the hydrodynamic and acoustic components for both jet Mach numbers at axial positions  $x/D = 3.3, 4.6, 6.1, 7.4, 8.7$ . Experimental *PDFs* are compared with a standard Gaussian distribution. It is observed that, unlike  $p_A$ , the probability distribution of the hydrodynamic pressure deviates from the Gaussian one. For the case  $M_j = 0.6$  the *PDFs* of  $p_H$  exhibits higher negative tails as the axial distance from the nozzle exhaust increases. This behaviour is related to the turbulence development and the generation of intermittent peaks of vorticity associated with large pressure drops (Grizzi and Camussi, 2012; Abry et al., 1994).

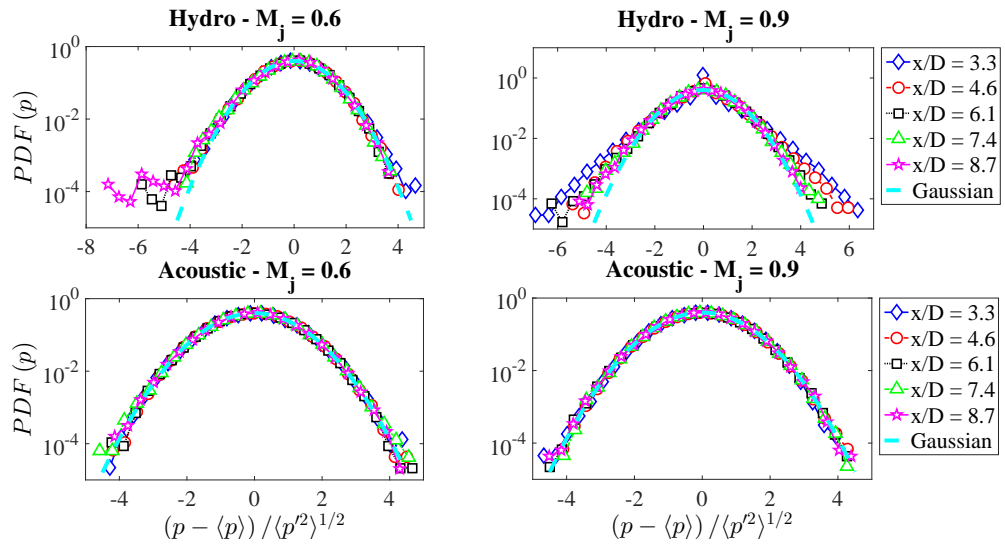


Figure 6.30: Wavelet technique WT1: axial evolution of the probability density functions of the hydrodynamic and acoustic pressures for both jet Mach numbers.



## **Part III**

### **Jet-surface interaction**





# Chapter 7

## Introduction

Despite its importance in the design process of new aircraft configurations, few studies were devoted in the literature to the installation effects of a wing or fuselage panel surface close to a jet on wall pressure and velocity fields. This represents the main motivation of the present work.

Indeed, the physics of jets impinging on surfaces has been extensively investigated in the past, but only for surfaces normal or inclined at large angles with respect to the jet axis (see among many the early papers by Donaldson and Snedeker (1971) and Lamont and Hunt (1980)).

As regards the installation effects, attention has been focused only on the estimation of the far-field noise and its modification under the presence of a solid surface parallel, or slightly inclined, with respect to the jet axis. The pressure far-field for a variety of jet conditions from subsonic to supersonic regimes was deeply investigated by Brown (2013): the different positioning of the surface with respect to the jet plume and the observer in the far field was exploited to study the shielding or the scattering effects produced by the surface. The shielding effect on far-field noise generated by an airframe surface was also studied by Papamoschou and Mayoral (2009) in order to develop a noise reduction methodology for new concept aircraft. Experimental analyses of the effect on the aerodynamic field induced by the presence of a flat-plate close to a jet were carried out by Al-Qutub and Budair (1995). The relationship between the jet aerodynamics, modified by a rigid plate, and the emitted noise has been also studied recently by Smith and Miller (2013) who carried out a Reynolds Averaged Navier-Stokes (RANS) numerical investigation of a jet flow altered by the presence of a plate located at different radial distances from the nozzle axis. The modification of the turbulent mixing of the jet plume due to the surface was used to predict the noise radiated in the far field. The installation effects were also studied by Podboy (2012), who exploited the beamforming technique to provide noise source localization maps addressing the effect of the surface geometry as well as the impact of different nozzle operating conditions. The shielding/scattering effect of a flat-plate installed tangentially to a compressible jet was deeply investigated by Cavalieri et al. (2014), who derived a prediction model for far-field noise in installed configurations based on a wave-packet source deduced from the free-jet case. The effect of the sweep angle of the trailing edge was further addressed in a more recent paper (Piantanida et al., 2015). The issue of the installation effects of a flat-surface on the aerodynamic field was investigated by Brown and Wernet (2014), who performed Particle Image Velocimetry measurements for different lengths of the surface. The experimental database was exploited by the authors to lay the foundations

for far-field noise prediction tools relying on CFD/CAA.

Nevertheless a clear understanding of the driving parameters of the jet-surface interaction was still far to be reached. Piantanida et al. (2015) outlined that for jet-surface radial distances of the order of the nozzle diameter a strong deformation of the aerodynamic field induced by the surface is expected. As pointed out by Di Marco et al. (2013), the knowledge of the wall pressure statistics is the basis to derive reliable prediction models for vibro-acoustic response of the panels and acoustic emissions aiming at the development of noise control devices. Far-field noise can be predicted by Amiet's model giving as input the measured wall pressure spectrum (Amiet, 1975, 1976). Such approach was adopted by Lawrence et al. (2011) to assess that the far-field noise in installed configurations is essentially driven by the scattering dipole source from the trailing edge. The necessity to investigate the incident pressure field on the surface together with the scattered one was clearly addressed by Vera et al. (2015).

In the present approach, the interaction of a high bypass ratio air-breathing engine with a wing or an aircraft fuselage is reproduced on a simplified laboratory-scale model by a jet impinging tangentially on a flat-plate positioned at different distances from the nozzle axis.<sup>1</sup> The experimental investigation consisting of simultaneous velocity and wall pressure measurements offers a basis for physical understanding of the jet-surface interaction phenomena and helps to lay the foundations for modelling strategies of the turbulent jet flow. Velocity measurements were performed by a hot-wire anemometer moved along the direction normal to the flat-plate for different axial positions in order to characterize the surface effect on the velocity field statistics. The flow acceleration field was computed from the point-wise velocity measurements and characterized in both free-jet and installed conditions. A pressure transducer as well as a stream-wise and span-wise microphone array were used to provide the axial and transverse evolution of the wall pressure fluctuations field. Cross-statistical analysis of the velocity/acceleration and wall pressure fluctuations is provided as well in the time and frequency domains. Flow structures induced by the jet-surface interaction and linked to the velocity/acceleration and wall pressure fields are deduced by the application of a conditional averaging procedure based on the wavelet transform of the velocity/acceleration and pressure signals. The effect of the jet-plate distance as well as of the stream-wise location and cross-wise position in the direction orthogonal to the surface is explicitly addressed.

For details on the wall pressure characterization and modelling the reader can refer to Di Marco et al. (2015, 2016), whereas for details on the cross-statistics between velocity/acceleration and wall pressure fluctuations and the wavelet analysis the reader may refer to Mancinelli et al. (2016a, 2017a) and Mancinelli and Camussi (2017).

---

<sup>1</sup>With respect to the real industrial problem of an engine jet interacting with an airframe component, the study carried out surely presents some limitations. Specifically, the compressibility effects on the jet-surface interaction as well as the presence of a background flight velocity are neglected in order to simplify the analysis. The infinite flat-plate also represents a simplified geometry (e.g. trailing edge and high lift devices effects are not taken into account). Nevertheless, due to the novelty of the approach, this experimental investigation offers a basis for physical understanding and theoretical modelling of the jet-surface interaction. Indeed, Di Marco et al. (2013) observed that the wall pressure statistics in supersonic Turbulent Boundary Layers (TBLs) exhibits a behaviour very similar to the one detected in incompressible flow conditions. The spectral and statistical features of wall pressure fluctuations were found to be not significantly affected by Mach and Reynolds numbers variation. Such an outcome suggests that the results obtained in the present test-case could be likely extended to configurations with higher jet velocities. Furthermore, the analysis of the jet-surface interaction in a static case is essential to subsequently quantify the impact of a flight velocity on the installation effects.

# Chapter 8

## Experimental apparatus

### 8.1 Jet facility description

Experiments were performed in the Aerodynamics and Thermo-fluid dynamics Laboratory of the Department of Engineering at University ROMA TRE. An incompressible jet facility reproducing the apparatus at the Trinity College of Dublin described in Chatellier and Fitzpatrick (2005) was used. The layout of the jet facility is shown in figure 8.1. The air is generated by a centrifugal blower which is powered by an asynchronous electric motor of about  $550\text{ W}$  and controlled by a variable frequency inverter drive. The velocity of the jet flow is varied adjusting the inverter frequency. The air is then sent to a wide angle diffuser through a constant section duct, which ends with a honeycomb panel and a turbulence grid (Hon1 and S1 in figure 8.1). The wide angle diffuser of  $1120\text{ mm}$  length and  $21^\circ$  divergence angle is located upstream of the settling chamber. Two fine turbulence screens (S2 and S3 in figure 8.1) are installed in the middle and outlet sections of the divergent duct in order to avoid flow separation. The  $990\text{ mm} \times 990\text{ mm} \times 990\text{ mm}$  settling chamber consists of a straightening section made of a hexagonal honeycomb and two fine screens with the same porosity (Hon2, S4 and S5 in figure 8.1). The ratio of the stream-wise length to single-cell hydraulic diameter of the honeycomb as well as the porosity of the turbulence screens were designed to obtain the desired flow quality in terms of velocity profiles and turbulence intensity. Downstream of the settling chamber the flow evolves in a nozzle which increases the flow speed. The length of the convergent duct is  $210\text{ mm}$ , the nozzle outlet diameter is  $D = 52\text{ mm}$  and the contraction ratio is  $\approx 15$ . The jet issues in a large room in order to avoid disturbances or re-circulations over the jet flow.

The contraction ratio and the power of the motor enable the jet flow to achieve a maximum velocity at the nozzle exhaust ( $U_j$ ) of around  $50\text{ m s}^{-1}$  corresponding to a maximum Mach number,  $M_j$ , of  $\approx 0.15$ . The velocity at the nozzle exhaust can be varied from  $U_j = 3\text{ m s}^{-1}$  up to the maximum velocity, spanning a Reynolds number range between  $Re_D \approx 10^4$  and  $Re_D = 1.7 \cdot 10^5$ , being  $Re_D$  based on  $U_j$  and the nozzle diameter  $D$ .

The measurement campaign was carried out at  $U_j = 42\text{ m s}^{-1}$ , corresponding to  $M_j \approx 0.12$  and  $Re_D \approx 1.5 \cdot 10^5$ , which classifies the jet as a moderate Reynolds number jet (Bogey et al., 2012a), and a Taylor Reynolds number  $Re_T = \langle u'^2 \rangle^{1/2} \lambda_T / \nu \approx 382$ , where  $\lambda_T$  is the Taylor micro-scale and  $\langle u'^2 \rangle^{1/2}$  is the standard deviation of the velocity signal.

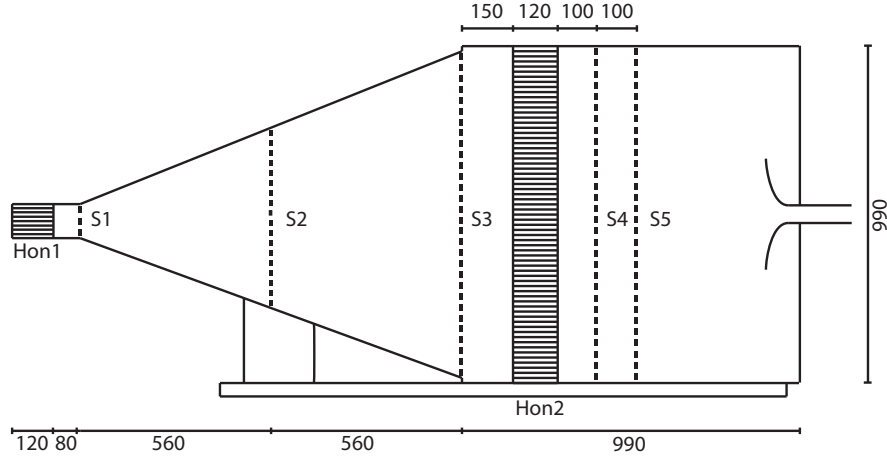


Figure 8.1: Representation of the jet facility. Hon# and S# indicate the honeycomb panels and the mesh screens, respectively.

## 8.2 Experimental set-up

In order to study the installation effects, a rigid flat-plate representing the airframe model was placed parallel to the nozzle axis. A schematic representation of the set-up and the reference frame adopted is provided in figure 8.2. The flat-plate was installed on a rigid traverse structure facilitating the accurate positioning in the direction perpendicular to the plate ( $z$ -axis). Small rotation angles are allowed along the  $x$ - and  $y$ -directions in order to align the surface to the flow direction. The size and material of the flat-plate were chosen to avoid border effects and to obtain an optimal stiffness. The precise radial distance and alignment of the flat-plate with respect to the nozzle axis were carefully checked using a laser levelling instrument.

The experimental tests were carried out with the flat-plate placed at different radial distances  $H$  from the nozzle axis, spanning the range  $1D$  to  $2.5D$  with a step of  $0.5D$

## 8.3 Instrumentation

Velocity measurements were obtained using a single hot-wire probe DANTEC 55P11 of  $1\text{ mm}$  length and  $5\mu\text{m}$  diameter. Due to the finite length of the wire, the fine-scale velocity fluctuations are attenuated. It has been estimated that the probe length is one order of magnitude larger than the Kolmogorov's scale. The hot-wire was carefully mounted with the probe stem parallel to the  $y$ -direction in bi-normal position in order to reduce flow disturbances and provide the accurate measurement of the axial velocity component (parallel to the  $x$ -direction). The movement of the probe in the  $z$ -direction was performed by a precision rail traversing system which allowed to reach a minimum distance between the hot-wire and the surface  $\zeta = 5\text{ mm}$ . The probe was connected to a constant temperature anemometer system AN-1003 Lab-System.

Pressure fluctuations on the flat-plate were measured by Microtech Gefell M360 electret microphones whose full scale value is  $138\text{ dB}$  and whose frequency response is flat up to  $20\text{ kHz}$ . Microphones were cavity mounted according to the scheme reported in figure 8.3. The size of the cavity was designed in order to move the Helmholtz

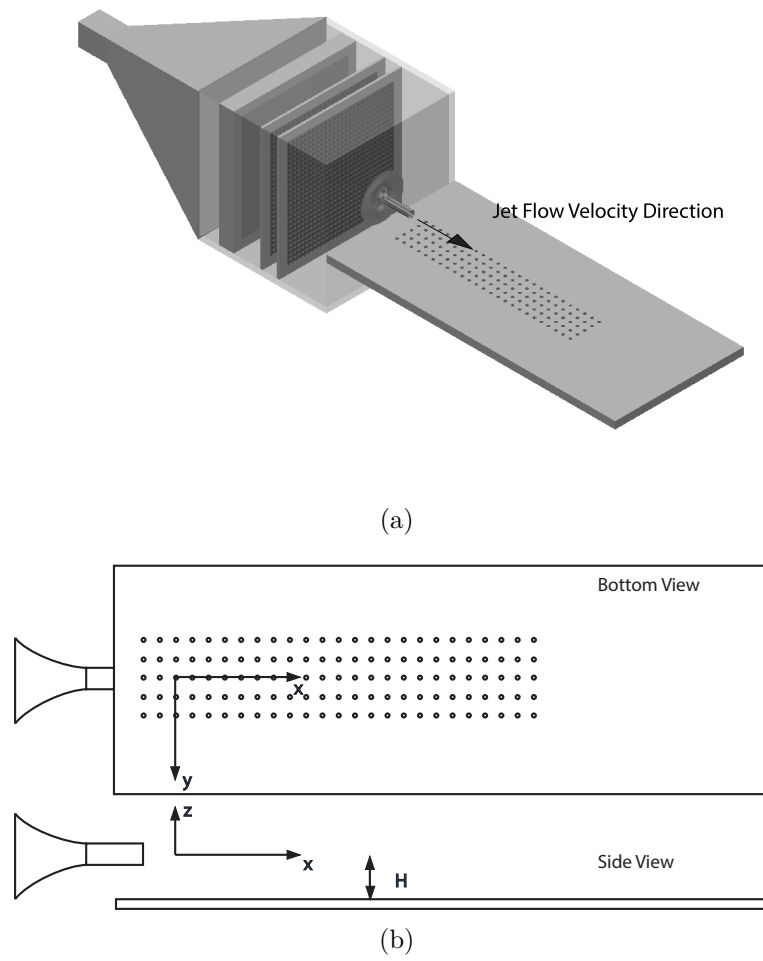


Figure 8.2: Sketch of the experimental set-up for the jet-plate configuration.

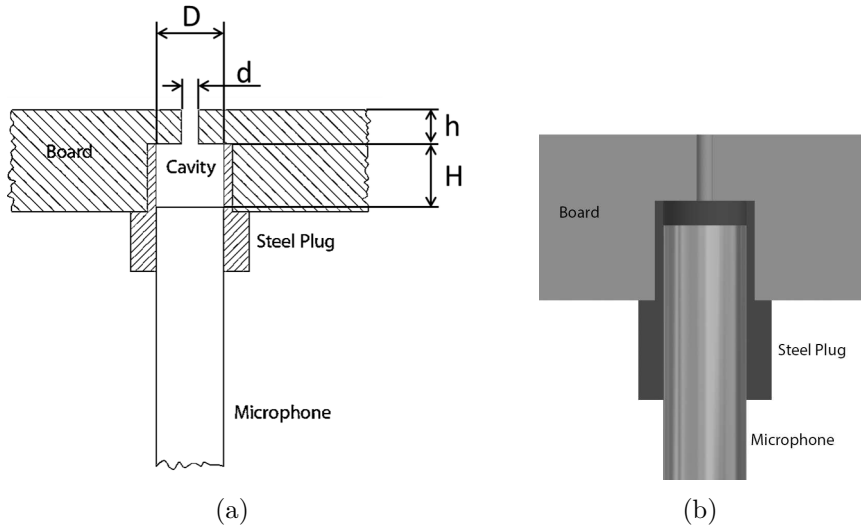


Figure 8.3: Representation of the pin-hole design for the wall pressure measurements on the flat-plate.

resonant peak out of the measured frequency range.<sup>1</sup>

A preliminary test campaign was carried out to assess the uncertainty of all measurements. Acquisition time and sampling frequency rate were chosen to obtain a minimum confidence level of 95% with a maximum uncertainty of 2% for all the statistical moments of interest.

Two experimental test campaigns were carried out to investigate the jet-plate interaction phenomena. The first investigation was mainly devoted to the wall pressure field characterization. An array of three microphones was used to acquire simultaneously pressure signals in the stream-wise and span-wise directions. Pressure signals were acquired by a National Instruments acquisition system (SCXI-1600) with a sampling frequency set to 40  $kHz$  for an acquisition time of 10 s. In order to characterize the overall effect of the jet flow on the wall pressure intensity, mean pressure measurements were performed as well. The above described pin-holes were connected to a pressure transducer (Kavlico P592) through a transmission line properly designed. Mean wall pressures were acquired for 10 s with a sampling frequency of 1  $kHz$ . Velocity measurements were

<sup>1</sup>The characteristic frequency of the Helmholtz resonator is given by the following formula:

$$f_H = \frac{c_\infty}{2\pi} \sqrt{\frac{S}{Vh}} \quad S = \frac{\pi d^2}{4} \quad V = \frac{\pi D^2}{4} H \quad (8.1)$$

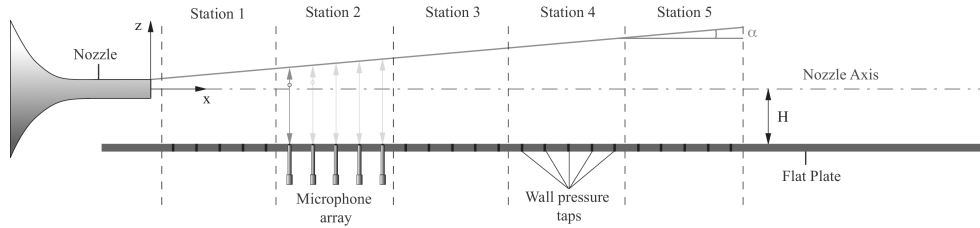
where  $c_\infty$  is the ambient speed of sound,  $S$  is the section of the pin-hole and  $V$  is the volume of the cavity, respectively. The pin-hole was designed in order to move the frequency peak out of the frequency range  $f = [10, 10^4]$   $Hz$ . The formulation above-mentioned provided the dimensions resumed in the following:

- $d = 3 \text{ mm}$
- $D = 1/4''$
- $h = 2 \text{ mm}$
- $H = 3 \text{ mm}$

thus leading to a resonant frequency of 11  $kHz$ .

Plate	Velocity $y/D = 0, \pm 1, \pm 2$	Pressure fluctuations $y/D = 0, \pm 1, \pm 2$	Mean pressure $y/D = 0, \pm 1, \pm 2$
$H/D = 1$	$x/D = 1$	from $x/D = 1$ to $x/D = 25$	from $x/D = 0$ to $x/D = 25$
	$x/D = 5$		
	$x/D = 10$		
	$x/D = 15$		
	$x/D = 20$		
$H/D = 1.5$	$x/D = 1$	from $x/D = 1$ to $x/D = 25$	from $x/D = 0$ to $x/D = 25$
	$x/D = 5$		
	$x/D = 10$		
	$x/D = 15$		
	$x/D = 20$		
$H/D = 2$	$x/D = 1$	from $x/D = 1$ to $x/D = 25$	from $x/D = 0$ to $x/D = 25$
	$x/D = 5$		
	$x/D = 10$		
	$x/D = 15$		
	$x/D = 20$		
$H/D = 2.5$	$x/D = 1$	from $x/D = 1$ to $x/D = 25$	from $x/D = 0$ to $x/D = 25$
	$x/D = 5$		
	$x/D = 10$		
	$x/D = 15$		
	$x/D = 20$		

Table 8.1: Summary of the experiment configurations in the first test campaign.

Figure 8.4: Sketch of the instrumentation set-up.  $\alpha$  is the jet spreading angle.

taken as well both in the free-jet condition and with the flat-plate installed at different radial distances from the nozzle axis in order to preliminarily characterize the effect of the plate on the aerodynamic field. Velocity signals were acquired by a National Instruments acquisition system (PCI-6221). The sampling frequency was set to  $100\text{ kHz}$ , the anti-aliasing low-pass filter frequency cut-off at  $14\text{ kHz}$  and the acquisition time to  $11\text{ s}$ . A summary of the configurations analyzed and the measurements performed is given in table 8.1.

In the second test campaign simultaneous velocity and wall pressure measurements were carried out. The area of interest was divided into 5 measurement "stations", each station being identified by 5 axial positions  $x$ . A 5-microphone array was placed at each station while a hot-wire probe was moved for each axial distance along the  $z$ -direction, i.e. the direction orthogonal to the flat-plate. Data were acquired by a digital scope Yokogawa DL708E for an acquisition time  $T_A = 20\text{ s}$  at a sampling frequency  $f_s = 50\text{ kHz}$ . A representation of the instrumentation set-up as well as of the reference system adopted is shown in figure 8.4. A summary of the experiment configurations is reported in table 8.2.

Flat-plate radial distances			
$H/D = 1$	$H/D = 1.5$	$H/D = 2$	$H/D = 2.5$
Measurement	MICs position	HW stream-wise position	HW cross-wise position
Station 1	$x/D = 1, 2, 3, 4, 5$	$x/D = 1$	from $z \approx -H$ to jet upper limit
		$x/D = 2$	
		$x/D = 3$	
		$x/D = 4$	
		$x/D = 5$	
Measurement	MICs position	HW stream-wise position	HW cross-wise position
Station 2	$x/D = 6, 7, 8, 9, 10$	$x/D = 6$	from $z \approx -H$ to jet upper limit
		$x/D = 7$	
		$x/D = 8$	
		$x/D = 9$	
		$x/D = 10$	
Measurement	MICs position	HW stream-wise position	HW cross-wise position
Station 3	$x/D = 11, 12, 13, 14, 15$	$x/D = 11$	from $z \approx -H$ to jet upper limit
		$x/D = 12$	
		$x/D = 13$	
		$x/D = 14$	
		$x/D = 15$	
Measurement	MICs position	HW stream-wise position	HW cross-wise position
Station 4	$x/D = 16, 17, 18, 19, 20$	$x/D = 16$	from $z \approx -H$ to jet upper limit
		$x/D = 17$	
		$x/D = 18$	
		$x/D = 19$	
		$x/D = 20$	
Measurement	MICs position	HW stream-wise position	HW cross-wise position
Station 5	$x/D = 21, 22, 23, 24, 25$	$x/D = 21$	from $z \approx -H$ to jet upper limit
		$x/D = 22$	
		$x/D = 23$	
		$x/D = 24$	

Table 8.2: Summary of the experiment configurations in the second test campaign.



## Chapter 9

# Wavelet-based conditional sampling procedure

The eduction of the flow structures underlying the jet-surface interaction phenomena was achieved by the application of a wavelet conditioning procedure based on the detection of energetic events. The main concepts of the procedure are discussed in Camussi and Guj (1999) and Camussi et al. (2010).

As reported in 2.2, the Continuous Wavelet Transform (CWT) of a given time function  $f(t)$  is given by the following formula:

$$w(s, t) = C_\psi^{-1/2} s^{-1/2} \int_{-\infty}^{+\infty} f(\tau) \Psi^* \left( \frac{t - \tau}{s} \right) d\tau \quad (9.1)$$

In the present work the CWT was computed using a Mexican Hat kernel by means of the *Matlab*<sup>®</sup> wavelet toolbox, providing a multi-resolution analysis of the flow field from the smallest scale, i.e. twice the sampling time, to the coarsest one, that is of the order of the integral scale. The CWT was applied to time signals in order to select a set of reference times of high-energy events. Indeed, the extraction of the coherent signatures is based on an energetic criterion. As pointed out by Farge (1992), the energy content of a time signal can be evaluated by the computation of the Local Intermittency Measure (*LIM*):

$$LIM(s, t) = \frac{w^2(s, t)}{\langle w^2(s, t) \rangle_t} \quad (9.2)$$

where the symbol  $\langle \rangle_t$  denotes a time average. This function enhances non-uniform distributions of energy in time because the quantity  $w^2(s, t)$  can be interpreted as the energy contained in the signal at the scale  $s$  and the instant  $t$  (see the recent application in Pagliaroli et al. (2015)).

Camussi and Guj (1997) introduced a coherent structures identification procedure based on the idea that the passage of a high-energy flow structure of a characteristic size  $s_i$  at the instant  $t_k$ , should induce a burst in the *LIM* at the corresponding time-scale location. The *LIM* can be thresholded, fixing a proper trigger level  $T_l$ , to select relative maxima which satisfy the condition  $LIM(s_i, t_k) > T_l$ .

Once reference time instants  $t_k^*$  fulfilling the triggering condition are selected, a set of signal segments centred in the time instants  $t_k^*$  is extracted and an ensemble average of the set is performed revealing the time signatures hidden in the original signal. The

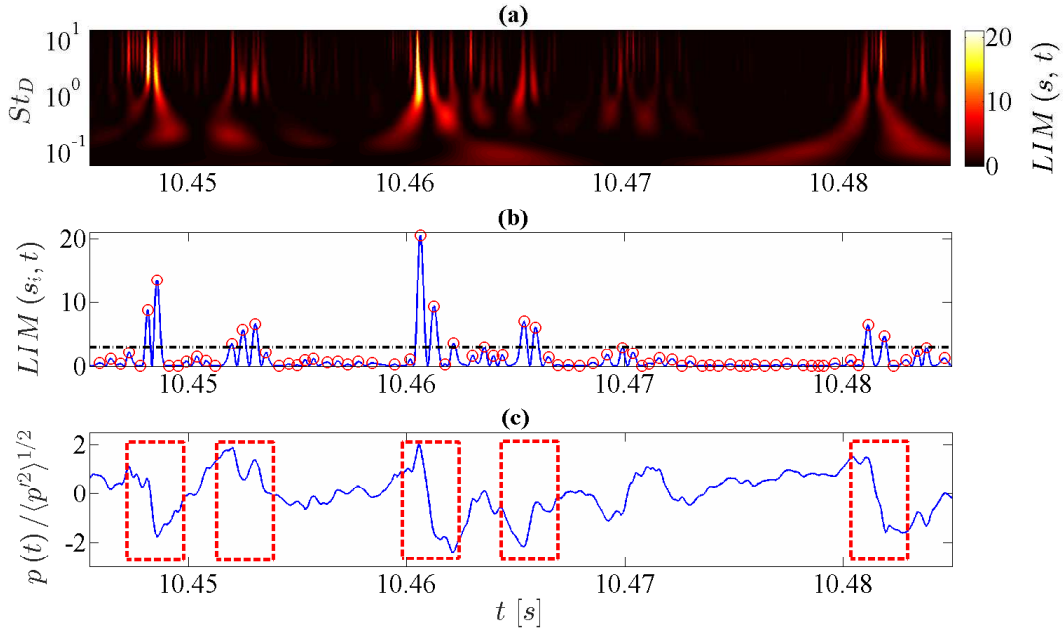


Figure 9.1: Example of the selection procedure of the most energetic events in a time signal based on the  $LIM$  computation. (a) Time-frequency map of the  $LIM$ . (b) 1D plot of the  $LIM$  at a given scale/frequency; the local maxima are highlighted with a circle whereas the trigger threshold level is represented by a dash-dotted line. (c) Portion of the wall pressure signal; the segments corresponding to large values of the  $LIM$  are highlighted with a dashed-line window.

independence of the educed signatures from the selected threshold level  $T_l$  has been verified (see also Camussi et al. (2010)).

The procedure is applied to the time signals of the present experiment and a description of the selection process illustrated above is depicted in figure 9.1. As an example, the wall pressure signal at an axial distance  $x/D = 10$  for a jet-plate distance  $H/D = 1$  has been considered. Figure 9.1a represents the time-frequency map of the  $LIM$ ; the pseudo-frequencies, which are inversely proportional to the scales, are expressed in terms of a Strouhal number based on the nozzle diameter and the jet velocity. For each scale (or frequency), the time instants of the most energetic events are identified by the relative maxima exceeding a threshold level (figure 9.1b). The resulting set of events allows the extraction of centred portions of signal (dashed rectangles in figure 9.1c) from the original time series that are used to perform the ensemble average.

## 9.1 Auto-conditioning procedure

The auto-conditioning procedure is based on the selection of events from a time signal  $x(t)$  and the conditional average of the signal itself. As a result, the educed time signature represents the shape of the flow structure embedded in the chaotic signal. The ensemble average of the signal segments centred in time at the instants  $t_k^*$  corresponding to high-energy events is performed according to the following formula:

$$\langle x(t) | x(t) \rangle = \frac{1}{N_e} \sum_{k=1}^{N_e} x(t_k^* - \Delta t, t_k^* + \Delta t) \quad (9.3)$$

where  $N_e$  is the number of events corresponding to the condition  $LIM(s_i, t_k) > T_l$  and  $\Delta t$  is a proper time window dependent on the estimated persistence of the effect of the detected singularity (see Camussi and Guj (1999)). In the present approach  $\Delta t$  was selected one order of magnitude greater than the integral time-scale of the signal  $x(t)$ . The integral time-scale was evaluated as the first zero of the auto-correlation function.

In the present work the auto-conditioning procedure has been applied to wall pressure and velocity/acceleration signals in free-jet conditions and for all the jet-plate configurations at different axial and transverse positions.

## 9.2 Cross-conditioning procedure

The conditioning method described above can be applied to two signals acquired simultaneously. The ensemble average of signal segments  $y(t)$  conditioned on  $x(t)$  and centred in time at instants  $t_k^*$  is calculated according to the following formula:

$$\langle y(t) | x(t) \rangle = \frac{1}{N_e} \sum_{k=1}^{N_e} y(t_k^* - \Delta t, t_k^* + \Delta t) \quad (9.4)$$

The educed signatures  $\langle y(t) \rangle$  represent the shape of the coherent content of  $y(t)$  responsible for energetic events in the signal  $x(t)$ .

Furthermore, the time-delay associated with the extracted ensemble average can be retrieved providing information on the propagation velocity of the educed structure between the measurement points of the two signals (Guj et al., 2003; Camussi et al., 2010).

In the present approach the triggering signal  $x(t)$  is given by the wall pressure time series, whereas the conditioned signals  $y(t)$  were either wall pressure signals measured by another microphone of the array or a velocity/acceleration signal measured by the hot-wire anemometer.



# Chapter 10

## Results

### 10.1 Free-jet characterization

#### 10.1.1 Velocity field

The jet flow qualification was carried out through hot-wire velocity measurements. An in-situ calibration of the probe was made before every test. The results provided profiles of the axial velocity along the  $z$ -direction for different axial distances, spanning from  $x/D = 1$  to  $x/D = 20$ , thus covering both the jet potential core region and the fully developed turbulent region. Examples of mean velocity profiles obtained at different distances from the jet exit are shown in figure 10.1. The profiles close to the jet orifice are characterized by the well-known top hat shape, whereas in the turbulent region the typical Gaussian-like shapes are achieved. In the fully developed turbulent region a very good collapse of the self-similar profiles is found normalizing the mean velocity amplitude by its value on the jet axis ( $U_m$ ) and the radial distance by the jet half width, denoted as  $b_u$ . The latter is defined as the radial distance from the axis for which the mean velocity amplitude is  $\langle U \rangle = 0.5 U_m$ .

The evolution of the significant statistical quantities along the jet axis is reported in figure 10.2. The mean axial velocity normalized by  $U_j$  and the square of the turbulence intensity relative to  $U_m$  are given in 10.2(a). It is shown that the mean velocity remains about constant up to  $x/D = 6$  and correspondingly to this axial position the turbulence intensity starts to increase. This transition region corresponds to the end of the potential core. As pointed out in Grizzi and Camussi (2012), the potential core length is further determined by the evolution of the skewness and flatness factors, which exhibit their peak values at around  $x/D = 6$  (see figure 10.2(b)).

The linear fit of the centreline mean axial velocity in the fully developed flow region, represented in figure 10.3, provides a decay coefficient  $K_1 \approx 7$ , in quite good agreement with recent literature results (Or et al., 2011). For what concerns the potential core length, an empirical model was derived by Fischer et al. (1979):

$$\frac{U_m}{U_j} = \frac{K_1}{(x - x_0)/D} = \frac{L - x_0}{x - x_0} \quad (10.1)$$

where  $x$  is the axial distance from the nozzle exhaust,  $x_0$  is the virtual origin, which can be expressed as  $x_0 = K_2 D$ , and  $L$  is the potential core length, whose expression can be elaborated as follows:

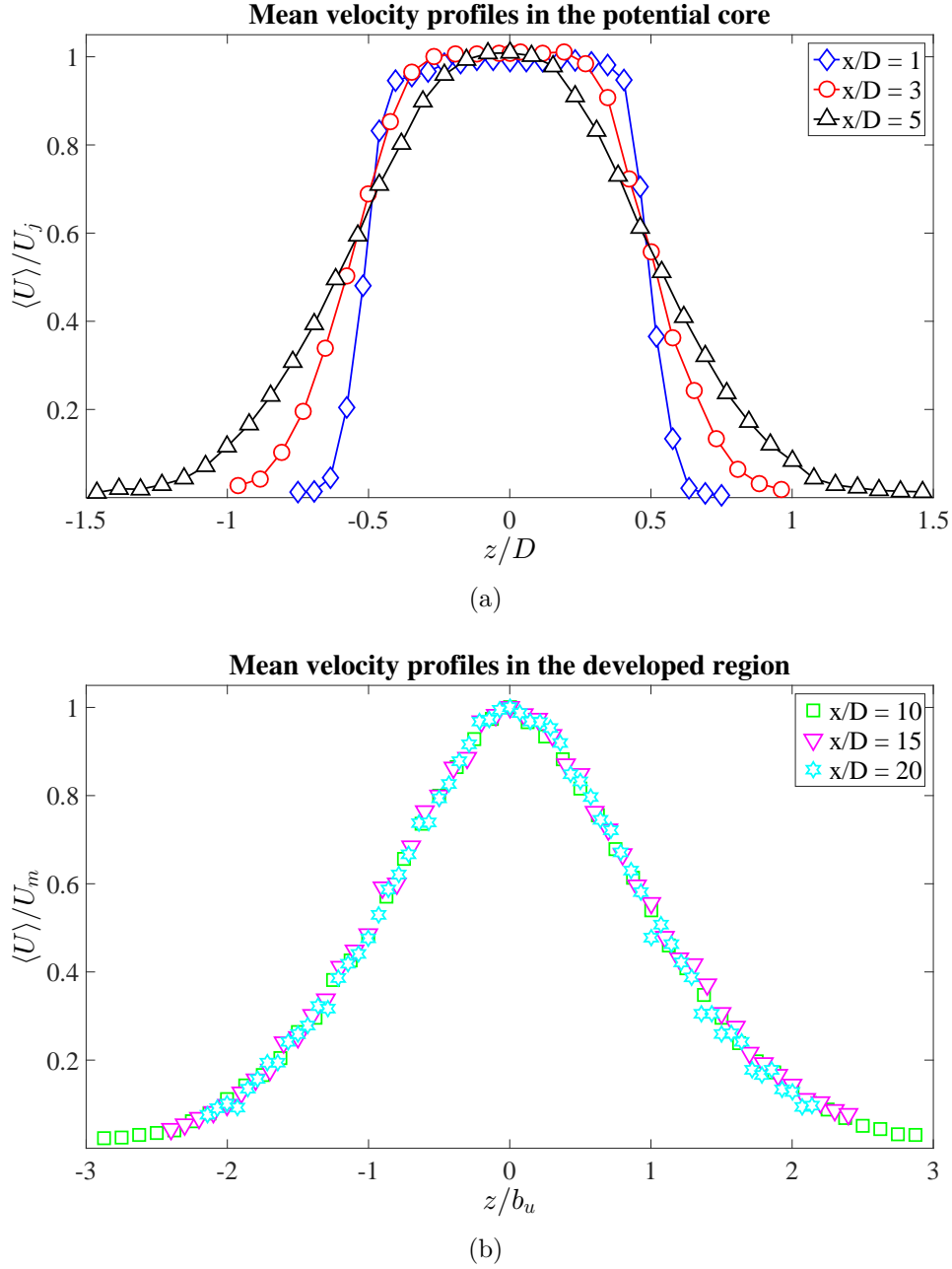


Figure 10.1: Mean velocity profiles along the  $z$ -axis. (a) Velocity profiles in the potential core region normalized by the nozzle exhaust velocity. (b) Velocity profiles in the turbulent jet region normalized by the mean velocity along the jet axis and radial distance normalized by the jet half width.

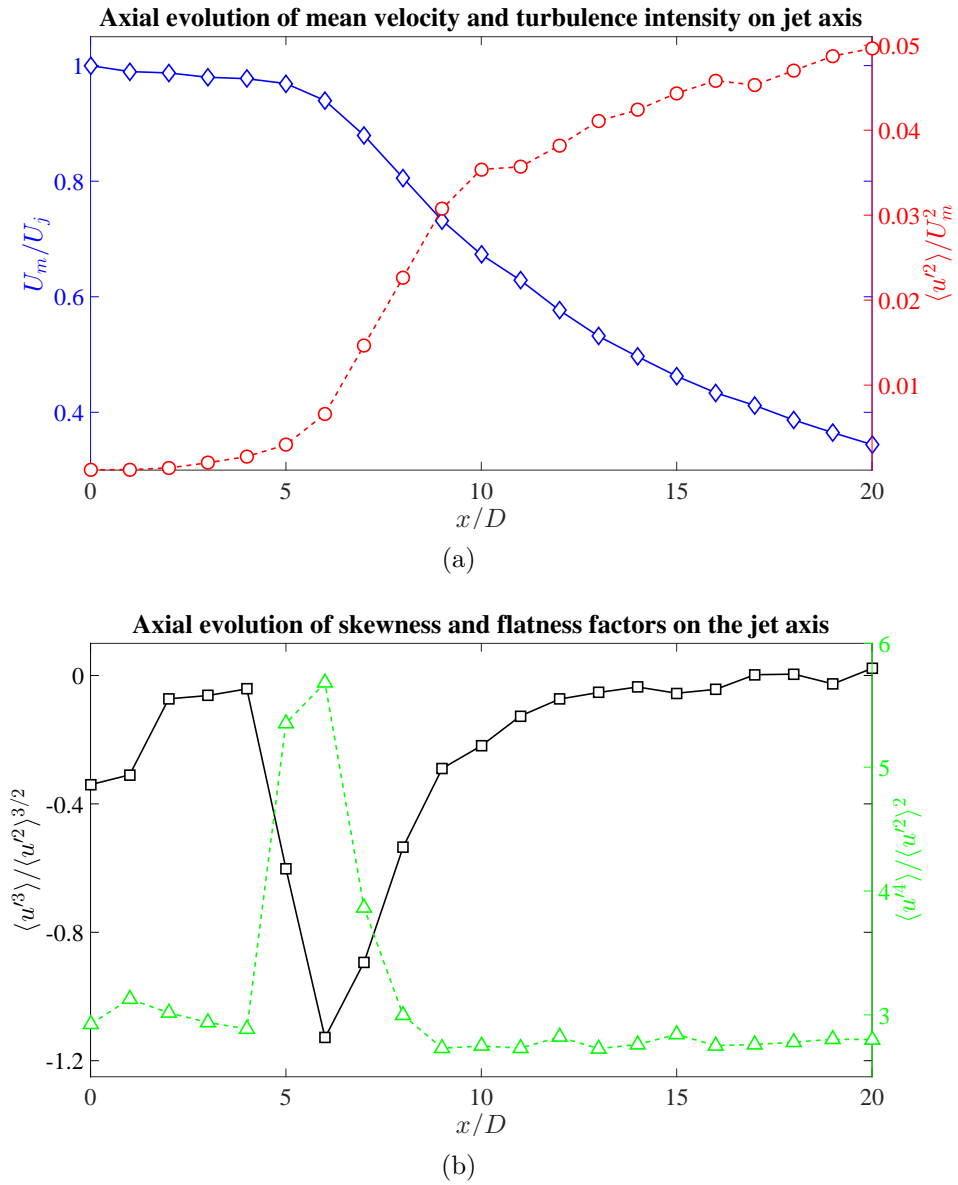


Figure 10.2: Evolution along the jet axis of the velocity statistical moments. (a): mean axial velocity normalized by the jet velocity and velocity variance normalized by the square mean velocity on the jet axis. (b): skewness and flatness factors.

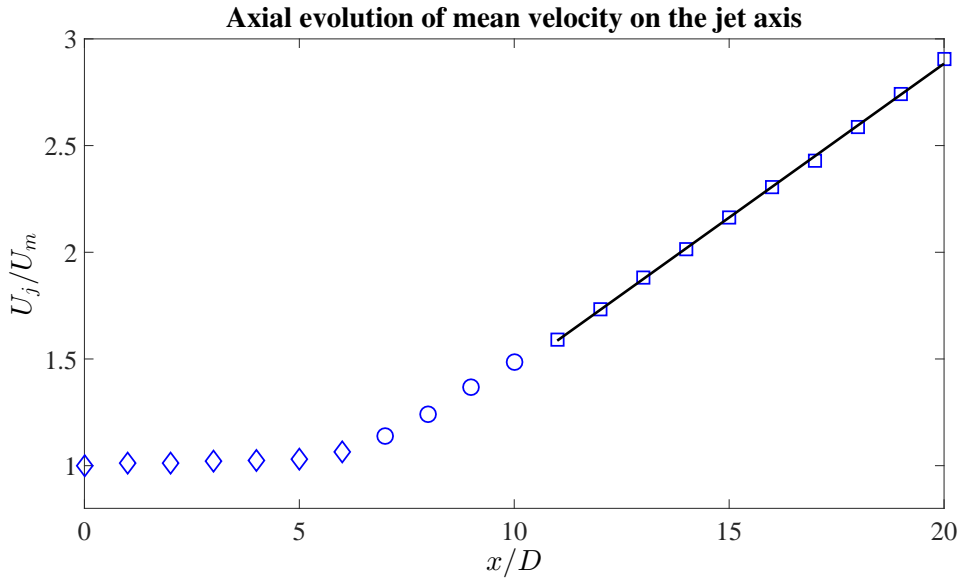


Figure 10.3: Inverse of the ratio between mean axial velocity and jet velocity along axial distance:  $\diamond$  potential core region,  $\circ$  transition region,  $\square$  developed flux region.

$$L = K_1 D + K_2 D \quad (10.2)$$

Antoine et al. (2001) and Uddin and Pollard (2007) found that the constant  $K_2$  can also assume negative values depending on the inlet turbulence intensity. The potential core length estimated by (10.2) provides  $L = 6.6 D$ , in good agreement with the present experimental results.

From the overall aerodynamic characterization the jet spreading angle evaluated by hot-wire anemometer measurements was found to be close to  $8^\circ$ .

The aerodynamics of the free jet is examined in more details by computing the spectra of the fluctuating axial velocity. The evolution of the velocity *PSDs* along the jet axis is reported in figure 10.4 in dimensionless form. The *PSD* amplitudes normalized by the square of  $U_j$  are represented as a function of the Strouhal number  $St_D = fD/U_j$ . It is observed that for axial distances close to the nozzle exhaust (figure 10.4(a)) an energy peak at  $St_D \approx 0.47$  clearly emerges, this peak being the signature of the Kelvin-Helmholtz instability mode (Danaila et al., 1997). Higher harmonics are found in the velocity spectra for axial distances  $x/D \leq 4$ . As the axial distance increases the turbulence level rises and, in the fully developed turbulent region, all the spectra tend to collapse and exhibit the typical Kolmogorov's  $f^{-5/3}$  power-law decay (Kolmogorov, 1941).

A global picture of the spectral content of the velocity signal is depicted in figure 10.5, which shows the dimensionless *PSD* map along the jet axis. For small stream-wise positions the signature of the Kelvin-Helmholtz instability is clearly observed. As the axial distance increases, the spectra become more broadband and the maximum energy content moves to lower frequencies, such a behaviour being related to the development of larger turbulent structures in the jet plume.



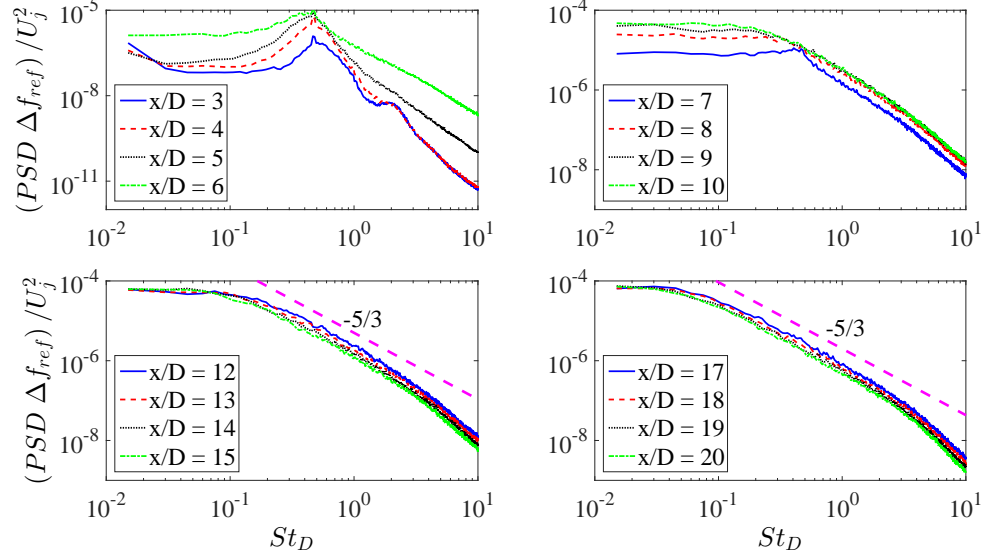


Figure 10.4: Axial evolution of dimensionless velocity power spectral density along the jet axis. Dashed straight line refers to Kolmogorov's decay law.

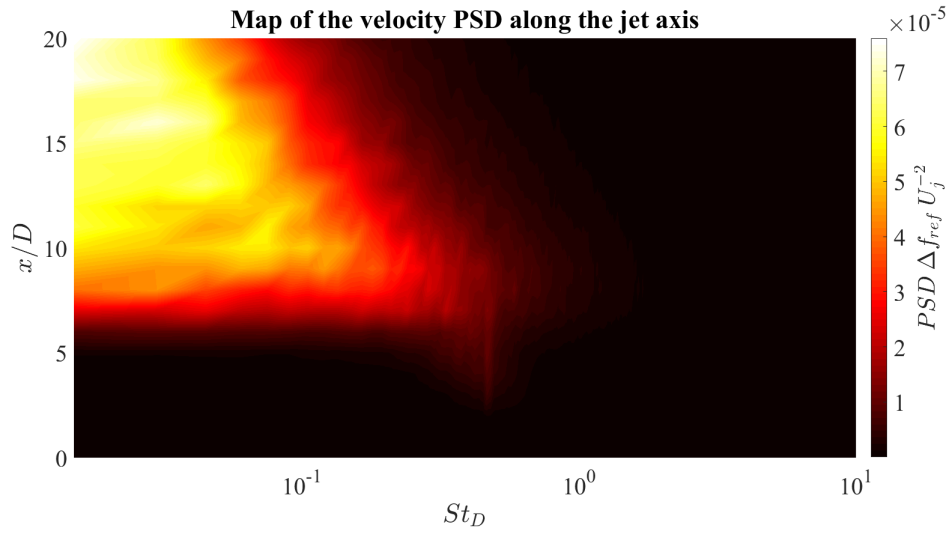


Figure 10.5: Velocity  $PSD$  map along the jet axis in free-jet conditions.

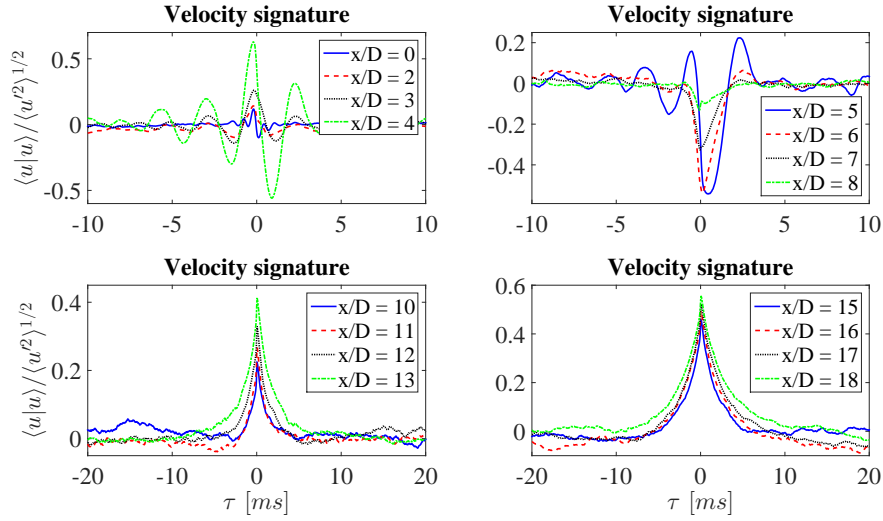


Figure 10.6: Stream-wise evolution of the auto-conditioned velocity signatures along the jet axis.

#### 10.1.1.1 Auto-conditioned velocity signatures

The velocity signatures educed by the application of the auto-conditional sampling procedure described in §9.1 are presented in the following. For the sake of brevity, only the signatures obtained along the jet axis are here considered in order to provide a stream-wise evolution of the coherent flow structures in the jet plume. Figure 10.6 shows the axial trend of the velocity ensemble averages. The signatures are represented in dimensionless form dividing by the local velocity standard deviation at each axial location. Oscillating shapes were detected for axial positions included in the potential core, the oscillations being enhanced as the potential core end approached, such a behaviour being ascribed to the Kelvin-Helmholtz instability that brings about the roll-up of the shear layer. For  $x/D$  immediately downstream the potential core end, the oscillating shape turned into a negative spike associated with a velocity reduction with respect to the mean value, this signature being related to the vortex pairing and braid formation phenomena (Camussi and Guj, 1999). For stream-wise positions further downstream in the jet plume a positive-spike shape clearly appeared, such signature being ascribed to a coherent ring-like vortex structure convected by the mean flow (Camussi and Guj, 1997). Globally, the time-scale of the ensemble averages enlarged as the axial distance increased, such feature being related to the development of larger turbulent structures further downstream in the jet plume.

#### 10.1.2 Acceleration field

The acceleration field in the jet plume was derived from the point-wise velocity measurements performed by the hot-wire anemometer. To the best of the author's knowledge, this represents the first attempt to investigate experimentally the acceleration of a turbulent jet. The main motivation of the present study lies in the Navier-Stokes' equation. Specifically, for the case of zero mass forces with negligible heat transfer and production and for  $Re \rightarrow \infty$  (as it is in real aircraft applications), the equation of the momentum conservation reduces to the Euler's equation, as following reported:

$$\rho \frac{D\mathbf{u}}{Dt} = -\nabla p \quad (10.3)$$

The Euler's equation establishes a relation between the material derivative of the velocity, i.e the acceleration, and the pressure gradient, i.e. a quantity that is strictly related to the noise emissions in a turbulent jet. Hence, the statistical and spectral analysis of the acceleration field could be relevant in order to have a deeper insight on the jet noise production mechanism providing further information with respect to the investigation of the velocity field.

### 10.1.2.1 Acceleration computation

The computation of the acceleration starting from velocity measurements has been performed according to the argumentation reported in the following. The single hot-wire probe adopted for the experimental tests provides the measurement of the axial component  $u$  of the velocity, the velocity vector being described by the components  $\mathbf{u} = (u, v, w)$  in a Cartesian reference system. Hence, only the material derivative of the axial velocity has been computed to calculate the acceleration, such approximation being considered acceptable taking into account the jet has a 'preferred' development direction so that the transverse velocity components are generally negligible with respect to the axial one.

The derivative of the axial velocity can be written in explicit form as follows:

$$\frac{Du}{Dt} = \frac{\partial u}{\partial t} + u \frac{\partial u}{\partial x} \quad (10.4)$$

The convective term was simplified exploiting the Taylor's hypothesis of frozen turbulence (Taylor, 1938), i.e.  $x = Ut$ , where  $U$  is the mean component of the axial velocity  $u^1$ . Thus, the acceleration  $a$  can be expressed by the following formula:

$$a = \frac{Du}{Dt} = \frac{\partial u}{\partial t} + \frac{u}{U} \frac{\partial u}{\partial t} = \frac{\partial u}{\partial t} \left(1 + \frac{u}{U}\right) \quad (10.5)$$

The Taylor's hypothesis allowed to express the spatial derivatives in equation (10.5) in terms of time derivatives<sup>2</sup>. The local time derivative was computed by means of a finite difference method with a forward scheme. The  $k^{th}$  element of the velocity derivative is finally computed as follows:

$$\left. \frac{\partial u}{\partial t} \right|_k = \frac{u_{k+1} - u_k}{T_s} \quad (10.6)$$

where  $T_s$  is the sampling time.

---

<sup>1</sup>As underlined by Lin (1953), the Taylor's hypothesis is applicable for low turbulence intensity (about 25%) and high Taylor Reynolds number ( $> 200$  according to Heskestad (1965)). The jet analysed in the present experiment satisfies the above conditions.

<sup>2</sup>Experiments with a double-component parallel hot-wire have been planned to directly measure the velocity spatial derivative in order to validate the results in the present approach. To this extent, PIV measurements could be performed as well. Indeed, a validation of the model here presented could be achieved exploiting LES data. The convective term of the material derivative could be evaluated with the Taylor's hypothesis approach or directly computing the spatial derivative. Then, the accelerations obtained should be compared, the degree of similarity between the two values being an estimator of the efficiency of the proposed approach and a definitive validation.

### 10.1.2.2 Statistics of the acceleration field

The statistical characterization of the acceleration field is presented in the following. Figure 10.7 shows the dimensionless profiles of mean and fluctuating acceleration components along the  $z$ -direction for different axial distances. The characteristic acceleration adopted to normalize both the acceleration values was estimated as the ratio between the square jet velocity  $U_j^2$  and the nozzle diameter  $D$ . The mean profiles exhibit zero acceleration in the central part of the jet and a deceleration for transverse positions in the proximity of the mixing layer of the jet for axial positions inside the potential core, as shown in figure 10.7(a). It has to be pointed out that the zero acceleration is found for  $z$ -positions for which the velocity profiles exhibited a constant velocity value in the top-hat shape, whereas the deceleration in the mixing layers due to the interaction with the ambient flow at rest becomes less significant as the axial distance increases. For stream-wise locations downstream the potential core, the mean acceleration profiles show a negative bell-like shape, the deceleration values being less significant as the axial distance increases. For what concerns the fluctuating component of the acceleration (see figure 10.7(b)), the fluctuation intensity is small in the central part of the jet and larger in the proximity of the mixing layers. For axial positions downstream the potential core, a simil-Gaussian profile shape appears.

The evolution along the jet axis of the main statistical moments is reported in figure 10.8. The mean acceleration is zero for  $x/D \leq 4$ , it decreases for axial positions downstream the potential core up to  $x/D = 9$ , where the maximum deceleration is observed, then it increases again recovering almost the initial amplitude. The acceleration standard deviation shows exactly the opposite trend with respect to the mean component (see figure 10.8(a)). The evolution of the skewness and flatness factors along the jet axis is reported in figure 10.8(b). It is observed that the skewness factor shows negative values for small stream-wise locations and positive ones for large axial distances, whereas the kurtosis exhibits values larger than 3 for all the axial positions considered. Both the third and fourth order statistical moments exhibit a singularity for the axial position  $x/D = 4$ .

### 10.1.2.3 Spectral characterization

Figure 10.9 shows the evolution along the jet axis of the dimensionless acceleration spectra. The *PSDs* have been normalized multiplying by a reference frequency  $\Delta f_{ref} = 1 \text{ Hz}$  and dividing by the square of the ratio  $U_j^2/D$ . The spectra for all the axial positions show a steep ascent at low frequencies with a more significant spectral energy content in the high frequency range. Such a behaviour is related to the derivative operation in the time domain that implies in the Fourier domain the multiplication of the velocity signal by the quantity  $i\omega$ . The effect of this operation is the enhancement of the energy content at high frequencies. More specifically, for axial positions included in the potential core region, the spectra clearly exhibit the energy peak related to the Kelvin-Helmholtz instability. As the axial distance increases, the energy content shows a more broadband distribution at middle-high frequencies. A global picture of the spectra evolution along the jet axis is depicted in figure 10.10, which shows the contour map of the *PSDs* along the stream-wise direction. It is observed that the energy content is mainly concentrated at high frequencies. For axial positions inside the potential core, the energy peak related to the Kelvin-Helmholtz instability mode clearly emerges.

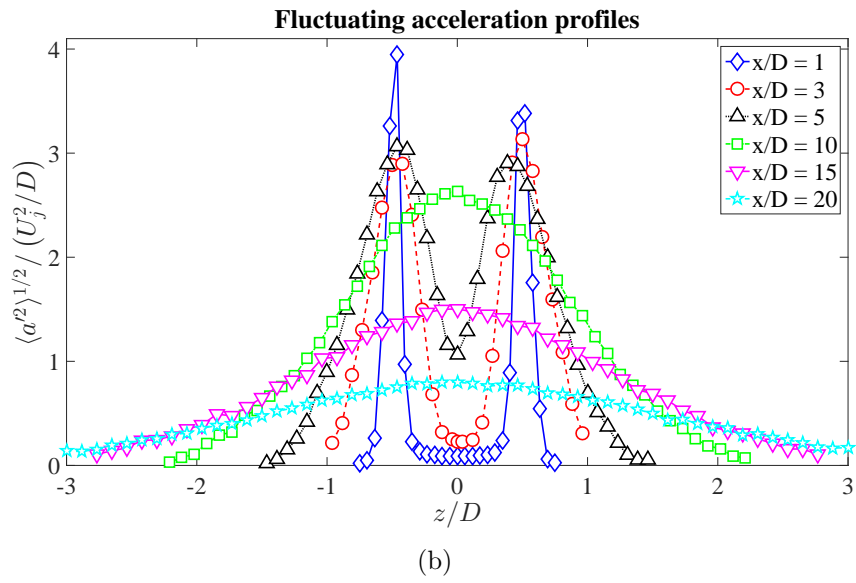
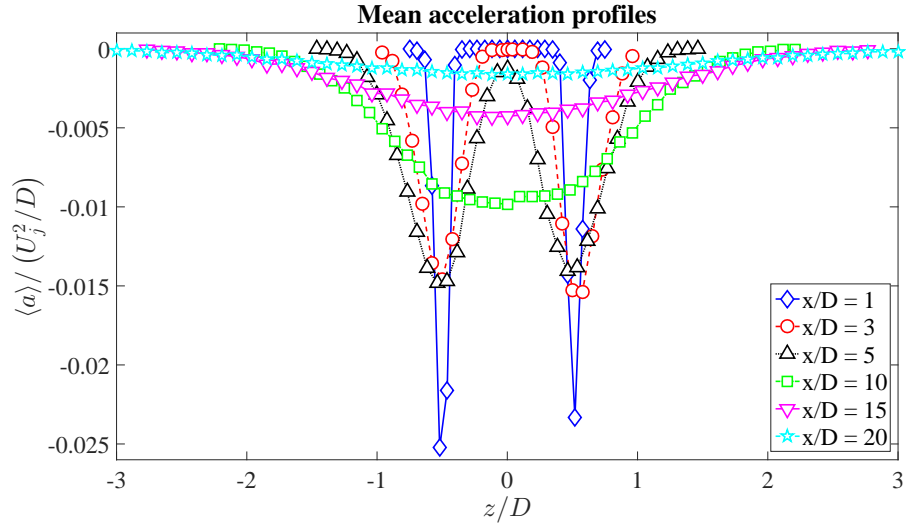


Figure 10.7: Dimensionless mean and fluctuating acceleration profiles along the  $z$ -direction for different axial distances. (a) mean component, (b) standard deviation.

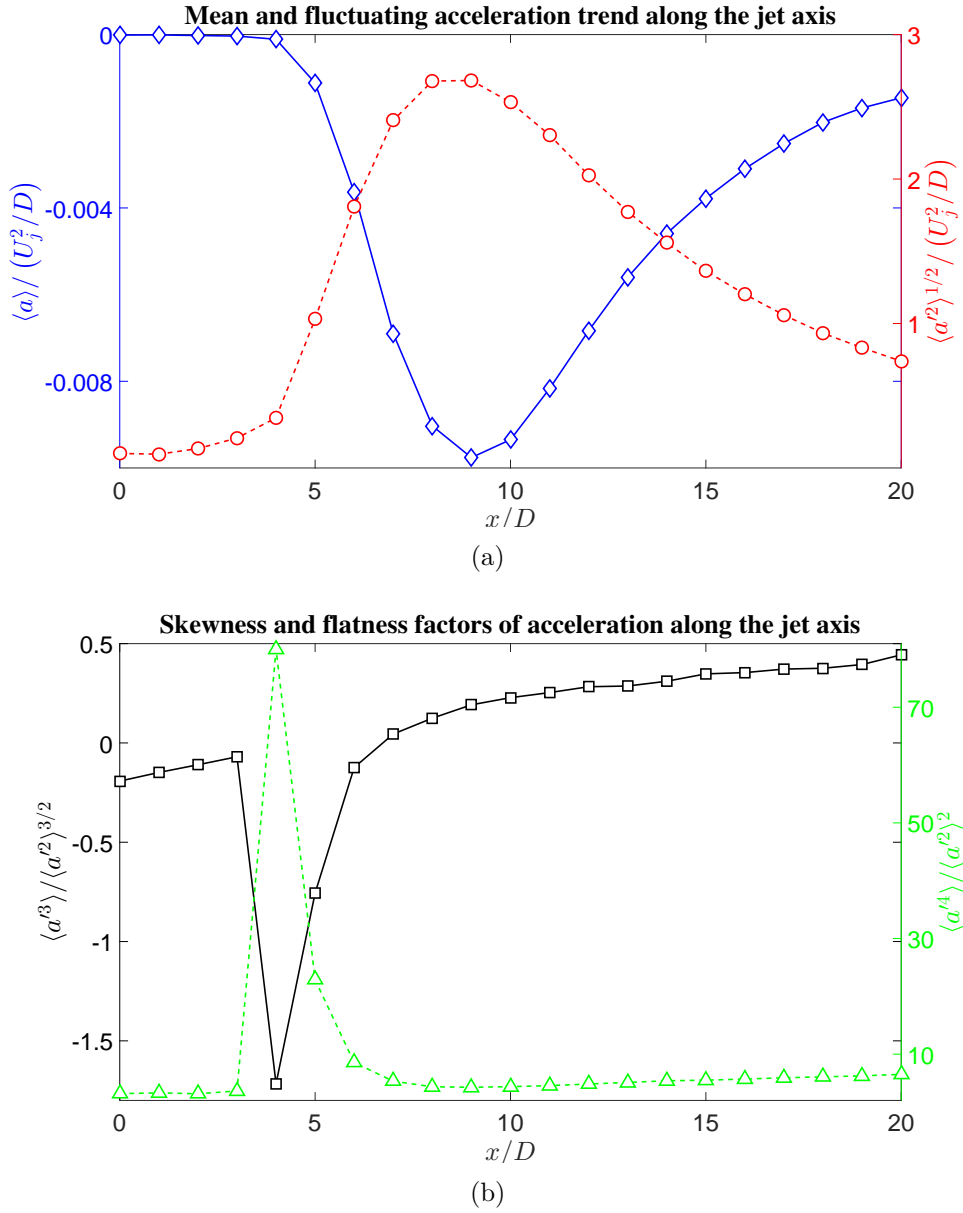


Figure 10.8: Evolution along the jet axis of the main statistical moments of acceleration. (a) mean and standard deviation, (b) skewness and flatness factors.

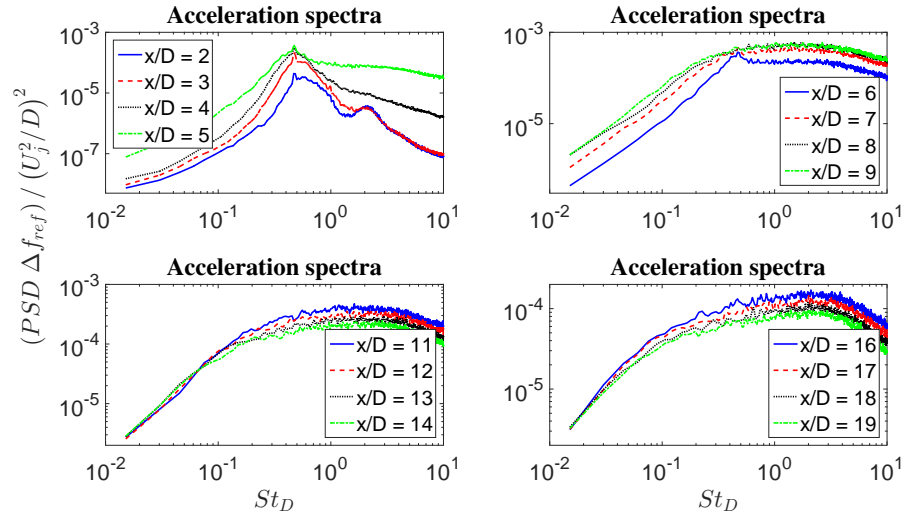


Figure 10.9: Stream-wise evolution of the dimensionless  $PSDs$  of acceleration signal along the jet axis.

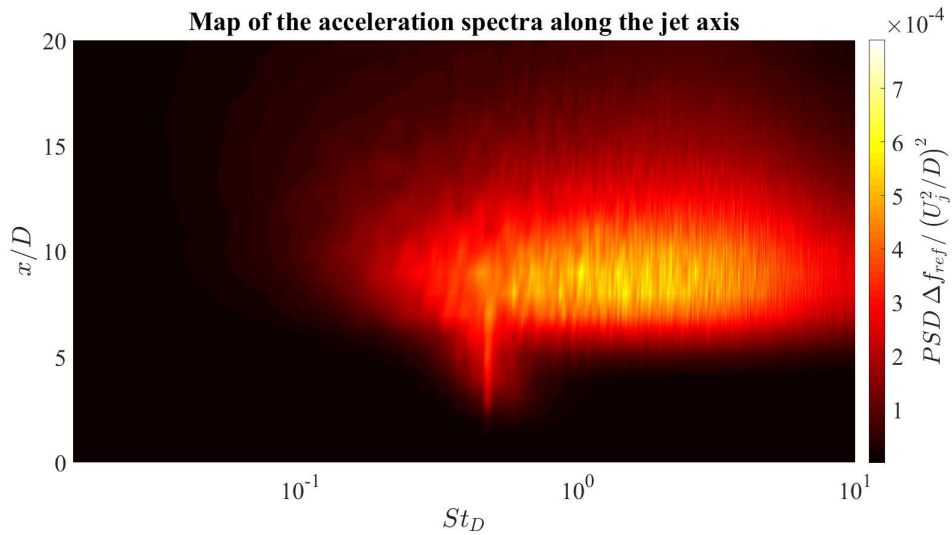


Figure 10.10: Contour map of the dimensionless  $PSD$  of the acceleration signals along the jet axis.

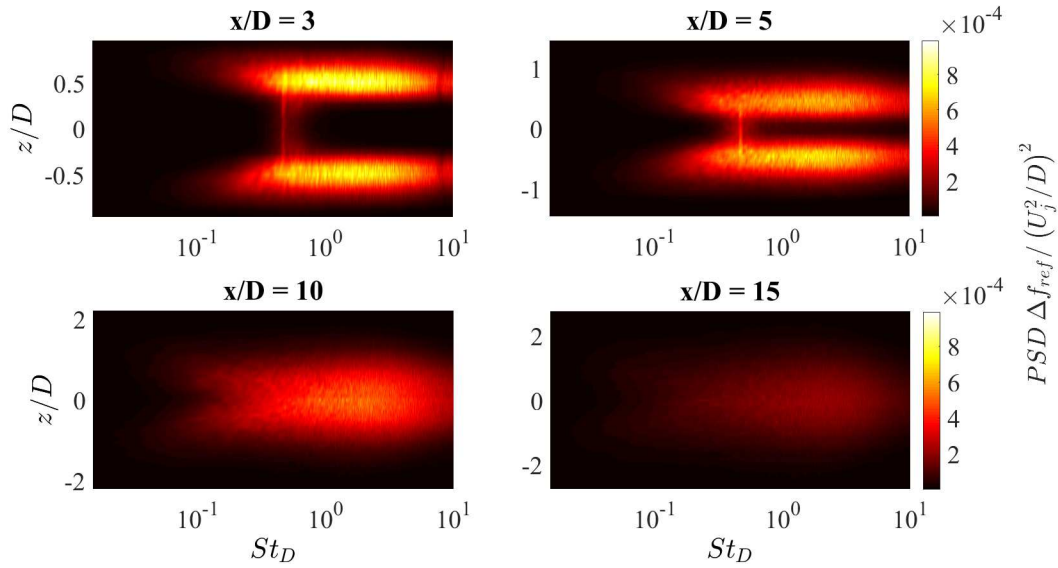


Figure 10.11: Contour map of the dimensionless  $PSD$  of the acceleration signals along the  $z$ -direction for different axial positions.

Figure 10.11 shows the evolution of the spectral energy content along the transverse direction  $z$  for different axial distances. The signature of the Kelvin-Helmholtz instability is still detected for small axial distances, although the spectral energy is mainly concentrated for  $z$ -positions in the proximity of the mixing layers. As the axial distance increases, the spectra amplitude decreases and the energy spreads on a wider range of transverse positions, the maximum energy being located in the proximity of the jet axis.

#### 10.1.2.4 Auto-conditioned acceleration signatures

The acceleration signatures educed by the application of the sampling procedure described in §9.1 are reported in figure 10.12, which shows the stream-wise evolution of the auto-conditioned ensemble averages along the jet axis. An oscillatory signature, very similar to the wave-packet shape reported by Jordan and Colonius (2013), is observed for  $x/D \leq 4$ . It has to be pointed out that an oscillatory trend was also detected for the velocity signatures at the same axial distances. For the axial position  $x/D = 5$  for which the skewness and flatness factors exhibited a singularity a negative spike is clearly detected. As the axial distance increased, such acceleration drop turned into a positive-negative bump shape, such signature being congruent with the positive spike educed from the velocity signals. Specifically, the increase of the velocity in the spike is associated with an acceleration, whereas the decrease of the velocity in the spike is coupled with a deceleration.

## 10.2 Plate effect on the velocity field

The installation effect of the surface on the velocity field is analysed in terms of variation of the statistical moments up to the fourth order in the plane  $x - z$ , i.e. the plane orthogonal to the plate and parallel to the nozzle axis. The description of the velocity field statistics is achieved by point-wise HW anemometer measurements.



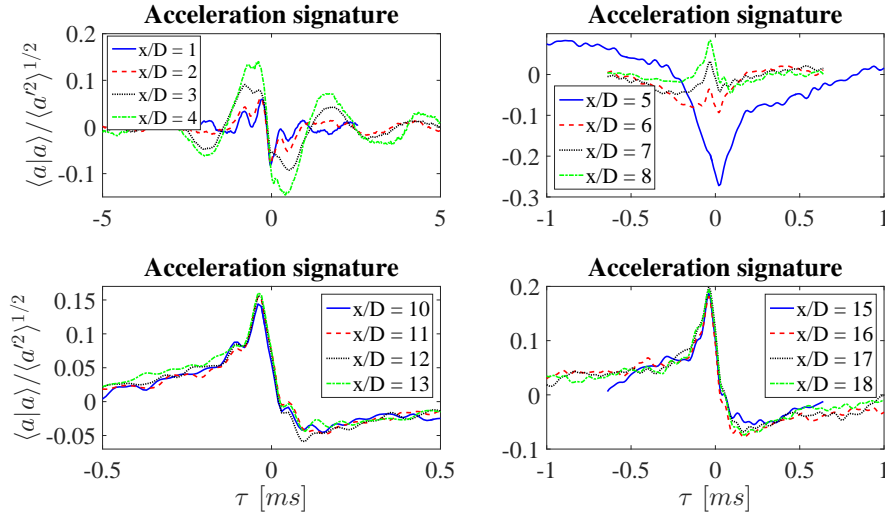


Figure 10.12: Stream-wise evolution of the auto-conditioned acceleration signature.

The profiles of mean axial velocities parametrized in terms of  $H$  and for different  $x/D$  are presented in figure 10.13. In order to enhance the variation of the velocity profile shape induced by the presence of the rigid surface, the mean velocity is normalized with respect to its maximum ( $U_{MAX}$ ) measured along the  $z$ -direction at a fixed  $x/D$  position. It is observed that the interaction with the flat-plate influences the axisymmetry of the jet especially at large distances from the nozzle exit. The main effect induced by the plate is an increase of the mean velocity magnitude and a shift of the velocity profiles in the jet region close to the flat-plate, i.e. for  $z/D < 0$ . It is interesting to note that the mean velocity maximum is found at  $z/D > 0$  for small  $x/D$  and it moves to  $z/D < 0$  further downstream. This behaviour can be clearly observed in figure 10.14 where the  $z/D$  coordinate of the mean velocity maximum is reported as a function of  $x/D$ . It is shown that the  $z$ -position where the maximum mean velocity is reached changes significantly as the axial distance increases. This means that the jet axis moves from positive radial positions to negative ones and, as the plate distance from the nozzle axis increases, the transition becomes less sharp but still detectable. Furthermore, for small axial distances, i.e. very close to the nozzle exhaust, as in the case  $x/D = 1$ , the jet axis location is about constant for any distance  $H/D$  whereas it varies significantly for larger  $x/D$ . Such a behaviour can be related to the jet flow evolution since the jet-plate interaction appears to be weaker in the initial part of the jet flow, close to the nozzle exhaust, and becomes more significant when the jet reaches a fully developed condition.<sup>3</sup> In summary, the presence of the flat-plate brings about the departure of the jet axis from the geometrical nozzle axis. The jet axis is defined hereinafter as the

<sup>3</sup>Neither experimental nor numerical data could be found in the literature to compare the effects due to jet-surface interaction on the mean velocity field. Hence, in order to verify qualitatively the trend found in the experiments, a numerical 3D simulation was carried out through a standard RANS approach, such a model being able to accurately predict aerodynamic changes in the mean field variables. The simulation was performed using the software *Fluent*<sup>®</sup> and adopting a standard  $k - \epsilon$  turbulence model. A mesh sensitivity analysis was carried out leading to a final mesh of 3 million cells non-uniformly distributed in order to reasonably resolve the region close to the flat-plate overflowed by the jet flow. Even though qualitatively, the numerical results confirmed the shift of the jet axis location as a function of the axial distance from the nozzle exhaust. It was also confirmed that for the plate position closer to the jet the transition was faster and sharper.

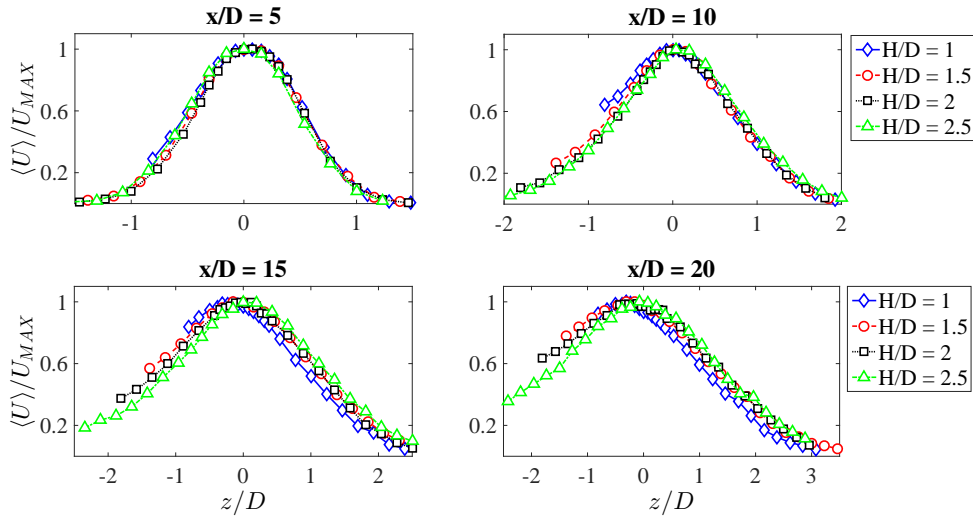


Figure 10.13: Velocity profiles normalized by  $U_{MAX}$  as a function of  $z/D$  at different axial distances.

$z$ -positions, function of the axial distance  $x$ , where the maximum values of the mean velocity were measured.

A global picture of the mean aerodynamic field is depicted in figure 10.15, which shows the contour maps of the dimensionless mean velocity field for all the jet-plate configurations. The mean velocity is normalized by the jet velocity  $U_j$ , whereas the axial distance  $x$  and the transverse distance  $z$  are divided by the nozzle diameter  $D$ . It can be observed that the jet bends over the surface for all the plate radial distances, such a behaviour being ascribed to the so-called Coanda effect (Launder and Rodi, 1983). The Coanda effect is strongly dependent on the parameter  $H$ , the jet deflection being more significant as the flat-plate gets closer to the jet.

The relative turbulence intensity as a function of the radial position is represented in figure 10.16. The velocity standard deviation is divided by  $U_{MAX}$  and parametrized as in figure 10.13. In all the cases, the presence of the rigid surface induces an asymmetry of the turbulence profiles, the maximum being moved towards the side of the jet opposite to the plate position. Unlike the mean aerodynamic field, the effects on the fluctuating velocity field observed in the experiments were compared with numerical data found in the literature. The results achieved in the present work are in good agreement with the turbulence evolution provided by Smith and Miller (2013). The plate effect on the fluctuating velocity field is further addressed in figure 10.17, which shows the contour maps of the  $RTL$ . It is clear that the velocity fluctuations are reduced in the jet region close to the surface, such an effect being stronger for closer jet-plate configurations. Furthermore, the turbulence level globally lowers as the surface distance decreases.

The statistical description of the jet-plate interaction is further provided by the evolution of higher order statistical moments of the velocity field. Figure 10.18 shows the contour maps of the skewness factor. It is observed that the third order statistical moment is close to 0 in the jet plume except for the internal and external shear layer regions where negative and positive values are respectively found. The positive skewness values in the outer shear layers can be ascribed to positive velocity fluctuations due to the injection of ambient flow associated with the entrainment effect of the jet. Conversely, the distribution of the negative skewness values clearly defines the potential core shape.

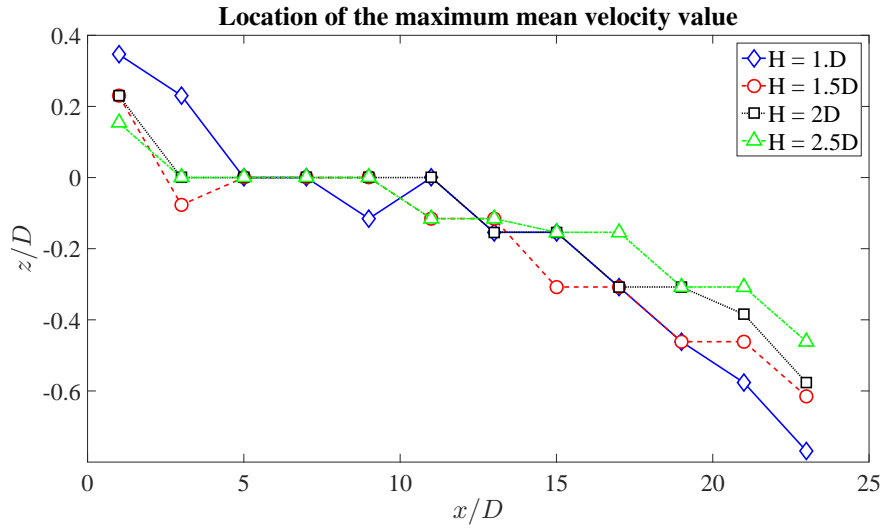


Figure 10.14: Jet axis location at different axial positions from the nozzle exhaust for different plate distances.

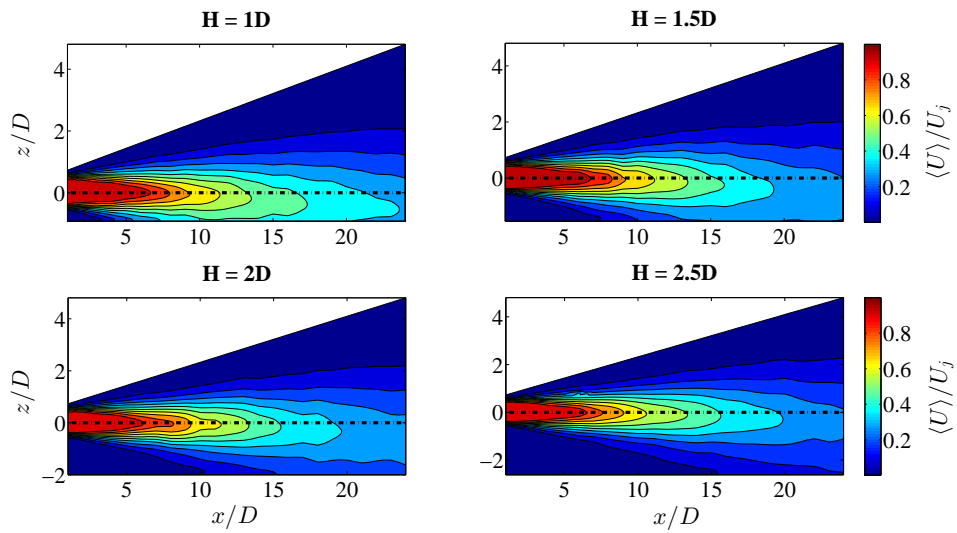


Figure 10.15: Dimensionless mean velocity field in the plane  $x - z$  for all the jet-plate configurations. Dash-dotted lines represent the nozzle axis.

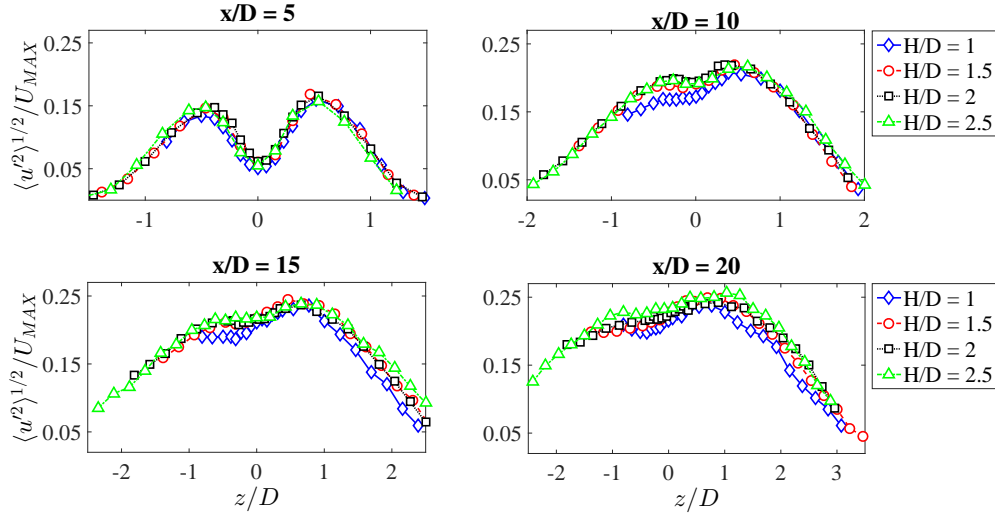


Figure 10.16: Turbulence intensity profiles as a function of  $z/D$  at different axial distances.

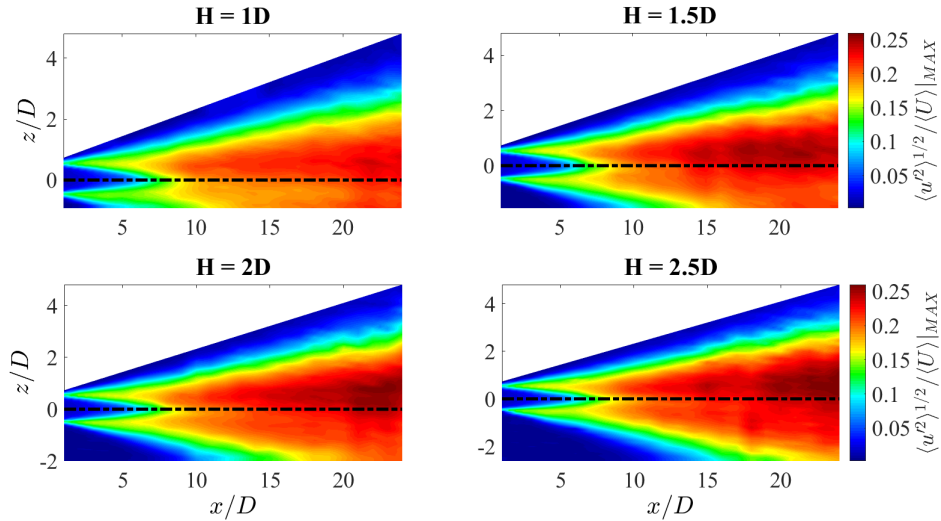


Figure 10.17: Turbulence intensity field in the plane  $x - z$  for all the jet-plate distances. Dash-dotted lines represent the nozzle axis.

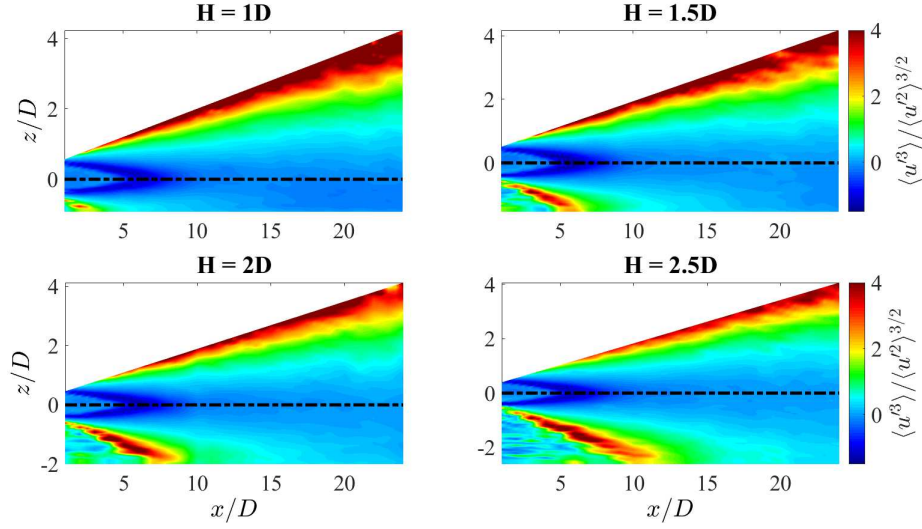


Figure 10.18: Skewness factor of the velocity field in the plane  $x - z$  for all the jet-plate configurations. Dash-dotted lines represent the nozzle axis.

Figure 10.19 shows the contour maps of the flatness factor. As for the skewness factor, the fourth order statistical moment is always close to 3 except for the outer and inner shear layers where larger kurtosis values associated with regions of strong intermittency are found. It can be noted that the effect of the plate is to prevent the development of the outer shear layer in the jet side close to the surface, thus reducing the generation of intermittent events which are strictly related to the turbulence production. Such inference is further supported by the reduction of the turbulence intensity observed in figure 10.17.

### 10.3 Plate effect on the acceleration field

As reported for the velocity, the effect of the flat-plate on the acceleration field is analysed in terms of variation of the statistical moments up to the fourth order in the plane  $x$ - $z$ .

Figure 10.20 shows the dimensionless mean acceleration map for all the jet-plate configurations. As observed in the free-jet conditions, negative accelerations are detected in the mixing layers of the jet for small axial distances and around the jet centreline for stream-wise positions downstream the potential core end. Such decelerations are associated with the reduction of the jet mean velocity at the interface with the ambient flow and in the fully developed region. The maps of the dimensionless standard deviation of the acceleration signals are represented in figure 10.21 for all  $H/D$ . Consistently with the mean acceleration trend, the fluctuations intensity is stronger in the mixing layers of the jet and downstream the potential core end. Except for an asymmetry of the acceleration fields, the profiles being slightly moved towards the surface along the  $z$ -direction, no significant effects of the flat-plate on the mean and fluctuating acceleration components were observed.

The contour maps of the third and fourth order statistical moments of the acceleration are presented in figures 10.22 and 10.23, respectively. As previously found for the velocity, the most significant variations of skewness and flatness factors were observed in the

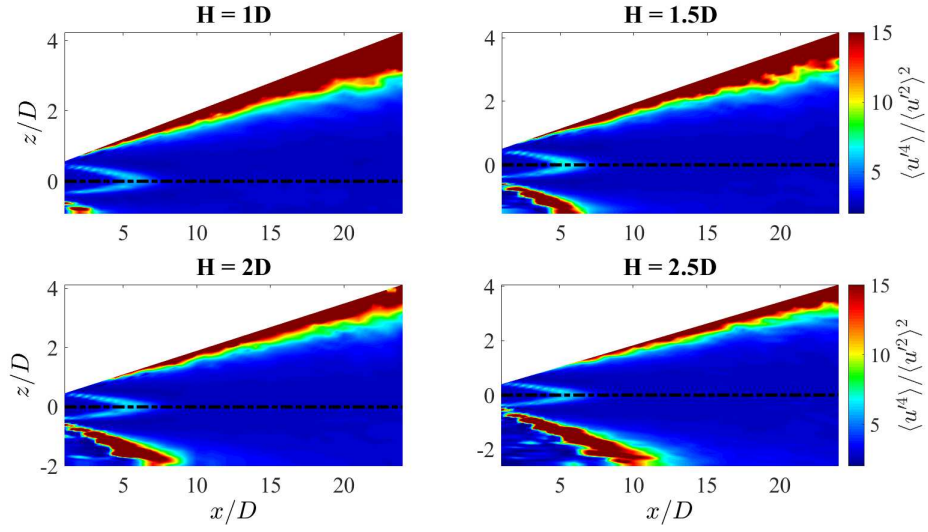


Figure 10.19: Flatness factor of the velocity field in the plane  $x - z$  for all the jet-plate configurations. Dash-dotted lines represent the nozzle axis.

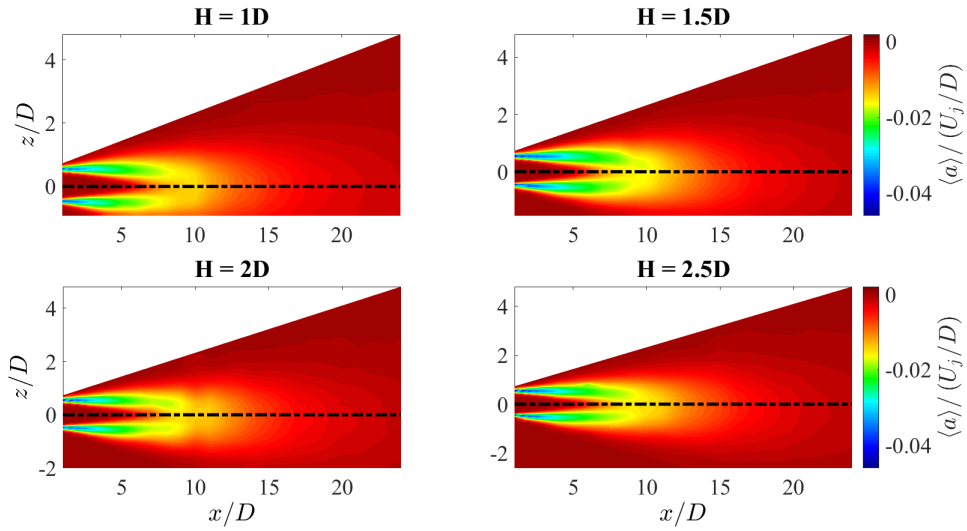


Figure 10.20: Contour map of the dimensionless mean acceleration in the plane  $x - z$  for all the jet-plate configurations.

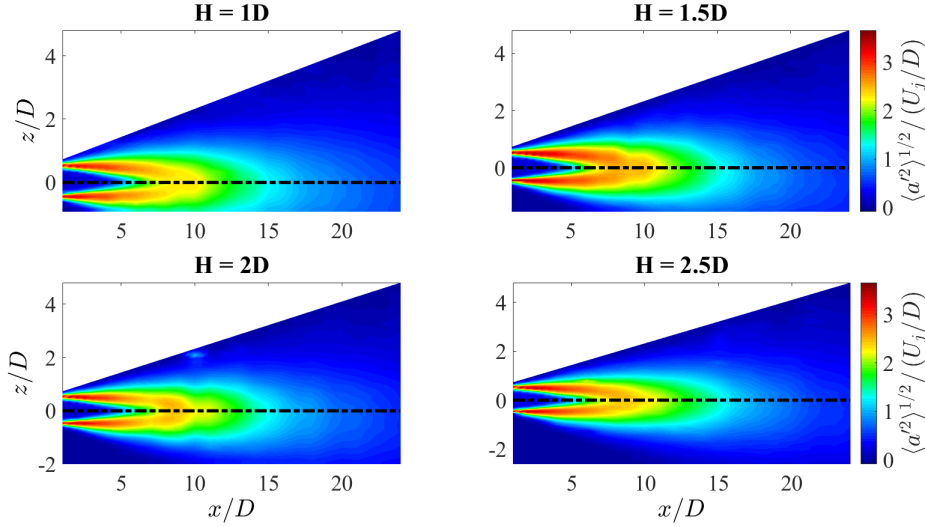


Figure 10.21: Contour map of the dimensionless acceleration standard deviation in the plane  $x$ - $z$  for all the jet-plate configurations.

outer and inner shear layers of the jet, the skewness factor and kurtosis values being slightly larger than 0 and 3, respectively, in the other regions of the jet. Specifically, the skewness showed a succession of positive and negative values in the external shear layer, such a behaviour being ascribed to the entrainment effect of the jet, and significant negative values associated with velocity reductions in the internal shear layer. As underlined for the velocity, the plate has the effect to prevent the development of the outer shear layer in the jet side close to the surface.

## 10.4 Wall pressure field characterization

As pointed out in 8.3, a well detailed description of the pressure field on the flat-plate for different radial positions is provided. Wall pressure measurements were performed with an array of three 1D-spaced microphones. Point-wise measurements with a pressure transducer were also carried out. The pressure evolution was studied both in the stream-wise direction, from  $x/D = 0$  to  $x/D = 25$ , and in the span-wise direction, from  $y/D = -2$  to  $y/D = 2$ . It will be shown that the physical features of the wall pressure field are strongly dependent on whether the jet has impinged or not on the surface. Specifically, the stream-wise location where the jet impacts on the surface affects significantly the wall pressure characteristics.

### 10.4.1 Statistical analysis

The wall pressure statistics changes significantly if the jet impact on the plate occurs correspondingly to the potential core region, the transition region or the fully developed region. A quasi-equilibrium TBL on the surface can be established only at large distances from the impact region, this behaviour being related to the relationship between the radial position of the plate and the axial location where the jet hits the surface. An overall picture of the mean and fluctuating wall pressure evolution is given in figure 10.24, where the time-averaged and the root mean square pressure coefficients along



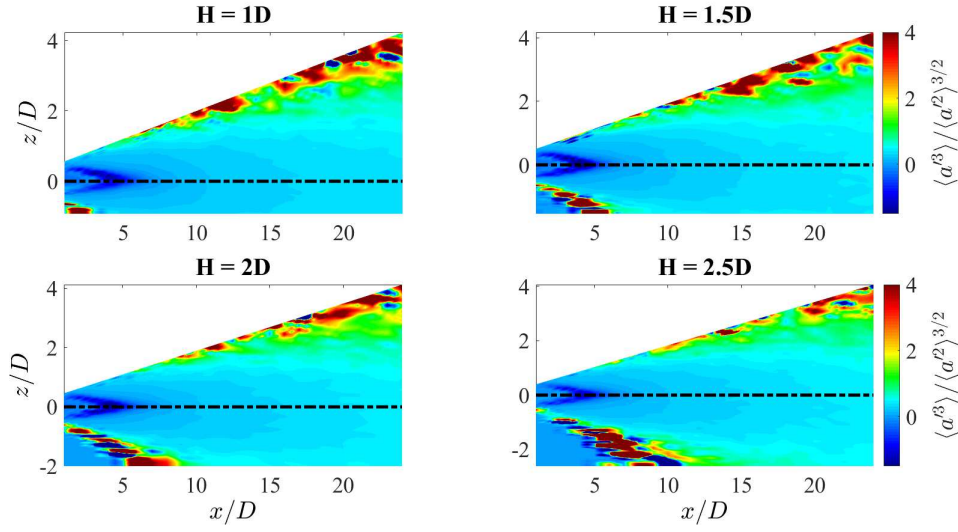


Figure 10.22: Contour map of the acceleration skewness factor in the plane  $x$ - $z$  for all the jet-plate configurations.

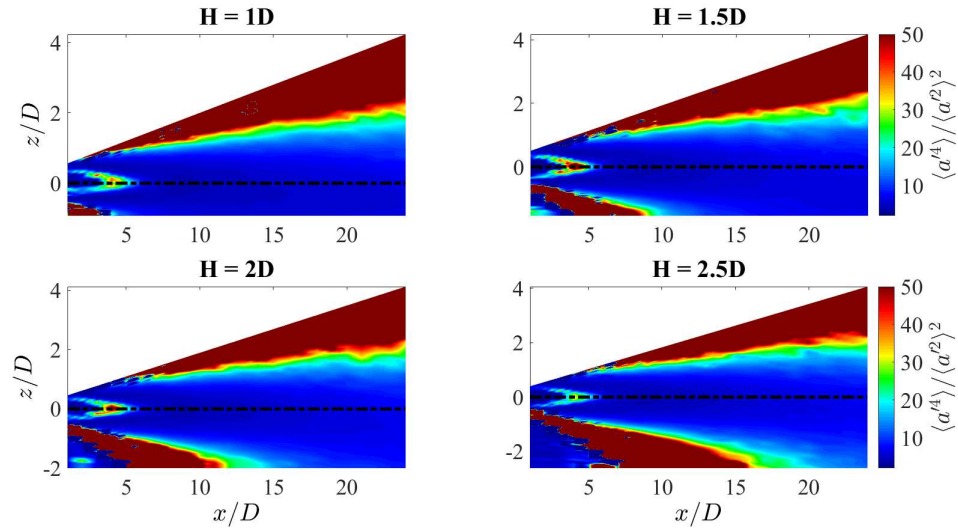


Figure 10.23: Contour map of the acceleration flatness factor in the plane  $x$ - $z$  for all the jet-plate configurations.



Flat-plate distance	Mean pressure evaluation	HWA evaluation
$H/D = 1$	$x/D = 4$	$x = 3.5D$
$H/D = 1.5$	$x/D = 7$	$x = 6.8D$
$H/D = 2$	$x/D = 10$	$x = 10.3D$
$H/D = 2.5$	$x/D = 13$	$x = 13.7D$

Table 10.1: Summary of the jet impact axial positions on the flat-plate.

the jet axis are reported. The pressure coefficients are respectively defined as follows:

$$c_p = \frac{\langle p \rangle - p_{amb}}{\frac{1}{2}\rho U_j^2} \quad (10.7)$$

$$c_{p_{RMS}} = \frac{p_{RMS}}{\frac{1}{2}\rho U_j^2} \quad (10.8)$$

where  $\langle p \rangle$  and  $p_{RMS}$  are the ensemble average of the transducer pressure signals and the root mean square of the microphone pressure signals, respectively.<sup>4</sup>  $p_{amb}$  and  $\rho$  are the ambient pressure and the density. The pressure coefficients trend is different depending on jet-plate separation distance, but some analogies are found. Except for the largest  $H/D$ , three regions can be identified.

- First region: the mean pressure coefficient remains about constant and the  $c_{p_{RMS}}$  increases;
- Second region: the mean pressure coefficient increases reaching its maximum and the  $c_{p_{RMS}}$  remains about constant;
- Third region: the mean pressure coefficient and the  $c_{p_{RMS}}$  both decay. The mean pressure recovers almost the initial amplitude, whereas the pressure fluctuations remain larger as an effect of the development of a boundary layer.

The different behaviour observed for the largest  $H/D$  can be ascribed to the fact that in this configuration the plate is quite far from the jet and the jet impact occurs far from the nozzle exhaust, approximately around  $x/D = 13$ . At such a distance, the jet can be considered fully turbulent, its mean kinetic energy being much lower than that in the region closer to the jet orifice. It is reasonable to suppose that the beginning of the second region corresponds approximately to the point where the jet flow impacts the plate. This idea is supported by the results reported in table 10.1, where the position of the impact estimated by the measured spreading angle of the jet is compared with the positions where the mean pressure coefficient starts to rise. As it can be observed, a very good agreement between the two estimations is found. Table 10.2 clarifies and summarizes the distinction between the three regions described above. Except for the case  $H/D = 2.5$ , where it is not possible to clearly detect the end of region 2, the separation between the three regions appears reasonable.

<sup>4</sup>It has to be pointed out that the  $p_{RMS}$  coincides with standard deviation of the pressure as the microphone signal has zero mean.

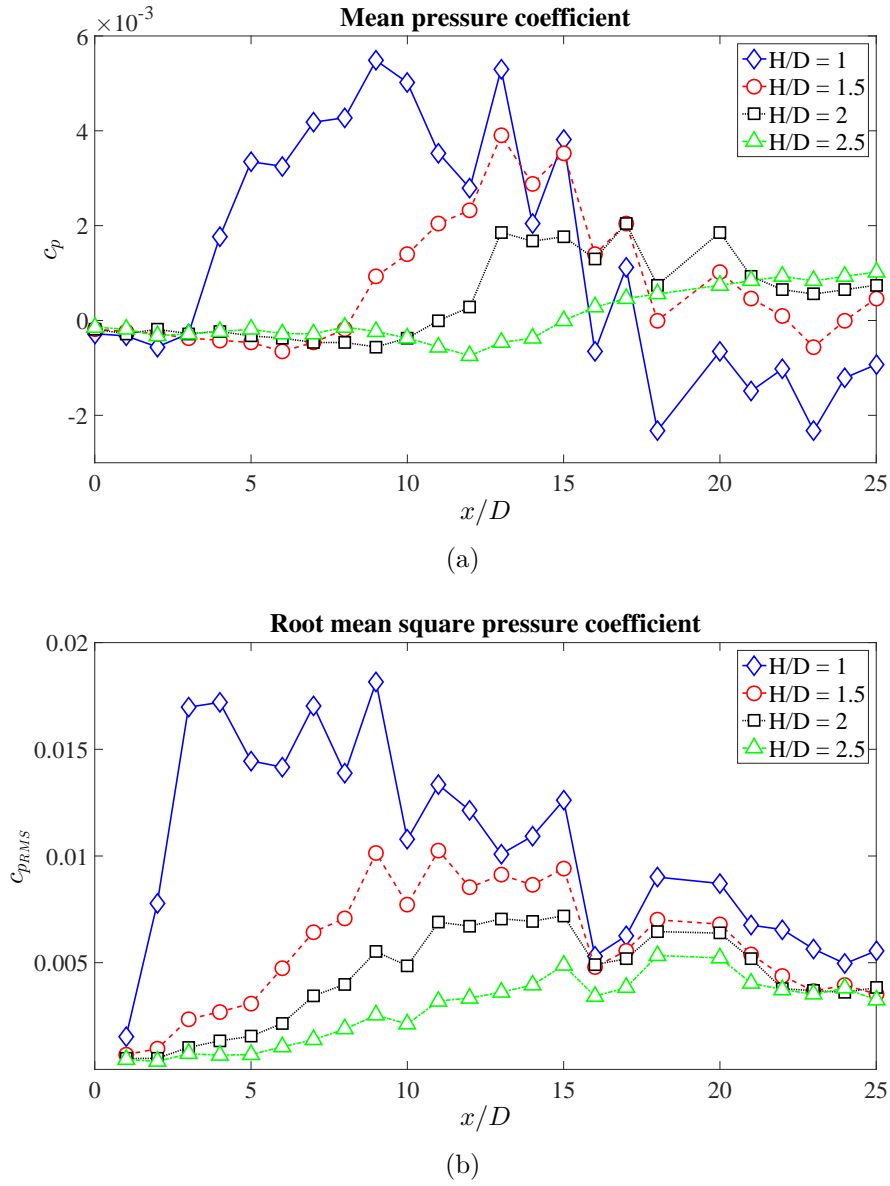


Figure 10.24: Pressure coefficients on the flat-plate along the jet axis: (a) mean pressure, (b) root mean square pressure.

	Flat-plate distance	Axial position
End of region 1	$H/D = 1$	$x/D = 3$
	$H/D = 1.5$	$x/D = 6$
	$H/D = 2$	$x/D = 9$
	$H/D = 2.5$	$x/D = 12$
End of region 2	$H/D = 1$	$x/D = 9$
	$H/D = 1.5$	$x/D = 13$
	$H/D = 2$	$x/D = 13$
	$H/D = 2.5$	?

Table 10.2: Axial locations of the jet-plate interaction regions.

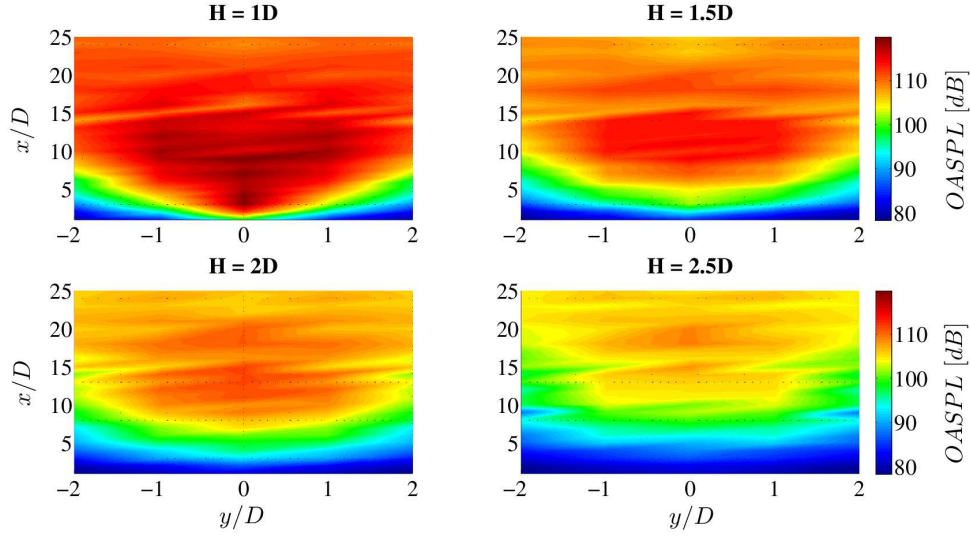


Figure 10.25: *OASPL* map on the flat-plate for all the surface radial distances from the nozzle axis.

In order to have a global picture of the fluctuating pressure field, the OverAll Sound Pressure Level has been computed at each axial and transverse location and for each  $H/D$ . The *OASPL* contour maps are reported in figure 10.25. It can be noticed that the closer is the position of the flat-plate the higher is the *OASPL* over the whole surface. The pressure footprint is clearly observed closely downstream of the nozzle exit for  $H/D = 1$ . As the plate separation distance increases, the pressure footprint becomes weaker and the axial position where the maximum noise level is found moves further downstream. Furthermore, in the region of the surface corresponding to the fully turbulent jet the *OASPL* variation along the transverse direction reduces significantly.

#### 10.4.1.1 Probability Density Functions

The wall pressure statistics is also studied in terms of Probability Density Function distributions. The comparison of the *PDF* distributions is presented in figure 10.26 for different  $H/D$  and axial distances. The pressure variable is expressed in reduced form, i.e. normalized in order to have zero mean value and unitary standard deviation. *PDF*s achieved from the experiments are compared with the standard Gaussian distribution. All the pressure distributions deviate from the Gaussian one, such discrepancy becoming more significant as the axial distance increases. The positive skewness observed for  $x/D = 10$  at  $H/D = 1$ ,  $H/D = 1.5$  and  $H/D = 2$  can be ascribed to the intermittent large amplitude velocity fluctuations induced by the jet flow structures that impact on the flat-plate and evolve over it.<sup>5</sup> Another aspect which has to be pointed out is that the *PDF* tails become larger than the Gaussian distribution for increasing axial distances. This behaviour is more evident in figure 10.27, where the axial evolution of the *PDF*s is given for all the  $H/D$  considered. The *PDF* tails follow an exponential evolution as the  $x/D$  position increases, such a behaviour being typical in fully developed turbulence (Tsuji et al., 2007).

<sup>5</sup>Additional experiments with flow visualization techniques are planned to confirm this hypothesis.

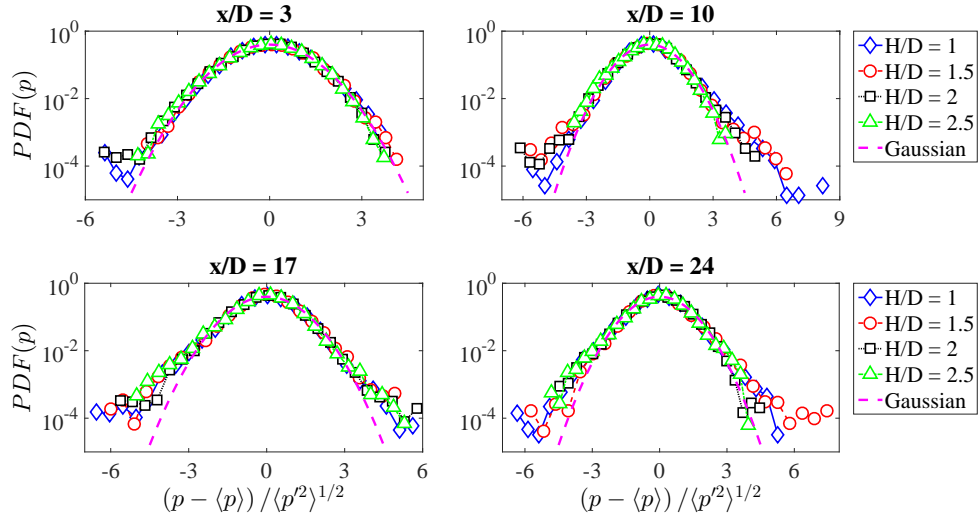


Figure 10.26: Pressure  $PDF$ s at different axial positions for all the jet-plate configurations.

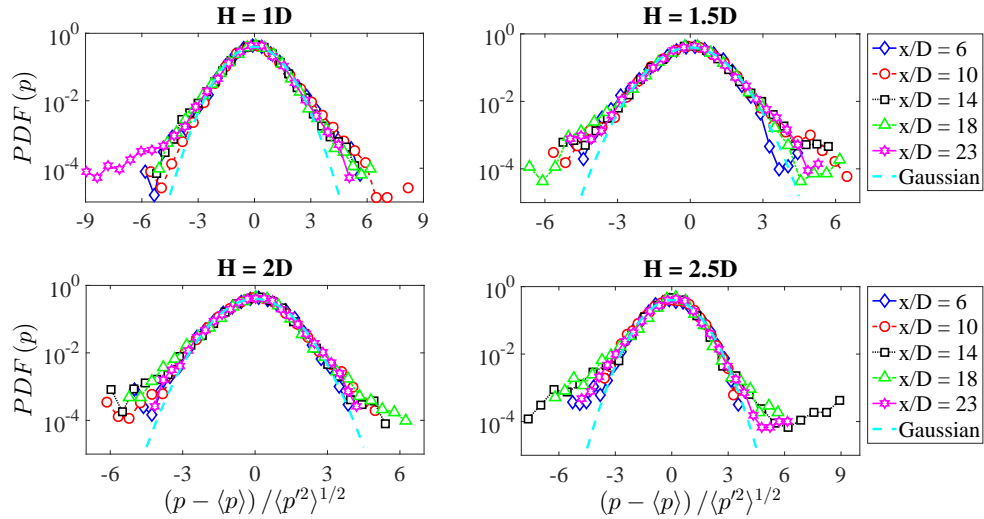


Figure 10.27: Axial evolution of the pressure  $PDF$ s for all the plate positions.

### 10.4.1.2 Cross-correlation between wall pressure signals

Wall pressure statistics is investigated in the time domain through the cross-correlation function computed between two contiguous microphones. The cross-correlation is defined as:

$$R_{pp}(\xi, \tau) = \langle p(x, t), p(x + \xi, t + \tau) \rangle \quad (10.9)$$

where  $\xi$  is the distance between microphones (in the present study  $\xi = 1D$ ),  $\tau$  is the time-lag and the symbol  $\langle \rangle$  denotes an ensemble average. The cross-correlation coefficient  $\rho_{pp}$ , obtained normalizing the cross-correlation function by the product of the standard deviations of each pressure signal, is plotted in figure 10.28 for different  $H/D$  and axial positions. For axial distances close to the nozzle exhaust  $\rho_{pp}$  is always asymmetric, whereas, as the jet becomes completely turbulent, the cross-correlation shape becomes symmetric. Furthermore, flow structures of larger size convected through the flow cause the cross-correlation coefficient to become wider as  $H/D$  increases. Thus, the jet-plate interaction has the effect to break the large turbulent structures as the plate approaches to the jet. This result is in agreement with the turbulence intensity profiles reported in figure 10.16, in which a decrease of the turbulence intensity was observed in the jet region close to the flat-plate.

Cross-correlations were exploited to evaluate the convection velocity ( $U_c$ ) along the jet axis.  $U_c$  is determined as the ratio between the microphone distance  $\xi$  and the time-lag at which the cross-correlation maximum is detected. The convection velocity as a function of the stream-wise position along the jet axis is reported in figure 10.29. The value found in the potential core region is in good agreement with the literature results, i.e.  $U_c \approx 0.6 U_j$  (Picard and Delville, 2000). As the axial distance increases and the jet mean velocity decreases, the convection velocity decreases as well, reaching  $U_c/U_j \approx 0.25$  for very large  $x/D$ . A significant dependence of  $U_c$  upon  $H$  is observed for large  $x/D$ , whereas at small distances from the jet a more universal behaviour is detected. Specifically, smaller values of convection velocity are detected for further jet-plate distances as a consequence of the larger size of the associated turbulent structures for increasing  $H$ .

### 10.4.2 Spectral characterization

Figure 10.30 shows the Sound Pressure Spectrum Level as a function of the Strouhal number  $St_D$  for each plate distance and for a set of axial positions along the nozzle axis ranging from  $x = 1D$  to  $x = 25D$ . The amplitude and the spectral shape change significantly as the jet-plate separation distance decreases. Specifically, for small axial distances the spectra show a higher energy content over the whole frequency range. It has to be pointed out that the peaks emerging in the spectra for  $St_D > 1$  for the large  $H/D$  are related to the background noise and have no physical meaning. As the axial distance increases, the energy of the fluctuating pressure increases and the shape of the spectra changes accordingly.

The *SPSLs* obtained in the span-wise direction for the axial distances  $x/D = 15$  and  $x/D = 25$  and for each plate separation distance are presented in figures 10.31 and 10.32, respectively. The transverse positions  $y/D = 0, 1, 2$  were here considered. For  $x/D = 15$  the difference between each transverse location is more significant: the spectra for  $y/D = 0$  show a higher amplitude especially in the middle frequency range.

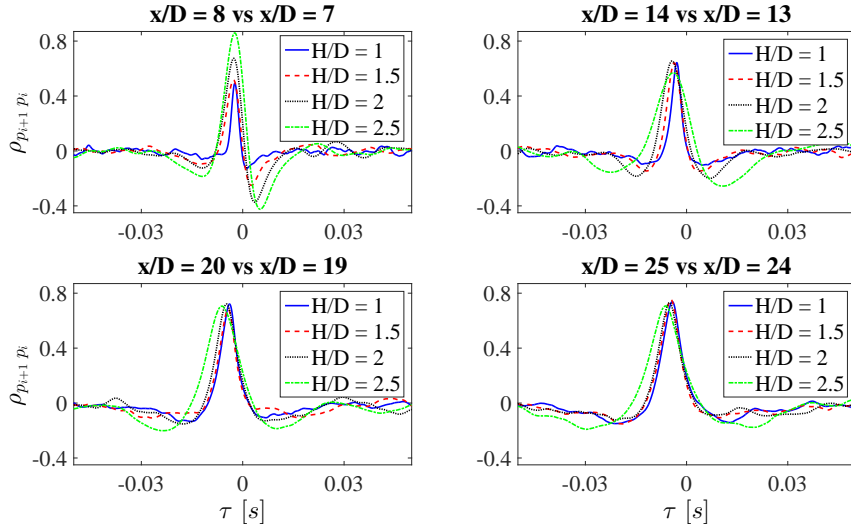


Figure 10.28: Wall pressure cross-correlation coefficient between consecutive stream-wise microphone signals on the jet axis at different axial positions for all the jet-plate configurations.

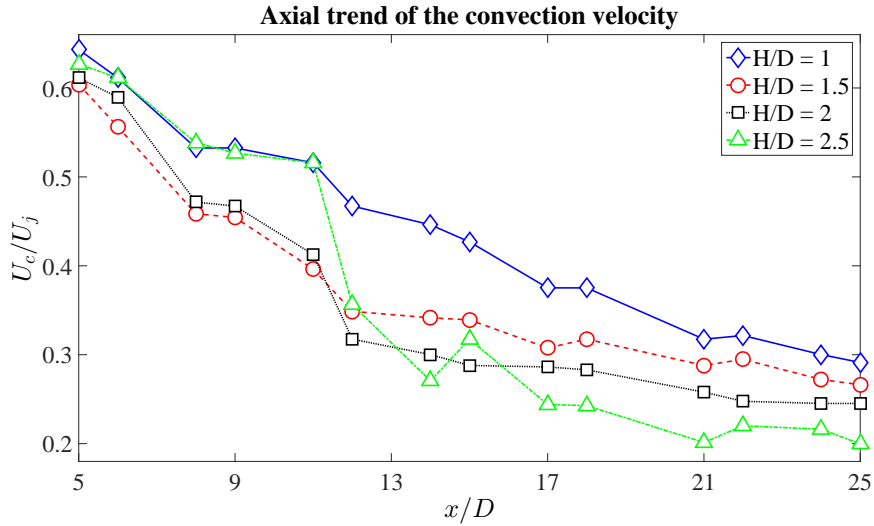


Figure 10.29: Convection velocity along the stream-wise direction on the jet axis for all the flat-plate radial distances.

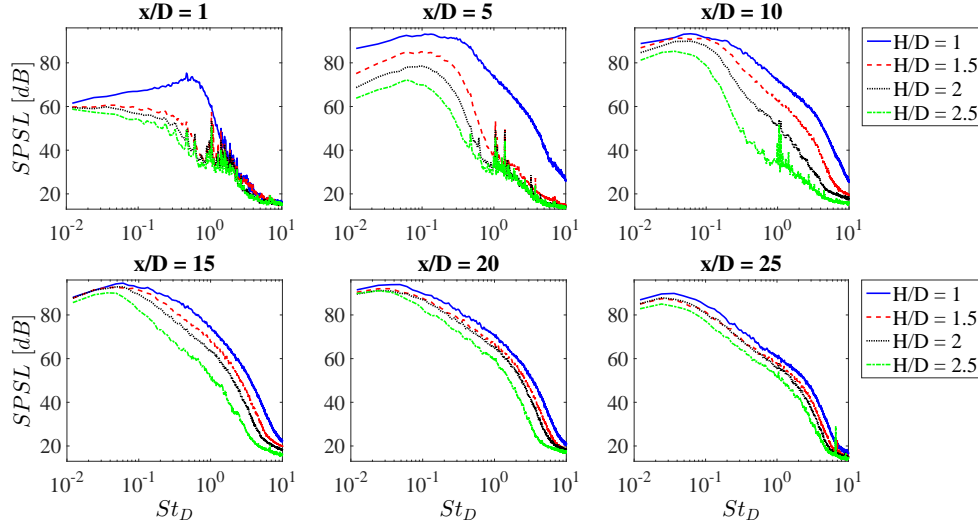


Figure 10.30:  $SPSSL$  vs Strouhal number at different axial distances for all the jet-plate configurations.

As the span-wise distance increases, the spectral energy decreases and the peaks related to the background noise emerge. For large axial distances, i.e. in the fully turbulent jet region, the spectra collapse in the low and mid frequency range and exhibit a steeper energy decay in the high frequency range as the transverse distance increases.

As it has been shown in figure 10.30, the amplitude and shape of the wall pressure auto-spectra depend significantly upon the flat-plate distance and the axial position of the microphone with respect to the jet exit. For large  $x/D$ , where the jet has completely developed on the flat-plate, a more universal trend can be found as an effect of the development of a TBL over the wall (Hwang et al., 2009). Figure 10.33 shows the spectra for all  $H/D$  determined at an axial distance of  $x/D = 25$ . A slope  $\propto f^{-1}$  is found in the frequency range immediately after the spectrum peak, according to the energy decay law commonly observed in the overlap region for fully developed TBL wall pressure spectra. In the mid frequency range an energy decay law  $\propto f^{-7/3}$ , typical of fully turbulent flows, is observed. In the high frequency range, the spectral shape is affected by viscosity and an energy decay law close to  $f^{-5}$  is found.

### 10.4.3 Wall pressure fluctuations modelling

#### 10.4.3.1 Scaling criterion for auto-spectra

A unique scaling criterion able to lead all the spectra to collapse cannot be found due to the spectra shape dependence on the different geometrical configurations considered. For positions downstream the jet impact point on the surface a scaling criterion is proposed using external aerodynamic variables,  $H$  and  $U_j$ , as reference length and velocity scales, respectively. The typical time-scale to be used is related to the time occurring to a fluid particle convected by the mean flow to reach the flat-plate. Therefore, it is estimated by the ratio  $H/U_c$  being  $U_c$  the convection velocity determined above. Accordingly, the  $PSDs$  and the frequency are normalized as follows:

$$PSD_{scaled} = \frac{PSD}{\tau_c q_c^2} \quad \tau_c = \frac{H}{U_c} \quad q_c = 0.5\rho U_c^2 \quad (10.10)$$

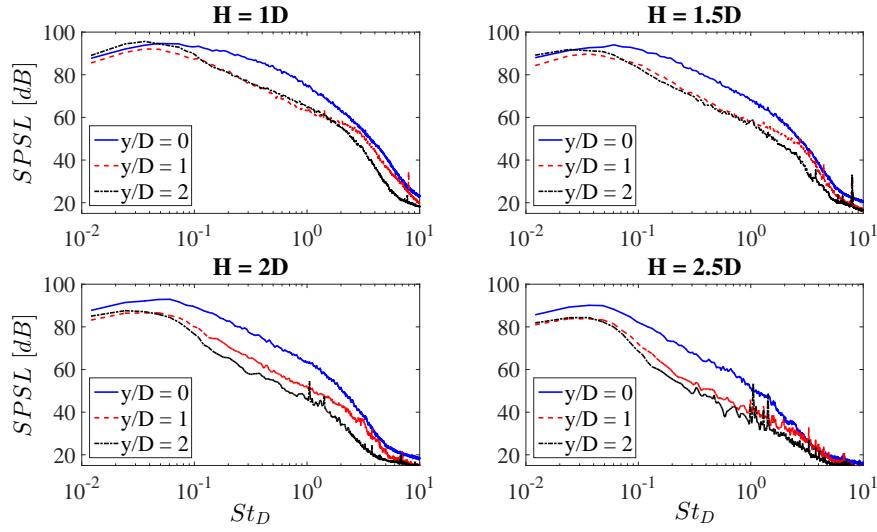


Figure 10.31:  $SPSL$  vs Strouhal number along the span-wise direction at  $x/D = 15$  for all the flat-plate radial distances.

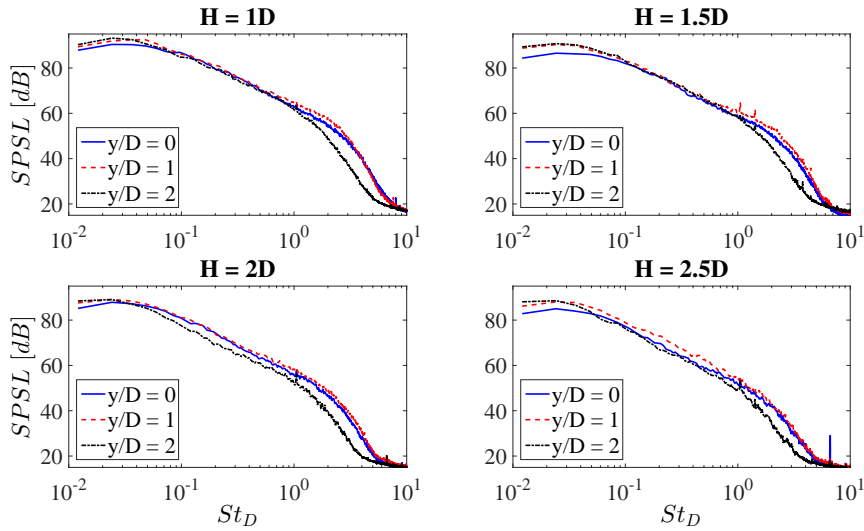


Figure 10.32:  $SPSL$  vs Strouhal number along the span-wise direction at  $x/D = 25$  for all the flat-plate radial distances.



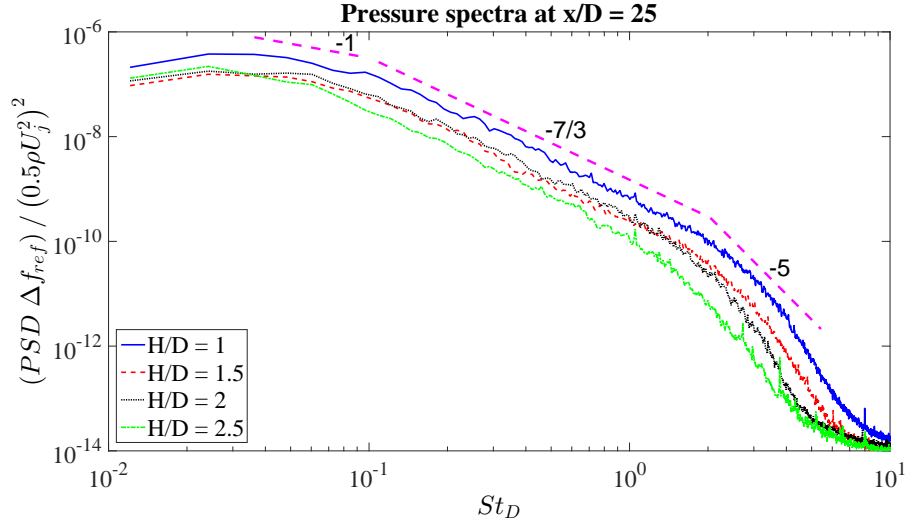


Figure 10.33: Dimensionless  $PSDs$  of wall pressure signals at axial distance  $x/D = 25$  for all the jet-plate configurations. Energy decay laws function of the frequency range considered are also reported.

$$St_H = \frac{f H}{U_j} \quad (10.11)$$

The normalization was applied to auto-spectra referred to all the surface radial distances at different axial locations far from the nozzle exhaust. As shown in figure 10.34, according to the definitions given in Table 10.2, a satisfactory collapse was found for spectra corresponding to positions at the end of region 2 and in different axial positions in region 3. The results of figure 10.34 suggest that the wall pressure auto-spectra become universal once the jet flow has impacted the wall, this behaviour occurring before a fully developed TBL is reached.

#### 10.4.3.2 Coherence function

Interesting conclusions can be inferred by the analysis of the coherence function determined along the jet axis and evaluated as follows (Di Marco et al., 2013):

$$\gamma(\xi, \omega) = \frac{|\Phi_{p_{i+1} p_i}(\xi, \omega)|}{[\Phi_{p_{i+1}}(\omega) \Phi_{p_i}(\omega)]^{1/2}} \quad (10.12)$$

where  $\omega$  is the angular frequency,  $\Phi_{p_{i+1} p_i}$  the cross-spectrum,  $\Phi_{p_{i+1}}$  and  $\Phi_{p_i}$  the auto-spectra of two consecutive microphones separated in the stream-wise direction by  $\xi = 1D$ . Based on the results summarized in table 10.1, the coherence function was calculated beyond the axial positions where the jet impacts the flat-plate. Experimental results were compared with the Corcos' model formulation (Corcos, 1963; Finnveden et al., 2005) providing a prediction of the coherence function that is defined as follows:

$$\gamma(\xi, \omega) = \exp\left(-\beta \frac{\omega \xi}{U_c}\right) \quad (10.13)$$

where the constant  $\beta$  was empirically determined by a least mean square optimization algorithm. The coherence spectra versus the normalized angular frequency  $\omega \xi / U_c$

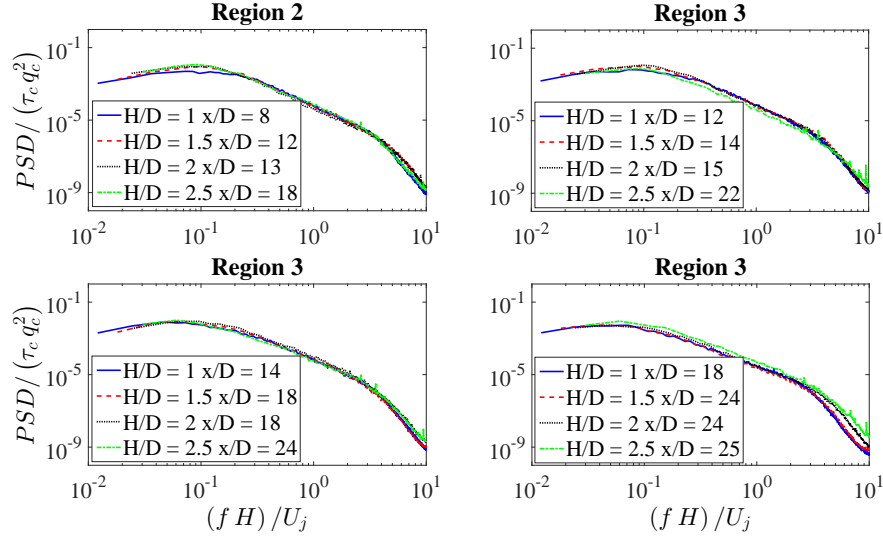


Figure 10.34: Scaled wall pressure spectra at different axial positions and flat-plate distances depending on the region reported in table 10.2.

(Farabee and Casarella, 1991) are shown in figure 10.35 for all  $H/D$  and at axial distances  $x/D \geq 14$ . The exponential decay along the normalized frequency typical of the Corcos' formulation is well reproduced by the experiments. For small axial distances a small discrepancy of the experimental data with respect to the Corcos' model is found as the distance  $H/D$  increases. Moving downstream in the jet and thus approaching a developed TBL, the experimental points become less scattered for all the flat-plate distances. This behaviour is confirmed by figure 10.36, which shows the axial evolution along the nozzle axis of the coherence function for all  $H/D$ . It can be observed that the exponential decay is well reproduced and the decay coefficient decreases for increasing  $x/D$ .

Figure 10.37 summarizes the axial evolution of the Corcos' coefficient  $\beta$  for all  $H/D$ . Values of  $\beta$  ranging from 0.1 to 0.19, found in literature (see, e.g. Bull (1967) and Brooks and Hodgson (1981)) are also reported. For the smallest  $H/D$  it is found  $|\beta| \simeq 0.2$  for all the considered axial positions, which is surprisingly in very good agreement with the amplitude reported in the literature for equilibrium TBLs. At larger  $H/D$ , the measured Corcos' coefficients are higher than those found in literature. The larger is  $H/D$  the larger is the coefficient, but for increasing  $x/D$  the amplitude of  $|\beta|$  decreases and the tendency is to reproduce again the amplitude 0.2 expected for equilibrium TBLs.

## 10.5 Cross-statistics between velocity and wall pressure fluctuations

Simultaneous velocity and wall pressure measurements performed with the HW at different stream-wise and cross-wise positions and the 5-microphone array in the stream-wise direction for  $y/D = 0$  were exploited to carry out a cross-statistical analysis in both the time and frequency domains. It will be shown that correlation and cross-spectrum amplitude and shape change with the flat-plate distance  $H$  and as a function of the position in the plane  $x$ - $z$ . Indeed, as pointed out in §10.4.1, the physics of the jet-plate

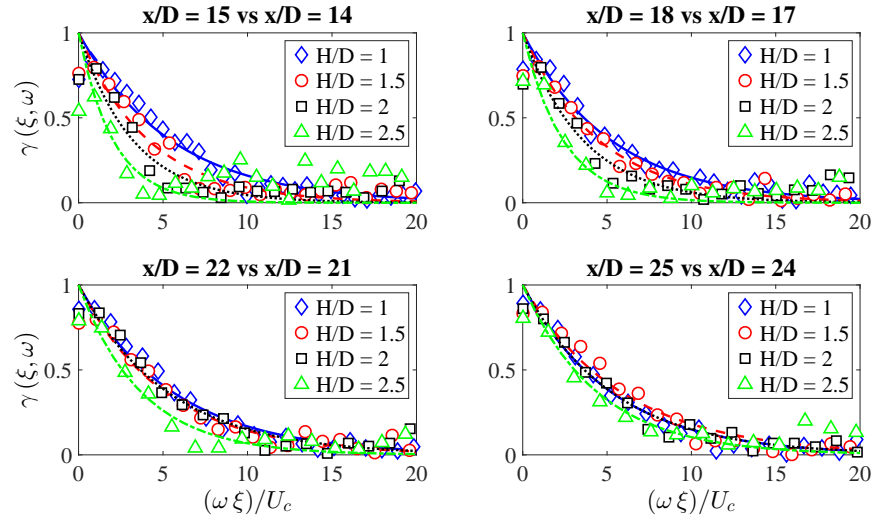


Figure 10.35: Coherence function parametrized by the flat-plate distance for different axial positions. Markers are for experimental data and lines for Corcos' model fits.

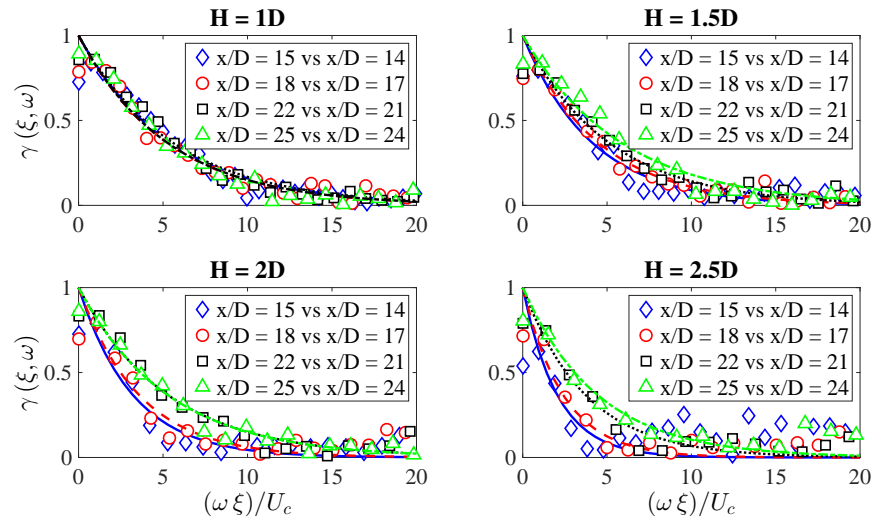


Figure 10.36: Stream-wise evolution of the coherence function for all the flat-plate distances from the jet. Markers are for experimental data and lines for Corcos' model fits.

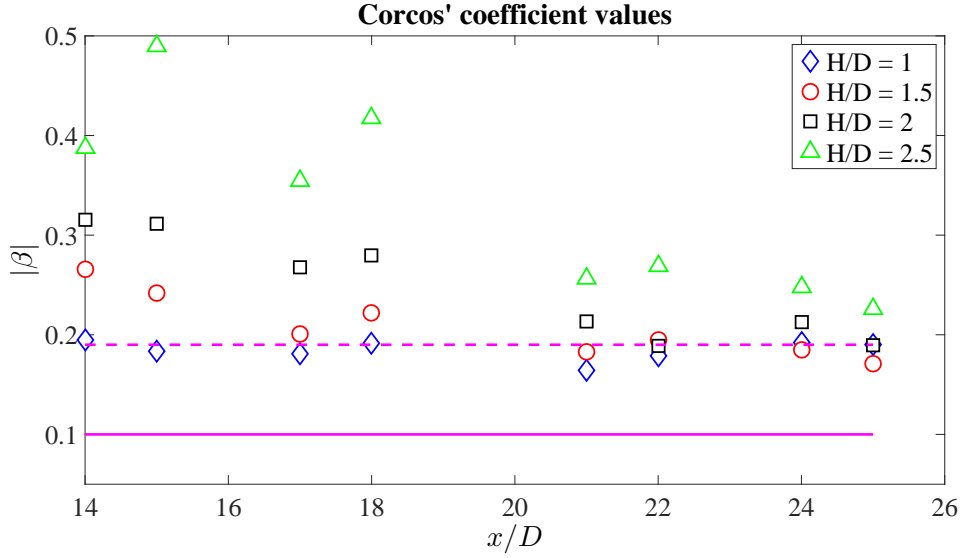


Figure 10.37: Axial evolution of the Corcos' coefficient from  $x/D = 14$  to  $x/D = 25$  for all the jet-plate distances. Solid and dashed lines refer to the lower and upper limit values of the Corcos' coefficient, respectively.

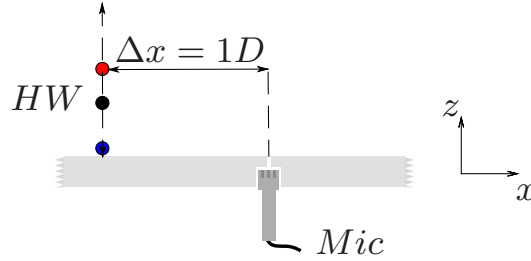


Figure 10.38: Sketch of the hot-wire and microphone disposition for the computation of the cross-correlations and cross-spectra. Red color refers to HW transverse position on the nozzle axis, black color to the jet axis position, blue color to the  $\zeta$  position (for more details on the definition of the cross-wise positions see §8.2 and §10.2).

interaction can be essentially divided into three regions: (i) the first zone in which the jet has not yet impinged on the plate; (ii) the second zone in which the jet impacts the surface; (iii) the third zone in which the development of the flow over the surface leads to a quasi-equilibrium TBL. Based on the above regions, different cross-correlations and cross-spectra are obtained.

Cross-correlations and cross-spectra of velocity and wall pressure signals are presented addressing the effect of the plate distance from the jet as well as of the positions of the hot-wire and microphones. The velocity/pressure cross-statistics is obtained according to the scheme depicted in figure 10.38. Specifically, pressure signals from the microphone in the  $i^{th}$  axial position are correlated with velocity signals obtained by the hot-wire probe in the  $(i - 1)^{th}$  axial position.

### 10.5.1 Cross-correlations

The cross-correlation between axial velocity and wall pressure signals is computed according to the following formula:

$$R_{u_i p_{i+1}}(\xi, \tau) = \langle u(x, t) p(x + \xi, t + \tau) \rangle \quad (10.14)$$

Where  $\xi$  is the streamwise distance between the hot-wire and the microphone (in the present study  $\xi = 1D$ ) and  $\tau$  is the time-lag. The cross-correlation coefficient  $\rho_{u_i p_{i+1}}$  is obtained normalizing the cross-correlation by the product between the standard deviations of the velocity and wall pressure signals.

Figure 10.39 shows the cross-correlation coefficient between the velocity and wall pressure signals at different axial positions of the hot-wire probe:  $x/D = 4, 9, 16, 23$  for the plate position closest to the jet, i.e.  $H/D = 1$ . Three different locations of the hot-wire on the  $z$ -axis are shown: the closest distance to the plate, denoted as  $\zeta$ , the nozzle axis position ( $z = 0$ ) and the jet axis position, as formally defined in 10.2. It can be observed that both the amplitude and the shape of the correlation change depending on the axial and transverse positions. For  $x/D = 4$  an oscillatory shape can be found for all the  $z$ -positions. Moving downstream within the jet plume the turbulence intensity increases and the shape of the correlation changes accordingly, showing a larger time-scale related to the development of large turbulent structures. For the HW transverse locations corresponding to the nozzle and jet axes, the correlation exhibits a positive-negative bump. Conversely, a significant variation of the correlation trend is detected for the probe position closest to the plate. A positive spike-shape is clearly observed for axial positions  $x/D = 9, 16$ , and  $23$ , the correlation maximum being located at a time-delay corresponding to the negative peak of the correlation associated with the nozzle and jet axes positions. It is interesting to point out that the trend described above is not dependent on the plate distance  $H$ . An overview of the cross-wise evolution of the correlation between velocity and wall pressure signals for  $H/D = 1$  is reported in figure 10.40, which shows the cross-correlation coefficient maps along the  $z$ -axis for the same axial positions listed above. It is observed that the highest correlation level is found for transverse positions in the proximity of the nozzle axis. Furthermore the correlation shape changes as the hot-wire approaches the flat-plate. Such different correlation trends could be ascribed to a phase shift, the velocity and wall pressure signals being in phase opposition for cross-wise locations close to the nozzle axis and in-phase for transverse positions close to the plate (Lau et al., 1972).

Figure 10.41 shows the cross-correlation coefficient maps along the  $x$ -axis for all  $H$ . The hot-wire location on the  $z$ -axis corresponds to the jet axis position for each axial distance considered. According to Fuchs (1972), the correlation coefficient exhibits a narrow oscillatory shape for small stream-wise positions within the potential core region. Such a pseudo-periodic behaviour is ascribed to the signature of the Kelvin-Helmholtz instability. As illustrated above, moving downstream in the jet plume the turbulence development produces a positive-negative bump-shape whose time-scale enlarges as the axial distance increases. Such a trend is in agreement with the results presented by Henning et al. (2013) for the case of a free jet. It has to be underlined that for  $H/D = 1$  the highest correlation value is found in the potential core region. On the contrary, for larger values of  $H$ , the maximum correlation level is observed for axial positions increasingly further from the nozzle exhaust. Globally, the correlation amplitude decreases as the flat-plate is moved away from the jet.

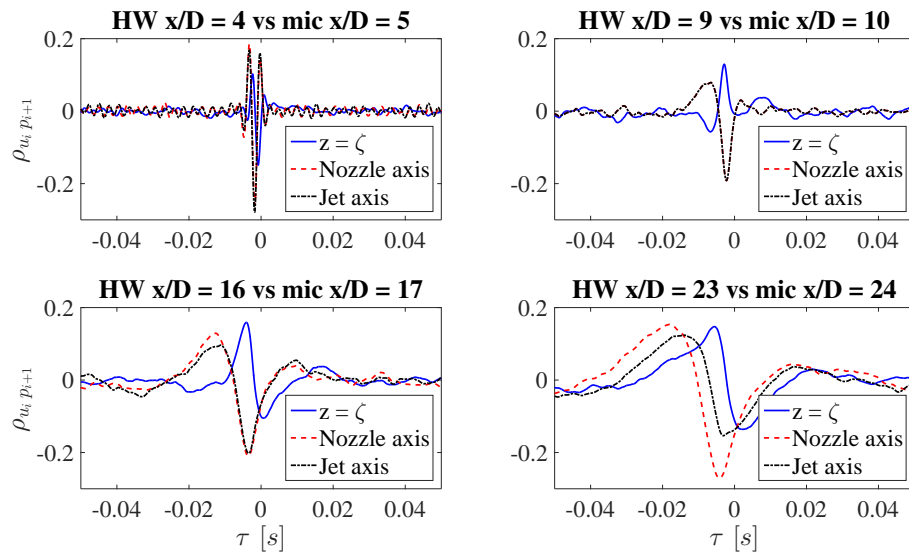


Figure 10.39: Cross-correlation coefficient between velocity and wall pressure signals for  $H/D = 1$  at different axial positions.

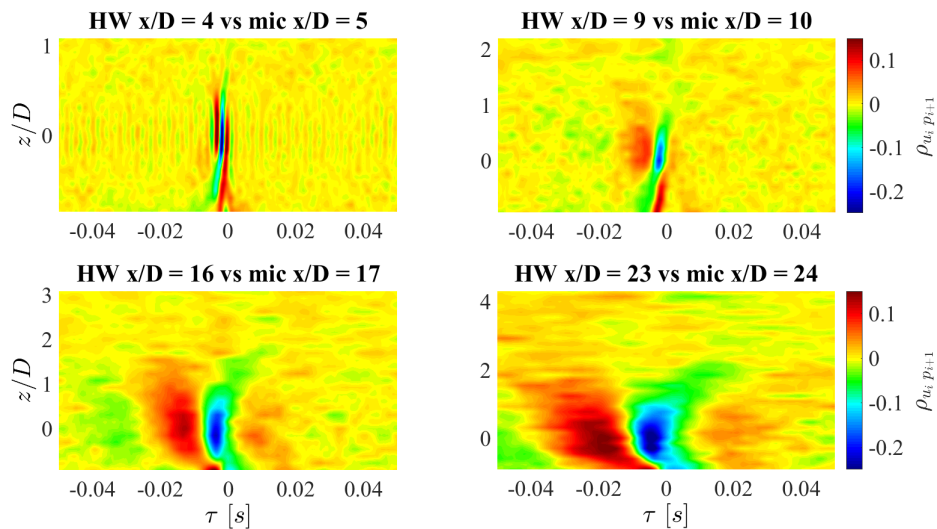


Figure 10.40: Cross-correlation coefficient maps along the  $z$ -axis between velocity and wall pressure signals for the plate radial distance  $H/D = 1$ .

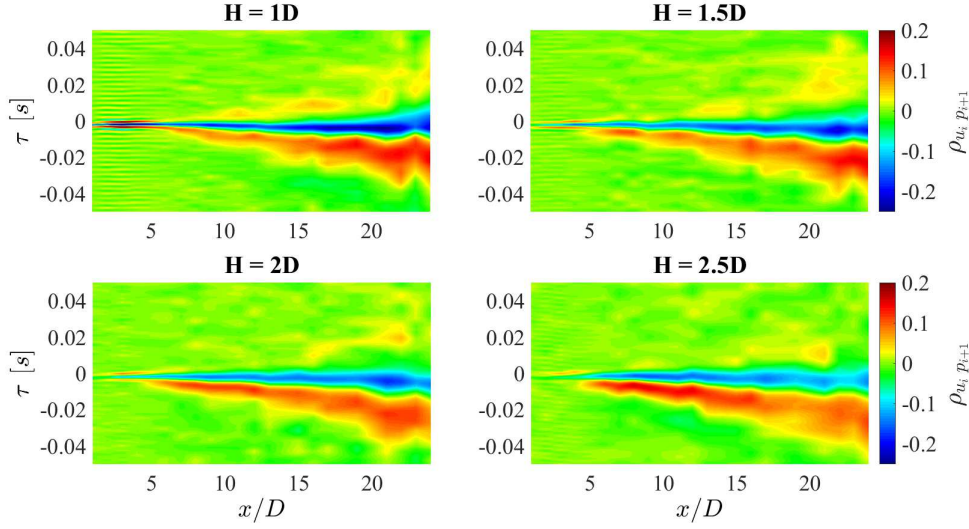


Figure 10.41: Cross-correlation coefficient maps along the axial distance for hot-wire transverse positions corresponding to the jet axis.

The cross-correlation coefficient maps along the axial distance for all the flat-plate radial distances and for the hot-wire transverse position  $\zeta$  are shown in figure 10.42. The correlation close to the nozzle exhaust decreases for increasing  $H$  and becomes negligible for the largest plate distance, i.e.  $H/D = 2.5$ . This behaviour is ascribed to the relation between  $H$  and the axial position where the jet impacts the surface. Specifically, non-zero correlation values are found for axial positions close or beyond the impact point (for more details see §10.4.1). For such positions positive-negative bump shape correlations are found, whereas as the flow develops over the surface a positive spike-shape correlation clearly appears.

The effect of  $H/D$  on the correlation is shown in figure 10.43, which shows the cross-correlation coefficient at the HW axial distances  $x/D = 4, 9, 16, 23$  and for the hot-wire transverse location on the jet axis. It can be seen that the evolution along the stream-wise direction described above is not significantly affected by the radial distance  $H$ . A stronger effect is detected considering the correlation for the hot-wire position closest to the flat-plate. Figure 10.44 shows the cross-correlation coefficient for the hot-wire position  $\zeta$  at the axial positions  $x/D = 2, 11, 17, 24$ . It is observed that both the correlation amplitude and shape change as the axial distance increases. As reported above, zero-correlation values are found for small axial positions where the jet had not yet impinged on the surface. Moving away from the impact point, a positive spike-shape is detected. It is interesting to point out that for  $H/D \leq 1.5$ , a positive-negative bump shape appears again for large axial distances.

### 10.5.2 Cross-spectra

The cross-statistics between the velocity and wall pressure signals has been analysed in the frequency domain as well. The cross-spectrum between the axial velocity and the wall pressure signals is defined as the Fourier transform of the cross-correlation function, as formalized in the following:

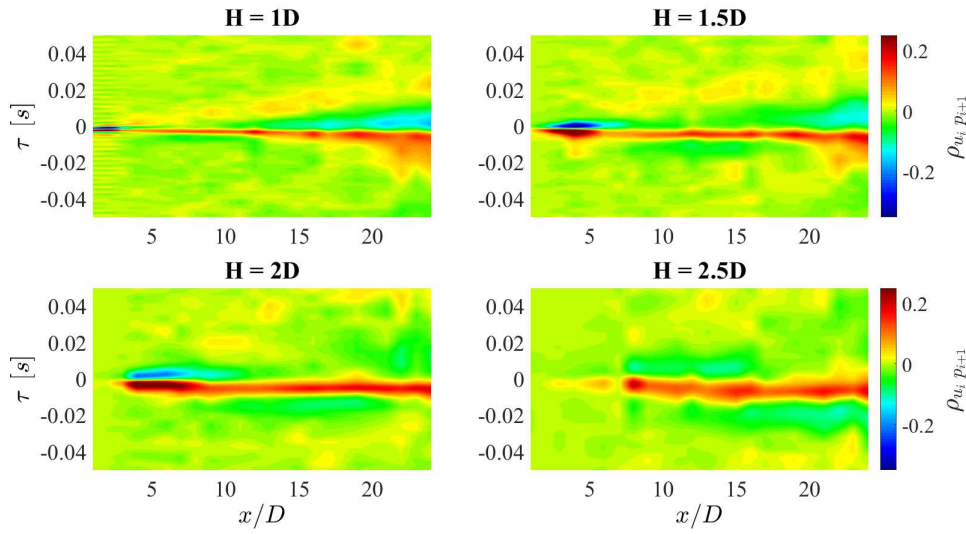


Figure 10.42: Cross-correlation coefficient maps along the axial distance for hot-wire transverse position  $\zeta$ .

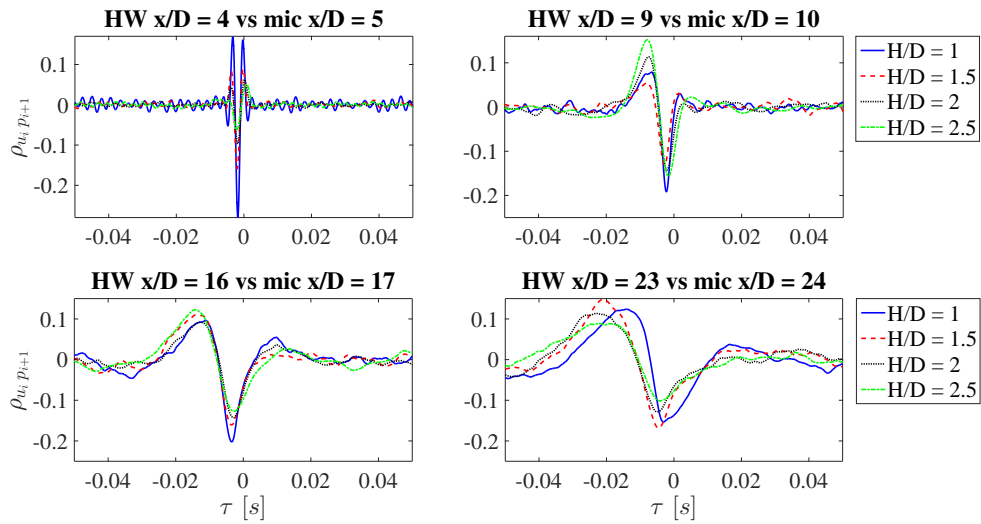


Figure 10.43: Effect of the plate radial distance on the cross-correlation coefficient between velocity and wall pressure signals for the hot-wire transverse positions on the jet axis.



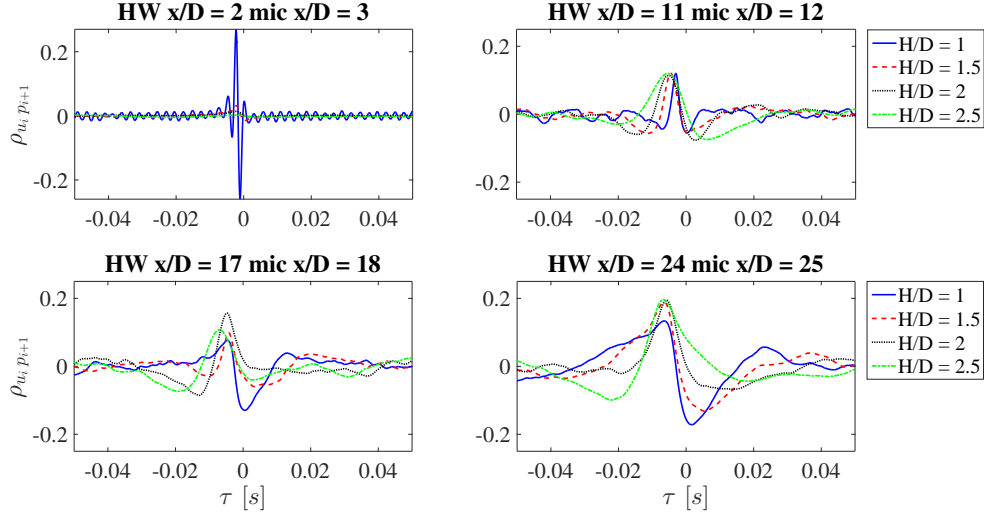


Figure 10.44: Effect of the plate radial distance on the cross-correlation coefficient between velocity and wall pressure signals for the hot-wire transverse positions corresponding to  $\zeta$ .

$$\Phi_{u_i p_{i+1}}(\xi, f) = \int_{-\infty}^{+\infty} R_{u_i p_{i+1}}(\xi, \tau) e^{-j2\pi f\tau} d\tau \quad (10.15)$$

In the present approach the cross-spectrum was computed using the Welch's method with a Hamming window and an overlap of 50%. A dimensionless Cross-Power Spectral Density (*CPSD*) was defined according to the following formula:

$$CPSD = \frac{|\Phi_{u_i p_{i+1}}| \Delta f_{ref}}{U_j p_{ref}} \quad (10.16)$$

where  $|\Phi_{u_i p_{i+1}}|$  is the modulus of the cross-spectrum.

Figure 10.45 shows the dimensionless *CPSD* map along the  $z$ -axis for HW axial positions  $x/D = 3, 7, 13, 21$ . Since the dependency upon  $H$  is weak, only the case  $H/D = 1$  is presented. The frequency is expressed in terms of Strouhal number based on  $D$  and  $U_j$  at the nozzle exhaust. It is observed that for small axial distances within the potential core region the highest values of the cross-spectrum are found for transverse locations corresponding to the mixing layers of the jet. Furthermore, a tonal component for a Strouhal number  $\approx 0.47$  is clearly detected for all the transverse positions, such signature being related to the Kelvin-Helmholtz instability mode and in agreement with the trend shown in the cross-correlations. As the axial distance increases, the cross-spectral energy rises and spreads over a wider range of transverse positions, the maximum level being moved to lower frequencies and towards negative  $z$ -coordinates, i.e. in the jet region closer to the surface.

The effect of  $H$  on the cross-spectra is addressed in figure 10.46. The cross-spectra are computed at the jet axis positions for hot-wire axial positions  $x/D = 3, 9, 17, 22$ . It is observed that the energy content decreases as  $H$  increases, the amplitude discrepancy being more significant for small stream-wise locations. As the axial distance increases the cross-spectra tend to collapse. It is interesting to underline that for stream-wise positions within the potential core, the energy peak associated with the

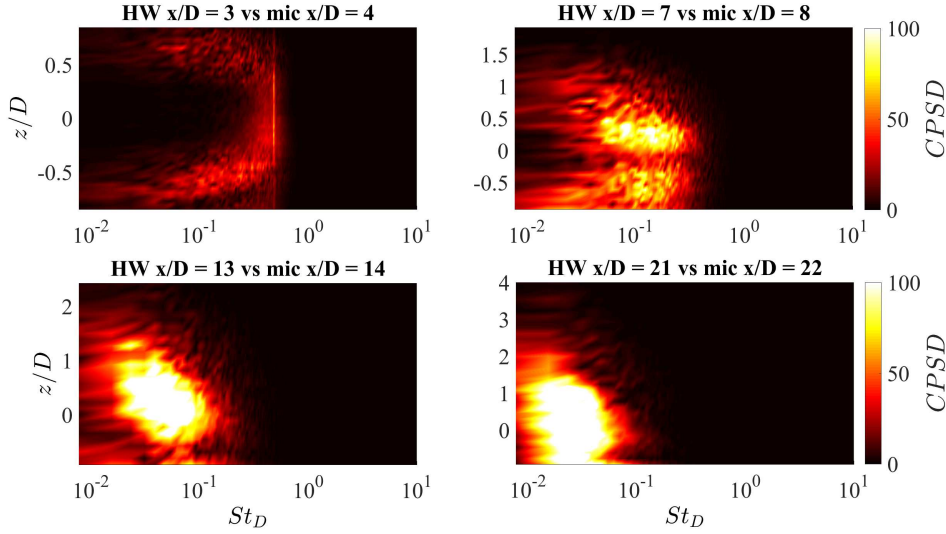


Figure 10.45: Dimensionless Cross-Power Spectral Density maps along the  $z$ -direction for  $H/D = 1$  at different axial positions.

Kelvin-Helmholtz instability is clearly detected, this signature being more significant as  $H$  increases.

An overview of the stream-wise evolution of the cross-spectral energy for velocity signals at transverse positions corresponding to the jet axis is reported in figure 10.47, for all  $H/D$ . The amplitude of the cross-spectra increases for decreasing  $H$  and the maximum cross-spectral energy moves from high to low frequencies as the axial distance increases. Such a trend is related to the development of larger turbulent eddies moving downstream in the jet plume, in agreement with the results shown up to now.

## 10.6 Cross-statistics between acceleration and wall pressure fluctuations

The cross-statistics between the wall pressure fluctuations and the acceleration (computed as defined in §10.1.2.1) was investigated. Cross-correlations and cross-spectra between acceleration and wall pressure signals are presented addressing the effect of the plate distance from the jet as well as of the positions of the hot-wire and microphones. As reported for the velocity, the acceleration/pressure cross-statistics is achieved considering the microphone in the  $i^{th}$  axial position and the hot-wire probe in the  $(i - 1)^{th}$  axial position.

### 10.6.1 Cross-correlations

Likewise for the velocity, the cross-correlation between acceleration and wall pressure signals is computed according to the following formula:

$$R_{a_i p_{i+1}}(\xi, \tau) = \langle a(x, t) p(x + \xi, t + \tau) \rangle \quad (10.17)$$

The cross-correlation coefficient  $\rho_{a_i p_{i+1}}$  is obtained normalizing the cross-correlation by the product between the standard deviations of the acceleration and wall pressure

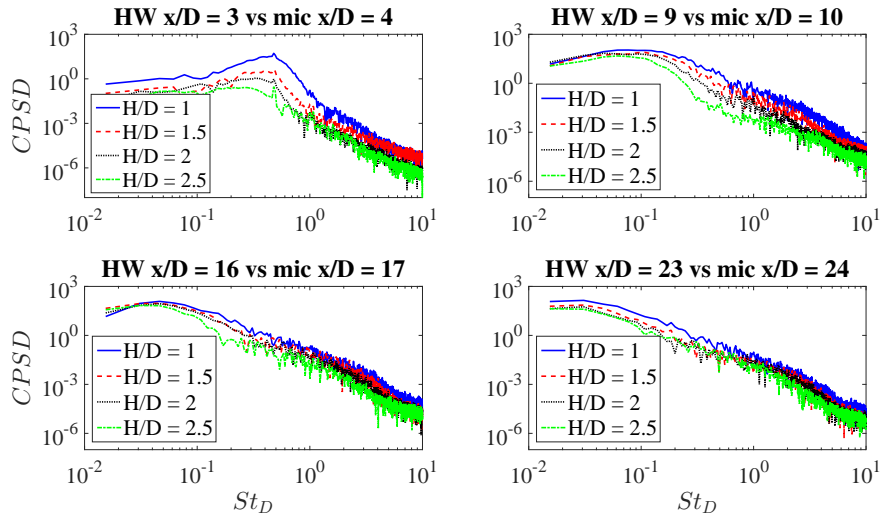


Figure 10.46: Effect of the plate radial distance from the jet on the Cross-Power Spectral Density between consecutive velocity and wall pressure signals at axial positions.

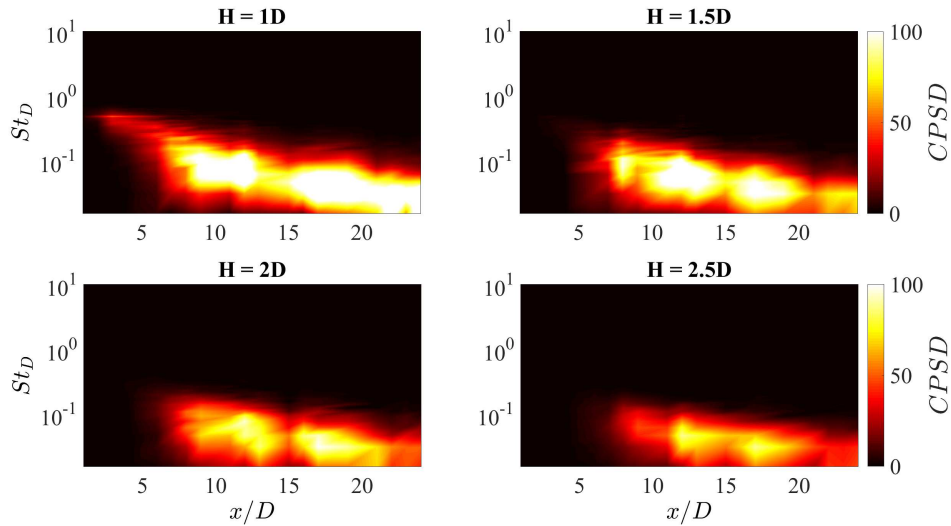


Figure 10.47: Dimensionless Cross-Power Spectral Density maps along the  $x$ -axis for hot-wire transverse positions corresponding to the jet axis.

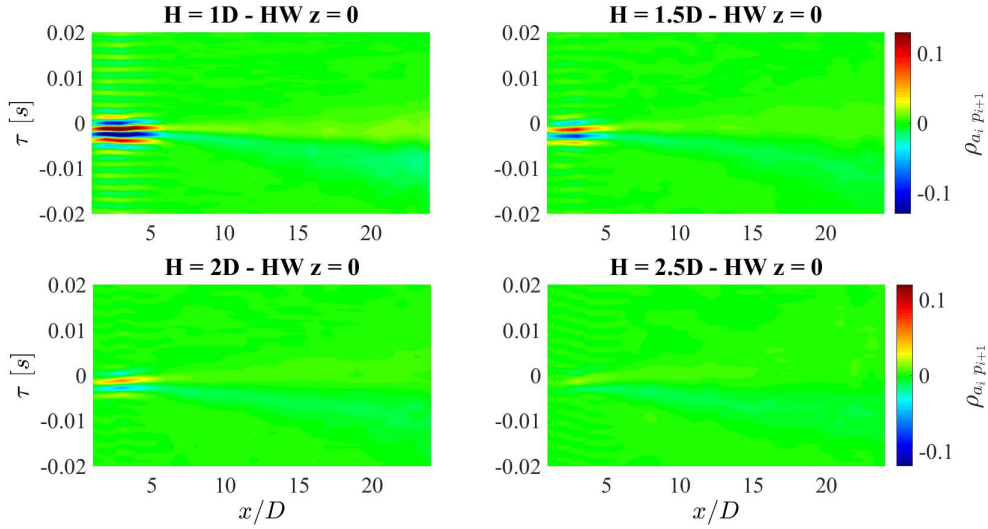


Figure 10.48: Stream-wise evolution of the cross-correlation coefficient between acceleration and wall pressure signals at the HW transverse position on the nozzle axis for all the jet-plate configurations.

signals.

Figure 10.48 shows the contour map of the stream-wise evolution of the cross-correlation coefficient between acceleration and wall pressure signals along the nozzle axis for all the jet-plate configurations. It is observed that significant correlation values were found only for axial positions within the potential core, the correlation level being negligible for stream-wise locations further downstream in the jet plume. The correlation exhibits an oscillatory shape typical of the wavepacket signature reported by Cavalieri et al. (2011), such a behaviour being ascribed to the Kelvin-Helmholtz instability. It is interesting to point out that the cross-correlation coefficient amplitude decreases for further radial distances of the flat-plate from the jet.

The axial evolution of the cross-correlation coefficient between wall pressure and acceleration signals at the HW transverse position  $\zeta$  for all the radial distances of the surface from the jet is shown in figure 10.49. It is noted that both the correlation shape and amplitude are strongly dependent on the jet-plate configurations and the stream-wise region of the jet considered, the larger correlation values being found for increasing axial distances as the flat-plate was moved away from the jet. For  $H/D = 1$  a narrow oscillatory correlation shape was detected immediately downstream the nozzle exhaust. For further jet-surface distances the oscillations reduce and a dominant negative drop appears. For the largest separation distance between the jet and the plate a weaker positive-negative bump-shape correlation was found downstream the potential core end.

Based on the outcome reported above, the evolution along the  $z$ -direction of the cross-correlation coefficient between acceleration and wall pressure signals for different HW axial distances and different jet-plate configurations is shown in figure 10.50. The stream-wise locations  $x/D = 2, 3, 6$ , and  $7$  were considered for the flat-plate distances  $H/D = 1, 1.5, 2, 2.5$ , respectively. For the closest jet-surface configuration, significant correlation levels were found for transverse positions in the proximity of the nozzle axis and close to the plate. As already found for the velocity/pressure correlation, the oscillations in the correlation exhibited a phase shift between the central and the outer  $z$ -locations of the jet. The same trend along the cross-wise direction can be found for

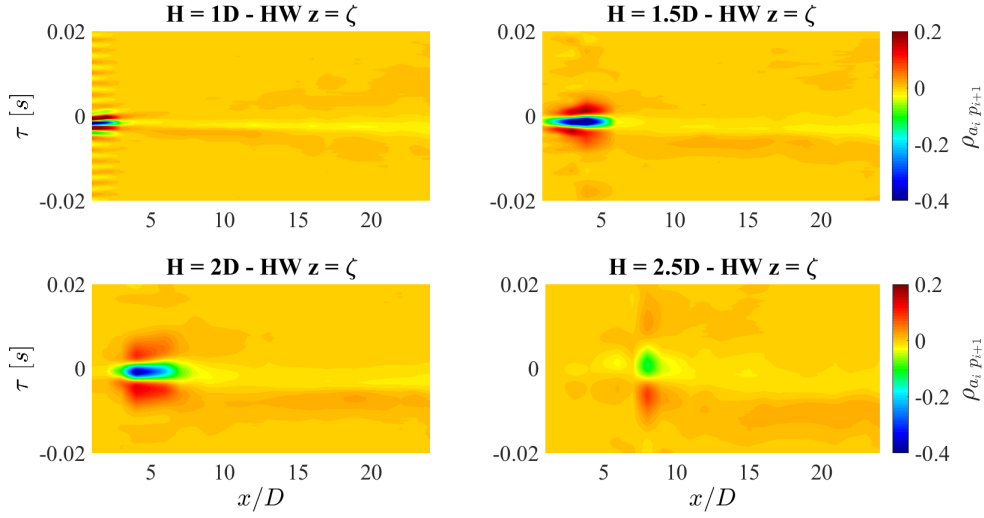


Figure 10.49: Stream-wise evolution of the cross-correlation coefficient between acceleration and wall pressure signals at the HW transverse position closest to the flat-plate for all the jet-surface configurations.

$H/D = 1.5$ , the correlation shape for  $z = \zeta$  being characterised by a dominant negative peak. For  $H/D \geq 2$  negligible correlation levels were found in the centreline of the jet, whereas a significant positive-negative bump shape correlation was observed for transverse positions close to the flat-plate.

### 10.6.2 Cross-spectra

Likewise for the velocity, the cross-spectrum between the acceleration and the wall pressure signals is defined as the Fourier transform of the cross-correlation function, as formalized in the following:

$$\Phi_{a_i p_{i+1}}(\xi, f) = \int_{-\infty}^{+\infty} R_{a_i p_{i+1}}(\xi, \tau) e^{-j2\pi f \tau} d\tau \quad (10.18)$$

A dimensionless cross-power spectral density between acceleration and pressure signals was defined according to the following formula:

$$CPSD_a = \frac{|\Phi_{a_i p_{i+1}}| \Delta f_{ref}}{(U_j^2/D) p_{ref}} \quad (10.19)$$

where  $|\Phi_{a_i p_{i+1}}|$  is the modulus of the cross-spectrum.

Figure 10.51 shows the cross-wise evolution of the cross-spectrum amplitude for the HW axial distances  $x/D = 3, 7, 13, 21$ . Only the results for the jet-plate configuration  $H/D = 1$  were here reported, the trend described being independent of the radial distance of the surface from the jet. It is observed that the spectral energy is mainly concentrated in the mixing layers of the jet for small axial distances, where a strong energy peak associated with the Kelvin-Helmholtz instability is found for all the transverse positions. As the axial distance increases, the energy content spreads on a wider range of  $z$ -locations. It is interesting to point out that, unlike the cross-spectra between velocity and wall pressure signals, the higher energy content is found for

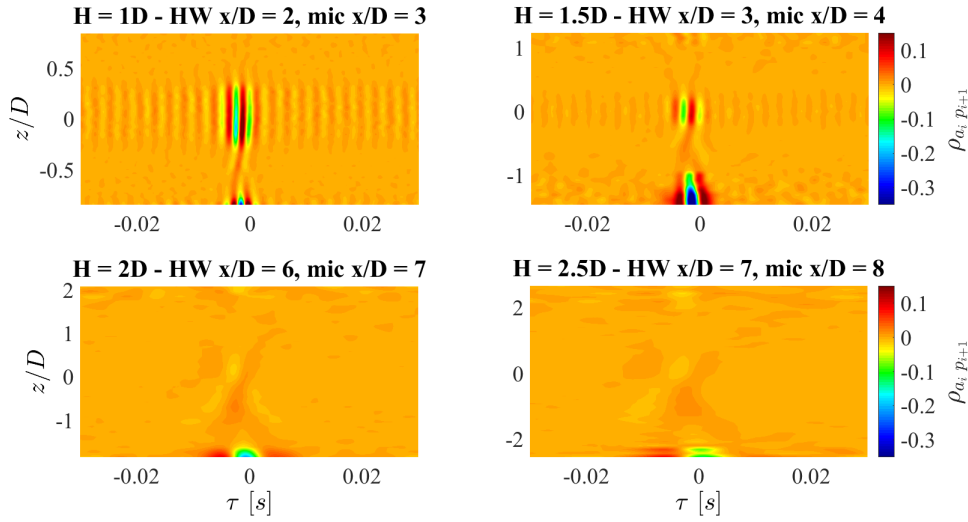


Figure 10.50: Cross-wise evolution of the cross-correlation coefficient between acceleration and wall pressure signals at different HW axial positions function of the jet-surface radial distance.

stream-wise positions within the potential core region, this outcome representing an expected behaviour. Indeed, as underlined in §10.1.2, the time derivative operation performed to compute the acceleration implies an enhancement of the energy content at the middle-high frequency range where the Kelvin-Helmholtz instability is dominant and represents the most efficient mode of the jet in terms of noise emissions (Cavalieri et al., 2013).

The trend described above can be clearly seen in figure 10.52, which shows the axial evolution of the cross-spectra along the nozzle axis for all the jet-plate configurations. It is evident that the spectral energy is higher for small axial distances with a significant peak for  $St_D \approx 0.47$ . Furthermore it has to be underlined that the cross-spectrum amplitude decreases for further radial distances of the plate from the jet.

## 10.7 Wavelet analysis

According to the conditioning procedure described in §9, the auto- and cross-conditioned ensemble averages of velocity/acceleration and wall pressure signals are here presented. The averaged signatures are reported in dimensionless form dividing the amplitude by the standard deviation of the original signal.

### 10.7.1 Velocity auto-conditioning

The stream-wise evolution along the nozzle axis of the averaged auto-conditioned velocity signatures is shown in figure 10.53 for all  $H$ . The signatures change significantly with the axial position of the hot-wire. In the potential core region, where the Kelvin-Helmholtz instability is dominant, an oscillating shape is detected. For stream-wise positions immediately downstream the potential core, a negative peak-shape related to the transitional behaviour of the jet flow is detected (Camussi and Guj, 1999). Further downstream in the jet plume a positive spike-shape signature associated with

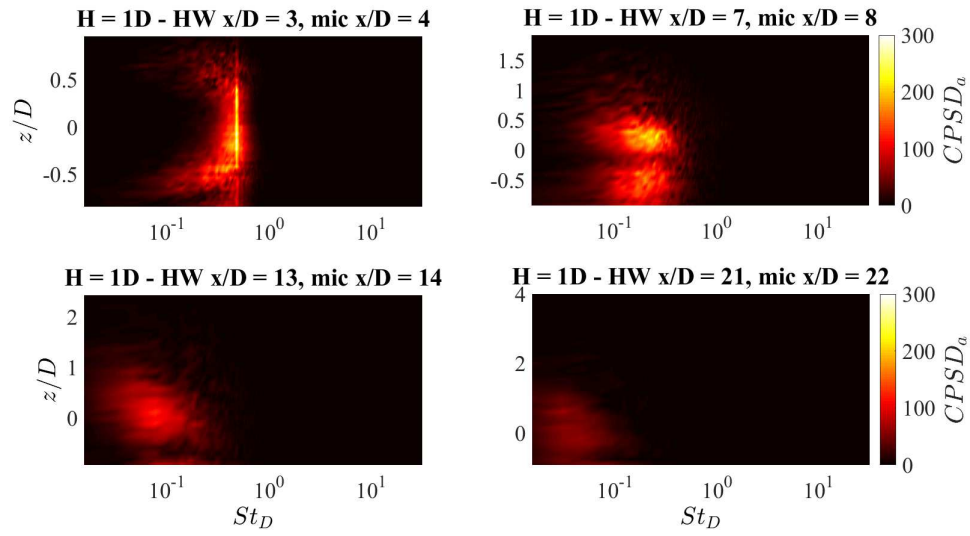


Figure 10.51: Cross-wise evolution of the dimensionless cross-power spectral density between acceleration and wall pressure signals at different axial distances for the jet-plate distance  $H/D = 1$ .

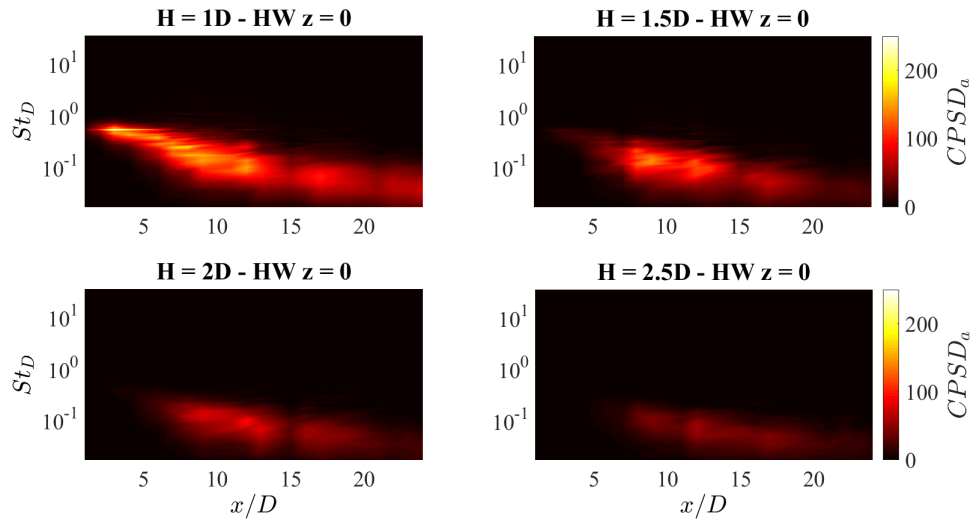


Figure 10.52: Stream-wise evolution of the dimensionless cross-power spectral density between acceleration and wall pressure signals along the nozzle axis for all the jet-plate distances.



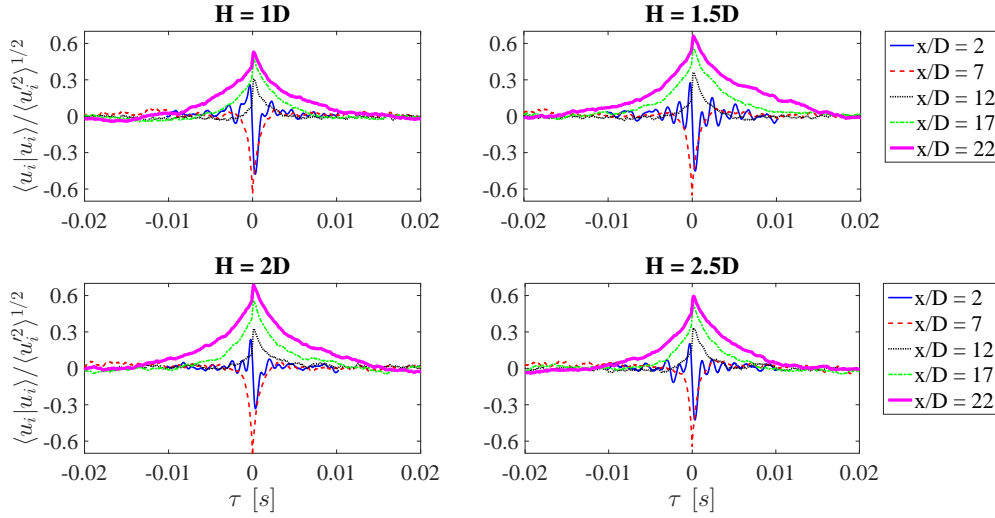


Figure 10.53: Axial evolution of the auto-conditioned velocity signatures along the nozzle axis for all the jet-plate configurations.

coherent ring-like vortices is observed (Camussi and Guj, 1997). The contour maps along the stream-wise direction of the velocity signatures on the nozzle axis for all  $H$  are represented in figure 10.54. It is observed that in the proximity of the potential core end, i.e. for  $x/D \approx 6$  (see §10.1), the oscillating shape of the velocity signature is significantly enhanced. It is interesting to underline that the flow signatures evolution seems not to be modified by the presence of the flat-plate since the results are very similar to the ones detected in free-jet conditions in the present experimental tests campaign and to those obtained by Camussi and Guj (1999) in analogous analyses carried out in another free-jet case.

The same results are obtained for hot-wire locations along the jet axis, and are not presented here for the sake of brevity.

Different results are found for the HW transverse location closest to the flat-plate, i.e. the position  $\zeta$ . Figure 10.55 shows the contour maps of the velocity signatures along the  $x$ -axis for all  $H$ . Positive spike-shape signatures emerge for all the surface radial distances only downstream the jet impact point on the plate. It can be observed that both the amplitude and the characteristic time-scale of the educed structures are larger in the proximity of the jet impact point.

The effect of the radial distance of the flat-plate from the jet is addressed in figure 10.56, which shows the velocity signatures for the hot-wire position  $\zeta$  at the axial positions  $x/D = 16, 18, 21, 23$ . The stream-wise positions were chosen so that the jet had already impacted the surface. It is observed that the amplitude of the velocity ensemble averages increases for increasing  $H$ . Furthermore the characteristic time-scale of the signatures enlarges as the jet-plate distance increases, thus implying that the associated flow structures are characterized by a larger scale. Hence the flat-plate has the effect to induce the large-scale structures break-down. The trend just described can explain the reduction of the turbulence intensity observed in figure 10.17 for low  $H$  values (refer to §10.2) and is in agreement with results shown up to now (see e.g. §10.4.1.2 and specifically figure 10.28).



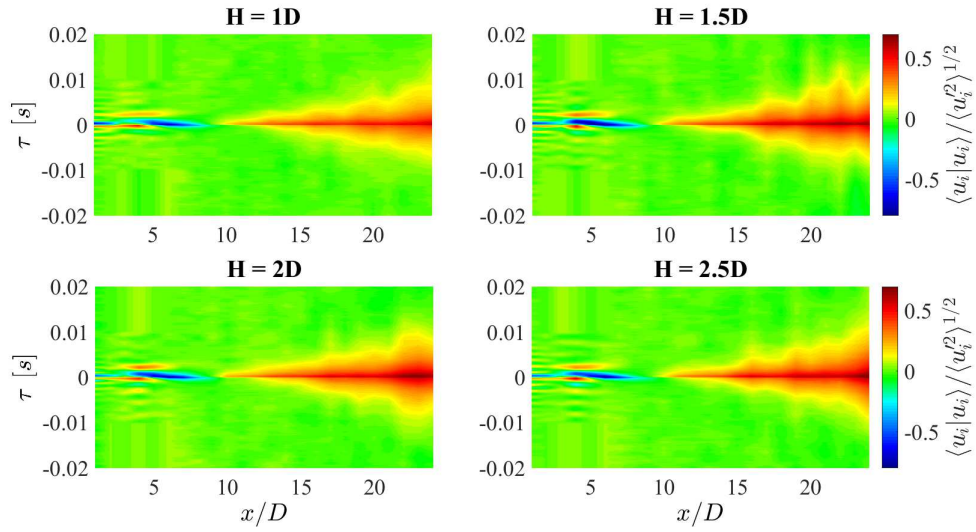


Figure 10.54: Contour maps of the auto-conditioned velocity signatures along the nozzle axis for all the jet-plate configurations.

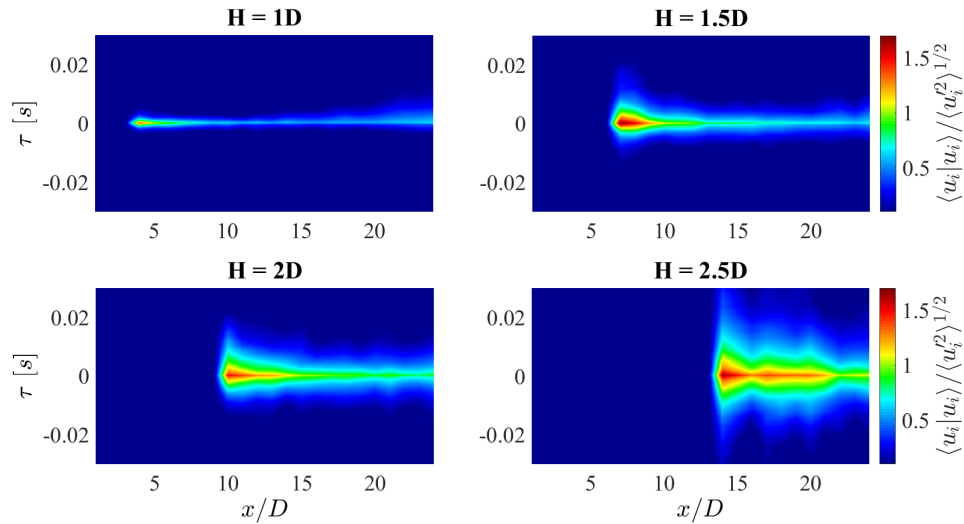


Figure 10.55: Contour maps of the auto-conditioned velocity signatures along the stream-wise direction at the hot-wire transverse position  $\zeta$  for all the jet-plate configurations.

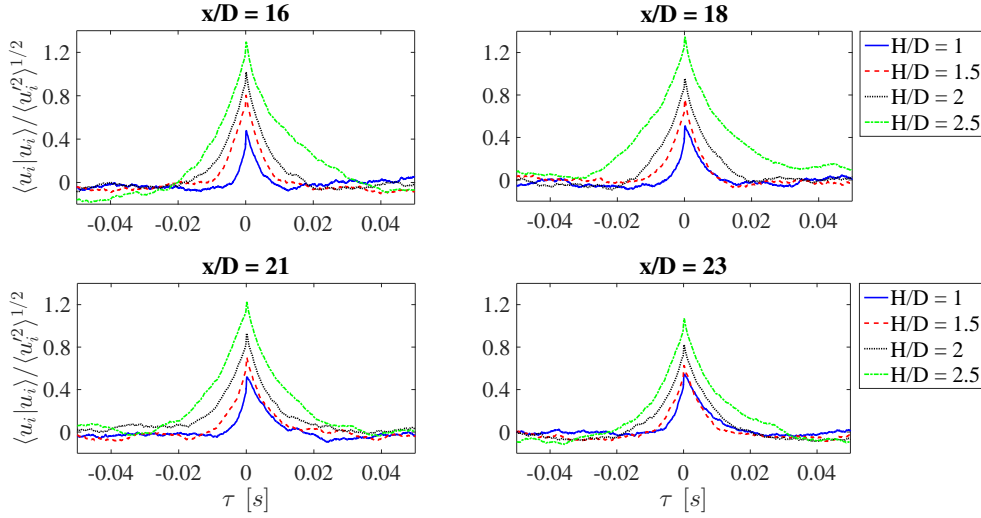


Figure 10.56: Auto-conditioned velocity signatures at the hot-wire transverse position  $\zeta$  for all the flat-plate radial distances.

#### 10.7.1.1 Scaling criterion for velocity signatures

A scaling criterion was derived for the auto-conditioned velocity signatures at the hot-wire transverse position  $\zeta$ . The proposed scaling criterion is based on the external aerodynamic variables  $U_c$  and  $U_j$  and the main geometrical length-scale  $H$ . The convection velocity  $U_c$  was estimated from the time-delay of the cross-correlation peak between consecutive wall pressure signals in the stream-wise direction, that depends on  $H/D$  as reported in §10.4.1.2 (see figure 10.29). The velocity signatures are normalized multiplying by the ratio  $U_c/U_j$  and dividing by the local standard deviation of the velocity signal. Conversely, the characteristic time-scale to be adopted is related to the time occurring to a fluid particle convected by the mean flow to reach the flat-plate. Such a time-scale is estimated, by the ratio  $H/U_c$ . Accordingly, the adopted scaling is defined as follows:

$$\langle u_i | u_i \rangle^* = \frac{\langle u_i | u_i \rangle}{\langle u_i'^2 \rangle^{1/2}} \frac{U_c}{U_j} \quad (10.20)$$

$$\tau^* = \tau \frac{U_c}{H} \quad (10.21)$$

Figure 10.57 shows the scaled velocity signatures for all the jet-plate configurations. For the sake of brevity the results concerning the axial positions  $x/D = 18$  and  $x/D = 22$  are shown. A good collapse is observed for all  $H$  in terms of both amplitude and time-scale, although a small discrepancy is detected for the closest flat-plate position ( $H/D = 1$ ). It has to be pointed out that the same scaling parameters have been successfully used to scale the wall pressure auto-spectra (see §10.4.3.1). Such a behaviour implies a significant result: the aerodynamic and geometrical variables adopted to scale both the velocity signatures and the spectral content of the wall pressure fluctuations are representative of the parameters governing the jet-plate interaction phenomena.

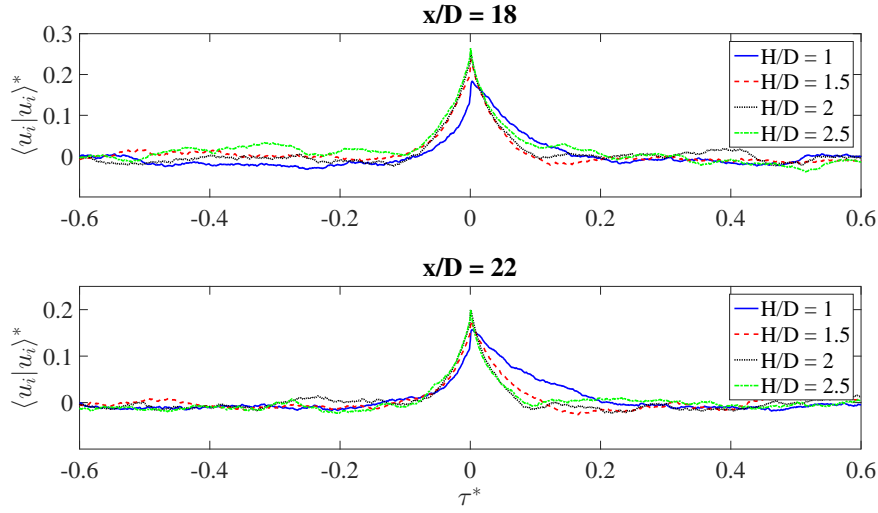


Figure 10.57: Scaled auto-conditioned velocity signatures at the hot-wire transverse position  $\zeta$  for all the jet-plate distances.

### 10.7.2 Wall pressure auto-conditioning

The auto-conditioned wall pressure signatures are presented in the following. For what concerns the wall pressure field, as pointed out by Jayasundera et al. (1996), two organized flow motions can be associated with pressure events over the wall surface:

- an ejection motion associated with positive pressure events;
- a sweep motion associated with negative pressure events.

Figure 10.58 shows the contour maps of the wall pressure signatures along the stream-wise direction for all the jet-plate distances. It is observed that no relevant signatures can be appreciated for axial positions close to the nozzle exhaust. For small stream-wise positions a positive-negative bump related to a burst-sweep event (Dhanak et al., 1997) is detected, except for the furthest plate radial distance. As the axial distance increases and a TBL is established, a negative pressure drop associated with sweep motion is observed, as reported by Johansson et al. (1987) for an equilibrium TBL.

The effect of  $H$  on the educed structures is addressed in figure 10.59, which shows the pressure signatures at axial distances  $x/D = 5, 10, 13, 18$ . The ensemble averages obtained for the largest value of  $H$  are characterized by a larger time-scale, such a trend being in agreement with the results presented in the previous sections. For small axial distances the signature amplitude is larger for lower  $H$ , whereas an opposite trend is detected further downstream in the jet plume. It is interesting to underline that the appearance of sweep or burst-sweep events is strongly related to the plate distance from the jet and the stream-wise position considered. Such a behaviour is due to the relation between the jet-plate separation and the axial distance for which the jet impinges on the plate. Specifically ejection events were detected for low stream-wise positions and small  $H/D$  (1, 1.5), whereas sweep motions are found for larger jet-plate and axial distances.

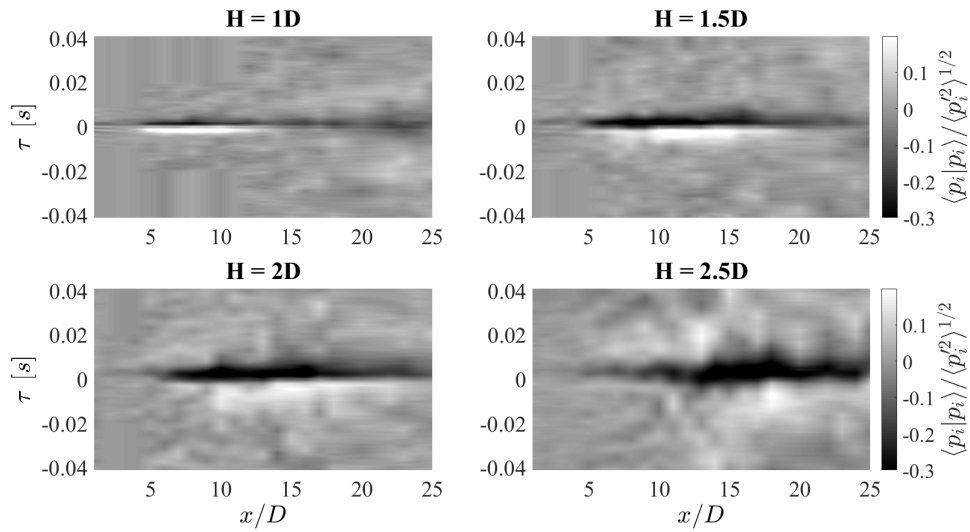


Figure 10.58: Contour maps along the stream-wise direction of the wall pressure signatures derived from the auto-conditioning technique for all the jet-plate distances.

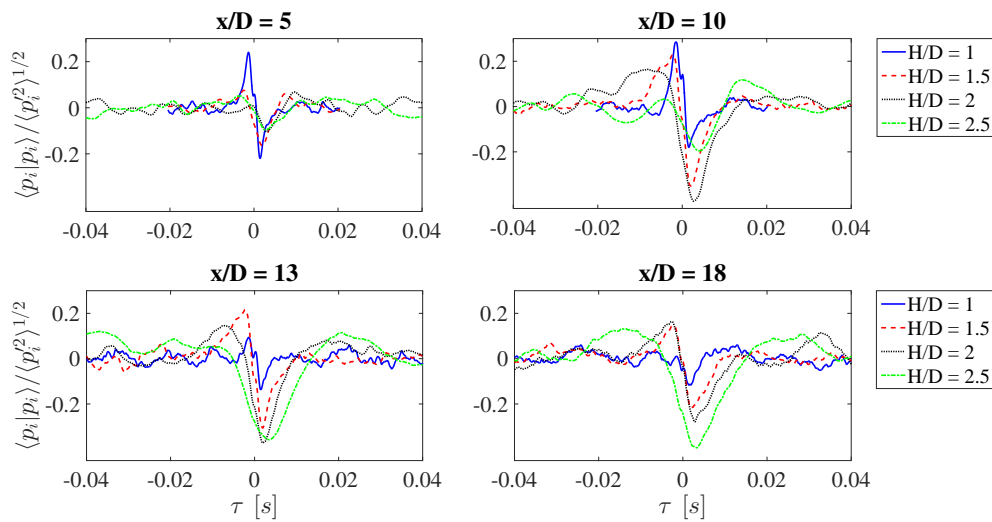


Figure 10.59: Effect of the jet-plate distance on the auto-conditioned wall pressure signatures at different axial positions.

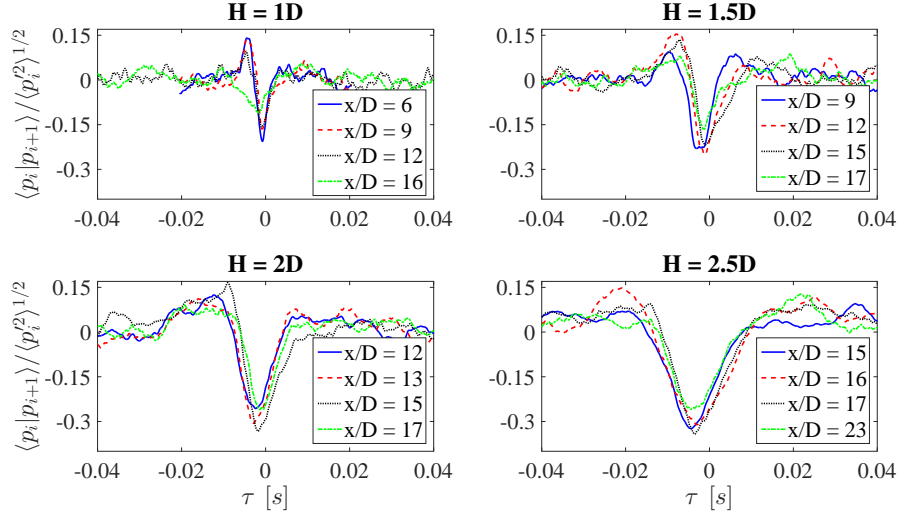


Figure 10.60: Stream-wise evolution of the cross-conditioned wall pressure signatures for all the jet-plate configurations at different axial distances.

### 10.7.3 Pressure/pressure cross-conditioning

The cross-conditioning procedure was applied using as triggering signal the wall pressure signal and as conditioned signal the wall pressure time series of an adjacent microphone. For the sake of brevity, the results concerning the cross-conditioned wall pressure signatures are not extensively discussed, the shape and the axial evolution of the educed structures being similar to the ones obtained from the auto-conditioning procedure illustrated above. Figure 10.60 shows the stream-wise evolution of the cross-conditioned wall pressure signatures for all  $H$ . Positive-negative bumps are extracted for small axial distances and for  $H/D \leq 1.5$ , confirming the results discussed above. Negative drop signatures related to sweep motion are detected for larger axial positions and for  $H/D > 1.5$ , the shape being in agreement with the results obtained by Camussi et al. (2008) for a fully developed TBL. According to Guj et al. (2003), taking into account the separation distance between the microphones and the time-delay of the signature, a phase velocity can be computed. The velocity values obtained are a fraction of the jet velocity  $U_j$ , thus implying that the educed signatures are associated with hydrodynamic turbulent structures convected by the mean flow (Camussi et al., 2008).

### 10.7.4 Velocity/pressure cross-conditioning

The velocity conditioned on the wall pressure is presented in the following. Velocity signatures are derived for consecutive stream-wise positions of the hot-wire probe and microphone, according to the scheme depicted in figure 10.38. Figure 10.61 shows the contour maps along the  $z$ -axis of the velocity signatures obtained from the cross-conditioning technique for all the jet-plate distances. The HW probe is placed at  $x/D = 24$ . Non-zero velocity signatures with a positive spike shape ascribed to a ring-like vortex convected by the mean flow were obtained only for hot-wire positions close to the flat-plate. As the probe moves away from the surface, signatures are no longer detected.

Figure 10.62 shows the contour maps of the cross-conditioned velocity signatures

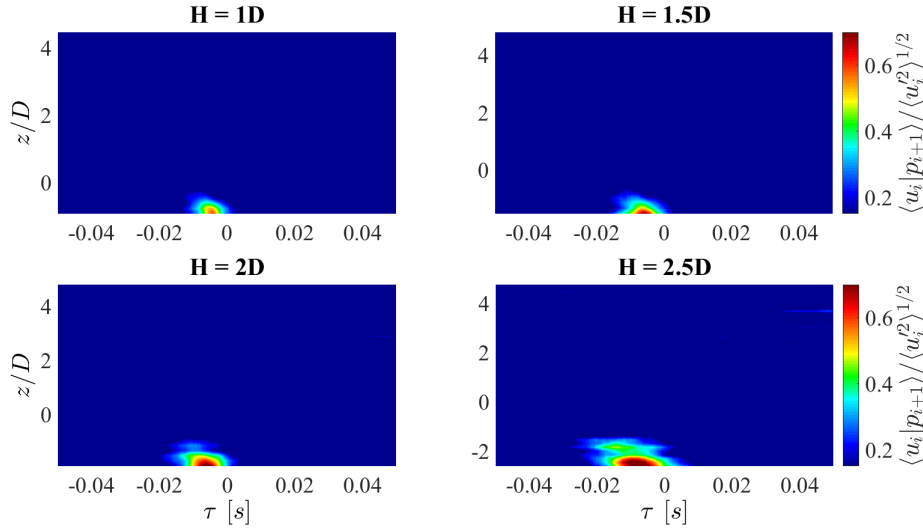


Figure 10.61: Effect of the HW transverse position on the cross-conditioned velocity signatures at the axial location  $x/D = 24$  for all the jet-plate configurations.

along the stream-wise direction at the transverse location  $\zeta$  for all the jet-plate configurations. Appreciable velocity signatures were obtained only for axial positions beyond the impact point of the jet on the surface, their amplitude being larger for increasing stream-wise positions.

It has to be pointed out that the signatures educed by the conditional averaging procedure are not dependent on the wavelet scale of the wall pressure signal considered. This result can be clearly observed in figure 10.63, which shows the contour maps of the cross-conditioned velocity signatures as a function of the pseudo-frequencies, expressed in terms of Strouhal number. The velocity signals are measured from the hot-wire probe placed at  $x/D = 24$ . The shape of the ensemble averages is independent of the wavelet scale (or frequency) considered, thus implying that the educed flow structures excite the wall pressure field at all scales.

The effect of the radial distance  $H$  is addressed in figure 10.64, where the HW axial positions considered are  $x/D = 17, 19, 22, 24$ . It can be observed that the amplitude of the signatures is generally larger for increasing  $H$ . Furthermore the time-scale of the educed structures is larger as the flat-plate is moved away from the jet. Such a behaviour is in agreement with the outcome obtained by the auto-conditioning approach and it represents a further proof that the size of the flow structures becomes smaller as the flat-plate gets closer to the jet. It is interesting to underline that the time-delays of the signature peaks are strongly dependent on the jet-plate distance. A propagation velocity based on the time-lag of the signature peak and the distance between the hot-wire and microphone probes was computed for all  $H$  and for axial positions beyond the impact point. Figure 10.65 shows the stream-wise evolution of the propagation velocity normalized by the jet velocity at the nozzle exhaust. The propagation velocity is a fraction of the jet velocity for all the flat-plate distances considered. Such a result confirms that the flow structures responsible for the most energetic wall pressure events can be related to turbulent eddies convected by the mean flow. As expected, the velocity decreases as the axial distance increases, although for the plate positions  $H/D = 2$  and 2.5 a quasi-constant trend along the stream-wise direction is found. It is interesting to observe that the phase velocity decreases as the flat-plate distance from the jet increases.

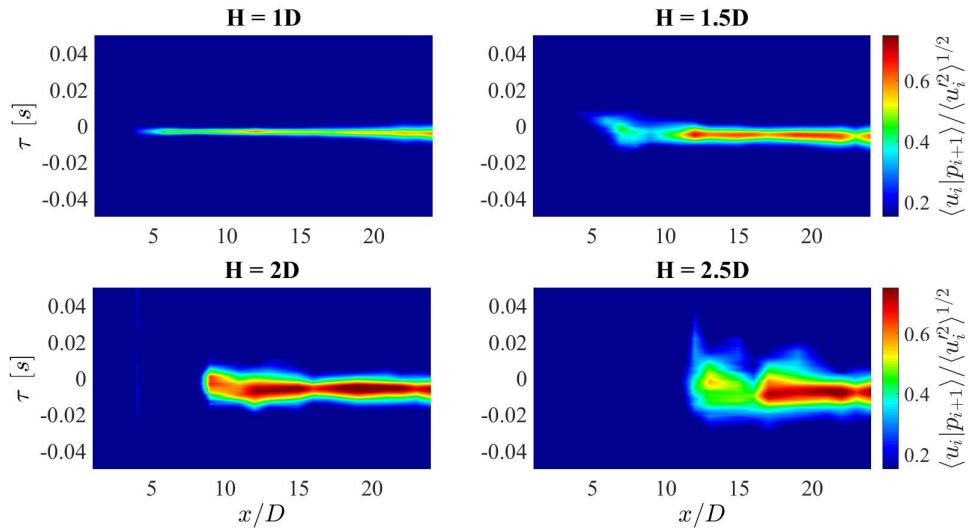


Figure 10.62: Contour maps of the cross-conditioned velocity signatures along the stream-wise direction at the hot-wire transverse location  $\zeta$  for all the jet-plate configurations.

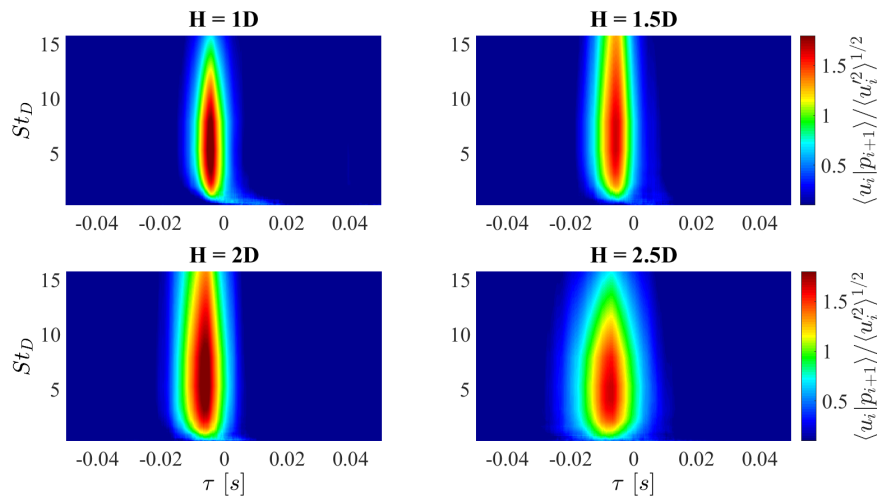


Figure 10.63: Contour maps of the cross-conditioned velocity signatures as a function of the dimensionless frequency/scale for all the jet-plate configurations. HW axial position  $x/D = 24$ , mic axial position  $x/D = 25$ .



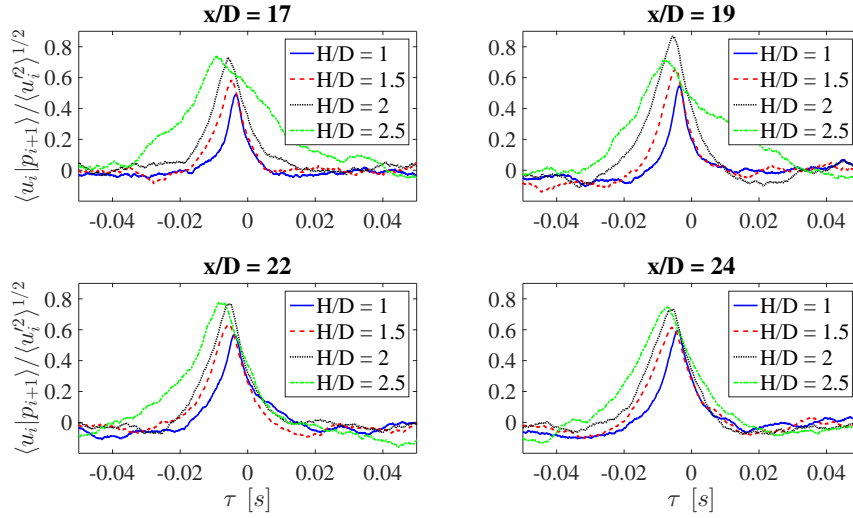


Figure 10.64: Effect of the jet-plate distance on the velocity signatures conditioned on wall pressure signals for different HW axial positions.

According to the results shown throughout the manuscript, such a behaviour is ascribed to the larger size of the educed turbulent structures for larger  $H/D$ .

#### 10.7.4.1 Implications for velocity signatures modelling

Figure 10.67 shows the shape of the educed flow structures for all the jet-plate configurations addressing the effect of the stream-wise separation between the probes. The velocity signal measured in  $\zeta$  and  $x/D = 21$  is conditioned on the pressure signals from the microphones placed in  $x/D = 22, 23, 24, 25$ , as depicted in figure 10.66. The time-shift associated with the signature peaks changes depending on the distance between the probes. Such a behaviour implies that the conditioning procedure adopted can provide information about the location of the extracted structures and track their spatial evolution. Furthermore, it is interesting to underline that the amplitude of the averaged signatures decreases as the distance between the hot-wire and the microphone increases. Nevertheless, a non-zero signature is detected also for the largest separation distance ( $4D$ ) between the probes. This result suggests that the flow structures responsible for the most energetic events in the wall pressure signals are represented by large vortices whose spatial coherence is significant in the stream-wise direction.

It has to be pointed out that the amplitude decrease of the educed signatures is coupled with an energy spread over the time, thus implying that the dissipation of the extracted flow structures is mainly due to diffusive effects. To further support such inference, some theoretical implications are briefly discussed. It has to be underlined that the argumentation reported in the following is exploited to verify in a qualitative way the experimental results illustrated above. The 1D Burgers' equation has been considered for the momentum equation:

$$\frac{\partial u}{\partial t} + u \frac{\partial u}{\partial x} = \nu \frac{\partial^2 u}{\partial x^2} \quad (10.22)$$

The solution of the Burgers' equation, performing a Fourier series expansion and neglecting the non-linear terms, can be written as follows:



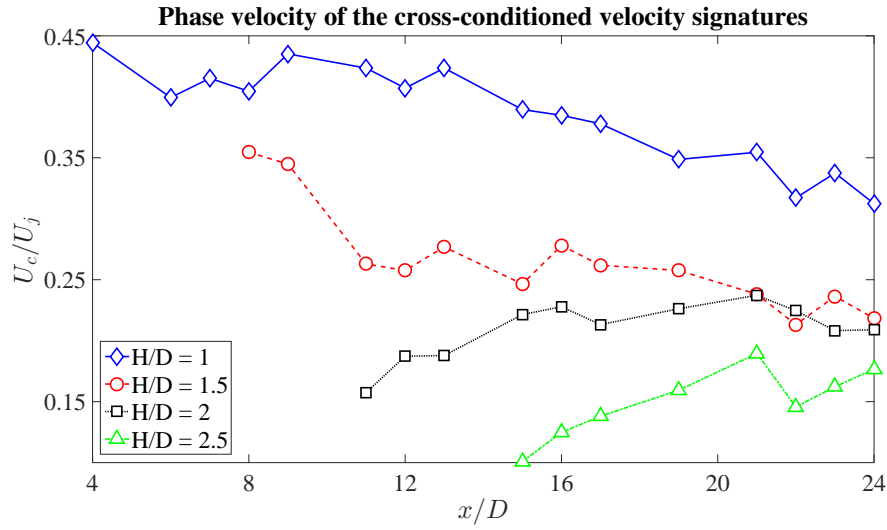


Figure 10.65: Axial evolution of the normalized convection velocity computed from the time-delay of the velocity signature peaks conditioned on the wall pressure events for all the jet-plate distances:  $\diamond$   $H/D = 1$ ,  $\circ$  to  $H/D = 1.5$ ,  $\square$  to  $H/D = 2$ ,  $\triangle$  to  $H/D = 2.5$ .

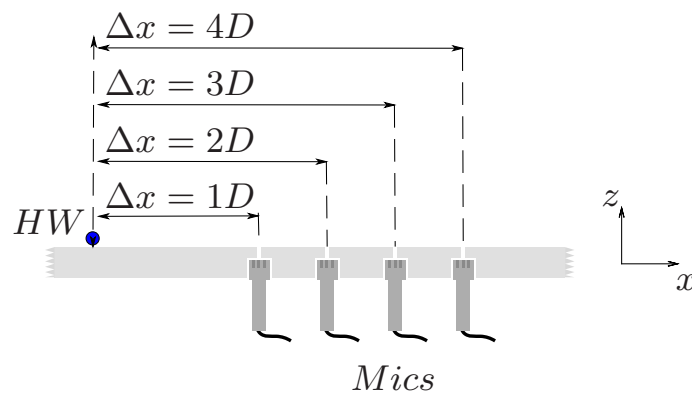


Figure 10.66: Scheme of the disposition of the HW and microphone array to assess the effect of the separation distance between the probes on the cross-conditioned velocity signatures.

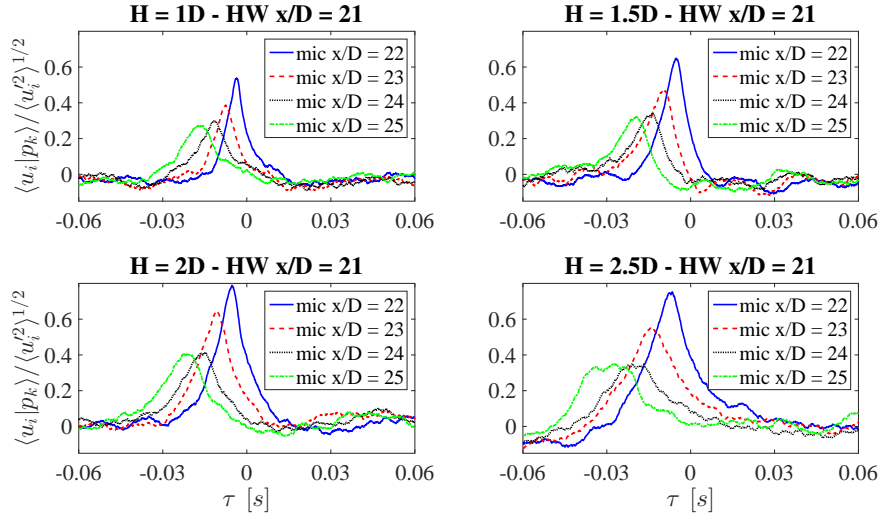


Figure 10.67: Effect of the stream-wise separation between the probes on the flow structures educed by the cross-conditioning technique for the HW probe in  $\zeta$  and  $x/D = 21$  and for all the jet-plate configurations.

$$u_n(t) = u_{n0} e^{-\nu k_n^2 t} \quad (10.23)$$

Where  $\nu$  is the kinematic viscosity,  $t$  is the time variable and  $u_n$  and  $k_n$  are respectively the  $n^{th}$  Fourier coefficient and wavenumber, whereas  $u_{n0}$  is a proper initial condition. This solution provides the time evolution of a given flow-scale structure, whose wavenumber is estimated from the associated wavelet scale<sup>6</sup>, in the case of dominant diffusive effects due to the viscosity. Hence, the above equation can be used to predict analytically the decay of the cross-conditioned velocity signature maxima using as initial condition the peak value corresponding to the smallest separation distance between the probes. It has to be pointed out that the signatures educed by the wavelet conditioning procedure are referred to the fluctuating axial velocity component. Thus, a turbulent viscosity  $\nu_t$  has to be adopted in (10.23), whose value was experimentally estimated according to the  $K - \epsilon$  model assumed for the RANS approach:

$$\nu_t = C_\nu \frac{K^2}{\epsilon} \quad (10.24)$$

$C_\nu$  is a constant usually equal to 0.09 (Chen and Kim, 1987).  $K$  and  $\epsilon$  are respectively the turbulent kinetic energy and the turbulent kinetic energy dissipation rate associated with the longitudinal velocity component, which are defined in the following:

$$K = \frac{1}{2} \langle u'^2 \rangle \quad (10.25)$$

$$\epsilon = \frac{(\langle u'^2 \rangle^{1/2})^3}{L} \quad (10.26)$$

<sup>6</sup>As reported in §2.2, the frequency  $f$  is inversely proportional to the wavelet scale  $s$ . By computing the angular frequency  $\omega = 2\pi f$ , the wavenumber can be easily obtained by the expression  $k = \omega/c$ , where  $c$  is the speed of sound.

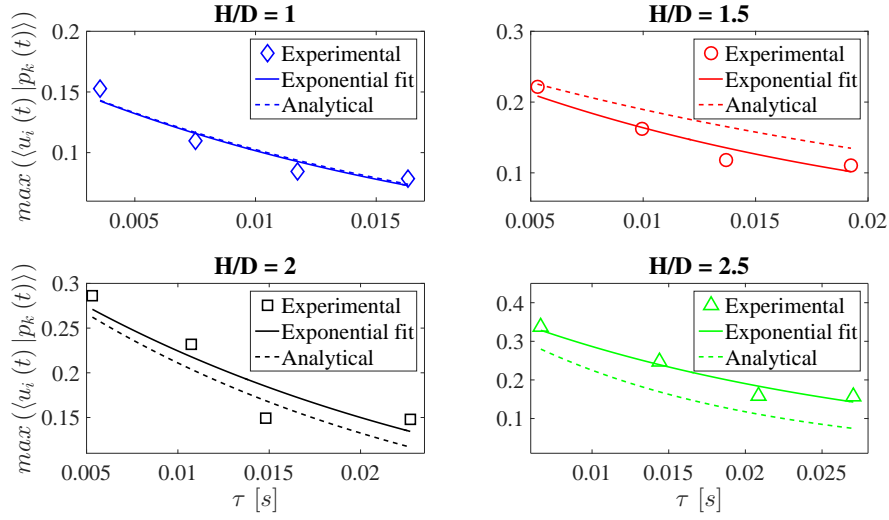


Figure 10.68: Time evolution of the cross-conditioned velocity signature peaks represented in figure 10.67 for all the jet-plate distances.

Where  $L$  is the integral length-scale<sup>7</sup>. Figure 10.68 shows the time evolution of the signature peaks and its exponential fit together with the decay predicted by the analytical approach discussed above. We observe that the exponential fit of the experimental data well reproduces the evolution along the time of the maxima of the educed signatures. Furthermore the analytical trend is quite close to the experimental one especially for close-coupled jet-surface configurations. As the plate is moved away from the jet, an increasing discrepancy between the experimental exponential fit and the predicted one is detected. This result appears to be reasonable, the viscosity effects being expected to be less significant as the flat-plate is moved away from the jet. Further analyses have to be carried out to investigate such behaviour.

### 10.7.5 Acceleration/pressure cross-conditioning

The acceleration signatures conditioned on the wall pressure events are presented in the following. It has to be pointed put that, unlike the velocity signatures, ensemble averages were detected only for stream-wise positions before the jet impact on the plate. Specifically, the most significant signatures were detected for axial positions within the potential core. Furthermore, the amplitude of the educed averages decreased for further jet-plate distances, the resulting signatures being globally noisier. Hence, results obtained for the flat-plate radial distance  $H/D \leq 1.5$  are herein reported.

Figure 10.69 shows the dimensionless cross-conditioned acceleration signatures for the HW axial distance  $x/D = 1$  and the jet-plate distance  $H/D = 1$ . It has to be underlined that appreciable signatures were educed only for transverse positions in the proximity of the shear layer in the jet side region close to the surface. The ensemble average exhibits a dumped oscillatory trend, the time-delay of the signature peak being associated with a phase speed of the order of the jet velocity ( $\approx 0.65U_j$ ). Such a behaviour could be ascribed to the signature of a Kelvin-Helmholtz hydrodynamic

<sup>7</sup>The integral length-scale  $L$  is estimated from the first zero of the auto-correlation function of the velocity signal, which identifies the integral time-scale  $\tau_L$ .  $L$  is, thus, computed exploiting the Taylor's hypothesis as the product between  $\tau_L$  and the local mean velocity.

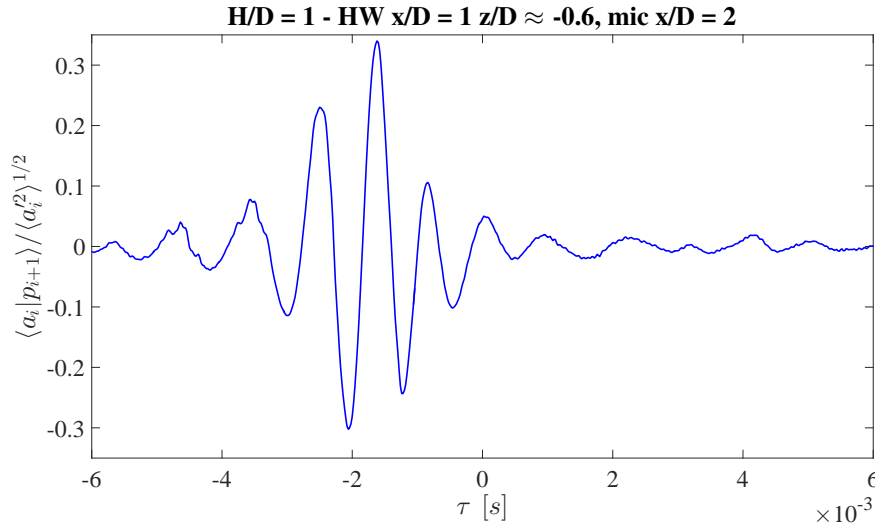


Figure 10.69: Acceleration signature conditioned on wall pressure events at the HW axial distance  $x/D = 1$  and the transverse position  $z/D \approx -0.6$  for the jet-plate distance  $H/D = 1$ .

wavepacket (Cavalieri et al., 2013), this outcome being in agreement with other results presented throughout the manuscript (see §10.6).

It is interesting to point out that the educed signature is independent of the wavelet scale considered, as represented in figure 10.70. Such a behaviour implies that the flow structure extracted by the wavelet-based conditional sampling procedure excited the wall pressure fluctuations field at all the flow-scales.

Figure 10.71 shows the cross-wise evolution of the cross-conditioned acceleration signatures at different HW axial distances within the potential core for the jet-plate configurations  $H/D = 1$  and 1.5. As underlined above, significant averages were detected in the outer shear layer of the jet close to the surface. It is observed that, as the axial distance increased, the region for which non-zero signatures were educed was found for lower transverse positions  $z$ , the ensemble averages computed being characterised by a wave-packet shape. It is interesting to point out that signatures disappear as soon as the jet impinges on the surface. The pictures of the contour maps in the  $z$ - $t$  space of the extracted signatures appear as the snapshots of the same flow structure captured in its spatial evolution along the stream-wise distance  $x$ , the track of the flow signature in the plane  $x$ - $z$  being highlighted with an arrow.

In summary, it has to be pointed out that the cross-conditioning between acceleration and wall pressure signals provides different results with respect to the ones between velocity and wall pressure signals. Specifically, relevant acceleration signatures were detected for stream-wise positions where zero velocity signatures were found, i.e. before the jet impact on the plate. The acceleration signatures were characterized by a completely different shape with respect to the velocity ones, such a behaviour implying that different flow structures were educed. Indeed, the application of the cross-conditioning procedure to the acceleration signals permitted to reveal wavepacket structures, especially within the potential core region, that are known to be the most efficient sources of jet noise (Cavalieri et al., 2011; Jordan and Colonius, 2013).

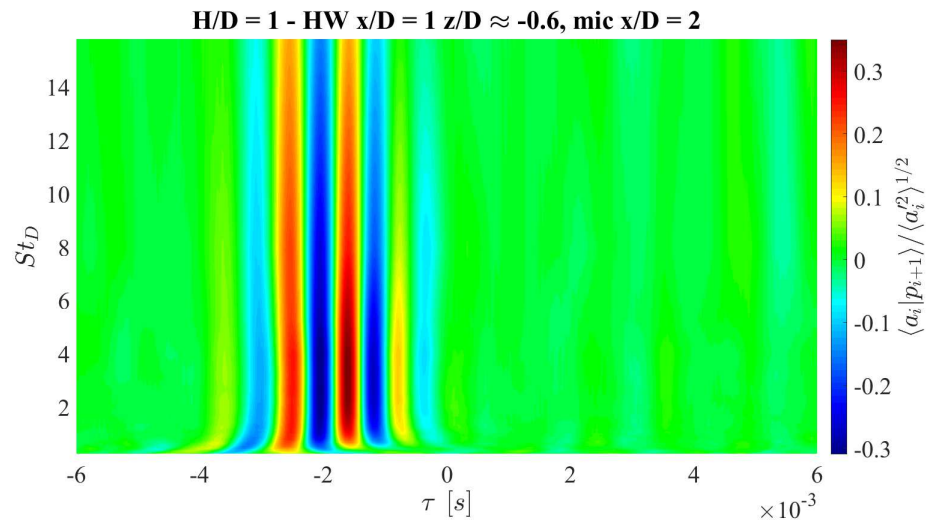


Figure 10.70: Contour map of the dimensionless acceleration signature conditioned on wall pressure events as a function of the wavelet scale/pseudo-frequency expressed as Strouhal number. HW axial distance  $x/D = 1$ , HW transverse position  $z/D \approx -0.6$ , jet-plate distance  $H/D = 1$ .

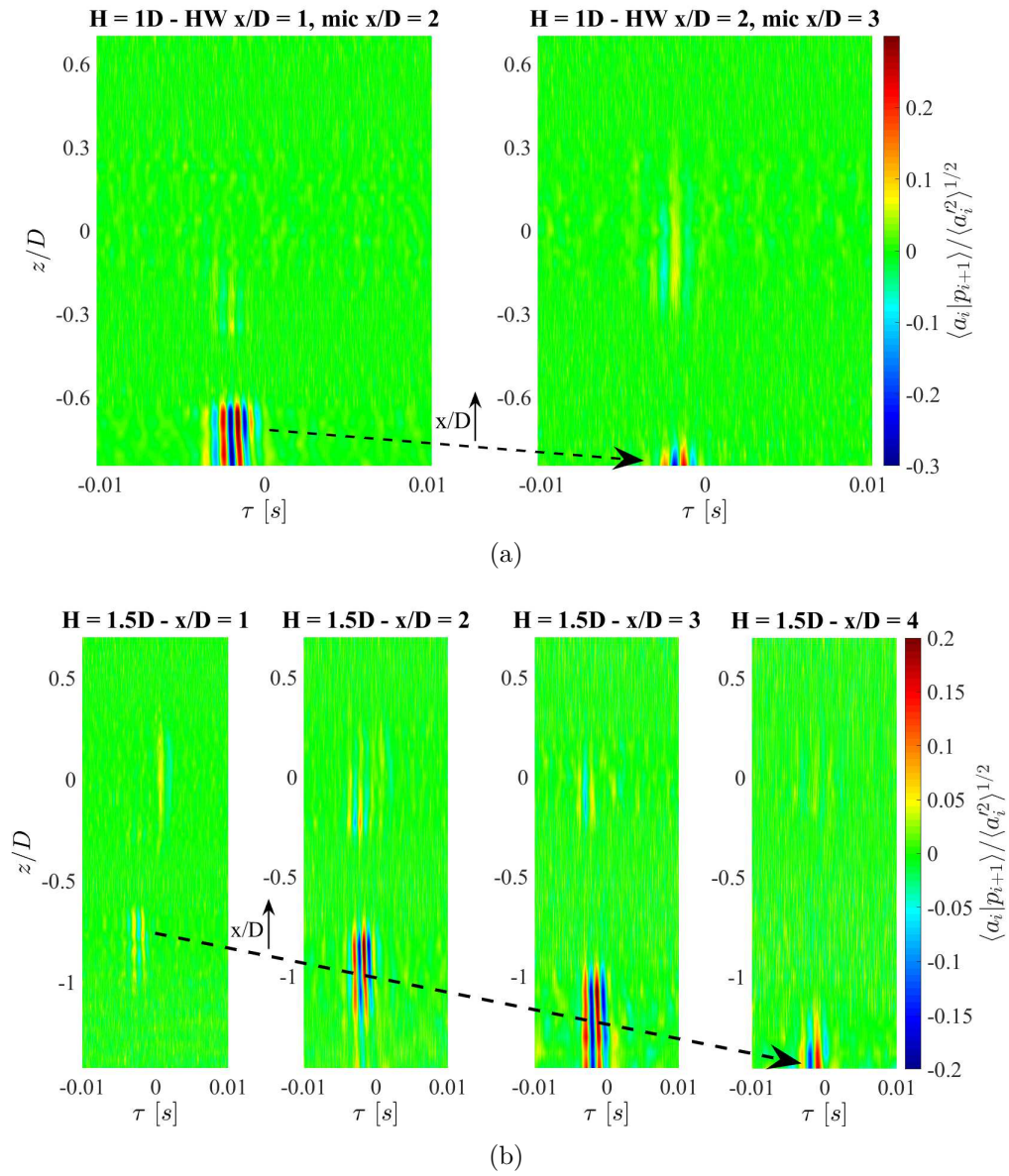


Figure 10.71: Cross-wise evolution of the dimensionless acceleration signature conditioned on wall pressure events at different HW axial distances for jet-plate distances  $H/D = 1$  and  $1.5$ .

# **Part IV**

## **Conclusions**





# Chapter 11

## Final remarks

In the present work the aerodynamics and aeroacoustics of compressible and incompressible jets have been analysed in free and installed configurations, respectively. The investigation was carried out through advanced time-frequency analysis procedures. Specifically, Fourier- and wavelet-based techniques were applied to experimental databases involving velocity and pressure measurements. The aim of the study was to exploit the time-frequency analysis approach to get a knowledge improvement of the jet physics, the jet noise production mechanism and the jet-surface interaction phenomena (installation effects). Foundations for jet noise modelling were laid as well.

### 11.1 Hydrodynamic/acoustic pressure separation

In the present work three novel signal processing techniques based on wavelet transform providing the decomposition of the near pressure field of a jet into hydrodynamic and acoustic components were introduced and validated. An experimental database involving simultaneous near- and far-field measurements of pressure fluctuations was exploited to derive the innovative methods. The experimental investigation was carried out on a single-stream jet at high Reynolds number and for two Mach numbers available in the anechoic wind tunnel of the Centre Acoustique of Laboratoire de Mécanique des Fluides et d'Acoustique at the École Centrale de Lyon. Preliminary aerodynamic and aeroacoustic qualifications of the jet were provided in terms of main statistical quantities, spectral content, cross-correlation trend and noise levels in the near field as well as in the far field.

The experimental results obtained by the application of the novel techniques were compared with the outcome provided by two further separation procedures found in the literature. The first one is a Fourier filtering technique in which the hydrodynamic and acoustic pressures are extracted based on their phase velocity in the wavenumber-frequency spectrum. The second technique is a wavelet-based procedure in which pseudo-sound and sound components are extracted from a pair of near-field pressure signals by a proper thresholding procedure.

The improvement of the efficiency of the latter method aimed at a further simplification of the set-up required to perform the hydrodynamic/acoustic pressure decomposition as well as a better understanding of the jet noise physics motivated the present work. The choice of the above-mentioned threshold was achieved establishing different convergence criteria based on the intrinsic nature of the hydrodynamic and acoustic

pressures.

1. In the wavelet technique WT1 one near-field and one far-field microphones acquiring simultaneously are required to perform the separation. The assumption underlying this procedure is that the acoustic component in the near field is associated with the pressure fluctuations destined to reach the far field. Whereas the hydrodynamic component is characterised by a very rapid decay as the radial distance from the jet axis increases. The pseudo-sound and sound components were iteratively separated until the cross-correlation peak between the near-field acoustic pressure and the far-field pressure reached a maximum. It has been shown that the choice of the polar position of the far-field microphone used to perform the separation did not affect the decomposition of the hydrodynamic and acoustic pressures. Such a result means that the separation is not dependent on the dominant noise component in the far field, i.e. large/fine-scale turbulent structures in the aft/forward arc.
2. Based on the statistical analysis of the far-field pressure, a separation technique requiring only one microphone in the near field was developed. The assumption underlying the technique WT2 is the nearly Gaussian nature of the acoustic pressure. The hydrodynamic and acoustic pressures were iteratively separated until the difference between the *PDF* of the sound component and the standard Gaussian distribution was lower than a tolerance value.
3. Based on the assumption that the hydrodynamic component is related to pressure fluctuations induced by localized coherent turbulent structures and on account of the relation between hydrodynamic pressure and vorticity, a wavelet technique used to extract the coherent structures of the vorticity field has been applied to the pressure data. In the wavelet technique WT3 the pseudo-sound and sound components were iteratively separated until the number of the wavelet coefficients related to the acoustic pressure became constant.

The proposed methods were validated against the reference separation techniques, highlighting that all the wavelet-based procedures led to very similar results.

The hydrodynamic and acoustic pressure fields have been analysed in the time and frequency domains in order to provide a statistical and spectral characterization. The axial evolution of the pseudo-sound and sound components has been described as well as the effect of the jet Mach number on the two pressure fields. Specifically, the spectral energy of the hydrodynamic pressure was found to rise as the axial distance increased. On the contrary, the energy content associated with the acoustic pressure was found to be higher for axial positions close to the nozzle exhaust. Unlike the hydrodynamic pressure spectra, the amplitude of the acoustic pressure spectra was strongly affected by the jet Mach number, the noise level being significantly enhanced for the highest jet velocity. Such a behaviour was also confirmed by the *OASPL* trends. The different characteristics of the two pressure components were highlighted by the cross-correlation trend between two consecutive near-field microphone signals. The hydrodynamic pressure was characterised by a typical negative-positive bump shape with a large time-scale related to the vortex convection. The acoustic pressure showed a narrower correlation with an oscillatory trend, its peak time-delay being related to a propagation velocity of the order of the speed of sound. The different nature of the two

pressure components also arose from the axial evolution of the third and fourth order statistical moments and of the probability density function distributions. Such results shed light on the intermittent and nearly Gaussian nature of the hydrodynamic and acoustic pressures, respectively.

Finally, with the intention of performing the hydrodynamic and acoustic pressure separation, it has to be pointed out that the  $k - \omega$  technique requires a large microphone array in order to have an acceptable resolution in the wave-number domain. On the contrary the wavelet techniques proposed require a very simple set-up consisting of two microphones at most: one in the near field and one in the far field.

Furthermore it has to be underlined that, unlike both the reference methods found in the literature, the separation achieved with the techniques proposed herein is not based on the propagation velocity of the two contributions. Hence, the present techniques could be used to separate hydrodynamic and acoustic pressures also in near-sonic and supersonic conditions.

### 11.1.1 Future developments

These methods can be easily applied to pressure signals (e.g. obtained by wind tunnel measurements) as an important device to filter out the hydrodynamic component induced by the jet flow and retain just the pressure fluctuations related to sound emissions. This aspect could be relevant, for instance, when using noise sources detection algorithm such as the beamforming technique in order to have a better identification of noise sources location and level.

The simplicity of the required set-up to perform the hydrodynamic/acoustic separation makes the proposed methods (especially the ones based on one microphone in the near field) attractive for a large variety of engineering applications, such as jet noise control and wall-bounded flows. Indeed, the separation between the acoustic component and the hydrodynamic counterpart could be likely achieved in the case of turbulent boundary layers. Such feature could be essential to develop improved prediction models for the vibrations transmitted through the surface (e.g. the interior noise transmitted to the aircraft/car cockpit). Indeed, the proposed techniques could be applied to experimental or numerical databases involving wall pressure fluctuations induced by a compressible jet on a surface, in order to separate the hydrodynamic and acoustic contributions in the incident and, successively, scattered pressure field. Hence, the separation methods could be applied to the same experimental case studied in §III, but considering a compressible jet. This task is currently underway by the author.

Future activities could concern the prediction of the far-field noise starting from the separated near-field acoustic component. The predicted results should be compared with the far-field pressure measured experimentally in order to further validate the wavelet approach herein presented.

Finally, it is author's opinion that the multi-variate and conditioned statistics between the velocity/acceleration fields generated by the jet and the separated hydrodynamic and acoustic pressures should be deeply investigated in the future in order to provide a clearer picture of the jet physics and to detect the flow structures mostly responsible for the noise emissions.

As underlined in §10.1.2, the Euler's equation establishes a relation between the acceleration and the pressure gradient. Considering only the axial component of the jet velocity  $u$ , the equation of the momentum equation can be written as follows:

$$\rho \frac{Du}{Dt} = -\nabla p \quad (11.1)$$

The left hand-side of equation (11.1) can be elaborated as described in the following. According to the Reynolds decomposition, the axial velocity can be written as the linear superimposition between the mean ( $U$ ) and fluctuating ( $u'$ ) components:

$$u(x, t) = U(x) + u'(t) \quad (11.2)$$

Hence, the material derivative of the velocity is defined as follows:

$$\frac{Du}{Dt} = \frac{\partial u}{\partial t} + u \frac{\partial u}{\partial x} = \frac{\partial (U + u')}{\partial t} + (U + u') \frac{\partial (U + u')}{\partial x} \quad (11.3)$$

After some mathematical manipulations and exploiting the Taylor's hypothesis, the acceleration is expressed by the following formula:

$$a(x, t) = \frac{\partial u'}{\partial t} \left( 2 + \frac{u'}{U} \right) \quad (11.4)$$

The right hand-side of (11.1) can be reformulated considering the near-field pressure as the linear superimposition between the mean, the hydrodynamic and acoustic components  $p(\mathbf{x}, t) = \langle p \rangle(\mathbf{x}) + p_H(\mathbf{x}, t) + p_A(\mathbf{x}, t)$ . If the pressure in the near field is acquired experimentally by microphone measurements, the mean component can be neglected and the Euler's equation reduces to the form:

$$\rho \frac{\partial u'}{\partial t} \left( 2 + \frac{u'}{U} \right) = -(\nabla p_H + \nabla p_A) \quad (11.5)$$

In summary, the analysis of the cross-statistics between the separated pseudo-sound/sound pressures and the velocity/acceleration fields as reformulated with the two terms on the left hand-side in the above equation could be helpful to better identify the noise generation mechanism in the jet.

## 11.2 Jet-plate interaction

The interaction between an incompressible jet and a flat-plate parallel to the nozzle axis was investigated experimentally through velocity and wall pressure measurements carried out for different radial distances  $H$  of the rigid surface from the nozzle axis. The core of the work was focused on the analysis of the effect of the surface on the velocity field statistics and on the investigation of the wall pressure fluctuations induced by the tangential jet flow, an issue that has never been studied before neither experimentally nor numerically. The aerodynamic field was investigated through point-wise hot-wire anemometer measurements, whereas the wall pressure fluctuations were measured by a cavity-mounted microphone array in both the stream-wise and span-wise directions. First of all, a preliminary characterization of the free jet was performed. The acceleration field computed from the HW velocity measurements exploiting the Taylor's hypothesis of frozen turbulence was deeply investigated as well. It was shown that the time derivative operation performed on the velocity signals had the effect to enhance the energetic content in the middle-high frequency range for which the Kelvin-Helmholtz instability mode is dominant.

The flat-plate effect on the velocity field has been deeply investigated, providing contour maps of the velocity statistical moments in the plane  $x$ - $z$  orthogonal to the flat-plate and parallel to the nozzle axis ( $x$  is the stream-wise or axial direction,  $z$  is the cross-wise or transverse direction). The mean aerodynamic field was found to be strongly affected by the interaction with the surface, which induces a positive or negative shift in the  $z$ -direction of the velocity and turbulence intensity profiles. Positive shifts in the  $z$ -direction of the mean velocity profiles are found at downstream positions close to the nozzle exit, whereas for increasing axial distances the velocity profiles moved towards the plate (negative shift), the jet bending towards the plate due to the Coanda effect. Hence, a distinction between the nozzle axis and the jet axis was made, the jet axis being the transverse location for which the maximum mean velocity value was measured. The fluctuating velocity profiles were found to be shifted in the positive direction along the  $z$ -axis, i.e. in the jet region opposite to the flat-plate. Globally, the turbulence intensity was found to decrease as the plate got closer to the jet. The asymmetry and the reduction of the velocity fluctuations intensity were further supported by the trend of the third and fourth order statistical moments. Such statistical analysis showed that large values of skewness and kurtosis associated with high intermittency regions were found in the inner and outer shear layers. The flat-plate had the effect to prevent the development of the outer shear layer in the jet side close to the surface, thus reducing the intermittent events strictly related to the turbulence generation.

The outcome derived from the analysis of the velocity field was confirmed by the results obtained from the analysis of the acceleration field. The profiles of the mean and fluctuating accelerations exhibited an asymmetry due to the presence of the plate. Furthermore, the larger variations of the statistical moments of the acceleration were detected in the mixing layers of the jet, the flat-plate having the effect to prevent the development of the outer shear layer of the jet close to the surface.

Wall pressure measurements on the surface were firstly carried out by an array of three cavity mounted microphones moved over a grid of points which spanned  $25D$  in the stream-wise direction and  $5D$  in the span-wise direction. The objective of this test campaign was the statistical and spectral characterization of the wall pressure field. Specifically, the energy content and the spectral shape was found to change significantly for different stream-wise locations depending on the flat-plate distance. As the axial distance increased and the jet impact on the flat-plate had occurred, spectra showed higher energy content. Far downstream of the nozzle exhaust, the pressure spectra showed a self-similar shape and energy decay laws typical of TBL wall pressure could be applied. In the span-wise direction, large differences in terms of amplitude and spectral shape are found at axial positions close to the nozzle exhaust. As the transverse distance  $y$  from the nozzle axis increased the energy content decreased. In the fully developed jet region, the spectra in the span-wise direction became very similar and tended to collapse. A global description of the fluctuating pressure field on the flat-plate was given by the *OASPL* contour map on the surface. The *OASPL* map confirmed the development in the stream-wise and span-wise directions illustrated above.

For what concerns the axial evolution of the wall pressure field, three regions were detected based on the mean and root mean square pressure distribution over the flat-plate.

- First region: the jet had not yet impacted on the flat-plate and the mean pressure coefficient was almost constant.

- Second region: the jet had impacted on the surface. The axial position of the jet impact derived from the mean pressure distribution was confirmed by the impact point obtained from the jet spreading angle evaluated by hot-wire measurements.
- Third region: the mean pressure decreased with oscillations which could be related to the large structures convected by the jet flow over the flat-plate after the jet impact. This region represents a transition to a quasi-equilibrium TBL. This assertion is confirmed by the energy decay laws typical of TBL wall pressure spectra found at large axial positions and for all the jet-plate distances.

Basic issues useful for the wall pressure spectral modelling have been also addressed. A scaling criterion for pressure auto-spectra based on global aerodynamic quantities was derived for region 2 and region 3. The scaling law is based on the convection velocity, the flat-plate distance from the nozzle axis and the mean jet velocity at the nozzle exhaust. The collapse of the normalized spectra was satisfactory. Furthermore, the coherence function along the stream-wise direction was computed for axial locations beyond the impact zone over the surface and for all the flat-plate distances. Experimental results were compared with the Corcos' model prediction. The experimental data satisfied the exponential decay of the Corcos' formulation. Specifically, for increasing axial distances from the nozzle exhaust the wall flow developed towards a fully developed TBL and the coefficient values detected for all the jet-plate configurations tended to be within the range found in the literature for the Corcos' model.

Simultaneous velocity and wall pressure fluctuation measurements were successively performed. A cross-statistical analysis between the velocity and wall pressure signals in the time and frequency domains was carried out. It has been demonstrated that the cross-statistics depends on: (i) the transverse position of the hot-wire; (ii) the stream-wise location of the hot-wire and microphones; (iii) the radial distance of the flat-plate from the jet. Specifically, it was observed that both correlation amplitude and shape were affected by the HW transverse location, the correlation level being higher for positions close to the nozzle axis. As the hot-wire was moved towards the plate, the positive-negative bump-shape turned into a positive spike, such a behaviour being ascribed to a phase shift. The cross-correlation variation as a function of the stream-wise location was studied for different HW transverse positions, focusing on the jet axis location and on the position closest to the plate. For the jet axis position an oscillatory correlation shape related to the Kelvin-Helmholtz instability was found for small axial distances. Moving downstream in the jet plume, a positive-negative bump appeared, whose time-scale enlarged due to the development of larger turbulent structures. For the HW position closest to the surface, non-zero positive spike-shape correlations were found for axial positions downstream the jet impact point on the plate.

For what concerns the cross-statistics between velocity and wall pressure signals in the frequency domain, the cross-spectra showed that for small axial distances the maximum spectral energy was found for transverse positions corresponding to the mixing layers of the jet. An energy peak for a Strouhal number  $\approx 0.47$  was clearly detected, confirming that the Kelvin-Helmholtz instability mode is dominant for axial positions within the potential core. As the axial distance increased, the cross-spectra amplitude raised spreading on a wider transverse positions range, the maximum energy being moved towards low frequencies and transverse positions close to the flat-plate.

The cross-statistics between acceleration and wall pressure fluctuations was analysed as well. The cross-correlation amplitude and shape were found to be strongly dependent on the jet-plate configuration coupled with the HW position considered. An oscillatory trend ascribed to the signature of the Kelvin-Helmholtz instability was found for transverse positions in the proximity of the nozzle axis and for axial distances inside the potential core. A reduction of the oscillations intensity was observed for HW transverse positions approaching the flat-plate, for which a dominant negative peak clearly appeared. The cross-spectra between acceleration and wall pressure exhibited a dominant energy peak for the Strouhal number characteristic of the Kelvin-Helmholtz instability. Unlike the cross-spectra between velocity and wall pressure, the spectral energy of the acceleration/pressure cross-spectrum reduced for the increasing axial distances.

A wavelet-based conditional averaging procedure was applied to educe the flow structures related to the velocity/acceleration and wall pressure fluctuation fields. The conditioning procedure is based on an energetic criterion for which time instants related to high-energy events are selected and conditioned ensemble averages of signal segments are computed. An auto-conditioning procedure was adopted to extract signatures embedded in the wall pressure and velocity/acceleration signals. A cross-conditioning procedure was also applied to wall pressure and velocity/acceleration signals in order to detect the flow structures responsible for energetic wall pressure events.

The auto-conditioned velocity signatures on the nozzle axis showed an axial evolution typical of the free-jet case. An oscillating signature was detected for axial positions within the potential core, whereas a negative spike was found immediately downstream the potential core due to the transitional behaviour of the jet. A positive spike related to a ring-like vortex was found further downstream in the jet plume. A different trend was observed for the HW transverse position closest to the flat-plate. Non-zero signatures were detected only downstream the jet impact point on the surface, their amplitude and time-scale being significantly larger for increasing jet-plate distances. According to the results concerning the turbulence intensity field, such an outcome suggests that the plate had the effect to induce the large-scale structures break-down. A scaling criterion based on the same external aerodynamic variables and main geometrical length-scales adopted to scale the wall pressure spectra was used for the velocity signatures corresponding to the HW position closest to the surface. The collapse of the velocity ensemble averages was verified, proving that the scaling variables adopted are representative of the parameters governing the jet-surface interaction phenomena.

The auto-conditioned and cross-conditioned wall pressure signatures were found to be strongly dependent on the radial distance of the flat-plate from the jet. Non-zero ensemble averages were detected for axial positions downstream the jet impact point. Specifically, for small axial and jet-plate distances positive-negative bumps associated with burst-sweep events were found. As the axial distance increased, negative pressure drops typical of the signatures detected in fully developed TBLs were observed.

Velocity signatures conditioned on wall pressure events were found for stream-wise locations downstream the jet impact point and for hot-wire positions close to the surface. It has been demonstrated that the extracted signatures were not dependent on the wavelet scale considered and exhibited a positive spike-shape associated with a convected ring-like vortex. Both the amplitude and the time-delay of the signatures were dependent on the separation distance between the hot-wire and microphones, thus highlighting the capability of the conditioning procedure of tracking the spatial evolution

of the educed structures. The stream-wise dissipation of the extracted structures was found to be essentially dominated by diffusive effects. Furthermore, it was observed that the time-scale of the signatures was larger for further plate distances from the jet, such a behaviour being another proof that the large turbulent structures are 'broken' by the effect of a closer jet-plate distance. Finally the propagation velocities of the detected structures were computed, their values being of the order of the convection velocity.

Acceleration signatures conditioned on wall pressure events were found for axial positions inside the potential core for which the jet had not yet impinged on the plate, the oscillatory shape being ascribed to a Kelvin-Helmholtz hydrodynamic wavepacket. The conditional sampling procedure adopted in the present approach appeared to be able to track the spatial evolution of the educed flow structure in the  $x$ - $z$  space up to the impact point on the plate.

### 11.2.1 Future developments

The experimental study of the jet-plate interaction phenomena in the case of a subsonic/transonic jet is a task currently under-way by the author. Such analysis has to be carried out in order to address the compressibility effects on the jet-surface interaction phenomena, this test-case being also closer to the real industrial problem of a jet interacting with an airframe surface. Indeed, in order to investigate a fully real problem, the presence of a background flight stream velocity should be definitely considered. The boundary layer of the flight stream flow over the surface is expected to have a strong impact on the installation effects of the plate close to the jet. Such issue could be investigated by performing the experimental tests in an anechoic wind tunnel facility.

Furthermore, as underlined in §11.1.1, the decomposition between the hydrodynamic and acoustic components of the wall pressure field by the application of the wavelet-based separation procedures described in §4 could be relevant to better define the vibrations transmitted through the surface (e.g. the interior noise transmitted into the aircraft cockpit) and the pressure perturbations scattered by the surface itself (noise emissions in the aeroacoustic field).



# Bibliography

- Abry, P., Fauve, S., Flandrin, P., and Laroche, C. (1994). Analysis of pressure fluctuations in swirling turbulent flows. *J. Phys. II*, 4(5):725–733.
- Al-Qutub, A. M. and Budair, M. O. (1995). Experiments on the flow over a flat surface impinged by a supersonic jet. In *31<sup>st</sup> AIAA, ASME, SAE, and ASEE, Joint Propulsion Conference*, page 2935.
- Amiet, R. K. (1975). Acoustic radiation from an airfoil in a turbulent stream. *J. Sound Vib.*, 41(4):407–420.
- Amiet, R. K. (1976). Noise due to turbulent flow past a trailing edge. *J. Sound Vib.*, 47(3):387–393.
- Antoine, Y., Lemoine, F., and Lebouché, M. (2001). Turbulent transport of a passive scalar in a round jet discharging into a coflowing stream. *Eur. J. Mech. B. Fluids*, 20(2):275–301.
- Arndt, R. E. A., Long, D. F., and Glauser, M. N. (1997). The proper orthogonal decomposition of pressure fluctuations surrounding a turbulent jet. *J. Fluid Mech.*, 340:1–33.
- Azzalini, A., Farge, M., and Schneider, K. (2005). Nonlinear wavelet thresholding: A recursive method to determine the optimal denoising threshold. *Appl. Comput. Harmon. Anal.*, 18(2):177–185.
- Bogey, C. and Bailly, C. (2007). An analysis of the correlations between the turbulent flow and the sound pressure fields of subsonic jets. *J. Fluid Mech.*, 583:71–97.
- Bogey, C., Marsden, O., and Bailly, C. (2012a). Effects of moderate Reynolds numbers on subsonic round jets with highly disturbed nozzle-exit boundary layers. *Phys. Fluids*, 24(10):105107.
- Bogey, C., Marsden, O., and Bailly, C. (2012b). Influence of initial turbulence level on the flow and sound fields of a subsonic jet at a diameter-based Reynolds number of  $10^5$ . *J. Fluid Mech.*, 701:352–385.
- Brooks, T. F. and Hodgson, T. H. (1981). Trailing edge noise prediction from measured surface pressures. *J. Sound Vib.*, 78(1):69–117.
- Brown, C. and Wernet, M. (2014). Jet-surface interaction test: Flow measurement results. In *20<sup>th</sup> AIAA/CEAS Aeroacoustics Conference*, page 3198. American Institute of Aeronautics and Astronautics.

- Brown, C. A. (2013). Jet-surface interaction test: Far-field noise results. *J. Eng. Gas Turbines Power*, 135(7):071201.
- Bull, M. K. (1967). Wall-pressure fluctuations associated with subsonic turbulent boundary layer flow. *J. Fluid Mech.*, 28(4):719–754.
- Camussi, R. and Di Felice, F. (2006). Statistical properties of vortical structures with spanwise vorticity in zero pressure gradient turbulent boundary layers. *Phys. Fluids*, 18(3):035108.
- Camussi, R., Grilliat, J., Caputi Gennaro, G., and Jacob, M. C. (2010). Experimental study of a tip leakage flow: wavelet analysis of pressure fluctuations. *J. Fluid Mech.*, 660:87–113.
- Camussi, R. and Grizzi, S. (2014). Statistical analysis of the pressure field in the near region of a  $m = 0.5$  circular jet. *Int. J. Aeroacoust.*, 13(1-2):169–181.
- Camussi, R. and Guj, G. (1997). Orthonormal wavelet decomposition of turbulent flows: intermittency and coherent structures. *J. Fluid Mech.*, 348:177–199.
- Camussi, R. and Guj, G. (1999). Experimental analysis of intermittent coherent structures in the near field of a high Re turbulent jet flow. *Phys. Fluids*, 11(2):423–431.
- Camussi, R., Guj, G., and Ragni, A. (2006). Wall pressure fluctuations induced by turbulent boundary layers over surface discontinuities. *J. Sound Vib.*, 294(1):177–204.
- Camussi, R., Robert, G., and Jacob, M. C. (2008). Cross-wavelet analysis of wall pressure fluctuations beneath incompressible turbulent boundary layers. *J. Fluid Mech.*, 617:11–30.
- Cavaleri, A. V. G., Jordan, P., Agarwal, A., and Gervais, Y. (2011). Jittering wavepacket models for subsonic jet noise. *J. Sound Vib.*, 330(18):4474–4492.
- Cavaleri, A. V. G., Jordan, P., Wolf, W. R., and Gervais, Y. (2014). Scattering of wavepackets by a flat plate in the vicinity of a turbulent jet. *J. Sound Vib.*, 333(24):6516–6531.
- Cavaleri, A. V. G., Rodríguez, D., Jordan, P., Colonius, T., and Gervais, Y. (2013). Wavepackets in the velocity field of turbulent jets. *J. Fluid Mech.*, 730:559–592.
- Chatellier, L. and Fitzpatrick, J. (2005). Spatio-temporal correlation analysis of turbulent flows using global and single-point measurements. *Exp. Fluids*, 38(5):563–575.
- Chen, Y. S. and Kim, S. W. (1987). Computation of turbulent flows using an extended  $k-\epsilon$  turbulence closure model. *NASA STI/Recon Technical Report N*, 88.
- Chernoff, H. and Lehmann, E. L. (1954). The use of maximum likelihood estimates in  $\chi^2$  tests for goodness of fit. *Ann. Math. Stat.*, 25(3):579–586.
- Corcos, G. M. (1963). Resolution of pressure in turbulence. *J. Acoust. Soc. Am.*, 35(2):192–199.

- Danaila, I., Dušek, J., and Anselmet, F. (1997). Coherent structures in a round, spatially evolving, unforced, homogeneous jet at low Reynolds numbers. *Phys. Fluids*, 9(11):3323–3342.
- Daubechies, I. (1992). *Ten lectures on wavelets*, volume 61. SIAM.
- Dhanak, M. R., Dowling, A. P., and Si, C. (1997). Coherent vortex model for surface pressure fluctuations induced by the wall region of a turbulent boundary layer. *Phys. Fluids*, 9(9):2716–2731.
- Di Marco, A., Camussi, R., Bernardini, M., and Pirozzoli, S. (2013). Wall pressure coherence in supersonic turbulent boundary layers. *J. Fluid Mech.*, 732:445–456.
- Di Marco, A., Mancinelli, M., and Camussi, R. (2015). Pressure and velocity measurements of an incompressible moderate Reynolds number jet interacting with a tangential flat plate. *J. Fluid Mech.*, 770:247–272.
- Di Marco, A., Mancinelli, M., and Camussi, R. (2016). Flow-induced pressure fluctuations of a moderate reynolds number jet interacting with a tangential flat plate. *Adv. Aircr. Spacecr. Sc.*
- Donaldson, C. and Snedeker, R. (1971). A study of free jet impingement. part 1. mean properties of free and impinging jets. *J. Fluid Mech.*, 2:281–319.
- Donoho, D. L. and Johnstone, J. M. (1994). Ideal spatial adaptation by wavelet shrinkage. *Biometrika*, 81(3):425–455.
- Ebbesen, S., Kiwitz, P., and Guzzella, L. (2012). A generic particle swarm optimization matlab function. In *American Control Conference*, pages 1519–1524. IEEE.
- Farabee, T. M. and Casarella, M. J. (1991). Spectral features of wall pressure fluctuations beneath turbulent boundary layers. *Phys. Fluids*, 3(10):2410–2420.
- Farge, M. (1992). Wavelet transforms and their applications to turbulence. *Annu. Rev. Fluid Mech.*, 24(1):395–458.
- Farge, M. and Schneider, K. (2006). Wavelets: application to turbulence. *Encyclopedia of Mathematical Physics*, pages 408–20.
- Farge, M. and Schneider, K. (2015). Wavelet transforms and their applications to mhd and plasma turbulence: a review. *J. Plasma Phys.*, 81(06):435810602.
- Ffowcs Williams, J. E. (1969). Hydrodynamic noise. *Ann. Rev. Fluid Mech.*, 1(1):197–222.
- Finnveden, S., Birgersson, F., Ross, U., and Kremer, T. (2005). A model of wall pressure correlation for prediction of turbulence-induced vibration. *J. Fluids Struct.*, 20(8):1127–1143.
- Fischer, H. B., List, E. J., Koh, R. C. Y., Imberger, J., and Brooks, N. H. (1979). *Mixing in Inland and Coastal Waters*. Academic Press.

- Fuchs, H. V. (1972). Space correlations of the fluctuating pressure in subsonic turbulent jets. *J. Sound Vib.*, 23(1):77–99.
- Gabor, D. (1946). Theory of communication. part 1: The analysis of information. *J. I. Electron. Rad. Eng.*, 93(26):429–441.
- Goldstein, M. E. (1984). Aeroacoustics of turbulent shear flows. *Annu. Rev. Fluid Mech.*, 16(1):263–285.
- Grizzi, S. and Camussi, R. (2012). Wavelet analysis of near-field pressure fluctuations generated by a subsonic jet. *J. Fluid Mech.*, 698:93–124.
- Guillon, A., Jordan, P., Laurendeau, E., and Delville, J. (2007). Velocity dependence of the near pressure field of subsonic jets: understanding the associated source mechanisms. In *13<sup>th</sup> AIAA/CEAS Aeroacoustics Conference*, page 3661. American Institute of Aeronautics and Astronautics.
- Guj, G. and Camussi, R. (1999). Statistical analysis of local turbulent energy fluctuations. *J. Fluid Mech.*, 382:1–26.
- Guj, G., Carley, M., Camussi, R., and Ragni, A. (2003). Acoustic identification of coherent structures in a turbulent jet. *J. Sound Vib.*, 259(5):1037–1065.
- Hanjalić, K. and Mullyadzhanov, R. (2015). On spatial segregation of vortices and pressure eddies in a confined slot jet. *Phys. Fluids*, 27(3):031703.
- Heisenberg, W. (1927). Über den anschaulichen inhalt der quantentheoretischen kinematik und mechanik. *Zeitschrift für Physik*, 43(3-4):172–198.
- Heisenberg, W. (1983). The actual content of quantum theoretical kinematics and mechanics. Technical Report 84N17046, NASA.
- Henning, A., Koop, L., and Schröder, A. (2013). Causality correlation analysis on a cold jet by means of simultaneous particle image velocimetry and microphone measurements. *J. Sound Vib.*, 332(13):3148–3162.
- Heskestad, G. (1965). A generalized taylor hypothesis with application for high reynolds number turbulent shear flows. *J. Appl. Mech.*, 32(4):735–739.
- Howes, W. L. (1960). Distribution of time-averaged pressure fluctuations along the boundary of a round subsonic jet. Technical report NASA-TN-D-468, NASA.
- Huber, J., Drochon, G., Pintado-Peno, A., Cléro, F., and Bodard, G. (2014). Large-scale jet noise testing, reduction and methods validation "exejet": 1. project overview and focus on installation. In *20<sup>th</sup> AIAA/CEAS Aeroacoustics Conference*, page 3032. American Institute of Aeronautics and Astronautics.
- Huber, J., Omais, M., Vuillemin, A., and Davy, R. (2009). Characterization of installation effects for hbpr engine part iv: Assessment of jet acoustics. In *15<sup>th</sup> AIAA/CEAS Aeroacoustics Conference*, page 3371. American Institute of Aeronautics and Astronautics.

- Hwang, Y. F., Bonness, W. K., and Hambric, S. A. (2009). Comparison of semi-empirical models for turbulent boundary layer wall pressure spectra. *J. Sound Vib.*, 319(1-2):199–217.
- Jayasundera, S., Casarella, M., and Russell, S. (1996). Identification of coherent motions using wall pressure signatures. Technical report, DTIC Document.
- Johansson, A. V., Her, J., and Haritonidis, J. H. (1987). On the generation of high-amplitude wall-pressure peaks in turbulent boundary layers and spots. *J. Fluid Mech.*, 175:119–142.
- Jordan, P. and Colonius, T. (2013). Wave packets and turbulent jet noise. *Annu. Rev. Fluid Mech.*, 45:173–195.
- Jung, D., Gamard, S., and George, W. K. (2004). Downstream evolution of the most energetic modes in a turbulent axisymmetric jet at high Reynolds number. Part 1. The near-field region. *J. Fluid Mech.*, 514:173–204.
- Juvé, D., Sunyach, M., and Comte-Bellot, G. (1980). Intermittency of the noise emission in subsonic cold jets. *J. Sound Vib.*, 71(3):319–332.
- Kearney-Fischer, M., Sinha, A., and Samimy, M. (2013). Intermittent nature of subsonic jet noise. *AIAA J.*, 51(5):1142–1155.
- Kerhervé, F., Guitton, A., Jordan, P., Delville, J., Fortuné, V., Gervais, Y., and Tinney, C. (2008). Identifying the dynamics underlying the large-scale and fine-scale jet noise similarity spectra. In *14<sup>th</sup> AIAA/CEAS Aeroacoustics Conference*, page 3027. American Institute of Aeronautics and Astronautics.
- Kolmogorov, A. N. (1941). The local structure of turbulence in an incompressible fluid for very large Reynolds numbers. *Dokl. Akad. Nauk SSSR*, 30(4):301–305. Reprinted in *Proc. R. Soc. Lond A* (1991) **434**, 9–13.
- Lamont, P. J. and Hunt, B. L. (1980). The impingement of underexpanded, axisymmetric jets on perpendicular and inclined flat plates. *J Fluid Mech.*, 100:471–511.
- Landau, L. D. and Lifshitz, E. M. (1985). Fluid mechanics. Pergamon Press, Oxford.
- Lau, J. C., Fisher, M. J., and Fuchs, H. V. (1972). The intrinsic structure of turbulent jets. *J. Sound Vib.*, 22(4):379–406.
- Lauder, B. E. and Rodi, W. (1983). The turbulent wall jet measurements and modeling. *Annu. Rev. Fluid Mech.*, 15(1):429–459.
- Lawrence, J. L. T., Azarpeyvand, M., and Self, R. H. (2011). Interaction between a flat plate and a circular subsonic jet. In *17<sup>th</sup> AIAA/CEAS Aeroacoustics Conference*, page 2745. American Institute of Aeronautics and Astronautics.
- Lighthill, M. J. (1952). On sound generated aerodynamically I. General theory. *Proc. R. Soc. Lond. A*, 211(1107):564–587.
- Lilley, G. M. (1991). Jet noise classical theory and experiments. *Aeroacoust. Flight Vehicles*, 1:211–289.

- Lin, C. C. (1953). On Taylor's hypothesis and the acceleration terms in the Navier-Stokes equations. *Q. Appl. Math.*, 10(4):295–306.
- Mallat, S. G. (1989). A theory for multiresolution signal decomposition: the wavelet representation. *Trans. IEEE Pattern Anal. Machine Intell.*, 11(7):674–693.
- Mancinelli, M. and Camussi, R. (2017). Cross- and conditioned statistics between acceleration and wall pressure fluctuations generated by an incompressible jet in installed configuration (under revision). *C. R. Mécanique*.
- Mancinelli, M., Di Marco, A., and Camussi, R. (2016a). Cross-statistical and wavelet analysis of velocity and wall-pressure fields in jet-surface interaction. In *22<sup>nd</sup> AIAA/CEAS Aeroacoustics Conference*, page 2861.
- Mancinelli, M., Di Marco, A., and Camussi, R. (2017a). Multi-variate and conditioned statistics of velocity and wall pressure fluctuations induced by a jet interacting with a flat-plate (in press). *J. Fluid Mech.*
- Mancinelli, M., Pagliaroli, T., Di Marco, A., Camussi, R., and Castelain, T. (2017b). Wavelet decomposition of hydrodynamic and acoustic pressures in the near field of the jet. *J. Fluid Mech.*, 813:716–749.
- Mancinelli, M., Pagliaroli, T., Di Marco, A., Camussi, R., Castelain, T., and Léon, O. (2016b). Hydrodynamic and acoustic wavelet-based separation of the near-field pressure of a compressible jet. In *22<sup>nd</sup> AIAA/CEAS Aeroacoustics Conference*, page 2864.
- Meneveau, C. (1991). Analysis of turbulence in the orthonormal wavelet representation. *J. Fluid Mech.*, 232:469–520.
- Meyers, S. D., Kelly, B. G., and O'Brien, J. J. (1993). An introduction to wavelet analysis in oceanography and meteorology: With application to the dispersion of Yanai waves. *Mon. Weather Rev.*, 121(10):2858–2866.
- Moore, C. J. (1977). The role of shear-layer instability waves in jet exhaust noise. *J. Fluid Mech.*, 80(02):321–367.
- Or, C. M., Lam, K. M., and Liu, P. (2011). Potential core lengths of round jets in stagnant and moving environments. *J. Hydro-environ. Res.*, 5(2):81–91.
- Pagliaroli, T., Camussi, R., Giacomazzi, E., and Giulietti, E. (2015). Velocity measurement of particles ejected from a small-size solid rocket motor. *J. Propul. Power*, pages 1–8.
- Papamoschou, D. and Mayoral, S. (2009). Experiments on shielding of jet noise by airframe surfaces. In *15<sup>th</sup> AIAA/CEAS Aeroacoustics Conference*, page 3326.
- Perez, R. and Behdinan, K. (2007). Particle swarm approach for structural design optimization. *Comput. Struct.*, 85(19):1579–1588.

- Piantanida, S., Jaunet, V., Huber, J., Wolf, W., Jordan, P., and Cavalieri, A. V. G. (2015). Scattering of turbulent-jet wavepackets by a swept trailing edge. In *21<sup>st</sup> AIAA/CEAS Aeroacoustics Conference*, page 2998. American Institute of Aeronautics and Astronautics.
- Picard, C. and Delville, J. (2000). Pressure velocity coupling in a subsonic round jet. *Intl J. Heat Fluid Flow*, 21(3):359–364.
- Pierce, A. D. (1981). *Acoustics: an introduction to its physical principles and applications*. McGraw-Hill New York.
- Podboy, G. G. (2012). Jet-surface interaction test: phased array noise source localization results. In *ASME Turbo Expo 2012: Turbine Technical Conference and Exposition*, pages 381–414. American Society of Mechanical Engineers.
- Raffel, M., Willert, C. E., Wereley, S., and Kompenhans, J. (2007). *Particle Image Velocimetry: A Practical Guide*. Experimental Fluid Mechanics. Springer Berlin Heidelberg.
- Ribner, H. S. (1962). *Aerodynamic Sound from Fluid Dilatations: A Theory of the Sound from Jets and Other Flows*. UTIA report: Institute of Aerophysics. University of Toronto, Institute of Aerophysics.
- Ristorcelli, J. R. (1997). A pseudo-sound constitutive relationship for the dilatational covariances in compressible turbulence. *J. Fluid Mech.*, 347:37–70.
- Ross, S. M. (2014). *Introduction to probability and statistics for engineers and scientists*. Academic Press.
- Ruppert-Felsot, J., Farge, M., and Petitjeans, P. (2009). Wavelet tools to study intermittency: application to vortex bursting. *J. Fluid Mech.*, 636:427–453.
- Smith, M. J. and Miller, S. A. E. (2013). The effects of surfaces on the aerodynamics and acoustics of jet flows. In *19<sup>th</sup> AIAA/CEAS Aeroacoustics Conference*, page 2041.
- Suzuki, T. and Colonius, T. (2006). Instability waves in a subsonic round jet detected using a near-field phased microphone array. *J. Fluid Mech.*, 565:197–226.
- Tam, C. K. W., Golebiowski, M., and Seiner, J. M. (1996). On the two components of turbulent mixing noise from supersonic jets. In *2<sup>nd</sup> AIAA/CEAS Aeroacoustics Conference*, page 1716. American Institute of Aeronautics and Astronautics.
- Tam, C. K. W., Viswanathan, K., Ahuja, K. K., and Panda, J. (2008). The sources of jet noise: experimental evidence. *J. Fluid Mech.*, 615:253–292.
- Tanna, H. K. (1977). An experimental study of jet noise part i: Turbulent mixing noise. *J. Sound Vib.*, 50(3):405–428.
- Taylor, G. I. (1938). The spectrum of turbulence. In *Proc. R. Soc. Lond. A*, volume 164, pages 476–490. The Royal Society.
- Tinney, C. E. and Jordan, P. (2008). The near pressure field of co-axial subsonic jets. *J. Fluid Mech.*, 611:175–204.

- Tinney, C. E., Jordan, P., Hall, A. M., Delville, J., and Glauser, M. N. (2007). A time-resolved estimate of the turbulence and sound source mechanisms in a subsonic jet flow. *J. Turbul.*, 8(7):1–20.
- Torrence, C. and Compo, G. P. (1998). A practical guide to wavelet analysis. *Bull. Am. Meteorol. Soc.*, 79(1):61–78.
- Tsuji, Y., Fransson, J. H. M., Alfredsson, P. H., and Johansson, A. V. (2007). Pressure statistics and their scaling in high-reynolds-number turbulent boundary layers. *J. Fluid Mech.*, 585:1–40.
- Uddin, M. and Pollard, A. (2007). Self-similarity of coflowing jets: the virtual origin. *Phys. Fluids*, 19:068103.
- Ukeiley, L. S. and Ponton, M. K. (2004). On the near field pressure of a transonic axisymmetric jet. *Int. J. Aeroacoust.*, 3(1):43–65.
- Vera, J., Lawrence, J. L. T., Self, R. H., and Kingan, M. (2015). The prediction of the radiated pressure spectrum produced by jet-wing interaction. In 21<sup>st</sup> *AIAA/CEAS Aeroacoustics Conference*, page 2216. American Institute of Aeronautics and Astronautics.
- Viswanathan, K. (2004). Aeroacoustics of hot jets. *J. Fluid Mech.*, 516:39–82.
- Viswanathan, K. (2006). Scaling laws and a method for identifying components of jet noise. *AIAA J.*, 44(10):2274–2285.